

k-t-sub-Nyquist sampled Parallel Echo Planar Imaging in MRI



DISSERTATION
ZUR ERLANGUNG DES DOKTORGRADES
DER FAKULTÄT FÜR MATHEMATIK UND PHYSIK
DER ALBERT-LUDWIGS-UNIVERSITÄT
FREIBURG IM BREISGAU

VORGELEGT VON
REBECCA RAMB
GEBOREN AM 15. MAI 1987

FEBRUAR 2016

Dekan: Prof. Dr. Dietmar Kröner
Referent: Prof. Dr. Dr. h.c. Jürgen Hennig
Koreferent: Prof. Dr. Martin Schumacher
Tag der mündlichen Prüfung: 2. Mai 2016

Für meine Familie und Freunde

Contents

1	The general inverse problem in magnetic resonance imaging	1
2	Signal origin in nuclear magnetic resonance	9
2.1	Quantum mechanical description of spin	9
2.2	Spin induced magnetic moments	11
2.3	Macroscopic magnetization	13
2.4	Bloch equation	14
2.5	RF excitation	15
2.6	Relaxation	17
2.7	The MR signal	19
2.8	Field inhomogeneities and free induction decay	20
2.9	Noise in MR measurements	21
3	Fourier imaging	25
3.1	Slice selective excitation	25
3.2	Fourier encoding	27
3.2.1	Concept of k-space	28
3.2.2	Sampling of k-space	30
3.3	Fourier image reconstruction	31
3.3.1	Nyquist-Shannon sampling theorem	34
3.3.2	Point spread function and spatial resolution	37
3.3.3	Signal-to-noise-ratio (SNR) in Fourier image reconstruction	40
3.3.4	Summary of Fourier image reconstruction	44
3.4	Pulse sequences in magnetic resonance imaging	44
3.4.1	Gradient echo (GE) sequence	45
3.4.2	Echo Planar Imaging (EPI) sequence	48
3.4.3	Summary of Echo Planar Imaging	54
3.5	Partial-Fourier sampling and image reconstruction	54
3.5.1	Constrained phase reconstruction in Partial-Fourier sampling	55
3.6	Sub-Nyquist sampling	56
4	Parallel imaging	59
4.1	Multiple receive coils: Imaging in parallel	59
4.2	Short history of parallel imaging	60
4.3	Sensitivity encoding and the inverse problem in parallel imaging	61
4.3.1	Cartesian SENSE: unfolding in image space	64
4.4	Estimation of spatial harmonics: from SMASH to GRAPPA	65
4.5	In vivo sensitivities and the inverse problem of weight calibration	66
4.5.1	GRAPPA: estimation in k-space	68

4.5.2	GRAPPA in image space	70
4.6	SNR in parallel imaging	70
4.6.1	The SENSE g-factor	71
4.6.2	The GRAPPA g-factor	74
4.6.3	Summary of g-factors	76
4.7	Parallel imaging and sub-Nyquist sampled EPI	76
5	Dynamic magnetic resonance imaging	79
5.1	Concept and sampling of k-t-space	79
5.2	Fourier image reconstruction in dynamic MRI	81
5.3	Sub-Nyquist sampling in k-t-space	81
5.4	Time-resolved parallel imaging	82
5.4.1	Literature overview: Time-resolved parallel imaging	82
5.4.2	k-t-GRAPPA	85
5.5	Clinical applications of dynamic echo planar imaging	87
5.5.1	Dynamic susceptibility contrast weighted cerebral perfusion imaging	87
	Contributions of this thesis and current state of research	91
6	Towards a unified general framework for parallel imaging	93
6.1	Static imaging with SENSE and GRAPPA: differences and similarities	93
6.1.1	Theory: from SENSE to GRAPPA	94
6.1.2	Methods: truncated SENSE and extended GRAPPA	96
6.1.3	Results: influences of kernel extent and weight calibration	97
6.1.4	Discussion	98
6.2	From static to dynamic MRI: Generalized framework for k-t-based methods	100
6.2.1	Theory: k-t-GRAPPA and g-factors in x-f-space	101
6.2.2	Methods: signal and noise transfer analysis in cardiac MRI	106
6.2.3	Results: signal and noise transfer in a cardiac application	109
6.2.4	Discussion	119
6.3	Summary of the g-factor analysis in (time-resolved) parallel imaging	124
7	k-t-sub-Nyquist sampled parallel EPI	125
7.1	Goals	125
7.2	Methods	126
7.2.1	Data acquisition strategies	126
7.2.2	Image reconstruction for k-t-EPI	131
7.2.3	In vivo measurements with flip angle induced dynamics	132
7.2.4	First-pass bolus perfusion in vivo measurements	134
7.3	Results	136
7.3.1	Measurements with flip angle induced dynamics	136
7.3.2	DSC weighted cerebral perfusion	143
7.4	Discussion	147
8	Summary and outlook	155
	List of paper and conference contributions	159
	Bibliography	161

Acronyms	175
List of symbols	177
Acknowledgements	183

Chapter 1

The general inverse problem in magnetic resonance imaging

Tomographic imaging techniques always involve some sort of **encoding** of the imaged volume, where the imaged quantity m of an object space X is observed indirectly. These techniques may be generally expressed using a Fredholm integral of first order. In the measurement, the observations d of the domain \mathcal{K} are modeled by

$$d(\mathbf{k}) = \int_V E(\mathbf{k}, \mathbf{r})m(\mathbf{r})d\mathbf{r}, \quad \text{for } \mathbf{k} \in \mathcal{K}, \quad (1.1)$$

where V denotes the imaging volume. The encoding kernel function E is assumed to be known. Data are received by some detector for a number of samples N_{smp} . Assuming a linear response of the detector, this leads to measurement evaluations of

$$d_n = \int_V E(\mathbf{k}_n, \mathbf{r})m(\mathbf{r})d\mathbf{r}, \quad \text{for } n = 1, \dots, N_{\text{smp}}, \quad (1.2)$$

which can be collectively represented by a vector \mathbf{d} . Typical for tomographic imaging is that any individual observation contains information of m over the entire volume. Reconstructing the information m constitutes an **inverse problem**.

A general formulation of the inverse problem - beyond tomographic imaging - is presented in [Bertero et al., 1985], where X is any class of functions. The inverse problem is then expressed solely based on a set of functionals in X . Assuming X to be a Hilbert space, the Riesz representation theorem is used to characterize the inverse problem based on a set of functions as well as the inner product of X .

Definition 1.0.1 (The general inverse problem). *Let X be a Hilbert space with inner product $\langle \cdot | \cdot \rangle_X$. Given the set of functions $\{\phi_n\}_{n=1}^{N_{\text{smp}}}$, where $\phi_n \in X$, and the set of data samples $\{d_n\}_{n=1}^{N_{\text{smp}}}$, where $d_n \in \mathbb{C}$, the image reconstruction problem is to find $m \in X$ such that $\langle m | \phi_n \rangle_X = d_n$, for $n = 1, \dots, N_{\text{smp}}$.*

The process of solving the inverse problem has many names, depending on the context of usage. In the case of **magnetic resonance imaging (MRI)**, solving the inverse problem is referred to as **image reconstruction**.

Fourier encoding in MRI

In MRI, the tissue of interest within the imaging volume V , is exposed to a static magnetic field and the transverse magnetization density m is generated by radio-frequency (RF) pulse excitation. Spatial encoding is performed with spatially varying magnetic fields, such that signal is received in Fourier space as spatial frequencies. Therefore, the measured signal data follows the general form of (1.2), where the encoding kernels are determined by the Fourier basis. The main mechanisms of signal formation - based on nuclear magnetic resonance (NMR) - are described in Chapter 2.

For MRI, $\mathbf{r} \in \mathbb{R}^{\mathfrak{D}}$ comprises the spatial dimensions to be imaged, where $\mathfrak{D} = 2$ or $\mathfrak{D} = 3$ in two- or three-dimensional imaging, respectively. Limited spatial extent of the imaged area/volume justifies the assumption of a compact region $\Omega \subset \mathbb{R}^{\mathfrak{D}}$ of support for the reconstructed image function. In accordance with the encoding process, $m \in \mathcal{L}^2(\Omega, \mathbb{C})$ is assumed. In general, the measured signal depends on many further parameters besides spatial origin, such as temporal variations, diffusivity, signal relaxation and the spin density, which may be included in the signal model. Restricting considerations to the spatial coordinates, the encoding kernel function of **Fourier imaging** is given by

$$E(\mathbf{k}, \mathbf{r}) = \exp(-i\mathbf{k} \cdot \mathbf{r}), \quad (1.3)$$

where $\mathbf{k} \in \mathbb{R}^{\mathfrak{D}}$ are the coordinates in the encoding domain \mathcal{K} , which is referred to as **k-space** in MRI. Further, \cdot denotes the inner product of the two real-valued vectors.

The sampling of signal, hence the collection of encoding kernel functions, is chosen in accordance with the **Nyquist-Shannon sampling criterion**. A finite amount of discrete signal samples $\{d_n \in \mathbb{C}, n = 1, \dots, N_{\text{smp}}\}$, is acquired. Therefore, image reconstruction implies finding an approximation of m within a subspace of finite dimension. It is then evaluated for a set of pixels to form the digital image. The general inverse problem of Fourier imaging is formulated analogous to Def. 1.0.1.

Definition 1.0.2 (The general inverse problem in MRI). *Consider the Hilbert space $\mathcal{L}^2(\Omega, \mathbb{C})$, where $\Omega \subseteq V \subset \mathbb{R}^{\mathfrak{D}}$, and where $\langle \cdot | \cdot \rangle_{\mathcal{L}^2}$ denotes the inner product. Given the set of encoding functions $\{\phi_n\}_{n=1}^{N_{\text{smp}}}$, where $\phi_n := \exp(i\mathbf{k}_n \cdot \cdot)$ and the set of data samples $\{d_n\}_{n=1}^{N_{\text{smp}}}$, where $d_n \in \mathbb{C}$, the image reconstruction problem is to find $m \in \mathcal{L}^2(\Omega, \mathbb{C})$ such that*

$$\langle m | \exp(i\mathbf{k}_n \cdot \cdot) \rangle_{\mathcal{L}^2} := \int_V m(\mathbf{r}) \exp(-i\mathbf{k}_n \cdot \mathbf{r}) d\mathbf{r} = d_n, \quad \text{for } n = 1, \dots, N_{\text{smp}}.$$

Whenever the functions ϕ_n are linearly independent, the existence of a solution to the inverse problem is guaranteed. Nevertheless, the solution is not uniquely determined due to finite sampling. In this case and under the assumption of noiseless samples, the **minimum norm solution** (here denoted by I^\dagger) is typically chosen to obtain a unique solution [Bertero et al., 1985]. Figure 1.1 illustrates the general inverse problem of MRI and its solution in the case of (noiseless) Fourier imaging.

Fourier encoding and Fourier image reconstruction in MRI is specifically considered in Chapter 3. It is shown that the compact support allows for unique image reconstruction in the case of discrete - yet infinite - sampling when serving the Nyquist-Shannon sampling theorem. It is noted here that this could be likewise expressed in a more general picture, where the compact support is embedded - by periodic extension - in a \mathfrak{D} -Torus $\mathbb{R}^{\mathfrak{D}}/\mathbb{Z}^{\mathfrak{D}}$.

Noisy and hybrid encoding in MRI

In the (very likely) case that the functions ϕ_n are not linearly independent, the minimum norm solution for the problem defined in Def. 1.0.2 cannot be derived. In fact, linear independence can hardly be determined from the experiment itself, since measurement errors influence the encoding functions. The **least-squares method** as part of regression analysis is a typical approach in these cases.

If the functions ϕ_n cannot be assumed to be linearly independent and if the data d_n are affected by measurement errors, the inner product $\langle \cdot | \cdot \rangle_2$ of the data space $\mathbb{C}^{N_{\text{smp}}}$ is further necessary to characterize the inverse problem for these cases. With the definition of a linear operator

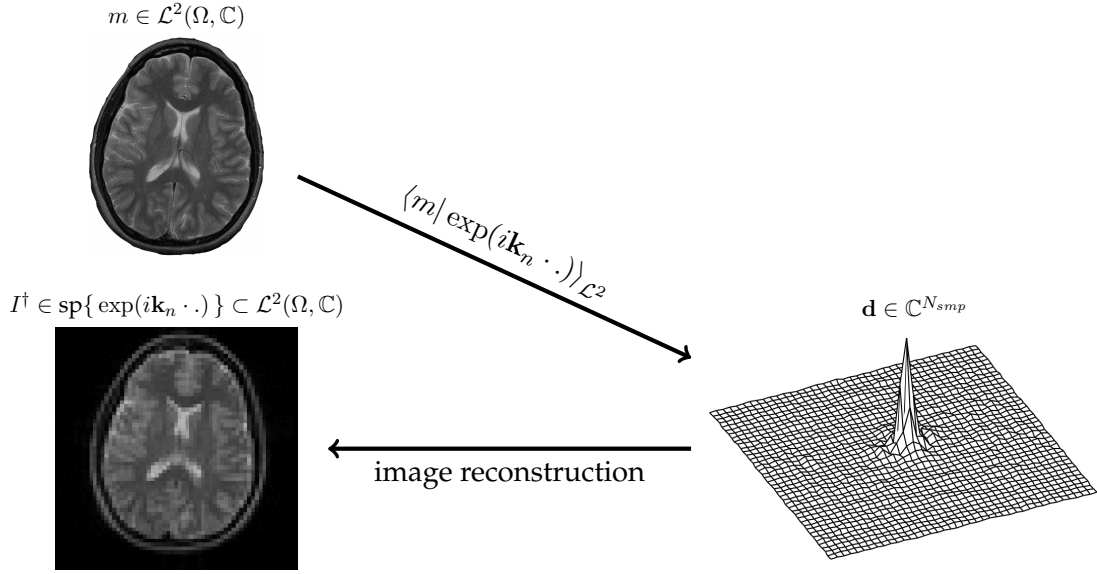


Figure 1.1: Given the finite set of encoding functions $\{\exp(i\mathbf{k}_n \cdot \cdot)\}_{n=1}^{N_{smp}}$ and the finite data set, the image function can only be derived in the subspace spanned by $\{\exp(i\mathbf{k}_n \cdot \cdot)\}_{n=1}^{N_{smp}}$. The minimum norm solution I^\dagger returns the projection of m in the object space $\mathcal{L}^2(\Omega, \mathbb{C})$ onto the subspace $\text{sp}\{\exp(i\mathbf{k}_n \cdot \cdot), n = 1, \dots, N_{smp}\}$. The digital image is obtained by evaluating the reconstructed image function for a set of pixels.

by the inner product of the object space $\langle \cdot | \cdot \rangle_{\mathcal{L}^2}$, the adjoint operator is derived based on the inner product of the data space $\langle \cdot | \cdot \rangle_2$. The sampled data is stacked into a vector $\mathbf{d} \in \mathbb{C}^{N_{smp}}$. As pointed out in [Bertero et al., 1985], if \mathbf{d} is contained in the range of the encoding operator, the solution is again obtained by the minimum norm as in the previous considerations. If \mathbf{d} is not contained in the range of the encoding operator, the solution can be approximated by the least-squares method.

Definition 1.0.3. Consider the linear operator $\check{E} : \mathcal{L}^2(\Omega, \mathbb{C}) \rightarrow \mathbb{C}^{N_{smp}}$ for the Hilbert spaces $\mathcal{L}^2(\Omega, \mathbb{C})$ and $\mathbb{C}^{N_{smp}}$ that is defined such that $(\check{E}m)_n = \langle m | \phi_n \rangle_{\mathcal{L}^2}$, for $m \in \mathcal{L}^2(\Omega, \mathbb{C})$, with respect to the set of encoding functions $\{\phi_n\}_{n=1}^{N_{smp}}$. Given the data $\mathbf{d} \in \mathbb{C}^{N_{smp}}$, the image reconstruction problem is to find $I^\dagger \in \mathcal{L}^2(\Omega, \mathbb{C})$ subject to

$$I^\dagger = \underset{I}{\operatorname{argmin}} \|\check{E}I - \mathbf{d}\|_2^2. \quad (1.4)$$

Whenever all the functions ϕ_n are linearly independent, the problem reduces to the one of Def. 1.0.2, otherwise it determines a set of *pseudosolutions*. The set of *pseudosolutions* of (1.4) can be found by solving $\check{E}'\check{E}I^\dagger = \check{E}'\mathbf{d}$ for the unknown I^\dagger . Thereby, $\check{E}' : \mathbb{C}^{N_{smp}} \rightarrow \text{sp}\{\phi_n\} \subset \mathcal{L}^2(\Omega, \mathbb{C})$ is the adjoint operator defined by $\langle \check{E}I | \mathbf{d} \rangle_2 = \langle I | \check{E}'\mathbf{d} \rangle_{\mathcal{L}^2}$. A unique solution is again found by selecting the pseudosolution with the minimum norm (according to $\langle \cdot | \cdot \rangle_{\mathcal{L}^2}$). Figure 1.2 illustrates the inverse problem and image reconstruction which now involve the inner products of both object and data space.

On top of the Fourier encoding in MRI, **parallel imaging** is used to augment the set of encoding kernels with sensitivity functions of multiple receive coil elements. The encoding kernel of parallel Fourier imaging is determined by $E_c(\mathbf{k}, \alpha, \mathbf{r}) = c_\alpha(\mathbf{r}) \exp(-i\mathbf{k} \cdot \mathbf{r})$, where $c_\alpha(\mathbf{r})$ denotes the sensitivity of coil $\alpha = 1, \dots, N_{\text{coils}}$ at $\mathbf{r} \in V$. These imaging scenarios are also referred to as **hybrid encoding** because of the extended set of functions

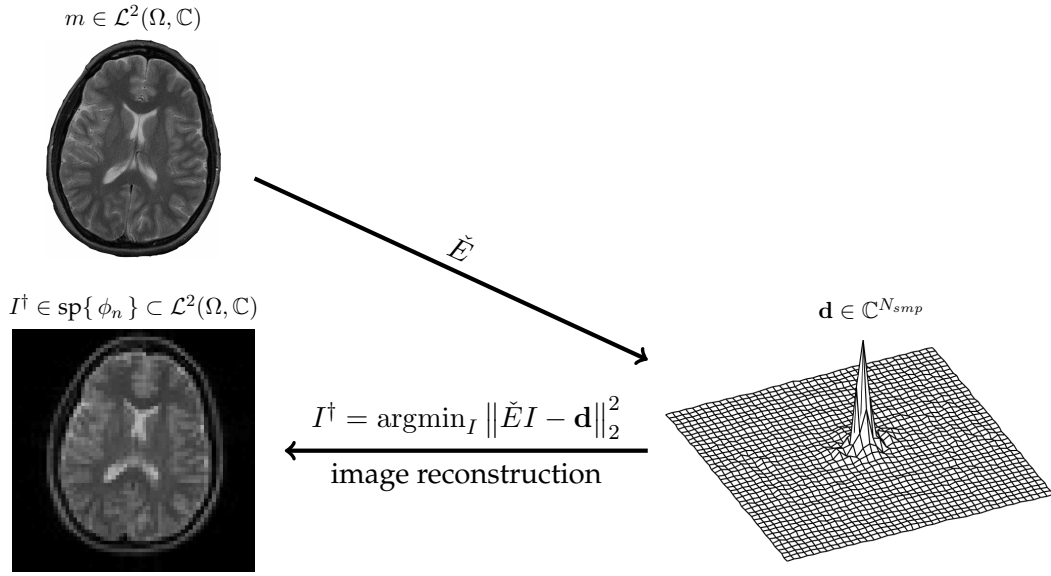


Figure 1.2: Given the linear operator $\check{E} : \mathcal{L}^2(\Omega, \mathbb{C}) \rightarrow \mathbb{C}^{N_{smp}}$ for the set of functions $\{\phi_n\}$ and given the acquired data \mathbf{d} , the image function is approximated based on the inner product of the data space by $I^\dagger = \text{argmin}_I \|\check{E}I - \mathbf{d}\|_2^2$. The pseudosolution with minimum norm I^\dagger is sought that solves the equation $\check{E}'\check{E}I^\dagger = \check{E}'\mathbf{d}$, where $\check{E}' : \mathbb{C}^{N_{smp}} \rightarrow \text{sp}\{\phi_n\} \subset \mathcal{L}^2(\Omega, \mathbb{C})$ denotes the adjoint operator. The solution now depends on the inner product of the data space.

$\{\phi_{(n,\alpha)} := c_\alpha^*(\mathbf{r}) \exp(i\mathbf{k} \cdot \mathbf{r}), n = 1, \dots, N_{smp}, \alpha = 1, \dots, N_{coils}\}$, where $*$ denotes the complex conjugate. In the case of pure Fourier encoding, the linear operator is determined by the sampling operator \check{S} and the Fourier transform, i.e. $\check{E}\{.\} := \check{S}\{\mathcal{FT}\{.\}\}$. In the case of parallel imaging, the linear operator further comprises the linear operator \check{C} of multiplication with coil sensitivities, i.e. $\check{E}_c\{.\} := \check{S}\{\mathcal{FT}\{\check{C}\{.\}\}\}$.

So far, the inverse problem has been formulated in an infinite-dimensional space based on discrete data, following [Bertero et al., 1985]. The problem formulated in (1.4) is often expressed directly in finite-dimensional spaces, such that $\mathbf{I} \in \mathbb{C}^{N_{pix}}$ is assumed according to the digital image representation by N_{pix} pixel. Although this is of course reasonable from a numerical and practicability viewpoint, note that the choice of the number of pixels as well as the mapping between the imaged volume compartments and pixels is restricting generality and requires additional reasoning. With the discretization, the linear operator \check{E} can be characterized by a matrix and the Moore-Penrose pseudo inverse [Moore, 1920, Penrose, 1955] provides a general solution. If \check{E} is injective, it is given by $\mathbf{I}^\dagger := (\check{E}^H \check{E})^{-1} \check{E}^H \mathbf{d}$, where H denotes the Hermitian transpose. Parallel imaging is considered in this context in Chapter 4.

Dynamic MRI and Echo planar imaging

In **dynamic MRI**, the overall acquisition is repeated several times to derive a time series of images, which reflects functional changes. The repeatedly measured k-space signal is binned into equivalence classes that are numbered consecutively by $t = 1, \dots, N_{time}$. These are referred to as *outer* time points or time frames, as opposed to the *inner* time points that indicate relative time points within the time interval of excitation and signal reception. The acquisition of multiple time frames further extends the data domain. Fourier imaging as well as parallel imaging in dynamic MRI is considered in Chapter 5.

As successively revealed in Chapters 2-5, the general signal equation of dynamic MRI is given by

$$d_{n,t,\alpha} = \int_V m(\mathbf{r}, t) c_\alpha(\mathbf{r}) \exp(-i\mathbf{k}_n \cdot \mathbf{r} - i\Delta\omega(\mathbf{r})\tau_n) d\mathbf{r} + \varepsilon(\mathbf{k}_n, t, \alpha), \quad (1.5)$$

where the measured data sample is given with respect to

- k-space position \mathbf{k}_n corresponding to their time of sampling τ_n (*inner* time points)
- coil element α with sensitivities $c_\alpha(\mathbf{r})$ for each $\mathbf{r} \in V$
- *outer* time points t , at which $m(\mathbf{r}, t)$ is observed

Whereas $\Delta\omega(\mathbf{r})$ describes the undesired local frequency variations referred to as *off-resonance* effects, $\varepsilon(\mathbf{k}_n, t, \alpha)$ denotes the Gaussian white noise stochastic process which influences the acquisition. Any confounding effects during signal encoding directly influence image reconstruction. Whereas off-resonance phenomena lead to systematic **artifacts**, thermal noise manifests itself as **image noise**.

MRI requires the consideration of both ends of the imaging process: encoding of the signal origin during data acquisition and solving the inverse problem for image reconstruction. Spatial encoding and the image reconstruction process are therefore strongly tied to each other. Spatial encoding based on varying the magnetic fields is the most time-consuming part in MRI. It is implemented as part of the **MRI pulse sequences** used in the acquisition.

Among MRI pulse sequences, a fast and efficient strategy in the case of dynamic MRI is provided by the **echo planar imaging (EPI)** sequence. It is the most commonly applied technique for dynamic MRI in the clinical routine. However, EPI is sensitive to off-resonance influences and acquisition noise due to its complex signal behavior. Therefore, the efficiency of EPI comes at the expense of image artifacts.

In order to save time in any MRI pulse sequence, **sub-Nyquist sampling** can be performed in combination with hybrid encoding and parallel imaging reconstruction. For dynamic MRI, parallel imaging methods that perform **k-t-sub-Nyquist sampling** and exploit spatio-temporal correlations in the image reconstruction process are typically termed **time-resolved parallel imaging methods**. These implicitly pose certain assumptions on the underlying data. The analysis of violating these, as well as the quantification of image noise, is of great importance: On the one hand, the knowledge gained is valuable in the optimization of the imaging scenario. On the other hand, it is crucial for clinical decisions to recognize artificial image errors in the clinical application.

Such an analysis reveals limitations of the applicability of these methods, particularly for EPI acquisitions that are influenced by measurement noise and signal instabilities, since the signal behavior of EPI is more complex. By the investigation of these limits, an understanding of the potentials is gained. Moreover, another beneficial aspect arises in the case of parallel imaging in EPI, its potential to actually mitigate some of the typical EPI artifacts. Due to the spatial encoding strategy of EPI, *prolonged signal readouts* are performed that lead to artifacts. Sub-Nyquist-sampling with parallel imaging reconstruction allows for the shortening of these readouts to a certain extent.

Core developments of this thesis

A noise quantification in time-resolved parallel imaging methods as well as the investigation of k-t-sub-Nyquist sampled EPI with time-resolved parallel imaging reconstruction are the main contributions of this thesis. These are mainly presented in Chapters 6 and 7.

As a consequence of sub-Nyquist sampled parallel imaging, image noise exhibits spatial variations and correlations. This leads to a spatially non-uniform **signal-to-noise ratio (SNR)**. The framework of **g-factors** allows for the description of image noise and the SNR in these methods. In dynamic MRI, k-t-sub-Nyquist sampled parallel imaging facilitates higher reductions of acquisition times with more benign g-factors.

Existing concepts are covered in Chapter 4. The g-factors are then used in developments towards a unified general framework of non-time-resolved and time-resolved parallel imaging methods in Chapter 6. The two most prominent representatives of standard parallel imaging methods are reformulated to express similarities and differences. In order to bridge methodologies between static and dynamic MRI, the g-factor framework is extended to time-resolved parallel imaging of dynamic MRI. The antagonistic behavior of improved image noise and reduced temporal accuracy is revealed and embedded in a theoretical framework.

The concept of EPI is introduced as part of Chapter 3 for Nyquist-sampled Fourier imaging. Its previous application in combination with sub-Nyquist sampling and standard parallel imaging methods is discussed as part of Chapter 4. It is then investigated in combination with k-t-sub-Nyquist sampling and time-resolved parallel imaging reconstruction in Chapter 7. The analysis of MRI inherent issues such as image noise and artifacts, as well as temporal fidelity allows for new insights in error propagation and implicitly posed assumptions in the reconstruction process.

Confounding influences during the encoding process such as off-resonance effects are particularly severe in EPI acquisitions that aim at high spatial resolution images. The developments of k-t-sub-Nyquist sampled parallel EPI provide the potential to enhance MRI in the clinical context of **cerebral perfusion**. With the proposed EPI strategy, high spatial resolution of **cerebral blood volume (CBV)** maps is achieved, while in-plane susceptibility artifacts are reduced.

This thesis is structured as follows:

- Chapter 2 describes the signal origin in the context of NMR and within the context of quantum mechanics, explains how m contributes to the signal.
- Chapter 3 describes Fourier imaging in a mathematical framework. Fourier encoding, $E(\mathbf{k}_n, \mathbf{r}) := \exp(-i\mathbf{k}_n \cdot \mathbf{r})$, and the corresponding image reconstruction is formulated. Practical aspects of sequence implementation are explained and EPI is considered in particular.
- Chapter 4 addresses acquisitions with multiple coil channels, hybrid encoding, where $E_c(\mathbf{k}_n, \alpha, \mathbf{r}) := c_\alpha(\mathbf{r}) \exp(-i\mathbf{k}_n \cdot \mathbf{r})$, and the corresponding parallel imaging reconstruction.
- Chapter 5 extends considerations to the additional *outer* temporal domain for dynamic MRI, including time-resolved parallel imaging reconstruction.
- Chapter 6 analyzes the transition between standard parallel imaging methods and time-resolved parallel imaging scenarios in dynamic MRI. A framework for g-factor quantification in time-resolved kernel-based parallel imaging methods is derived, in order to analyze noise propagation. Some of the contents of Chapter 6 were published in [Ramb et al., 2015a] and presented as conference contributions [Ramb et al., 2013a, Ramb et al., 2013b, Ramb and Schultz, 2013, Ramb et al., 2014a].

- Chapter 7 describes the development of a k-t-sub-Nyquist sampled echo planar imaging sequences (k-t-EPI) and image reconstruction schemes derived accordingly. The issues and implications balancing signal encoding and image reconstruction in these scenarios are discussed. The developed dynamic MR acquisition schemes are applied in dynamic susceptibility contrast (DSC) weighted cerebral perfusion imaging. Some of the contents were published (c.f. [Ramb et al., 2016b]) and presented as conference contributions [Ramb et al., 2014b, Ramb et al., 2015b, Ramb et al., 2015c, Ramb et al., 2016a].

Chapter 2

Signal origin in nuclear magnetic resonance

When exposed to a *magnetic field*, *atomic nuclei* can absorb photons in the radiofrequency range. When the excitation frequency matches the frequency specific for the nucleus, it is *in resonance*. This is the fundamental phenomenon underlying [nuclear magnetic resonance \(NMR\)](#). The system response for different nuclei at different frequencies reveal chemical and structural information of molecules within the tissue or object under investigation. This chapter addresses essential physical backgrounds of NMR in the framework of quantum mechanics. The aim is to provide a brief logical pathway how - within biological tissue - magnetized spins of nuclei lead to a macroscopic bulk magnetization and finally, the signal measured in NMR. Only the core information is provided, for more detailed discussions refer to [\[Liang and Lauterbur, 2000, Takhtajan, 2008, Haacke et al., 1999, Gustafson and Sigal, 2011\]](#).

Postulation of spin

The *Stern-Gerlach experiment* [\[Gerlach and Stern, 1922\]](#) revealed properties of nuclei beyond the classical physical description: an inherent property that is postulated as *spin*. The particles' intrinsic spin becomes evident in interaction with an external magnetic field. Spin influences and determines the macroscopic magnetization as can be measured in NMR experiments [\[Rabi et al., 1938, Bloch, 1946, Purcell et al., 1946\]](#).

2.1. Quantum mechanical description of spin

Quantum mechanics describes experimental findings in the microscopic range based on algebraic group theories. The property of *spin* is thereby described similar to an *impulse* with representation by basis operations in the *spin Hilbert space*. Employing the terminology of [\[Takhtajan, 2008\]](#), a quantum system, i.e. system of finitely many interacting particles, and its state is represented as follows.

Definition 2.1.1 (State Hilbert space). *A quantum system may be represented by an (in)finite-dimensional separable complex Hilbert space $\mathcal{H} := (\mathcal{H}, \langle \cdot | \cdot \rangle)$ with inner product $\langle \cdot | \cdot \rangle$. \mathcal{H} is called the **state Hilbert space** and the state of the quantum system is represented by a vector element $|\psi\rangle \in \mathcal{H}$.*

The set of all possible states of a quantum system is generally infinite. For many quantum systems, the vector $|\psi\rangle$ represents a wave function $\psi : \mathbb{R}^3 \times \mathbb{R} \rightarrow \mathbb{C}$, described with respect to its values $\psi(\mathbf{r}, t)$ in three dimensional space coordinates $\mathbf{r} \in \mathbb{R}^3$ and with respect to time $t \in \mathbb{R}$. For this representation, the norm induced by the inner product is given by $\|\psi\|^2 = \int |\psi(\mathbf{r}, t)|^2 d\mathbf{r}$. The Riesz representation theorem connects the state Hilbert space with its *dual space*, which is the space of all bounded linear functionals on \mathcal{H} .

Definition 2.1.2 (Dual Hilbert space). *Let \mathcal{H} be the state Hilbert space of a quantum system. Using the Riesz representation theorem, for each $|\psi\rangle \in \mathcal{H}$, there exists a unique $\langle\psi| \in \mathcal{H}^*$ defined by*

$$\begin{aligned}\langle\psi| : \mathcal{H} &\rightarrow \mathbb{C} \\ x &\mapsto \langle\psi|x\rangle.\end{aligned}$$

The space $\mathcal{H}^* := \{ \langle\psi| \mid \langle\psi| : \mathcal{H} \rightarrow \mathbb{C} \}$ is referred to as the **dual space** of \mathcal{H} .

The wave function ψ can be interpreted as a density function. In order to fulfill the properties of a density function, the state vectors $|\psi\rangle$ are normed by $\|\psi\|^2 = \langle\psi|\psi\rangle = 1$. An experimental measurement of a physical quantity is described by an *observable*. In order to get equivalently defined operators for mappings within both the state Hilbert space and its dual space, a requirement of observables is to be *self-adjoint*.

Definition 2.1.3 (Observables). *All measurable **observables** $\mathcal{A} : \mathcal{H} \rightarrow \mathcal{H}$ of a quantum system are represented by all self-adjoint operators on the respective state Hilbert space \mathcal{H} , i.e. $\langle\check{A}\phi|\psi\rangle = \langle\phi|\check{A}\psi\rangle$ for all $|\phi\rangle, |\psi\rangle \in \mathcal{H}$ and given an observable $\check{A} \in \mathcal{A}$.*

As opposed to the theory of classical mechanics, a measurement always interferes with the state of the quantum system in quantum mechanics, since the measurement of an observable $\check{A} \in \mathcal{A}$ forces the system into an *eigenstate* obtained by the *eigenvalue-eigenvector equation* of the operator. Possible outcomes of the observable \check{A} that can be uniquely measured are indicated by the *eigenvalues* of this operator. The prediction of the measurement outcome of an observable \check{A} with respect to a state $|\psi\rangle$ of the quantum system is provided in terms of the expectation value.

Definition 2.1.4 (Measurement). *The **measurement process** of an observable $\check{A} \in \mathcal{A}$ is described by the eigenvalue-eigenvector-equation of \check{A} , i.e.*

$$\check{A}|\psi\rangle = \lambda|\psi\rangle,$$

which determine the measurement outcome of \check{A} applied to an eigenstate $|\psi\rangle$ as a scaling of the eigenstate by λ . A **measurement** of the observable \check{A} given an arbitrary quantum system's state $|\psi\rangle$ is described by the expectation value of its probabilistic outcome, i.e.

$$\langle\psi|\check{A}|\psi\rangle = \lambda\langle\psi|\psi\rangle = \lambda.$$

When proceeding with the measurement of another observable, the previous system is again forced into the operator's eigenstate, in many cases making the previous measurement useless. Two observable are simultaneously measurable, hence do not disturb each other, when they act on the same eigenstates. The observation is mathematical described using the commutator of two observables.

Definition 2.1.5 (commutator). *Let $\check{A}, \check{B} \in \mathcal{A}$ be two observables of a quantum system represented by the Hilbert space \mathcal{H} . The commutator of \check{A} and \check{B} is defined by*

$$[\check{A}, \check{B}] := \check{A}\check{B} - \check{B}\check{A},$$

such that $\check{A}\check{B}|\psi\rangle - \check{B}\check{A}|\psi\rangle = 0$, for all $|\psi\rangle \in \mathcal{H}$.

Theorem 2.1.6. *Two observables $\check{A}, \check{B} \in \mathcal{A}$ can be measured simultaneously, if and only if they commute, i.e. $[\check{A}, \check{B}] = \check{A}\check{B} - \check{B}\check{A} = 0$.*

Spin Hilbert space

Postulation of an intrinsic angular momentum, referred to as *spin*, explained the findings of the Stern-Gerlach experiment [Uhlenbeck and Goudsmit, 1926]. Mathematically, the additional degrees of freedom induced by all possible spin setups are expressed by a Hilbert space \mathcal{H}_s .

Definition 2.1.7 (Spin Hilbert space). *The **spin Hilbert space** captures all possible spin configurations of a system and is described by the complex vector space*

$$\mathcal{H}_s = \mathbb{C}^{2s+1},$$

where s indicates the **spin quantum number** and is of form $s = \frac{n}{2}$, $n \in \mathbb{N}_0$ depending on the type of particle. The set of finitely many spin configurations are referenced by the **magnetic quantum number** m_s , which takes values in the set $\{-s, -s+1, \dots, s-1, s\}$. The combined representation of configurations of states and spin is the tensor product of the state Hilbert space and the spin Hilbert space, i.e. $\mathcal{H}_{comb} = \mathcal{H} \otimes \mathcal{H}_s$, and yields again a Hilbert space.

Remark 2.1.8. For **magnetic resonance imaging (MRI)**, the most frequently considered nuclei are the ^1H hydrogen nuclei. The spin number of the hydrogen atom is $s = \frac{1}{2}$.

Henceforth, only spin- $\frac{1}{2}$ -systems are considered, which provides two spin configurations $m_s = \pm\frac{1}{2}$. These are typically denoted by $|\uparrow\rangle$ and $|\downarrow\rangle$.

The intrinsic angular momentum is formulated by the spin operator $\check{\mathbf{S}} = (\check{S}_x, \check{S}_y, \check{S}_z)^T$. With the definitions $\tau(1) := x$, $\tau(2) := y$ and $\tau(3) := z$, the following algebraic relation of commutation holds:

$$[\check{S}_{\tau(j)}, \check{S}_{\tau(k)}] = i\hbar \sum_{l=1}^3 \varepsilon_{jkl} \check{S}_{\tau(l)}, \text{ for } j, k, l \in \{1, 2, 3\}, \quad (2.1)$$

where $\varepsilon_{jkl} \in \{-1, 0, 1\}$ denotes the Levi-Civita symbol and \hbar is the *Planck's constant*. Since $[\check{S}_{\tau(j)}, \check{S}_{\tau(k)}] \neq 0$ for $j \neq k$, a pair of spin operator components cannot be measured simultaneously. However, the spin's magnitude and the orientation allow for simultaneous measurement.

Theorem 2.1.9. *The operator $\check{S}^2 := \check{S}_x^2 + \check{S}_y^2 + \check{S}_z^2$ commutes with each $\check{S}_{\tau(i)}$, i.e. $[\check{S}^2, \check{S}_{\tau(i)}] = 0$, for $i = 1, \dots, 3$.*

Hence, it is possible to measure simultaneously the spin's magnitude $|\check{S}| = \sqrt{\check{S}^2}$ and one component of the spin operator.

2.2. Spin induced magnetic moments

Spin induces a magnetic moment. When exposed to an external magnetic field, different spin states correspond to different energy levels (*Zeeman effect*). The gap between these energy levels is equivalent to the energy of one photon with corresponding frequency (*Planck's energy-frequency relation*). This so-called *Larmor frequency* of a particle yields the fundamental property employed in spatial encoding of **MRI** (Chapter 3).

The magnetic field as part of any **MR** experiment is described by a mathematical vector field. Without loss of generality, the magnetic field is assumed to be directed parallel to the

z -axis throughout this thesis. Let $B_0 \in \mathbb{R}$ denote the field strength (or more precisely the magnetic flux) such that the magnetic field is described by elements $\mathbf{B}_0 = (0, 0, B_0)^T$ at each spatial position. When material is exposed to a magnetic field, it is magnetized according to its *susceptibility* characteristics, effectively changing the magnetic field. Near interfaces between different types of material, this leads to magnetic field *inhomogeneities*. State-of-the-art clinical scanner correct inhomogeneities up to quadratic terms based on a *magnetic field shim procedure*.

The spin operator $\check{\mathbf{S}}$ relates to the *magnetic moment operator* $\check{\boldsymbol{\mu}} = (\check{\mu}_x, \check{\mu}_y, \check{\mu}_z)^T$, of a particle by

$$\check{\boldsymbol{\mu}} = \gamma \check{\mathbf{S}}, \quad (2.2)$$

where γ is the so-called *gyromagnetic ratio*, a physical constant depending on the type of particle. This relation is derived from experimental observation, e.g. [Haacke et al., 1999].

Remark 2.2.1. The gyromagnetic ratio of the ^1H atom is $\gamma \approx 2.675 \cdot 10^8 \text{ rad}/(\text{Ts})$ or $\gamma = \frac{\gamma}{2\pi} \approx 42.58 \text{ MHz}/\text{T}$ in frequency units.

Lemma 2.2.2. The component $\check{\mu}_z$ of the magnetic moment operator results in the following two eigenvector-eigenvalue equations

$$\check{\mu}_z |\uparrow\rangle = \gamma \hbar \frac{1}{2} |\uparrow\rangle \quad \text{and} \quad \check{\mu}_z |\downarrow\rangle = -\gamma \hbar \frac{1}{2} |\downarrow\rangle.$$

The magnetic moment induced by spin interacts with the applied magnetic field \mathbf{B}_0 . This interaction is described by the *Hamilton operator* \check{H} , which captures the energy E of a particle in a spin state $|\psi\rangle$ according to the *Schrödinger Equation*, i.e.

$$\check{H} = -\check{\boldsymbol{\mu}} \cdot \mathbf{B}_0 \quad \text{and} \quad \check{H} |\psi\rangle = E |\psi\rangle, \quad (2.3)$$

where \cdot indicates the inner product. The different states of spins entail different energy levels:

$$\check{H} |\psi\rangle = -\gamma \hbar m_s B_0 |\psi\rangle, \quad (2.4)$$

where the magnetic quantum number is $m_s = \frac{1}{2}$ for states $|\uparrow\rangle$ and $m_s = -\frac{1}{2}$ for states $|\downarrow\rangle$. Hence, $|\uparrow\rangle$ implies a lower energy state than $|\downarrow\rangle$. The energy difference is referred to as *Zeeman effect*, i.e.

$$\Delta E = \gamma \hbar B_0. \quad (2.5)$$

According to the *Planck's energy-frequency relation* relating energy E and frequency ω_0 of a particle by $E = \hbar \omega_0$, the energy difference due to Zeeman splitting relates to the *Larmor frequency* of the spins.

Definition 2.2.3 (Larmor frequency). Exposed to an external magnetic field $\mathbf{B}_0 = (0, 0, B_0)^T$, the angular frequency ω_0 of so-called nuclear precession is given by

$$\omega_0 = -\gamma B_0, \quad (2.6)$$

where γ is the gyromagnetic ratio. The frequency ω_0 is called the **Larmor frequency**.

Remark 2.2.4. The negative sign in Def. 2.2.3 enforces a right handed system.

Remark 2.2.5. The Larmor frequency of a ^1H nucleus within a magnetic field $\mathbf{B}_0 = (0, 0, B_0)^T$ and field strength $B_0 = 1\text{T}$ is $|\omega_0| = 42.58 \text{ MHz}$.

2.3. Macroscopic magnetization

A large number of nuclear spins exposed to a magnetic field sum up to a macroscopic magnetic moment. The macroscopic magnetization allows for the description in the framework of classical mechanics. In MRI, the macroscopic magnetization is used to describe the underlying physical quantity, measured and manipulated during the experiment.

Definition 2.3.1 (macroscopic magnetization). *Consider an ensemble of N_s spins with state vectors $|\psi_n\rangle$, for each $n = 1, \dots, N_s$. The **macroscopic magnetization** or **bulk magnetization** is given by the sum of the expectation values of all spins, i.e.*

$$M_i = \sum_{n=1}^{N_s} \langle \psi_n | \check{\mu}_i | \psi_n \rangle, \quad \text{for } i \in \{x, y, z\}.$$

The macroscopic magnetization is denoted by $\mathbf{M} := (M_x, M_y, M_z)^T \in \mathbb{R}^3$.

In thermal equilibrium, the population of the energy levels are described by the Boltzmann relation,

$$\frac{N_\uparrow}{N_\downarrow} = \exp\left(\frac{\Delta E}{k_B T_s}\right) = \exp\left(\frac{\gamma \hbar B_0}{k_B T_s}\right), \quad (2.7)$$

where $k_B \approx 1.38 \cdot 10^{-23}$ J/K is the Boltzmann constant and T_s is the absolute temperature. Taylor expansion reveals a surplus of configurations $|\uparrow\rangle$ by approximately $\frac{\gamma \hbar B_0}{2k_B T_s}$. The corresponding magnitude of the generated bulk magnetization vector \mathbf{M}^0 points along the z -axis and M_z^0 is approximated by

$$M_z^0 \approx \frac{1}{2} \left(N_s \frac{\gamma \hbar B_0}{2k_B T_s} \right) \gamma \hbar = \frac{\gamma^2 \hbar^2 B_0 N_s}{4k_B T_s}, \quad (2.8)$$

which is proportional to N_s , the overall number of spins, the field strength, as well as inversely proportional to the absolute temperature. The Boltzmann distributed component M_z^0 in combination with vanishing components M_x^0 and M_y^0 , i.e. $M_z^0 = |\mathbf{M}^0|$, is referred to as *thermal equilibrium magnetization*.

Remark 2.3.2. *Given $\mathbf{B}_0 = (0, 0, B_0)^T$ with $B_0 = 1T$ and assuming room temperature, the fraction of surplus of configurations $|\uparrow\rangle$ in the ^1H nucleus is $\frac{N_\uparrow - N_\downarrow}{N_s} \approx 3 \cdot 10^{-6}$. Hence, only three of one million protons contribute to the measurable MRI signal.*

Decomposition of the macroscopic magnetization vector simplifies further discussions.

Definition 2.3.3 (longitudinal and transverse Magnetization). *For a macroscopic magnetization $\mathbf{M} = (M_x, M_y, M_z)^T$ in a magnetic field with main direction along the z -axis, define $M_\parallel := M_z$ and $M_\perp := M_x + iM_y$ of the individual components. Then M_\parallel is called **longitudinal magnetization** and M_\perp is referred to as **transverse magnetization**.*

Although the equilibrium magnetization \mathbf{M}^0 results from quantum mechanical consideration, it allows for a purely classical treatment. This is due to the high number of spins and weak interactions amongst spins as well as between the spins and the environment.

2.4. Bloch equation

The temporal evolution of the macroscopic magnetization is well described by the *Bloch equation*, when assuming a large ensemble of spins.

Definition 2.4.1 (Bloch equation). *Let \mathbf{B} denote the applied magnetic field. Consider a large ensemble of spins, all characterized by the same Larmor frequency ω_0 . Let \mathbf{M} describe the macroscopic magnetization. Then the **Bloch equation** is given by*

$$\frac{d\mathbf{M}(t)}{dt} = \gamma\mathbf{M}(t) \times \mathbf{B}(t) - \frac{1}{T_1} \begin{pmatrix} 0 \\ 0 \\ M_z(t) - M_z^0 \end{pmatrix} - \frac{1}{T_2} \begin{pmatrix} M_x(t) \\ M_y(t) \\ 0 \end{pmatrix}$$

where T_1 and T_2 express the relaxation times.

Remark 2.4.2. *The origins of relaxation constants T_1 and T_2 are briefly described in Sec. 2.6.*

Remark 2.4.3. *The Bloch equation [Bloch, 1946] was experimentally validated, but can be also derived from quantum statistics.*

The Bloch equation yields an *equation of motion* and describes the rate of change of the macroscopic nuclear magnetization.

Theorem 2.4.4. *Assuming a constant magnetic field $\mathbf{B}_0 = (0, 0, B_0)^T$ and neglecting relaxation, the Bloch equation is solved by*

$$\begin{pmatrix} M_x(t) \\ M_y(t) \\ M_z(t) \end{pmatrix} = \begin{pmatrix} \cos(-\gamma B_0 t) & -\sin(-\gamma B_0 t) & 0 \\ \sin(-\gamma B_0 t) & \cos(-\gamma B_0 t) & 0 \\ 0 & 0 & 1 \end{pmatrix} \begin{pmatrix} M_x(0) \\ M_y(0) \\ M_z(0) \end{pmatrix}. \quad (2.9)$$

This expresses a rotation of the magnetization around the z -axis. With decomposition into longitudinal and transverse magnetization, (2.9) simplifies to

$$M_{\perp}(t) = M_{\perp}(0) \exp(-i\gamma B_0 t) \quad \text{and} \quad M_{\parallel}(t) = M_{\parallel}(0). \quad (2.10)$$

The temporal evolution of the transverse component M_{\perp} demonstrates the nuclear precession at the Larmor frequency $\omega_0 = -\gamma B_0$ (Def. 2.2.3) around the directional axis of the external magnetic field. The change of basis of the next section simplifies the description in many cases.

Rotating Frame of Reference

It is often useful to describe the magnetization with respect to another basis than the canonical basis

$$e_1 := \begin{pmatrix} 1 \\ 0 \\ 0 \end{pmatrix}, e_2 := \begin{pmatrix} 0 \\ 1 \\ 0 \end{pmatrix}, e_3 := \begin{pmatrix} 0 \\ 0 \\ 1 \end{pmatrix}, \quad (2.11)$$

namely, given a *rotating* basis at a fixed angular frequency ω :

$$v_1(\omega, t) := \begin{pmatrix} \cos(\omega t) \\ -\sin(\omega t) \\ 0 \end{pmatrix}, v_2(\omega, t) := \begin{pmatrix} \sin(\omega t) \\ \cos(\omega t) \\ 0 \end{pmatrix}, v_3(\omega, t) := \begin{pmatrix} 0 \\ 0 \\ 1 \end{pmatrix}. \quad (2.12)$$

Basis transformation between the two basis sets $\mathcal{E} := \{e_1, e_2, e_3\}$ and $\mathcal{V} := \{v_1, v_2, v_3\}$ are given by the following basis transformation matrices:

$$\begin{aligned} T_{\mathcal{E}}^{\mathcal{V}}(\omega, t) &:= \begin{pmatrix} \cos(\omega t) & \sin(\omega t) & 0 \\ -\sin(\omega t) & \cos(\omega t) & 0 \\ 0 & 0 & 1 \end{pmatrix} \quad \text{and} \\ T_{\mathcal{V}}^{\mathcal{E}}(\omega, t) &:= \begin{pmatrix} \cos(\omega t) & -\sin(\omega t) & 0 \\ \sin(\omega t) & \cos(\omega t) & 0 \\ 0 & 0 & 1 \end{pmatrix} \end{aligned} \quad (2.13)$$

Definition 2.4.5 (Larmor-rotating frame of reference). *The Larmor-rotating frame of reference is defined in terms of the basis elements $\mathcal{V} := \{v_1(\omega, t), v_2(\omega, t), v_3(\omega, t)\}$ as described above and setting $\omega = \omega_0$, i.e. to the Larmor frequency of the considered ensemble of spins (of the same Larmor frequency), exposed to the magnetic field $\mathbf{B}_0 = (0, 0, B_0)^T$.*

From (2.9) follows that $\mathbf{M}(t) = T_{\mathcal{E}}^{\mathcal{V}}(\omega_0, t)\mathbf{M}^0$. Expressing the macroscopic magnetization \mathbf{M} with respect to the Larmor-rotating frame of reference then yields

$$\mathbf{M}_{\text{rot}}(t) := T_{\mathcal{V}}^{\mathcal{E}}(\omega_0, t)\mathbf{M}(t) = T_{\mathcal{V}}^{\mathcal{E}}(\omega_0, t)T_{\mathcal{E}}^{\mathcal{V}}(\omega_0, t)\mathbf{M}^0 = \mathbf{M}^0. \quad (2.14)$$

Hence, the precessing magnetization vector appears to be static in the Larmor-rotating frame of reference and the transversal magnetization with respect to both bases relate by

$$M_{\text{rot},\perp}(t) = M_{\perp}(t) \exp(-i\omega_0 t), \quad M_{\text{rot},\perp}(t) := M_{\text{rot},x}(t) + iM_{\text{rot},y}(t). \quad (2.15)$$

Generally, any frequency can be selected in the basis \mathcal{V} to express the frame of reference rotating at the chosen frequency.

Theorem 2.4.6 (e.g. [Bernstein et al., 2004]). *For an arbitrary frequency ω in the basis $\mathcal{V} := \{v_1(\omega, t), v_2(\omega, t), v_3(\omega, t)\}$, the rate of change of the magnetization with respect to this basis is obtained by*

$$\left(\frac{\partial \mathbf{M}(t)}{\partial t}\right)_{\mathcal{V}} = \left(\frac{\partial \mathbf{M}(t)}{\partial t}\right) - \begin{pmatrix} 0 \\ 0 \\ \omega_0 \end{pmatrix} \times \mathbf{M}(t) = (\omega_0 - \omega)\mathbf{M} \times e_3,$$

where e_3 denotes again the canonical basis vector according to (2.11).

Again, it is evident that the rate of change of the magnetization is zero when choosing $\omega = \omega_0$, the Larmor-rotating frame of reference.

2.5. RF excitation

In order to excite magnetization from thermal equilibrium, an external oscillating force is applied in form of an additional *time-dependent* magnetic field $\mathbf{B}_1(t)$, which is non-zero only within the finite time interval $[t_{p,0}, t_{p,1}] \subset \mathbb{R}$. It is referred to as a *radiofrequency (RF) pulse*. Here, a general - however not exclusive - description of an RF pulse used for signal excitation is stated.

Definition 2.5.1 (radiofrequency pulse). Let $\mathbf{B}_1(t)$ be a time-dependent magnetic field, defined for a given time interval $t \in [t_{p,0}, t_{p,1}]$ and of the form

$$\mathbf{B}_1(t) = \begin{pmatrix} B_{1,x}(t) \\ B_{1,y}(t) \\ B_{1,z}(t) \end{pmatrix} = \begin{pmatrix} B_1^e(t) \cos(\omega_{rf}t + \phi) \\ -B_1^e(t) \sin(\omega_{rf}t + \phi) \\ 0 \end{pmatrix},$$

at a specific angular frequency ω_{rf} , i.e. the **excitation frequency**, and given an initial phase ϕ . The time-dependent function $B_1^e(t)$ is referred to as **pulse envelope function**. In MRI, a magnetic field of this form is called a **radiofrequency (RF) pulse**.

Remark 2.5.2. Throughout this thesis, the interval of excitation is assumed to be symmetric with respect to the origin. Hence, define $t_{p,0} := -t_{p,1}$, such that half of the RF pulse is realized at $t = 0$.

Analogous to the Larmor-rotating frame of reference, the RF pulse can be expressed in the **RF-rotating frame of reference**.

Definition 2.5.3 (RF-rotating frame of reference). The **RF-rotating frame of reference** for the RF pulse \mathbf{B}_1 is defined in terms of the basis elements $\mathcal{V} := \{v_1(\omega, t), v_2(\omega, t), v_3(\omega, t)\}$ and choosing $\omega = \omega_{rf}$.

Without loss of generality, the initial phase is set to zero, i.e. $\phi = 0$, in further considerations. The RF pulse in the RF-rotating frame of reference is expressed by

$$\mathbf{B}_{1,rot}(t) := T_{\mathcal{V}}^{\mathcal{E}}(\omega_{rf}, t)\mathbf{B}_1(t) = \begin{pmatrix} B_1^e(t) \\ 0 \\ 0 \end{pmatrix}. \quad (2.16)$$

Thus, the RF pulse is described solely by its pulse envelope function $B_1^e(t)$ in the RF-rotating frame of reference.

The phenomenon of resonance is exploited by matching the excitation frequency to the Larmor frequency of the spin ensemble of interest, $\omega_{rf} = \omega_0$. Consider the combined magnetic field $\mathbf{B}(t) = \mathbf{B}_0 + \mathbf{B}_1(t)$ during the time interval of non-zero RF pulse contribution. Relaxation parameters are neglected since the RF pulse time interval is usually much shorter than typical T_2 and T_1 -times. Incorporating $\mathbf{B}(t)$ in the Bloch equation (Def. 2.4.1) and expressing the result in the RF-rotating frame of reference based on Thm. 2.4.6 demonstrates the effect of RF pulse excitation.

Theorem 2.5.4 (e.g. [Liang and Lauterbur, 2000, Bernstein et al., 2004]). Let $\mathbf{B}(t) = \mathbf{B}_0 + \mathbf{B}_1(t)$ be the combined static and time-dependent magnetic field defined as in previous considerations. Let the difference between excitation and Larmor frequency be defined by $\Delta\omega := \omega_{rf} - \omega_0$. Then the rate of change of the magnetization \mathbf{M} in the RF-rotating frame of reference is given by:

$$\begin{aligned} \left(\frac{dM_x(t)}{dt}\right)_{RF,rot} &= \Delta\omega M_y(t) \\ \left(\frac{dM_y(t)}{dt}\right)_{RF,rot} &= \gamma M_z(t) B_1^e(t) - \Delta\omega M_x(t) \\ \left(\frac{dM_z(t)}{dt}\right)_{RF,rot} &= -\gamma M_y(t) B_1^e(t). \end{aligned}$$

Two effects become evident from Thm. 2.5.4: first, whenever excitation frequency and Larmor frequency perfectly match each other - referred to as *on-resonance condition* -, the expression is identified with respect to the Larmor-rotating frame of reference. Solely contributions in the $z - y$ -plane are present. Second, in case of a difference between excitation and Larmor frequency, *off-resonance* contributions occur.

Under the on-resonance condition, the solution of the differential equations for an initial magnetization $\mathbf{M}_{\text{rot}} = (0, 0, M_z^0)$ is found to be

$$\begin{aligned} M_{x,\text{rot}} &= 0 \\ M_{y,\text{rot}} &= M_z^0 \sin\left(\int_{\tau_0}^{\tau_p} \gamma B_1^e(t) dt\right) \\ M_{z,\text{rot}} &= M_z^0 \cos\left(\int_{\tau_0}^{\tau_p} \gamma B_1^e(t) dt\right). \end{aligned} \quad (2.17)$$

This describes the rotation of the macroscopic magnetization away from the z -axis. After the RF pulse, the magnetization rotates about the z -axis according to Thm. 2.4.4. The change in orientation before and after the excitation is characterized by the *flip angle*.

Definition 2.5.5 (flip angle). *Given an initial magnetization $\mathbf{M}(\tau_0)$ and a resulting magnetization $\mathbf{M}(\tau_p)$ after applying an RF pulse, the angle between $\mathbf{M}(\tau_0)$ and $\mathbf{M}(\tau_p)$ is called **flip angle**.*

Under the on-resonance condition and in the case of a real-valued pulse envelope function in (2.17), the flip angle is given by $\alpha_{\text{fa}}(\tau_p) = \int_{\tau_0}^{\tau_p} \gamma B_1^e(t) dt$. In the case of off-resonance contributions, the dynamics are more complicated, but can be described by the *small-flip-angle approximation* (e.g. [Bernstein et al., 2004]). Assuming the flip angle to approach zero implies $M_z(t) \approx M_0$ after the time interval of the RF pulse and $\sin(\alpha_{\text{fa}}) \approx \alpha_{\text{fa}}$. With these approximate results, the spectra of off-resonance influences $\{\Delta\omega\}$ is approximated by

$$\alpha_{\text{fa}}(\Delta\omega) \approx \int_{\tau_0}^{\tau_p} \gamma B_1^e(t) \exp(i\Delta\omega t) dt. \quad (2.18)$$

The inverse Fourier transform (see Def. 3.2.5) of the pulse envelope function thereby implicitly defines the spectrum of frequencies which are excited. The finite time interval of excitation necessarily implies that only a finite bandwidth of frequencies can be addressed.

2.6. Relaxation

The shown impact of an RF pulse onto the macroscopic magnetization results in a non-zero, freely precessing transverse magnetization. However, the created transverse magnetization immediately starts to decay, due to loss of coherence by spin interactions. At the same time, the thermal equilibrium magnetization recovers. These processes are collectively referred to as *relaxation*.

The Bloch equation (Def. 2.4.1) takes into account *spin-lattice* and *spin-spin* interactions. The model includes statistical dependencies within the spin ensemble and with respect to the surrounding matter. As a complete discussion of the relaxation process is beyond the scope of this thesis, only the main aspects are described below. For more details, refer to Chapter 20 of [Levitt, 2001].

Due to thermal motion, the locally induced magnetic dipole moments as well as chemical interactions between particles fluctuate over time. Hence, random modulations of the magnetic field are locally induced as spins interact with the surroundings by exchanging energy, i.e. *spin-lattice* interaction. The order of fluctuations is statistically described by the mean square fluctuations of the field and the *autocorrelation* of the time variations. Based on this, the *probability of transitioning* between spin states can be derived as described in [Levitt, 2001], which leads to recovery of longitudinal magnetization (Def. 2.3.3).

Definition 2.6.1 (T_1 relaxation or spin-lattice relaxation). *The T_1 relaxation of the recovery of the longitudinal magnetization is described by the constant T_1 leading to the following rate of change for M_{\parallel} :*

$$\frac{dM_{\parallel}(t)}{dt} = \frac{1}{T_1} (M_{\parallel}^0 - M_{\parallel}(t)) \quad (2.19)$$

The solution to (2.19) is given by

$$M_{\parallel}(t) = M_{\parallel}^0 - (M_{\parallel}^0 - M_{\parallel}(t)) \exp\left(-\frac{t}{T_1}\right). \quad (2.20)$$

The longitudinal magnetization recovery is described by an exponential function characterized by T_1 .

Remark 2.6.2. *Values of T_1 of typical biological tissues increases with the main magnetic field strength. This influences also the signal behavior at MR systems with higher field strength.*

Further, *spin-spin* interaction, due to temporal variations of the magnetic dipole moments occur. Based on the *rotational correlation* over time, the *coherence* between spins is described [Levitt, 2001]. The constant T_2 is obtained to express the decay of the transverse magnetization (Def. 2.3.3).

Definition 2.6.3 (T_2 relaxation or spin-spin relaxation). *The transverse component is described by the constant T_2 leading to the following rate of change for M_{\perp} :*

$$\frac{dM_{\perp}(t)}{dt} = -\frac{1}{T_2} M_{\perp}(t) \quad (2.21)$$

The solution to (2.21) is given by

$$M_{\perp}(t) = M_{\perp}(0) \exp\left(-\frac{t}{T_2}\right). \quad (2.22)$$

The transversal magnetization decay is described by an exponential decay characterized by T_2 .

Both recovery and decay due to relaxation are expressed in the Bloch equation (Def. 2.4.1). In general, all processes leading to T_1 -recovery also influence T_2 -decay. The reverse, however, is not generally true. Recovering the thermal equilibrium as expressed in the T_1 -rate requires the transition into the initial population of the two energy states. The loss of coherence in the transverse magnetization not necessarily requires a transition between energy states. Therefore, T_2 usually cannot exceed T_1 , hence $T_2 \leq T_1$.

Remark 2.6.4. *Many further effects besides relaxation parameters can be incorporated into the Bloch equation, as for instance parameters accounting for the diffusion of particles. A more general variant, incorporating diffusion, is provided by the Bloch-Torrey equation [Torrey, 1956].*

Relaxation is an important property of the magnetized system as it defines its recovery after having disturbed the system. The time constants T_1 and T_2 strongly depend on the type of tissue. Thus, relaxation properties describe a characteristic signature of tissue which can then be exploited to create a *contrast* in the MR image.

2.7. The MR signal

After RF excitation, a rotating macroscopic magnetization is present, which evolves according to the Bloch equation. Due to the rotating magnetization, a voltage is induced in a *receive coil* following *Faraday's law of induction*.

Since the magnetization within the whole excitation volume creates the induced voltage, it is useful to address individual contributions in the formulation as well. The magnetization may vary spatially corresponding to its spatial distribution and usually comprises a spectrum of resonance frequencies $\{\Delta\omega\}$, all of which are additively integrated in the magnetization magnitude. In *MR imaging*, distinguishing spatial origins is required. In *MR spectroscopy*, variations with respect to resonance frequencies are used to distinguish chemical differences. To this end, the *spatial or spectral magnetization density* is defined. Since this work deals with MR imaging, the spectral magnetization density is introduced only to discuss off-resonance effects.

Definition 2.7.1 (spatial or spectral magnetization density). *The spatial magnetization density m_{\perp} or spectral magnetization density $m_{\perp}^{\Delta\omega}$ within the volume V is defined such as to fulfill the equations*

$$M_{\perp}(t) = \int_V m_{\perp}(\mathbf{r}, t) d\mathbf{r} \quad \text{or} \quad M_{\perp}(t) = \int_{-\infty}^{\infty} m_{\perp}^{\Delta\omega}(\Delta\omega, t) d\Delta\omega. \quad (2.23)$$

Remark 2.7.2. *Here, the definition is provided only for the transverse component of the magnetization. This is valid, since precession of the transverse magnetization determines the voltage induced in a coil.*

According to Faraday's law of induction, the derivative with respect to time of the magnetic flux describes the voltage induced in the coil. An MR experiment may include a single receive coil or an array of multiple receive coil elements. The induction additionally depends on the *spatial sensitivity* of the respective receiving coil element, since contributions within close proximity are for instance stronger than from remote origins. Given a coil, let $c(\mathbf{r})$, for each $\mathbf{r} \in \mathbb{R}^3$, describe its *spatial sensitivity*. Here, the coil sensitivities are defined by the voltage induced by a spatially constant magnetization.

Definition 2.7.3 (raw MR signal, sensitivity). *The raw MR signal is given by the voltage induced in a coil according to Faraday's law of induction:*

$$U(t) \propto \Re \left\{ -\frac{\partial}{\partial t} \left(\int_V c(\mathbf{r}) m_{\perp}(\mathbf{r}, t) d\mathbf{r} \right) \right\},$$

where $\{c(\mathbf{r}) \mid \mathbf{r} \in V\}$ denote the *sensitivity* of the coil.

Corollary 2.7.4. *With the same notation follows further for the raw MR signal that*

$$\begin{aligned} U(t) &\propto \Re \left\{ \int_V (i\omega(\mathbf{r}) - 1/T_2(\mathbf{r})) c(\mathbf{r}) m_{\perp}(\mathbf{r}, 0) \exp\left(i\omega(\mathbf{r})t - \frac{t}{T_2(\mathbf{r})}\right) d\mathbf{r} \right\} \\ &\approx \Re \left\{ i\omega \int_V c(\mathbf{r}) m_{\perp}(\mathbf{r}, 0) \exp\left(i\omega(\mathbf{r})t - \frac{t}{T_2(\mathbf{r})}\right) d\mathbf{r} \right\}. \end{aligned} \quad (2.24)$$

Remark 2.7.5. *The approximation in (2.24) is justified by the assumption that $\omega(\mathbf{r}) \gg 1/T_2(\mathbf{r})$ and that the spatial variation of $\omega(\mathbf{r})$ is small compared to the variation $m_{\perp}(\mathbf{r}, 0)$.*

Corollary 2.7.4 shows that the detected raw MR signal is rapidly oscillating that decays exponentially. In order to digitize the signal, it is usually transferred to the rotating frame of reference using *signal demodulation* [Bernstein et al., 2004]. It is thereby denoted as a complex valued signal.

Corollary 2.7.6 (complex MR signal). *The complex MR signal, in the rotating frame of reference with reference frequency ω_{rf} , is expressed by*

$$s(t) \propto \int_V c(\mathbf{r}) m_{\perp}(\mathbf{r}, 0) \exp\left(i(\omega(\mathbf{r}) - \omega_{rf})t - \frac{t}{T_2(\mathbf{r})}\right) d\mathbf{r}, \quad (2.25)$$

where ω_{rf} is the reference frequency and $\omega(\mathbf{r})$ denotes the Larmor frequency present at position $\mathbf{r} \in V$.

The complex MR signal expresses the induced voltage translated into the rotating frame of reference.

2.8. Field inhomogeneities and free induction decay

Performing an MR experiment based on the described RF excitation and acquisition of the complex MR signal reveals the signal decay to be even quicker than predicted by T_2 -decay. This occurrence is explained by the influence of spectral deviations from the employed reference frequency ω_{rf} , i.e. $\Delta\omega := \omega - \omega_{rf}$, for all ω . In this section, field inhomogeneities leading to so-called T_2^* -decay and a *free induction decay (FID) signal* are described.

T_2^* -decay

Considerations so far assumed a single Larmor frequency. However, spins from different locations may have dissimilar Larmor frequencies. The reason for spatial variations are manifold. On a macroscopic scale [mm], local static magnetic field variations locally alter Larmor frequencies, for instance at air-tissue-interfaces where the magnetic susceptibilities strongly vary. It also occurs on a microscopic scale [μm] where e.g. blood-enriched vessels exhibit a different susceptibility compared to surrounding tissue. The presence of different Larmor frequencies within the measured volume leads to a dephasing of the magnetization which locally diminishes the bulk transverse magnetization.

Local magnetic field variations impose a large problem in MRI, where the imaged volume is separated into *voxel* compartments in [mm]. Therefore T_2^* is not primarily a tissue property, but also a source of disturbance that becomes more severe with increasing voxel sizes. The effect depends on the width of the spectral magnetization density $m_{\perp}^{\Delta\omega}$ (as in Def. 2.7.1) within the voxel under consideration. For simplicity, the spectral magnetization density within a volume is often assumed to be described by a Cauchy distribution. This leads to an exponential decay rate. The signal decay of the transverse component due to static field inhomogeneities is typically modeled by the constant T_2^* and describes the rate of change of M_{\perp} by

$$\frac{dM_{\perp}(t)}{dt} = -\frac{1}{T_2^*} M_{\perp}(t). \quad (2.26)$$

The signal decay is thus described by T_2^* , which includes T_2 as well as local static field inhomogeneities, i.e. $\frac{1}{T_2^*} = \frac{1}{T_2} + \frac{1}{T_2'}$. This translates into an actual exponential signal decay of

$$M_{\perp}(t) = M_{\perp}(0) \exp\left(-\frac{t}{T_2^*}\right). \quad (2.27)$$

Even though this approach is a rather coarse approximation considering the manifold possibilities for spectral frequency distributions in living tissue, it turns out to be very useful in practice. Experimentally derived average T_2^* -values in the human brain measured with an MR system of field strength 3T [Wansapura et al., 1999] are:

frontal white matter	44.7 ± 1.2 ms
frontal gray matter	51.8 ± 3.3 ms
occipital white matter	48.4 ± 4.5 ms
occipital gray matter	41.6 ± 2.0 ms

Free induction decay (FID) signal

After the application of a single RF pulse, which tips the macroscopic magnetization by flip angle α_{fa} , the *free induction decay (FID)* signal can be observed as a consequence of free precession and relaxation of the system.

Definition 2.8.1 (Free induction decay signal). *The free induction decay (FID) signal is the complex MR signal after application of an RF pulse with flip angle α_{fa} to magnetization in thermal equilibrium, and subsequent signal reception during free precession of the excited spins, governed by the decay due to relaxation and dephasing. Expressing the such resulting signal with respect to the magnetization density yields*

$$\begin{aligned} s(t) &\propto \int_V c(\mathbf{r}) m_{\perp}(\mathbf{r}, 0) \exp\left(-\frac{t}{T_2(\mathbf{r})}\right) \exp(-i\Delta\omega(\mathbf{r})t) d\mathbf{r} \\ &\propto \int_V c(\mathbf{r}) m_{\perp}(\mathbf{r}, 0) \exp\left(-\frac{t}{T_2^*(\mathbf{r})}\right) d\mathbf{r} \end{aligned} \quad (2.28)$$

where $\Delta\omega(\mathbf{r})$ comprises the spatial-dependent Larmor and reference frequencies.

2.9. Noise in MR measurements

Even without exciting an MR signal, some 'signal' is received by the MR coil. The induced voltage arises from thermal motion of electrically charged particles. Hereby, the density and mobility of particles influence the noise component based on the interaction with the receive coil and Faraday's law of induction.

Underpinned by the *central limit theorem*, assume the 'noise' voltage induced by motion of particles with electric charge to be given by a Gaussian distributed random variable $U_{\epsilon} : \Omega_{\epsilon} \rightarrow \mathbb{C}$ defined on a probability space $(\Omega_{\epsilon}, \mathcal{A}, \mathbb{P})$, where \mathcal{A} denotes the σ -algebra of subsets of Ω_{ϵ} and \mathbb{P} is the probability measure. Assume U_{ϵ} to be normalized such that $U_{\epsilon} \sim \mathcal{N}(0, 1)$. Based on

N_{noise} noise measurements $\{U_\varepsilon(\omega)_n\}_{n=1}^{N_{\text{noise}}}$, the noise in an MR acquisition can be estimated by calculating the variance σ^2 thereof, i.e.

$$\sigma^2 := \frac{1}{N_{\text{noise}}} \sum_{n=1}^{N_{\text{noise}}} |U_\varepsilon(\omega)_n|^2. \quad (2.29)$$

The standard deviation $\sigma := \sqrt{\sigma^2}$ characterizes the noise level present in the acquisition. In practical settings, noise samples can be collected in an MR experiment with a flip angle of zero, hence, without excitation.

As observed by [Johnson, 1928, Nyquist, 1928], the noise level received in a coil is proportional to the Boltzman constant k_B , the frequency bandwidth of the sampling rate of signal aggregation BW_f (see Sec. 3.4.1), as well as the absolute temperature T_s , i.e.

$$\sigma^2 \propto 4k_B BW_f T_s. \quad (2.30)$$

Generally, more complex dependency on coil geometries and the experimental setup exist in particular for multiple receive coil elements, e.g. [Roemer et al., 1990, Pruessmann et al., 1999].

Remark 2.9.1. *The noise contribution of different spatial and spectral origin is independent and uncorrelated. Therefore, additive noise contributions yield the total noise contribution.*

Considering (2.30), two simple solutions to reduce the noise level in an acquisition become apparent: first, reducing the frequency bandwidth, second, reducing the local temperature. Whereas the first comes at the expense of measurement time, the latter is not practicable in the case of in vivo measurements.

Noise from multiple receive coils

For a generalization to MR acquisitions with multiple coils, the covariances between the individual receive coil elements are taken into account. The noise voltage induced in all coil elements is hereby collectively described by a vector-valued random variable.

Let $U_{\varepsilon,\alpha} : \Omega_\varepsilon \rightarrow \mathbb{C}$ be a normalized Gaussian distributed random variable describing the noise voltage induced in coil element α , for each $\alpha \in \{1, \dots, N_{\text{coils}}\}$ of the N_{coils} coil elements. Then

$$\mathbf{U}_\varepsilon := \begin{pmatrix} U_{\varepsilon,1} \\ \vdots \\ U_{\varepsilon,N_{\text{coils}}} \end{pmatrix} : \Omega_\varepsilon^{N_{\text{coils}}} \rightarrow \mathbb{C}^{N_{\text{coils}}}, \quad (2.31)$$

is a vector-valued random variable that captures the noise voltage of the multiple coil system. Based on a collection of sufficiently many noise samples $\{U_\varepsilon(\omega)_n\}_{n=1}^{N_{\text{noise}}}$, the noise covariance matrix $\Psi_{\text{coils}} \in \mathbb{C}^{N_{\text{coils}} \times N_{\text{coils}}}$ can be derived (see also Def. 4.6.2). Its elements consists of the noise (co-)variances which are estimated for each pair of coils $\alpha, \beta \in \{1, \dots, N_{\text{coils}}\}$ by

$$(\Psi_{\text{coils}})_{\alpha,\beta} = \frac{1}{N_{\text{noise}}} \sum_{n=1}^{N_{\text{noise}}} U_{\varepsilon,\alpha}(\omega)_n U_{\varepsilon,\beta}^*(\omega)_n, \quad (2.32)$$

where $*$ denotes the complex conjugate. In practical settings, the noise (co-)variances of the set of coils are likewise obtained from a zero-flip angle acquisition.

Remark 2.9.2. *A non-negative noise covariance between two different receive coil elements represents the noise correlation due to electromagnetic coupling between receive coils. In an ideal orthogonal setting, i.e. $\langle U_{\varepsilon,\alpha} | U_{\varepsilon,\beta} \rangle = 0$, for each $\alpha, \beta \in \{1, \dots, N_{coils}\}$, coil elements are mutually uncorrelated. The noise covariance matrix then reduces to a diagonal matrix consisting only of the non-negative, real-valued scalar variances for each coil individually.*

Summary

In this chapter, the complex MR signal as the basis of every MR acquisition was derived. The main elements of the physical foundation of MR were covered, introducing the nuclei specific property spin within magnetized biological tissue and explaining how it leads to an observable macroscopic magnetization. Further, signal reception after RF pulse excitation of biological tissue that is exposed to a magnetic field was described.

Chapter 3

Fourier imaging

The complex MR signal, excited by an RF pulse and received by a coil, is the integral of signal contributions from all spatial positions within the excited volume. Thus, only a global, superimposed signal is measured. Differentiation of signal contributions from distinct spatial origins requires spatial encoding. Spatial encoding and image reconstruction are closely linked in MRI, since the encoding schemes applied during image acquisition governs the reconstruction process.

In this chapter, encoding in three spatial dimensions in 2D-multi slice imaging scenarios is described. Slice selective excitation (Sec. 3.1) is used to encode the z -dimension and Fourier encoding (Sec. 3.2) is applied to encode the x - and y -dimensions. Along with Fourier encoding, Fourier image reconstruction (Sec. 3.3) is introduced. Limitations due to *finite* and *discrete* sampling scenarios are discussed, as well as its implications for spatial resolution and [signal-to-noise ratio \(SNR\)](#). Practical implementations by MR pulse sequences are covered (Sec. 3.4) and [echo planar imaging \(EPI\)](#) is in particular presented. A discussion of Partial-Fourier sampling (Sec. 3.5) or sub-Nyquist sampling (Sec. 3.6) to reduce acquisition times in Fourier imaging concludes this chapter.

Throughout this chapter, MR acquisitions using a single coil with a homogeneous sensitivity are assumed. Therefore, the explicit reference to coil sensitivities $c(\mathbf{r})$, for $\mathbf{r} \in V$ is omitted without loss of generality. Coil sensitivities are reintroduced in Chapter 4, in which acquisitions with multiple coils are considered.

3.1. Slice selective excitation

An intuitive way of determining spatial origin of the signal along one of three dimensions is to selectively excite only protons along a specified plane within a volume, i.e. a *slice*.

Without loss of generality, consider a slice oriented perpendicular to the main direction of the static magnetic field. Let $\Delta z \in \mathbb{R}$ define the slice thickness and assume the slice to be shifted from the origin by a shift factor $z_0 \in \mathbb{R}$. Then the corresponding *slice* is defined by the set

$$V := \left\{ (x, y, z)^T \in \mathbb{R}^3 \mid |z - z_0| < \frac{\Delta z}{2} \right\}. \quad (3.1)$$

As covered in Sec. 2.2, particles with spin exposed to an external magnetic field precess at the nuclei specific Larmor frequency ω_0 . The excitation frequency $\omega_{\text{rf}} = \omega_0$ needs to match the Larmor frequency for excitation of non-zero transverse magnetization (Sec. 2.5). Using both

relations, a spatial-dependent variation of the Larmor frequency is introduced by *gradients* for subsequent excitation of spins only within a defined slice volume.

Definition 3.1.1 (gradients). Denote $\mathbf{r} := (x, y, z)^T$ and let $\mathbf{B}_G(\mathbf{r}, t)$ be a magnetic field along the main direction of \mathbf{B}_0 , that varies with respect to time and space, i.e.

$$\mathbf{B}_G(\mathbf{r}, t) := \begin{pmatrix} 0 \\ 0 \\ G_x(t)x \end{pmatrix} + \begin{pmatrix} 0 \\ 0 \\ G_y(t)y \end{pmatrix} + \begin{pmatrix} 0 \\ 0 \\ G_z(t)z \end{pmatrix},$$

where $G_x(t)$, $G_y(t)$ and $G_z(t)$ are linear functions. The **gradient** $\mathbf{G}(t)$ is defined as the spatial derivative of $\mathbf{B}_G(\mathbf{r}, t)$ along the z -component, i.e.

$$\mathbf{G}(t) := \left(\frac{\partial}{\partial x}, \frac{\partial}{\partial y}, \frac{\partial}{\partial z} \right)^T (\mathbf{B}_G(\mathbf{r}, t))_z = (G_x(t), G_y(t), G_z(t))^T.$$

Remark 3.1.2. In Def. 3.1.1, gradients are defined to be linear, since all gradients applied in this work are linear. Nevertheless, non-linear gradients have also been actively applied in MRI, e.g. [Hennig et al., 2008, Gallichan et al., 2011, Schultz, 2013].

Consider a magnetic field $\mathbf{B}_{G_{\text{slc}}}(\mathbf{r}, t) = (0, 0, G_{\text{slc}}(t)z)^T$, where $G_{\text{slc}}(t)$ is linear, applied in addition to the static magnetic field \mathbf{B}_0 . Assume the gradient to provide a constant value in a given time interval, i.e. $G_{\text{slc}}(t) = G_{\text{slc}}$, for each $t \in [t_{\text{slc},0}, t_{\text{slc},1}]$. The overall magnetic field is within this time interval described by $(0, 0, B_0 + G_{\text{slc}}z)^T$. The linear variation of the z -component implies the Larmor frequency ω to spatially vary along the z -direction, i.e.

$$\omega(z) = -\gamma(B_0 + G_{\text{slc}}z) = \omega_0 - \gamma G_{\text{slc}}z, \quad (3.2)$$

where ω_0 refers to the Larmor frequency as solely dictated by the static magnetic field. Hence, designing an RF pulse such as to match only a narrow band of Larmor frequencies corresponding to the range inside the slice yields the desired slice selection excitation. The principle is only briefly sketched in the following, for more details refer to [Liang and Lauterbur, 2000, Bernstein et al., 2004].

For slice excitation with small flip angles, a pulse envelope function (Def. 2.5.1) can be obtained by Fourier transform (see Def. 3.2.4) of the desired slice profile. In the case of (3.1), the slice profile is a box function. The excitation frequency then has to match the Larmor frequency of the designated slice center z_0 . For a constant gradient G_{slc} , V is selectively excited by an RF pulse with excitation frequency ω_{rf} and pulse envelope function $B_1^e(t)$ of

$$\omega_{rf} = -\gamma(B_0 + G_{\text{slc}}z_0) \quad \text{and} \quad B_1^e(t) = \frac{\sin(\pi\gamma t G_{\text{slc}} \Delta z)}{\pi\gamma t G_{\text{slc}} \Delta z}, \quad \text{respectively.} \quad (3.3)$$

Selecting the pulse envelope function by the Fourier transform approximates the Bloch equation. However, this is an assumption valid only for small flip angles. The pulse envelope function for a slice described by a box function is a *sinc* function, $\text{sinc}(x) = \frac{\sin(x)}{x}$. Due to a necessarily finite realization of the pulse in the experiment, the sinc function is truncated. The truncation leads to *ringing artifacts* known as the *Gibbs phenomenon* [Gibbs, 1898] in the slice profiles. This is typically mitigated by applying a suitable window function to the pulse envelope, e.g. a Hann or a Hamming window.

Using slice selective excitation, signal is excited only within a volume of interest. The thereby applied gradient is referred to as *slice selection gradient*. The excited signal, however,

still exhibits superimposed signal contributions from all particles within the slice. In order to distinguish contributions according to both dimensions within the slice, further spatial encoding is required: *frequency encoding* and *phase encoding*.

3.2. Fourier encoding

In Fourier encoding, signal contributions from within the excited volume are weighted by changes of relative frequency - and consequently the accumulated phase changes - in the complex MR signal. The two main mechanisms to affect these frequency changes are referred to as *frequency encoding* and *phase encoding*. The encoded MR signal data are expressed using the concept of *k-space*. By the Fourier relation, image reconstruction is directly linked to the encoding principle and relies on how data is sampled within k-space.

Frequency encoding

Similar as for the slice selection gradient, the linear gradient $\mathbf{B}_{G_{fe}}(\mathbf{r}, t) = (0, 0, G_{fe}(t)x)^T$ is defined as non-zero in the time interval $[t_{fe,0}, t_{fe,1}]$ after the end of the RF pulse, i.e. $t_{p,1} < t_{fe,0}$. Applying gradient \mathbf{G}_{fe} along the x -direction implies modulation of the overall magnetic field to $(0, 0, B_0 + G_{fe}(t)x)^T$, for $t \in [t_{fe,0}, t_{fe,1}]$. With (2.6), the following frequency dependency on the x -component and on time results:

$$\omega(x, t) = -\gamma (B_0 + G_{fe}(t)x) = \omega_0 - \gamma G_{fe}(t)x. \quad (3.4)$$

The gradient $G_{fe}(t)$ is referred to as *frequency encoding gradient*.

Although slice selection and frequency encoding gradients only vary with respect to their gradient direction, functional differences arise due to their time of application. Whereas the slice selection gradient is applied in the time interval of RF pulse excitation $[t_{p,0}, t_{p,1}]$, the frequency encoding gradient is applied during the time window of signal readout by the [analog-digital converter \(ADC\)](#), e.g. $[t_{ADC,0}, t_{ADC,1}]$. Its effect becomes evident when inserting the derived frequency relation (cf. 3.4) into the FID signal equation (cf. 2.28). Due to the time dependency of $\omega(x, t)$, the previous multiplication, $\omega(\mathbf{r})t$, here becomes an integration, $\int_0^t G_{fe}(\tau)x d\tau$. With this and neglecting relaxation, the following signal relation results:

$$s(t) \propto \int_V m_{\perp}(\mathbf{r}, 0) \underbrace{\exp\left(-i\gamma \int_0^t G_{fe}(\tau)x d\tau\right)}_{\text{phase modulation along } x\text{-direction}} d\mathbf{r}. \quad (3.5)$$

Recall also that $t = 0$ occurs at the middle of the RF pulse excitation time interval (Rem. 2.5.2), which also determines the temporal integration interval. Such a signal is said to be *frequency encoded*.

Phase encoding

Frequency encoding allows to encode one spatial dimension of the excited slice profile and is performed during the readout of the excited signal. Encoding of further spatial dimensions requires several repetitions of slice-selective, frequency-encoded signal acquisition, where the

signal is prepared differently in each sequential step. This makes the *phase encoding* time-expensive.

Analogous to the frequency encoding gradient, the linear gradient is defined as $\mathbf{B}_{G_{pe}}(\mathbf{r}, t) = (0, 0, G_{pe}(t)y)^T$, and as non-zero in the time interval $[t_{pe,0}, t_{pe,1}]$ after the end of the RF pulse and before the readout acquisition begins, i.e. $t_{slc,1} \leq t_{pe,0} < t_{pe,1} \leq t_{fe,0}$. Then this gradient again imposes spatially dependent modulations of the overall magnetic field $(0, 0, B_0 + G_{pe}(t)y)^T$, for $t \in [t_{pe,0}, t_{pe,1}]$, but with respect to the y -component. The frequency modulations along the y -direction induce the following:

$$\omega(y, t) = -\gamma (B_0 + G_{pe}(t)y) = \omega_0 - \gamma G_{pe}(t)y. \quad (3.6)$$

The difference in acquiring a frequency encoded signal when previously the gradient $G_{pe}(t)$ was applied is given by the following additional phase:

$$s(t) \propto \int_V m_{\perp}(\mathbf{r}, 0) \exp\left(-i\gamma \int_0^t G_{fe}(\tau)x d\tau\right) \underbrace{\exp\left(-i\gamma \int_{t_{pe,0}}^{t_{pe,1}} G_{pe}(\tau)y d\tau\right)}_{\text{phase modulation along } y\text{-direction}} d\mathbf{r} \quad (3.7)$$

The gradient $G_{pe}(t)$ is called *phase encoding gradient*. Defining the combined gradient $\mathbf{G}(\tau) := (G_{fe}(\tau), G_{pe}(\tau), 0)$, then (3.7) is described by

$$s(t) \propto \int_V m_{\perp}(\mathbf{r}, 0) \exp\left(-i\gamma \int_0^t \mathbf{G}(\tau) \cdot \mathbf{r} d\tau\right) d\mathbf{r}. \quad (3.8)$$

The signal is said to be *frequency and phase encoded*. In the subsequent section, the concept of k -space is introduced which substitutes the time-dependency of the encoding functions by expressing phase modulations in coordinates of k -space.

3.2.1. Concept of k -space

Phase and frequency encoding gradients impose spatially varying phase modifications over the time course of signal acquisition (cf. 3.8). Hence, the transverse magnetization density $m_{\perp}(\mathbf{r}, 0)$ is projected onto a set of exponential functions modulated by phase variations according to the applied gradients. This change of perspective largely simplifies the expression [Ljunggren, 1983, Twieg, 1983].

Definition 3.2.1 (k -space, k -space coordinates). Define *k -space* as the set of vectors $\mathbf{k} \in \mathbb{R}^{\mathcal{D}}$ that are spanned by arbitrary gradient modulations after a certain time t , i.e.

$$\mathcal{K} := \left\{ \mathbf{k} \mid \mathbf{k} = \gamma \int_0^t \mathbf{G}(\tau) d\tau \right\} \quad (3.9)$$

The components of \mathbf{k} provide the *k -space coordinates* according to the orthogonal spatial encoding line dimensions. For $\mathcal{D} = 2$, the k -space coordinates (k_x, k_y) are given by

$$k_x := \gamma \int_0^t G_{fe}(\tau) d\tau \quad \text{and} \quad k_y := \gamma \int_0^t G_{pe}(\tau) d\tau. \quad (3.10)$$

Remark 3.2.2. The gyromagnetic ratio γ is expressed in units of $\text{rad}/(\text{Ts})$, hence, \mathbf{k} is given in rad/m .

Remark 3.2.3. *The k-space coordinates demonstrate the spatial rate of change:*

$$\mathbf{k}(t) = \left(\frac{\partial}{\partial x}, \frac{\partial}{\partial y}, \frac{\partial}{\partial z} \right)^T \left(\gamma \int_0^t \mathbf{G}(\tau) \mathbf{r} \, d\tau \right).$$

With Def. 3.2.1, the time-dependent frequency and phase encoded signal of (3.8) becomes

$$s(t) \propto \int_V m_{\perp}(\mathbf{r}, 0) \exp(-i\mathbf{k}(t) \cdot \mathbf{r}) \, d\mathbf{r}, \quad (3.11)$$

where $\mathbf{k}(t) = (k_x(t), k_y(t))^T$ indicates the k-space position or k-space coordinates at the time t of the measurement and according to the gradients $G_{fe}(t)$ and $G_{pe}(t)$. Definition of $\tilde{s}(\mathbf{k}) \equiv s(t)$ allows for the expression of the time-dependent encoded signal in terms of k-space, i.e.

$$\tilde{s}(\mathbf{k}) \propto \int_V m_{\perp}(\mathbf{r}, 0) \exp(-i\mathbf{k} \cdot \mathbf{r}) \, d\mathbf{r}. \quad (3.12)$$

This signal equation essentially shows the (two-dimensional) *Fourier transform* of the transverse magnetization densities $\{m_{\perp}(\mathbf{r}, 0), \mathbf{r} \in V\}$. The general form - as outlined in Chapter 1 - is obtained by defining Fourier encoding kernel functions according to the gradient imposed Fourier basis, as well as defining the encoding operator as the general Fourier transform.

For the definition of the Fourier transform and its inverse, $m_{\perp}(\mathbf{r}, 0)$ is assumed to be rapidly decreasing in the spatial domain. This assumption is well justified in MRI, since imaged objects are of limited extent and the MR scanner's field strength as well as the receive coil's signal sensitivities are decaying over spatial distance. It is explicitly assumed that $m_{\perp}(\cdot, 0) \in \mathcal{L}^2(V, \mathbb{C})$ is a square-integrable function, i.e. $\int_V |m_{\perp}(\mathbf{r}, 0)|^2 \, d\mathbf{r} < \infty$, where $V \subseteq \mathbb{R}^{\mathfrak{D}}$ and $\mathfrak{D} = 2$ for a 2D-slice volume.

Definition 3.2.4 (Fourier transform). *The Fourier transform of a square-integrable function $m_{\perp}(\cdot, 0) \in \mathcal{L}^2(V, \mathbb{C})$, where $V \subseteq \mathbb{R}^{\mathfrak{D}}$, in terms of angular frequencies is defined by*

$$\mathcal{FT}\{m_{\perp}(\cdot, 0)\}(\mathbf{k}) = \int_V m_{\perp}(\mathbf{r}, 0) \exp(-i\mathbf{k} \cdot \mathbf{r}) \, d\mathbf{r}. \quad (3.13)$$

The Fourier encoding kernel function is thereby given by

$$\begin{aligned} E &: \mathcal{K} \times V \rightarrow \mathbb{C} \\ E &: (\mathbf{k}, \mathbf{r}) \mapsto \exp(-i\mathbf{k} \cdot \mathbf{r}). \end{aligned} \quad (3.14)$$

With the definition, the Fourier encoded MR signal can be expressed by

$$\tilde{s}(\mathbf{k}) \propto \int_V m_{\perp}(\mathbf{r}, 0) E(\mathbf{k}, \mathbf{r}) \, d\mathbf{r} = \mathcal{FT}\{m_{\perp}(\cdot, 0)\}(\mathbf{k}). \quad (3.15)$$

In an 'ideal' encoding scenario, each location within the object is assigned with a unique frequency and phase offset. Then, a one-to-one correspondence would exist between spatial location and acquired frequency/phase information in the signal. This would require the main static magnetic field \mathbf{B}_0 and the RF excitation $\mathbf{B}_1(t)$ to be perfectly constant over the entire volume, referred to as *perfect B_0 and B_1 homogeneity*. Likewise, the exclusion of any signal disturbances due to unwanted gradient modulation or noise influences would be necessary. Furthermore, an idealized encoding scenario comprises infinite and continuous k-space data to be accessible, such that $\tilde{s}(\mathbf{k})$ can be acquired for all $\mathbf{k} \in \mathcal{K}$. Then the encoded content $\{m_{\perp}(\mathbf{r}, 0), \mathbf{r} \in V\}$ could be entirely recovered by taking the *inverse Fourier transform* as justified by the *Fourier inversion theorem*.

Definition 3.2.5 (inverse Fourier transform). Let $F \in \mathcal{L}^2(\mathcal{K}, \mathbb{C})$, where $\mathcal{K} \subseteq \mathbb{R}^{\mathfrak{D}}$. The *inverse Fourier transform* with respect to \mathbf{k} in terms of angular frequencies is defined by

$$\mathcal{FT}^{-1}\{F\}(\mathbf{r}) = \frac{1}{(2\pi)^{\mathfrak{D}}} \int_{\mathcal{K}} F(\mathbf{k}) \exp(i\mathbf{k} \cdot \mathbf{r}) d\mathbf{k}.$$

Theorem 3.2.6 (Fourier inversion theorem). Let $m_{\perp}(\cdot, 0) \in \mathcal{L}^2(V \subseteq \mathbb{R}^{\mathfrak{D}}, \mathbb{C})$. Then the following holds:

$$m_{\perp}(\mathbf{r}, 0) = \mathcal{FT}^{-1}\{\mathcal{FT}\{m_{\perp}(\cdot, 0)\}\}(\mathbf{r}).$$

Remark 3.2.7. A proof for the Fourier inversion theorem can be found in a more general form in [Stein and Shakarchi, 2011].

Although in practice, the continuous and infinite collection of all Fourier signals in MRI experiments is impossible, this theoretical example reflects the underlying Fourier relation between k-space and image space. Any imperfections in the assignment of frequency and phase offsets during the encoding process lead to artifacts and demand for either mitigation in the acquisition or correction during image reconstruction or post-processing. A realistic k-space sampling scenario is provided in the next section. Subsequent, the influences of finite and discrete data sampling for the image reconstruction is discussed in Sec. 3.3.

3.2.2. Sampling of k-space

Along the time course of signal acquisition, a series of k-space points are identified. The set of collected k-space data in the measurement yields a finite time series of k-space positions which allows for tracing the path in k-space according to the temporal order. This path in k-space is referred to as *k-space trajectory*.

Definition 3.2.8 (k-space trajectory). Assume a discrete sampling of N_{smp} signal data points, sampled at time points $t_1 < \dots < t_{N_{\text{smp}}}$. The corresponding time series of visited k-space points $\mathcal{K}_{\text{smp}} := \{\mathbf{k}_n := \mathbf{k}(t_n)\}_{n=1}^{N_{\text{smp}}}$ is referred to as *k-space trajectory*.

The definition of the k-space trajectory facilitates a unified description of different data acquisition techniques with individual gradient encoding procedures. It depicts the temporal path of discrete samples through the continuously defined k-space as steered by amplitude and duration of the gradients. Particular k-space trajectories will be discussed in Sec. 3.4, examples are displayed in Figs. 3.1 and 3.2.

To emphasize the discrete sampling of Fourier signals, the samples are referred to as *Fourier coefficients* of the imaged quantity $\{m_{\perp}(\mathbf{r}, 0), \mathbf{r} \in V\}$. A finite series of Fourier coefficients is collected in an MRI acquisition, i.e.

$$d_n = \int_V m_{\perp}(\mathbf{r}, 0) \exp(-i\mathbf{k}_n \cdot \mathbf{r}) d\mathbf{r}, \text{ for each } \mathbf{k}_n \in \mathcal{K}_{\text{smp}}. \quad (3.16)$$

Based on this series of data points the image reconstruction problem is posed.

3.3. Fourier image reconstruction

The image reconstruction problem in MRI is to find a feasible image representation $I \in \mathcal{L}^2(\Omega, \mathbb{C})$, where $\Omega \subseteq \mathbb{R}^{\mathfrak{D}}$, for a \mathfrak{D} -dimensional imaging scenario, which covers the area of interest and provides data consistency with the measurement data d . In Fourier imaging, the data consistency constraint simply implies that a feasible solution I fulfills

$$\check{S}\{\mathcal{FT}\{I\}\} = d, \quad \text{where} \quad d_n = \langle m_{\perp}(\cdot, 0) | \exp(i\mathbf{k}_n \cdot \cdot) \rangle_{\mathcal{L}^2}, \quad (3.17)$$

where \check{S} selects samples according to the k-space trajectory of the acquisition.

Since the signal of Fourier imaging is sampled with a Fourier encoding scheme, the information about the signal origin is contained in the different frequency and phase off-sets in the measured MR signal. Hence, a *spectral analysis of the Fourier encoded signal* discloses the spatial origin and strength of signal contributions. Infinite continuous signal information would allow for 'perfect' image reconstruction. However, there are three fundamental limitations in practical Fourier encoded MRI:

1. discrete (or frequency band-limited) data sampling
2. finite data sampling
3. negative correlation of signal-to-noise and spatial resolution

These will be individually discussed below. Various sections follow discussions presented in [Liang and Lauterbur, 2000]. Fourier and time series analysis are based on [Stein and Shakarchi, 2011, Brockwell and Davis, 2013]. Successively, data availability is restricted from the infinite continuous case to infinite discrete sampling, and to finite and discrete data accessible for image reconstruction. Subsequently, the interference of signal-to-noise (SNR) and spatial resolution is discussed. Without loss of generality, only one-dimensional scenarios ($\mathfrak{D} = 1$) are considered, wherefore \mathbf{k} and \mathbf{r} reduce to scalars k and r .

Discrete sampling

Assume an infinite number of data $d = \{d_n\}_{n=-\infty}^{\infty}$, sampled at constant k-space intervals of Δk and thus, forming a set of discrete points. Let \check{S} denote the corresponding sampling operator according to the infinitely many k-space coordinates sampled. An image function $I(r)$ yields a feasible reconstruction given the measurement data, if

$$d = \check{S}\{\mathcal{FT}\{I\}\}, \quad (3.18)$$

$$\text{where } d_n = \int_V m_{\perp}(r, 0) \exp(-in\Delta kr) dr, \text{ for each } n \in \mathbb{Z}.$$

Such a feasible image function is constructed - in analogy to the inverse Fourier transform - from the data samples by the *Fourier series*.

Definition 3.3.1 (Fourier series). *The **Fourier series** in terms of angular frequencies of an infinite complex sequence $\{d_n\}_{n=-\infty}^{\infty}$, such that $\sum_{n=-\infty}^{\infty} |d_n|^2 < \infty$, is defined by*

$$I(r) = \frac{1}{2\pi} \sum_{n=-\infty}^{\infty} d_n \exp(in\Delta kr). \quad (3.19)$$

The question of how closely the such derived image function I approximates the underlying true $m_{\perp}(\cdot, 0)$ is answered by investigation of the effect of discrete sampling at constant intervals.

Theorem 3.3.2 (discrete sampling). *Assume Fourier encoded data sampled at k -space intervals of length Δk as denoted in (3.18) and define $FoV := \frac{2\pi}{\Delta k}$. Then the following equality holds:*

$$\sum_{n=-\infty}^{\infty} d_n \exp(in\Delta kr) = FoV \sum_{n=-\infty}^{\infty} m_{\perp}(r - nFoV, 0) \quad (3.20)$$

Before proving the theorem, two lemmata are considered.

Lemma 3.3.3. *Assume the same notations as in Thm. 3.3.2. Let δ denote the Dirac delta distribution, which is defined such that*

$$\int_{-\infty}^{\infty} \phi(x)\delta(x)dx = \phi(0), \quad (3.21)$$

for each function ϕ that is continuous at the origin. Then the following equations hold:

- (i) $FoV \sum_{n=-\infty}^{\infty} \delta(x - nFoV) = \sum_{n=-\infty}^{\infty} \exp(in\Delta kx)$.
- (ii) $\mathcal{FT}\{FoV \sum_{n=-\infty}^{\infty} \delta(x - nFoV)\} = \sum_{n=-\infty}^{\infty} \delta(k - n\Delta k)$

Proof. (i): Consider the Dirac comb of equally spaced Dirac delta distributions defined by

$$comb_{FoV}(x) := \sum_{n=-\infty}^{\infty} \delta(x - nFoV). \quad (3.22)$$

The Dirac comb is periodic, since $comb_{FoV}(x + FoV) = comb_{FoV}(x)$. Hence, the function can be expressed as a Fourier series, i.e.

$$comb_{FoV}(x) = \sum_{n=-\infty}^{\infty} c_n \exp(i2\pi nx/FoV), \quad (3.23)$$

where the Fourier coefficients c_n are given by

$$\begin{aligned} c_n &= \frac{1}{FoV} \int_{-\frac{FoV}{2}}^{\frac{FoV}{2}} comb_{FoV}(x) \exp(-i2\pi nx/FoV) dx \\ &= \frac{1}{FoV} \int_{-\frac{FoV}{2}}^{\frac{FoV}{2}} \sum_{n=-\infty}^{\infty} \delta(x - nFoV) \exp(-i2\pi nx/FoV) dx \\ &\stackrel{(\star)}{=} \frac{1}{FoV} \int_{-\frac{FoV}{2}}^{\frac{FoV}{2}} \sum_{n=-\infty}^{\infty} \delta(x) \exp(-i2\pi nx/FoV) dx \\ &= \frac{1}{FoV}. \end{aligned} \quad (3.24)$$

The equality marked with (\star) follows from the periodicity of the Dirac comb of FoV which by the integration over the interval $[-\frac{FoV}{2}, \frac{FoV}{2}]$ is evaluated only for $n = 0$. Comparison of (3.22) and (3.23) implies

$$\sum_{n=-\infty}^{\infty} \delta(x - nFoV) = \frac{1}{FoV} \sum_{n=-\infty}^{\infty} \exp(i2\pi nx/FoV). \quad (3.25)$$

With the derived assertion and inserting $FoV = \frac{2\pi}{\Delta k}$, the following holds:

$$FoV \sum_{n=-\infty}^{\infty} \delta(x - nFoV) = \sum_{n=-\infty}^{\infty} \exp(i2\pi nx/FoV) = \sum_{n=-\infty}^{\infty} \exp(in\Delta kx). \quad (3.26)$$

(ii): Taking the Fourier transform on both sides of the result of part (i) yields

$$\mathcal{FT} \left\{ FoV \sum_{n=-\infty}^{\infty} \delta(x - nFoV) \right\} \quad (3.27)$$

$$= \mathcal{FT} \left\{ \sum_{n=-\infty}^{\infty} \exp(in\Delta kx) \right\} \stackrel{\text{linearity}}{=} \sum_{n=-\infty}^{\infty} \mathcal{FT} \{ \exp(in\Delta kx) \} \quad (3.28)$$

$$= \sum_{n=-\infty}^{\infty} \int_{-\infty}^{\infty} \exp(in\Delta kx) \exp(-ikx) dx. \quad (3.29)$$

$$= \sum_{n=-\infty}^{\infty} \int_{-\infty}^{\infty} \exp(-ix(k - n\Delta k)) dx. \quad (3.30)$$

The integral on the right side describes the Fourier transform of 1. The equality

$$\int_{-\infty}^{\infty} \delta(k - \Delta k) \exp(ix(k - n\Delta k)) dk = 1, \quad (3.31)$$

can be proven by approximating the Dirac delta within the integral by the Gaussian kernel function of infinitesimally small width [Stein and Shakarchi, 2011]. Inserting the Fourier transform of the left side of (3.30) for the Fourier transform of 1 in (3.30) yields

$$\sum_{n=-\infty}^{\infty} \int_{-\infty}^{\infty} \exp(in\Delta kx) \exp(-ikx) dx = \sum_{n=-\infty}^{\infty} \delta(k - n\Delta k). \quad (3.32)$$

□

Remark 3.3.4. Lemma 3.3.3 (ii) demonstrates how infinite discrete sampling at intervals of Δk in k -space results in infinitely many replica of length FoV in the image domain.

Proof of Thm. 3.3.2. Consider the left side of the equality and substitute d_n by its signal expression, i.e.

$$\sum_{n=-\infty}^{\infty} d_n \exp(in\Delta kr) = \sum_{n=-\infty}^{\infty} \left[\int_V m_{\perp}(\hat{r}, 0) \exp(-in\Delta k\hat{r}) d\hat{r} \right] \exp(in\Delta kr). \quad (3.33)$$

The limits may be interchanged, since both the sum and the integral exist due to the assumption of a rapidly decreasing $m_{\perp}(\cdot, 0)$, hence,

$$\sum_{n=-\infty}^{\infty} d_n \exp(in\Delta kr) = \int_{\mathbb{R}} m_{\perp}(\hat{r}, 0) \sum_{n=-\infty}^{\infty} \exp(in\Delta k(r - \hat{r})) d\hat{r}. \quad (3.34)$$

Together with the results of Lemma 3.3.3(i) it further follows that

$$\begin{aligned} \sum_{n=-\infty}^{\infty} d_n \exp(in\Delta kr) &= \int_{\mathbb{R}} m_{\perp}(\hat{r}, 0) FoV \sum_{n=-\infty}^{\infty} \delta((r - \hat{r}) - nFoV) d\hat{r} \\ &= FoV \sum_{n=-\infty}^{\infty} \int_{\mathbb{R}} m_{\perp}(\hat{r}, 0) \delta((r - \hat{r}) - nFoV) d\hat{r}. \end{aligned} \quad (3.35)$$

Evaluation of the Dirac delta distribution according to its definition then yields

$$\sum_{n=-\infty}^{\infty} d_n \exp(in\Delta kr) = FoV \sum_{n=-\infty}^{\infty} m_{\perp}(r - nFoV, 0), \quad (3.36)$$

which concludes the proof of the theorem. \square

Remark 3.3.5. The result of Thm. 3.3.2 reveals how constructing the Fourier series of discretely sampled Fourier coefficients of the underlying $m_{\perp}(\cdot, 0)$ leads to a periodic replication of $m_{\perp}(\cdot, 0)$ in intervals of FoV , inverse to the sampling intervals Δk .

The question of how closely the such derived image function I approximates the underlying true $m_{\perp}(\cdot, 0)$ is answered by investigation of the effect of discrete sampling at constant intervals. Therefore, the validness of the Fourier series I (Def. 3.3.1) depends on the extent of spatial support (Def. 3.3.6) of the underlying $m_{\perp}(\cdot, 0)$ as well as on the incorporated sampling intervals Δk . A well-known result in linking these is established by the *Nyquist-Shannon sampling theorem*.

3.3.1. Nyquist-Shannon sampling theorem

Definition 3.3.6 (support, support-limited). The **support** of a function $m_{\perp}(\cdot, 0) : V \subseteq \mathbb{R} \rightarrow \mathbb{C}$ is defined by

$$\text{supp}(m_{\perp}(\cdot, 0)) := \{r \in V \mid m_{\perp}(r, 0) \neq 0\}.$$

The function $m_{\perp}(\cdot, 0)$ is **support-limited**, if there exists $L \in \mathbb{R}$, $L > 0$, such that $\text{supp}(m_{\perp}(\cdot, 0)) \subseteq [-\frac{L}{2}, \frac{L}{2}]$.

Theorem 3.3.7 (Theorem of support-limited functions (Nyquist-Shannon)). Let $m_{\perp}(r, 0) : \mathbb{R} \rightarrow \mathbb{C}$ be a support-limited function. Without loss of generality, assume the support to be centralized (e.g. by spatial shifts) such that $\text{supp}(m_{\perp}(\cdot, 0)) = [-\frac{L}{2}, \frac{L}{2}]$, for $L > 0$. Consider a set $\{d_n\}_{n=-\infty}^{\infty}$ of discrete samples of Fourier coefficients of $m_{\perp}(\cdot, 0)$, acquired at intervals of Δk . Define the constant $FoV := \frac{2\pi}{\Delta k}$ and the interval $\mathbf{FoV} := [-\frac{FoV}{2}, \frac{FoV}{2}]$. Let $I : \mathbf{FoV} \rightarrow \mathbb{C}$ be the Fourier series constructed from the sampled data as in Def. 3.3.1. Then the following equivalence holds:

$$m_{\perp}(r, 0) = \Delta k I(r), \text{ for } r \in \mathbf{FoV} \quad \text{if and only if} \quad \Delta k \leq \frac{2\pi}{L}. \quad (3.37)$$

Proof. Let $\chi_{\mathbf{FoV}}$ be the characteristic function of the set \mathbf{FoV} , i.e. $\chi_{\mathbf{FoV}}(r) = 1$, if $r \in \mathbf{FoV}$ and zero otherwise. Let $r \in [-\frac{FoV}{2}, \frac{FoV}{2}]$. The definition of the Fourier series (Def. 3.3.1) and the

result of Thm. 3.3.2 imply:

$$\begin{aligned}
m_{\perp}(r, 0) &= \Delta k I(r) \chi_{\mathbf{FoV}}(r) \\
\Leftrightarrow m_{\perp}(r, 0) &= \frac{\Delta k}{2\pi} \sum_{n=-\infty}^{\infty} d_n \exp(-in\Delta kr) \chi_{\mathbf{FoV}}(r) \\
\Leftrightarrow m_{\perp}(r, 0) &= \sum_{n=-\infty}^{\infty} m_{\perp}\left(r - n\frac{2\pi}{\Delta k}, 0\right) \chi_{\mathbf{FoV}}(r).
\end{aligned} \tag{3.38}$$

The latter expression is valid if and only if the interval of periodicity is larger than the support of $m_{\perp}(r, 0)$, i.e. $FoV = \frac{2\pi}{\Delta k} \geq L$. Hence,

$$m_{\perp}(r, 0) = \Delta k I(r), \text{ for } r \in \mathbf{FoV} \Leftrightarrow \frac{2\pi}{\Delta k} \geq L. \tag{3.39}$$

□

The Theorem of support-limited functions according to Nyquist-Shannon demonstrates that in MRI, the underlying $m_{\perp}(\cdot, 0)$ can be completely restored given an infinite discrete data set sampled at sampling rates matching the threshold as dictated by the spatial support $\text{supp}(m_{\perp}(\cdot, 0))$.

Corollary 3.3.8. *Let $m_{\perp}(\cdot, 0)$ be support-limited, i.e. $\text{supp}(m_{\perp}(\cdot, 0)) \subseteq [-\frac{L}{2}, \frac{L}{2}]$, for $L > 0$. Assume infinitely many discrete data samples $d = \{d_n\}_{n=-\infty}^{\infty}$ to be given at sampling intervals $\Delta k \leq \frac{2\pi}{L}$. Then the image function*

$$I^{\dagger}(r) := \frac{\Delta k}{2\pi} \sum_{n=-\infty}^{\infty} d_n \exp(in\Delta kr), \text{ } r \in \mathbf{FoV}, \tag{3.40}$$

provides exact image reconstruction by $I^{\dagger}(r) = m_{\perp}(r, 0)$, for each $r \in \mathbf{FoV}$.

Definition 3.3.9 (full- or sub-Nyquist-sampled). *An acquired MRI data set is referred as **full-Nyquist-sampled** or **fully sampled**, if Δk is chosen in the limits of the Thm. 3.3.7. Otherwise, it is termed **sub-Nyquist-sampled** or **undersampled**.*

Definition 3.3.10 (field of view). *The **field of view (FoV)** in MRI is defined by $\mathbf{FoV} := [-\frac{FoV}{2}, \frac{FoV}{2}]$, where $FoV := \frac{2\pi}{\Delta k}$.*

Remark 3.3.11. *The image function support is chosen to match the field of view, i.e. $\Omega := \mathbf{FoV}$. In the case of Nyquist-sampling, the field of view necessarily covers the imaged object's support, i.e. $\text{supp}(m_{\perp}(\cdot, 0)) \subseteq \mathbf{FoV} = \Omega$.*

The field of view designates the image support in image reconstruction. Theorem 3.3.7 assures unique image representation under the condition of a limited object support and for discrete - yet infinite - sampling of k-space signal. Finite sampling, however, cannot result in an exact image reconstruction as will be covered in the next section. Nevertheless, with finite sampling, the signal can be approximated with arbitrary precision.

Finite sampling

Without loss of generality, let $N_{\text{smp}} \in \mathbb{N}$ denote an even number of data samples. Let $\{d_n\}_{n=-\frac{N_{\text{smp}}}{2}}^{\frac{N_{\text{smp}}}{2}-1}$ denote a finite and discrete set of data points that are Nyquist-sampled at intervals $\Delta k \leq \frac{2\pi}{L}$ (Def. 3.3.9). Based on the finitely many data samples, the image function can only be reconstructed in the space spanned by the finitely many data points. Let \check{S} denote the sampling operator that selects the N_{smp} samples according to the k-space trajectory. An image function I yields a feasible reconstruction given the finite set of equations if

$$d = \check{S}\{\mathcal{FT}\{I\}\},$$

$$\text{where } d_n = \int_V m_{\perp}(r, 0) \exp(-in\Delta kr) dr, \text{ for } n = -\frac{N_{\text{smp}}}{2}, \dots, \frac{N_{\text{smp}}}{2} - 1. \quad (3.41)$$

Assuming data consistency alone, Fourier coefficients for all n with $|n| > \frac{N_{\text{smp}}}{2}$ and $n \neq -\frac{N_{\text{smp}}}{2}$ can be freely chosen without violating the data consistency. Therefore, the minimum norm solution is sought as the optimal image function within the set of feasible images defined by:

$$I^{\dagger} = \underset{I \in \mathcal{L}^2(\Omega, \mathbb{C})}{\text{argmin}} \|I\|_{\mathcal{L}^2}^2, \text{ subject to } \check{S}\{\mathcal{FT}\{I\}\} = d. \quad (3.42)$$

Theorem 3.3.12. *Given the finite set of (discretely) Nyquist-sampled Fourier coefficients $\{d_n\}_{n=-\frac{N_{\text{smp}}}{2}}^{\frac{N_{\text{smp}}}{2}-1}$, the optimal, feasible image reconstruction solving (3.42) is obtained by*

$$I^{\dagger}(r) = \frac{\Delta k}{2\pi} \sum_{n=-\frac{N_{\text{smp}}}{2}}^{\frac{N_{\text{smp}}}{2}-1} d_n \exp(in\Delta kr). \quad (3.43)$$

Proof. The Fourier series as in Cor. 3.3.8 constructed from the finitely many data samples and an arbitrary set of coefficients $\{a_n \in \mathbb{C} \mid |n| > \frac{N_{\text{smp}}}{2}, n \neq -\frac{N_{\text{smp}}}{2}\}$, i.e.

$$I_{\{a_n\}}(r) = \frac{\Delta k}{2\pi} \sum_{n=-\frac{N_{\text{smp}}}{2}}^{\frac{N_{\text{smp}}}{2}-1} d_n \exp(in\Delta kr) + \frac{\Delta k}{2\pi} \sum_{|n| > \frac{N_{\text{smp}}}{2}, n \neq -\frac{N_{\text{smp}}}{2}} a_n \exp(in\Delta kr), \quad (3.44)$$

fulfills data consistency. The chosen set of coefficients leads to an optimal - in terms of (3.42) - image reconstruction I^{\dagger} if and only if

$$I^{\dagger} = \underset{I_{\{a_n\}}}{\text{argmin}} \|I_{\{a_n\}}\|_{\mathcal{L}^2}^2. \quad (3.45)$$

Parseval's theorem (e.g. [Stein and Shakarchi, 2011]) implies

$$\|I_{\{a_n\}}\|_{\mathcal{L}^2}^2 \text{ is minimal} \Leftrightarrow |a_n|^2 \text{ is minimal}. \quad (3.46)$$

Hence, the minimum norm solution for the image reconstruction is given by

$$I^{\dagger}(r) = \frac{\Delta k}{2\pi} \sum_{n=-\frac{N_{\text{smp}}}{2}}^{\frac{N_{\text{smp}}}{2}-1} d_n \exp(in\Delta kr). \quad (3.47)$$

□

Finite data sampling essentially yields data truncation in the Fourier domain. Whereas the Nyquist-Shannon theorem justified discrete data acquisition, the following shows how finite sampling cannot result in exact representation of the underlying magnetization densities.

3.3.2. Point spread function and spatial resolution

In signal processing, the **point spread function (PSF)** is used to characterize the response of an imaging modality to a point source. Its width - usually the **full width at half maximum (FWHM)** - reflects the *spatial resolution*. The PSF therefore characterizes *image blurring* in the reconstruction. For Fourier imaging, the PSF relates the measured k-space extent to the achievable spatial resolution.

Definition 3.3.13 (point spread function). *Assume an imaging and reconstruction scenario to be described by some function F . The **point spread function (PSF)** is defined for each r_0 in the imaging domain by $\text{PSF}_{r_0}(r) := F\{\delta(r - r_0)\}(r)$, for all r , where $\delta(r - r_0)$ denotes the delta distribution.*

Theorem 3.3.14. *Consider a point source at r_0 in the spatial domain $V \subseteq \mathbb{R}$ described by the delta distribution $\delta(r - r_0)$. Assume k-space values to be known on a compact interval $\mathcal{K}_{\text{finite}} := [-k_{\text{max}}, k_{\text{max}}]$. Then the continuous **point spread function (PSF)** for finite Fourier encoding scenarios is derived by*

$$\text{PSF}_{r_0}(r) = \frac{k_{\text{max}}}{\pi} \text{sinc}(k_{\text{max}}(r - r_0)).$$

Proof. Let $\chi_{\mathcal{K}_{\text{finite}}}$ be the characteristic function for the interval $\mathcal{K}_{\text{finite}} := [-k_{\text{max}}, k_{\text{max}}]$, i.e. $\chi_{\mathcal{K}_{\text{finite}}}(k) = 1$, for $k \in \mathcal{K}_{\text{finite}}$ and zero otherwise. Let $r_0 \in V$ and consider the delta distribution $\delta(r - r_0)$. With Fourier encoding and the inverse Fourier transform for image reconstruction follows:

$$\begin{aligned} \text{PSF}_{r_0}(r) &:= \mathcal{FT}^{-1} \left\{ \chi_{\mathcal{K}_{\text{finite}}}(k) \int_V \delta(\hat{r} - r_0) \exp(-ik\hat{r}) d\hat{r} \right\} (r) \\ &= \mathcal{FT}^{-1} \left\{ \chi_{\mathcal{K}_{\text{finite}}}(k) \exp(-ikr_0) \right\} (r) \\ &= \frac{1}{2\pi} \int_{-k_{\text{max}}}^{k_{\text{max}}} \exp(ik(r - r_0)) dk \\ &= \frac{1}{\pi(r - r_0)} \frac{\exp(ik_{\text{max}}(r - r_0)) - \exp(-ik_{\text{max}}(r - r_0))}{2i} \\ &= \frac{k_{\text{max}}}{\pi} \frac{\sin(k_{\text{max}}(r - r_0))}{k_{\text{max}}(r - r_0)} = \frac{k_{\text{max}}}{\pi} \text{sinc}(k_{\text{max}}(r - r_0)). \end{aligned} \tag{3.48}$$

□

Remark 3.3.15. *The $\text{PSF}_{r_0}(r)$ derived in Thm. 3.3.14 is determined solely by the relative spatial distance $\Delta r = r - r_0$, hence, denote $\text{PSF}_{r_0}(r) \equiv \text{PSF}(r - r_0) \equiv \text{PSF}(\Delta r)$.*

The PSF of Thm. 3.3.14 describes how the magnetization from single locations within the object contribute to a range of reconstructed image values within the image, solely due to finite acquisition. Point sources are blurred in the image according to the main lobe of the sinc function and leakage occurs according to the smaller side lobes. The PSF of Thm. 3.3.14 is derived for *continuous* sampling. The following shows that discrete sampling does not alter the blurring introduced by the main lobe of the *continuous* PSF, but further describes periodic replica. The *discrete* PSF therefore also reflects artifacts in the case of sub-Nyquist sampling.

Theorem 3.3.16. Consider a point source at r_0 in the spatial domain described by the delta distribution $\delta(r - r_0)$. Assume k -space samples to be given for $\left\{-\frac{N_{\text{smp}}}{2}\Delta k, \dots, \frac{N_{\text{smp}}}{2}\Delta k\right\}$, where N_{smp} is even. Then the discrete *point spread function* (PSF) for this finite and discrete Fourier encoding scenario is derived by

$$\text{PSF}(\Delta r) = \sum_{n=-\infty}^{\infty} \delta(\hat{r} - nFoV) * N_{\text{smp}} \text{sinc}\left(\frac{N_{\text{smp}}}{2}\Delta k\hat{r}\right) \Big|_{\hat{r}=\Delta r}$$

for $\Delta r \leq FoV$, where $FoV := \frac{2\pi}{\Delta k}$.

Proof. Let $\chi_{\mathcal{K}_{\text{finite},N}}$ denote the characteristic function of the k -space interval identified in the acquisition, $\mathcal{K}_{\text{finite},N} := \left[-\frac{N_{\text{smp}}}{2}\Delta k, \frac{N_{\text{smp}}}{2}\Delta k\right]$, such that $\chi_{\mathcal{K}_{\text{finite},N}}(k) = 1$, for $k \in \mathcal{K}_{\text{finite},N}$ and zero otherwise. Consider the Dirac comb $\sum_{n=-\infty}^{\infty} \delta(k - n\Delta k)$. Then the finitely many discrete lying k -space coordinates of the k -space trajectory are identified by

$$\chi_{\mathcal{K}_{\text{finite},N}}(k) \sum_{n=-\infty}^{\infty} \delta(k - n\Delta k), \text{ for } k \in \mathcal{K}.$$

Let $r_0 \in V$ and consider the delta distribution $\delta(r - r_0)$. With Fourier encoding and Fourier image reconstruction follows:

$$\begin{aligned} \text{PSF}_{r_0}(r) &:= \mathcal{FT}^{-1} \left\{ \chi_{\mathcal{K}_{\text{finite},N}}(k) \sum_{n=-\infty}^{\infty} \delta(k - n\Delta k) \int_V \delta(\hat{r} - r_0) \exp(-ik\hat{r}) d\hat{r} \right\} (r) \\ &= \mathcal{FT}^{-1} \left\{ \chi_{\mathcal{K}_{\text{finite},N}}(k) \sum_{n=-\infty}^{\infty} \delta(k - n\Delta k) \exp(-ikr_0) \right\} (r) \\ &\stackrel{\text{Convolution Thm}}{=} \left(\mathcal{FT}^{-1} \left\{ \sum_{n=-\infty}^{\infty} \delta(k - n\Delta k) \right\} * \mathcal{FT}^{-1} \left\{ \chi_{\mathcal{K}_{\text{finite},N}}(k) \exp(-ikr_0) \right\} \right) (r) \end{aligned} \quad (3.49)$$

The left part relates to the discrete sampling in intervals of Δk and results in replica of FoV in the image space according to Lemma 3.3.3(ii). The right part is known from Thm. 3.3.14. Hence,

$$\begin{aligned} \text{PSF}_{r_0}(r) &= FoV \sum_{n=-\infty}^{\infty} \delta(\hat{r} - nFoV) * N_{\text{smp}} \frac{\Delta k}{2\pi} \text{sinc}\left(\frac{N_{\text{smp}}}{2}\Delta k(\hat{r} - r_0)\right) \Big|_{\hat{r}=r} \\ &\stackrel{FoV = \frac{2\pi}{\Delta k}}{=} \sum_{n=-\infty}^{\infty} \delta(\hat{r} - nFoV) * N_{\text{smp}} \text{sinc}\left(\frac{N_{\text{smp}}}{2}\Delta k(\hat{r} - r_0)\right) \Big|_{\hat{r}=r}. \end{aligned} \quad (3.50)$$

Since the convolution commutes with translations and denoting $\Delta r := r - r_0$, this reduces to

$$\text{PSF}_{r_0}(r) = \sum_{n=-\infty}^{\infty} \delta(\hat{r} - nFoV) * N_{\text{smp}} \text{sinc}\left(\frac{N_{\text{smp}}}{2}\Delta k\hat{r}\right) \Big|_{\hat{r}=\Delta r} =: \text{PSF}(\Delta r). \quad (3.51)$$

□

Corollary 3.3.17. The Fourier reconstructed image from finite and discrete data sampling (cf. 3.43) relates to the underlying transverse magnetization density by

$$I^\dagger(r) = \int_V m_\perp(r, 0) \text{PSF}(r - \hat{r}) d\hat{r} = (m_\perp(\cdot, 0) * \text{PSF})(r). \quad (3.52)$$

Definition 3.3.18 (spatial resolution). *The **spatial resolution** is defined with respect to the **full width at half maximum (FWHM)** of the **PSF**.*

The PSF of Fourier imaging is described by a sinc function according to Thms. 3.3.14 and 3.3.16. The FWHM of the sinc function thereby depends on the maximum k-space position sampled in the finite data acquisition. The k-space position sampled is related to the k-space sampling intervals and the number of samples. The corollary below follows from the definition of spatial resolution and the derived PSF of Fourier imaging.

Corollary 3.3.19. *In Fourier imaging at given sampling intervals Δk , the spatial resolution increases if and only if the number of samples increases.*

High spatial resolution is desirable for good depiction quality. Likewise, Gibbs ringing [Gibbs, 1898] at spatial discontinuities and due to the finite acquisition, as well as partial-volume effects of different tissue within the same voxel, improve at higher spatial resolution. Unfortunately, a fundamental limitation of Fourier imaging is that as spatial resolution is increased, SNR decreases, which is discussed in Sec. 3.3.3.

Pixel size and image resolution

Spatial resolution in MRI is limited due to finite sampling. The FWHM of the PSF thereby sets the limits on spatial resolution. Extension to the 2-dimensional (or 3-dimensional) case of the considerations is straightforward. For a digital image representation, the derived image function $I^\dagger(r)$ is evaluated at a discrete set of finitely many *pixels*. This is simply performed by the *inverse discrete Fourier transform*.

In $2\mathcal{D}$ -slice imaging, the size of the field of view and the number of data samples may vary in both dimensions. The following notation is commonly applied: $FoV_x = \frac{2\pi}{\Delta k_x}$ and $FoV_y = \frac{2\pi}{\Delta k_y}$ corresponding to N_{fe} or N_{pe} acquired samples in frequency and phase encoding direction, respectively.

Definition 3.3.20 (pixel size). *For a field of view indicated by $FoV_x \times FoV_y = \frac{2\pi}{\Delta k_x} \times \frac{2\pi}{\Delta k_y}$ and $N_x \times N_y$ pixels, the **pixel size** is given by*

$$\Delta x := \frac{FoV}{N_x} = \frac{2\pi}{N_x \Delta k_x} \quad \text{and} \quad \Delta y := \frac{FoV}{N_y} = \frac{2\pi}{N_y \Delta k_y}.$$

Definition 3.3.21 (image resolution). *The **image resolution** is defined by the ratio of the number of pixels over the image extent, i.e. $\frac{N_x}{FoV_x}$ and $\frac{N_y}{FoV_y}$.*

Definition 3.3.22 (inverse discrete Fourier series). *The two-dimensional **inverse discrete Fourier series** DFT_{xy}^{-1} of the data set $\{d_{n,m} \mid n = 1, \dots, N_x, m = 1, \dots, N_y\}$ is defined - omitting the scaling*

factor $\frac{\Delta k_x}{2\pi}$ and $\frac{\Delta k_y}{2\pi}$ - by

$$\begin{aligned} I(x_p, y_q) &= I(p\Delta x, q\Delta y) \\ &= \frac{1}{N_x} \frac{1}{N_y} \sum_{n=-\frac{N_x}{2}}^{\frac{N_x}{2}-1} \sum_{m=-\frac{N_y}{2}}^{\frac{N_y}{2}-1} d_{n,m} \exp(in\Delta k_x p\Delta x) \exp(im\Delta k_y q\Delta y) \\ &= \frac{1}{N_x} \frac{1}{N_y} \sum_{n=-\frac{N_x}{2}}^{\frac{N_x}{2}-1} \sum_{m=-\frac{N_y}{2}}^{\frac{N_y}{2}-1} d_{n,m} \exp(i2\pi np/N_x) \exp(i2\pi mq/N_y), \end{aligned}$$

for $p = 1, \dots, N_x$ and $q = 1, \dots, N_y$.

Remark 3.3.23. In many cases, $N_x > N_{fe}$ and $N_y > N_{pe}$ are chosen for smoother image display. This increases image resolution according to Def. 3.3.21. Nevertheless, the spatial resolution remains the same, since it is determined by the PSF (Def. 3.3.18).

Remark 3.3.24. The set of pixels $\{(x_p, y_q) \mid p = 1, \dots, N_x, q = 1, \dots, N_y\}$ in terms of tuples can be likewise referred as series of pixel vectors $\{\mathbf{x}_m = (x_m, y_m)^T\}_{m=1}^{N_{\text{pix}}=N_x N_y}$.

Thereof, the *magnitude image* $|I|$ is typically composed to depict signal intensities. In terms of practical realization, the discrete Fourier transform has the additional advantage of a fast algorithm for computation according to the *Fast Fourier transform* [Cooley and Tukey, 1965].

3.3.3. Signal-to-noise-ratio (SNR) in Fourier image reconstruction

Noise is an inevitable contribution in MR measurements. As briefly encountered in Sec. 2.9, noise variances increase with the sampling bandwidth. In this section, noise influences in the data acquisition by spatial encoding and implications in image reconstruction by pixel evaluation are discussed. The severity of noise corruption is characterized by the *variance* and a commonly used measure for evaluating acquisition and image quality is the **signal-to-noise ratio (SNR)**. Particular characteristics in SNR of Fourier reconstructions are derived. Without loss of generality, the one-dimensional scenario is considered, as Fourier reconstruction of both spatial dimensions is separable.

Definition 3.3.25 (stationary stochastic Gaussian white noise process). Let $\{\varepsilon_d(k_n)\}_{k_n \in \mathcal{K}_{\text{smp}}}$ be a family of Gaussian random variables. It is called a **stationary stochastic Gaussian white noise process**, if the following holds:

- (i) it is of zero mean, i.e. $\mathbb{E}[\varepsilon_d(k_n)] = 0$
- (ii) it is of finite standard deviation, i.e. $\sigma_d(\varepsilon_d(k_n)) = \sqrt{\mathbb{E}[\varepsilon_d(k_n)\varepsilon_d^*(k_n)]} =: \sigma_d < \infty$
- (iii) it is uncorrelated, i.e. $\mathbb{E}[\varepsilon_d(k_i)\varepsilon_d^*(k_j)] = 0$, for $i \neq j$,

Remark 3.3.26. Note that all properties are independent of time ($k_n \equiv k_n(t)$), which implies stationarity. In particular properties (ii) and (iii) imply the autocorrelation function to only depend on the time lag, which is often used as a definition for stationarity. For more details on Gaussian white noise processes see [Brockwell and Davis, 2013] and related work of the author [Ramb et al., 2013c].

For MRI acquisitions, noise in data samples acquired according to the k-space trajectory is assumed to be described by a stationary stochastic Gaussian white noise process $\{\varepsilon_d(k_n)\}_{k_n \in \mathcal{K}_{\text{smp}}}$. The N_{smp} data samples corrupted by additive noise are represented by

$$\hat{d}_n = d_n + \varepsilon_d(k_n), \quad \text{for } n = 1, \dots, N_{\text{smp}}. \quad (3.53)$$

The image reconstructed from the noise corrupted data exhibits noise corruption as well. Hence, a noise corrupted image is formulated by

$$\hat{I}(x_m) = I(x_m) + \varepsilon_I(x_m), \quad \text{for } m = 1, \dots, N_{\text{pix}} = N_{\text{smp}}. \quad (3.54)$$

In order to gain insight about the *image noise* $\varepsilon_I(x_m)$ in each pixel x_m , noise characteristics are derived from the reconstruction of noise-only data (using Def. 3.3.22 omitting $\frac{\Delta k}{2\pi}$ for simplicity), hence,

$$\varepsilon_I(x_m) = \frac{1}{N_{\text{smp}}} \sum_{n=-\frac{N_{\text{smp}}}{2}}^{\frac{N_{\text{smp}}}{2}-1} \varepsilon_d(k_n) \exp(i2\pi nm/N_{\text{smp}}), \quad \text{for } m = 1, \dots, N_{\text{smp}}. \quad (3.55)$$

Therefore, the following assertion for image noise in Fourier reconstruction scenarios can be made.

Proposition 3.3.27. *The image noise $\{\varepsilon_I(x_m)\}_{m=1}^{N_{\text{pix}}=N_{\text{smp}}}$ in MR images based on the Fourier reconstruction formula applied to N_{smp} Nyquist-sampled k-space samples provides*

- (i) zero mean, i.e. $\mathbb{E}[\varepsilon_I(x_m)] = 0$,
- (ii) standard deviation of $\sigma(\varepsilon_I) \propto \frac{1}{\sqrt{N_{\text{smp}}}} \sigma_d$,
- (iii) uncorrelated noise across pixels, i.e. $\sigma^2(\varepsilon_I(x_k), \varepsilon_I(x_l)) = \mathbb{E}[\varepsilon_I(x_k) \varepsilon_I^*(x_l)] = 0$, for $k \neq l$.

Proof. [following [Liang and Lauterbur, 2000]] The number of samples/pixels is referred to by $N := N_{\text{smp}} = N_{\text{pix}}$ in the following.

- (i): Linearity of taking the mean and $\mathbb{E}[\varepsilon_d(k_n)] = 0$ (property (i) of the Gaussian white noise process) implies $\mathbb{E}[\varepsilon_I(x_m)] = \frac{1}{N} \sum_{n=-\frac{N}{2}}^{\frac{N}{2}-1} \mathbb{E}[\varepsilon_d(k_n)] \exp(i2\pi nm/N) = 0$.

(ii)+(iii): Let $p, q \in \{1, \dots, N\}$ with $p \neq q$. Then with (i) follows

$$\sigma^2(\varepsilon_I(x_p), \varepsilon_I(x_q)) = \mathbb{E}[\varepsilon_I(x_p) \varepsilon_I^*(x_q)] \quad (3.56)$$

$$= \mathbb{E} \left[\left(\frac{1}{N} \sum_{n=-\frac{N}{2}}^{\frac{N}{2}-1} \varepsilon_d(k_n) \exp(i2\pi np/N) \right) \left(\frac{1}{N} \sum_{m=-\frac{N}{2}}^{\frac{N}{2}-1} \varepsilon_d(k_m) \exp(i2\pi mq/N) \right)^* \right]. \quad (3.57)$$

Linearity of taking the mean leads to

$$\sigma^2(\varepsilon_I(x_p), \varepsilon_I(x_q)) = \frac{1}{N^2} \sum_{n=-\frac{N}{2}}^{\frac{N}{2}-1} \sum_{m=-\frac{N}{2}}^{\frac{N}{2}-1} \mathbb{E}[\varepsilon_d(k_n) \varepsilon_d^*(k_m)] \exp(i2\pi(np - mq)/N). \quad (3.58)$$

Since by property (iii) of the Gaussian white noise process follows for $n \neq m$ that $\sigma^2(\varepsilon_d(k_n), \varepsilon_d(k_m)) = \mathbb{E}[\varepsilon_d(k_n)\varepsilon_d^*(k_m)] = 0$, one can further conclude

$$\sigma^2(\varepsilon_I(x_p), \varepsilon_I(x_q)) = \frac{1}{N^2} \sum_{n=-\frac{N}{2}}^{\frac{N}{2}-1} \sigma^2(\varepsilon_d(k_n), \varepsilon_d(k_n)) \exp(i2\pi(p-q)n/N) \quad (3.59)$$

$$= \sigma_d^2 \frac{1}{N^2} \sum_{n=-\frac{N}{2}}^{\frac{N}{2}-1} \exp(i2\pi(p-q)n/N) \quad (3.60)$$

$$= \begin{cases} \frac{1}{N} \sigma_d^2 & \text{for } p = q \\ 0 & \text{otherwise} \end{cases} \quad (3.61)$$

Hence, proving the assertions made in (ii) and (iii), respectively. □

The ratio between signal strength and noise variance in the reconstructed image yields an important measure for image quality.

Definition 3.3.28 (SNR). The image **signal-to-noise ratio (SNR)** is defined by the ratio of the pixel magnitude over the intensity of the noise variance, i.e.

$$\text{SNR}(x_m) = \frac{|\hat{I}(x_m)|}{\sigma(\hat{I}(x_m))}. \quad (3.62)$$

An important relation between the number of samples given a fixed **field of view** and the **SNR** in Fourier reconstructions exist.

Proposition 3.3.29. Assume k -space signal to decay to zero in the outer part of k -space. In case of Fourier reconstructed images, for fixed bandwidth, absolute temperature, k -space sampling intervals and field of view, the average SNR of the image yields

$$\text{SNR}_{\text{avg}}^{\text{Fourier}} \propto \frac{1}{\sqrt{N_{\text{smp}}}}, \quad (3.63)$$

where N_{smp} denotes the number of data samples and is sufficiently large to cover the central k -space of main signal contributions.

Remark 3.3.30. Note that keeping a fixed bandwidth and a fixed k -space sampling interval Δk implies a fixed field-of-view, as it is defined by $\text{FoV} = \frac{2\pi}{\Delta k}$. Therefore, when increasing the number of samples, the pixel size $\frac{\text{FoV}}{N_{\text{pix}}} = \frac{\text{FoV}}{N_{\text{smp}}}$ necessarily decreases.

Proof. [following [Liang and Lauterbur, 2000]] Let $N := N_{\text{smp}} = N_{\text{pix}}$ denote the number of samples/pixels. The SNR's inverse proportionality to the square root of the sample size follows from calculating the average magnitude value of the image, i.e.

$$\begin{aligned} \hat{I}_{\text{avg}}^2 &= \frac{1}{N} \sum_{n=-\frac{N}{2}}^{\frac{N}{2}-1} \hat{I}(x_n) \hat{I}(x_n)^* = \frac{1}{N^3} \sum_{n=-\frac{N}{2}}^{\frac{N}{2}-1} \sum_{k=-\frac{N}{2}}^{\frac{N}{2}-1} \sum_{l=-\frac{N}{2}}^{\frac{N}{2}-1} \hat{d}_k \hat{d}_l^* \exp(i(k-l)n/N) \\ &= \frac{1}{N^2} \sum_{n=-\frac{N}{2}}^{\frac{N}{2}-1} |\hat{d}_n|^2. \end{aligned} \quad (3.64)$$

The series of partial sums $\mathfrak{S}_N := \sum_{n=-\frac{N}{2}}^{\frac{N}{2}-1} \left| \hat{d}_n \right|^2$ is monotonically increasing, since each $\left| \hat{d}_n \right|^2 \geq 0$ and $\left| \hat{d}_n \right|^2 \in \mathbb{R}$. Signal contributions in k-space are assumed to decay to zero for the outer part of k-space. Hence, one can assume the existence of a constant \hat{d}_{main}^2 such that $\mathfrak{S}_N \approx \hat{d}_{\text{main}}^2$, for $N \gg 0$. Then

$$\hat{I}_{\text{avg}}^2 \approx \frac{1}{N^2} \hat{d}_{\text{main}}^2. \quad (3.65)$$

Hence, employing the result of Prop. 3.3.27(ii), the average image SNR is approximated by

$$\text{SNR}_{\text{avg}} = \frac{\left| \hat{I}_{\text{avg}} \right|}{\sigma(\varepsilon_I)} \approx \frac{\left| \hat{d}_{\text{main}} \right|}{N \sigma(\varepsilon_I)} \stackrel{\text{Prop. 3.3.27(ii)}}{\propto} \frac{\sqrt{N} \left| \hat{d}_{\text{main}} \right|}{N \sigma_d} = \frac{\left| \hat{d}_{\text{main}} \right|}{\sqrt{N} \sigma_d}. \quad (3.66)$$

□

Thus, increasing the spatial resolution by increasing the number of samples while fixing the field-of-view results in a decrease of the average SNR for Fourier reconstructions.

Corollary 3.3.31. *From Prop. 3.3.29 follows directly for the case of two-dimensional Fourier reconstruction (Def. 3.3.22)*

$$\text{SNR}_{\text{avg}}^{\text{Fourier}} \propto \frac{1}{\sqrt{N_x} \sqrt{N_y}}.$$

Since noise is pixel-wise uncorrelated (Proposition 3.3.27 (iii)), the average SNR of a Fourier reconstructed image can be estimated from **regions of interest (ROIs)** for signal intensities and noise. Therefore a signal region, R_I , is selected incorporating pixels which depict signal intensities of the imaged object. Furthermore, a second ROI from a noise region, R_{ε_I} , is designated outside the object's image support and avoiding artifacts. The average signal strength is then derived based on the samples within R_I and the standard deviation of the noise component is obtained from R_{ε_I} .

SNR in magnitude images in Fourier image reconstruction

The SNR estimation based on signal and noise ROIs requires additional considerations when magnitude images are computed. In this case, the assumption of Gaussian distributed noise samples is not valid due to the non-linearity of taking absolute values of complex data. Signal intensities in magnitude images follow a *Rician* distribution which becomes a *Rayleigh* distribution in the special case of pure noise, e.g. [Henkelman, 1985, McGibney and Smith, 1993, Miller and Joseph, 1993, Gudbjartsson and Patz, 1995].

For SNR estimation of magnitude MR images in case of one receive coil element, [Henkelman, 1985] theoretically derived and experimentally validated the resulting bias in the SNR calculation. The bias depends on the standard deviation σ_d of the noise in the acquisition and affects the mean and standard deviation by $1.253\sigma_d$ and $0.655\sigma_d$, respectively, in an experimental scenario with zero amplitude. [Henkelman, 1985] suggests a correction factor of the signal strength based on a lookup table to account for the bias introduced by deriving the magnitudes. Moreover, several further correction options exist, e.g. [McGibney and Smith, 1993, Miller and Joseph, 1993, Gudbjartsson and Patz, 1995].

3.3.4. Summary of Fourier image reconstruction

In this section, the fundamental limitations of practical MR experiments based on Fourier encoding and Fourier image reconstruction were discussed and the following results were derived:

1. Discrete (or frequency band-limited) data sampling requires fulfilling the Nyquist-Shannon sampling criterion for full recovery of the image function.
2. Finite data sampling comes along with a loss of spatial information, i.e. blurring and Gibbs ringing occurs. The effect of finite sampling is expressed by a convolution of the underlying image function with a sinc function.
3. Spatial resolution and SNR are negatively correlated, hence, only a trade-off between them can be achieved.

The noise in Fourier imaging reconstructions follows a Gaussian distribution and becomes Rician when composing magnitude images. Fourier reconstruction yields uniform noise variances over the complete field-of-view, is pixel-wise uncorrelated and depends on the size of discretization chosen in the spatial encoding. The practical realization of Fourier encoding in actual data acquisition schemes performed by the MR scanner is covered in the next section.

3.4. Pulse sequences in magnetic resonance imaging

Data sampling according to the designed k-space trajectories is governed by gradient modulations. The gradient's amplitude and duration of application thereby determine velocity and distance traveled in k-space (cf. 3.9). The composition of RF pulse excitation and gradient waveforms is referred to as a *pulse sequence*. The diversity of combinations provides a whole range of MRI schemes. Here, only the main concepts relevant for the scope of this thesis are covered. A good overview over methodologies is given in Chapter 14 of [Bernstein et al., 2004].

The class of MR pulse sequences can be separated into two types of sequences, according to the formation of a *signal echo* during which data is recorded: **spin echo** [Hahn, 1950] or **gradient echo**. In *spin echo sequences*, additional *refocusing RF pulses* follow the excitation RF pulse to form a "spin echo". In *gradient echo sequences*, the imaging process is applied on top of the FID signal rather than forming a spin echo by quickly *dephasing* and *rephasing* the precessing transverse magnetization with the usage of gradients of alternating polarities.

In *echo train sequences*, several phase encoded readouts follow a single excitation to accelerate image acquisition. Whereas in the *RARE (Rapid Acquisition with Relaxation Enhancement)* sequence, invented by [Hennig et al., 1986], several refocused spin echoes are created, a series of de- and rephasings are performed in the *EPI (Echo Planar Imaging)* sequence, first described by [Mansfield, 1977].

The robustness with respect to field inhomogeneities of spin echo sequences provide a benign behavior of these acquisitions, however, the additional RF pulses require higher power emission and are - in combination with long T1-relaxation times - time-expensive. Gradient echo sequences exhibit high sensitivity to field inhomogeneities, yet, they are particularly suited for rapid image acquisition.

A great variety of signal preparation sequence modules exist, which allow to further mod-

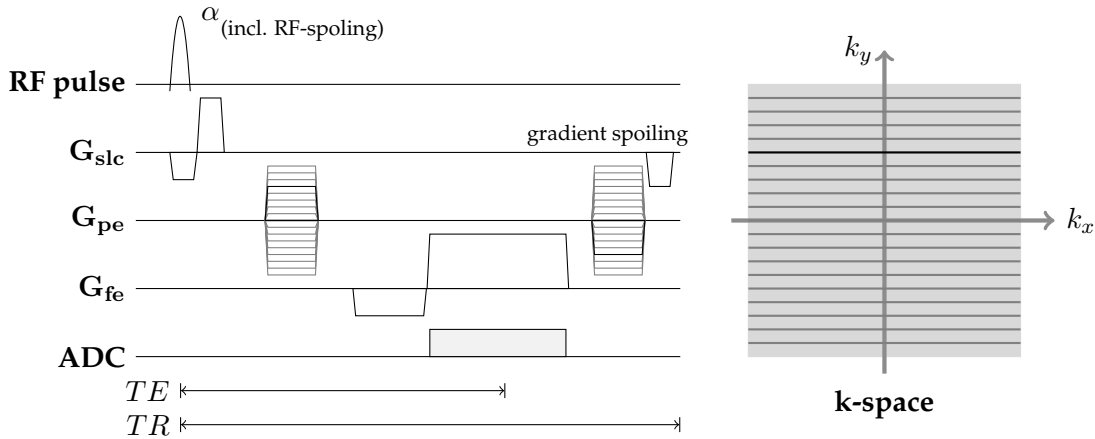


Figure 3.1: Pulse sequence diagram of the basic sequence block of a Gradient Echo (GE) sequence. The block corresponds to the readout of one k -space line, as illustrated black line in the k -space representation.

ulate the dominant contrast weighting with respect to specific tissue properties. A prominent example is the *FLAIR* (fluid attenuated inversion recovery) sequence that incorporates a module for fluid signal attenuation. FLAIR images are part of various clinical MR routines, as shown in the measurements of Chapter 7.

The MR pulse sequence developed and implemented within this work comprises Echo Planar Imaging with gradient echoes (GE-EPI). Therefore, the basic building blocks for - and issues of - GE sequences are described below. Subsequently, the EPI sequence is introduced and discussed.

3.4.1. Gradient echo (GE) sequence

Gradient echo (GE) sequences facilitate fast imaging scenarios by RF pulse excitation with a low flip angle, immediately followed by phase and frequency encoding. The whole setting is repeated at a high rate, usually $TR \ll T_1$, until all data has been collected [Haase et al., 1986]. The basic sequence building block consists of the encoding modules as introduced in the preceding sections:

1. slice selective excitation: an RF pulse is applied during a slice selection gradient
2. phase encoding: phase modulations are imposed by the phase encoding gradient
3. frequency encoding: signal readout is performed in presence of a frequency encoding gradient

A corresponding GE pulse sequence diagram for a Cartesian readout is depicted in Fig. 3.1, together with the path traveled in k -space. Frequency encoding is performed such that a symmetric interval around the k_x origin is acquired in each excitation. Each phase encoding preparation is used to travel to an individual k_y position before the frequency encoded readout is carried out. The complete set of k -space intervals are acquired in repeated measurements, each with varying phase encoding preparation. The latter is chosen such that a symmetric interval is sampled also around the k_y origin.

Steady state or dynamic equilibrium

The FID signal is short-lived due to T_2^* -decay, which restricts data sampling to a certain interval. Due to the fast repetition of excitation and acquisition in GE sequences, another relaxation parameter influences the setting: T_1 -decay. When beginning the next excitation before the longitudinal magnetization has completely recovered, the initial thermal equilibrium will not be reached. The series of RF pulse excitations gives rise to a definition of a *steady state* in this case.

Definition 3.4.1 (steady state). *Consider a series of RF pulse excitations. Then a **steady state** or **dynamic equilibrium** is reached after N_{state} measurement repetitions, if in all subsequent readout intervals $[t_0^i, t_1^i]_{i=N_{state}}^{N_{rep}}$ of the in total N_{rep} repetitions the transverse and longitudinal magnetization approximately reach the same value,*

$$M_{\parallel}(t_n^i) \approx M_{\parallel}(t_n^j) \quad \text{and} \quad M_{\perp}(t_n^i) \approx M_{\perp}(t_n^j),$$

for any pair of equivalent relative time points $t_n^i \in [t_0^i, t_1^i]$ and $t_n^j \in [t_0^j, t_1^j]$ within the readout intervals, hence for each $n = 1, \dots, N_{fe}$ and each $i, j = N_{state}, \dots, N_{rep}, i \neq j$.

As a consequence, several preparation scans are required in the beginning of the MR experiment with GE sequences in order to reach the steady state.

Residual transverse magnetization

It is known that despite T_2^* -decay, residual magnetization influences the imaging process in GE sequences. How residual magnetization is handled classifies GE sequences into three groups [Hargreaves, 2012]:

- *average* transverse magnetization, e.g. *gradient spoiled* sequences
- *recover* transverse magnetization, e.g. *balanced steady state free precession (bSSFP)* sequences with zero gradient moments
- *suppress* transverse magnetization, e.g. *RF-spoiled* sequences with gradient spoiling and phase variation of RF pulse excitations

The various techniques differ in signal magnitude, contrast and artifact behavior. Only the latter facilitates contrast purely influenced by T_1 . The GE sequence depicted in Fig. 3.1 is referred to as *Fast low-angle shot imaging (FLASH) sequence* (initial implementation without RF spoiling and rephasing of the phase encoding by [Haase et al., 1986]). The nowadays common incorporation of RF spoiling and spoiler gradients in FLASH is additionally illustrated in the diagram. The sequence implemented as part of this work incorporates gradient spoiling and thus belongs to the first type of GE sequence.

Contrast and timing

Contrast is provided in terms of differences between the physical tissue properties. The characteristics that are influential in MRI are: spin density, longitudinal relaxation T_1 , transversal relaxation T_2 and - due to static magnetic field inhomogeneities and mesoscopic tissue properties - T_2^* . The signal from different tissues relaxes differently over time. Therefore, the timing of signal readout has strong impacts on the magnitude intensities of different tissue type. Thus, timing influences the contrast in the MR image. The most effective sequence timing parameters

in GE sequences are the *time of echo formation* and the *time of repetition*, denoted by TE and TR , respectively. The flip angle is likewise influential in GE sequences, due to its impact on the steady state.

Definition 3.4.2 (TE). *The echo time (TE), is defined as the length of the time interval that begins at the center of the RF pulse excitation interval and ends at the time point of the ADC readout interval, for which the area under the frequency encoding gradient is zero. At this time point, the maximum in signal magnitude of the echo is expected. Thus, TE corresponds to the (nominal) time at which data at the k_x origin is sampled.*

Definition 3.4.3 (TR). *The time of repetition (TR) is defined as the time interval between two successive excitation RF pulses of the same volume.*

Definition 3.4.4. *The time of image acquisition T_{ACQS} is referred to as the time interval in which a set of k -space samples is acquired for one complete MR image.*

The actual time interval between two successive phase encoding steps in GE sequences is given by TR , since a single phase encoding per TR is performed. Let the number of performed phase encoding steps be N_{pe} , then the time of acquisition T_{ACQS} for the GE sequence example is given by $T_{ACQS} = N_{pe}TR$. Increasing the number of phase encoding steps (hence, spatial resolution) extends the overall acquisition time in GE sequences.

Choosing for example a long TE relative to T_2^* , favors signal magnitudes of tissues with slow T_2^* -relaxation. The MR signal becomes T_2^* -weighted. With respect to the steady state (depending on TR and the flip angle α_{fa}), choosing for example a short TR compared to T_1 , favors tissues of relatively fast T_1 -relaxation as magnitude intensities are higher. The MR signal becomes T_1 -weighted. In choosing a short TE together with a long TR , the magnitude intensities are mainly influenced by the proton densities of the respective tissues. The MR signal thus becomes *proton density (PD) weighted*. These are three typical MR signal weighting examples to define T_2^* -, T_1 - and PD-contrast in MR. However, MR is a powerful tool which allows to create many different contrasts based on various physical properties of the examined tissue.

Dwell time and bandwidth

Further important timing parameters of GE sequences are the *dwell time* of signal sampling and its inverse proportional, the *frequency bandwidth* of the readout. As evident from Sec. 2.9, increasing the frequency bandwidth increases noise influences. The relevant definitions are given below and are adjusted to phase encoding in the case of Echo Planar Imaging in the subsequent section.

Definition 3.4.5 (dwell time and frequency bandwidth). *The dwell time, denoted by $\Delta\tau$, is the signal sampling interval performed by the ADC. Its inverse determines the frequency bandwidth: $BW_f := \frac{1}{\Delta\tau}$.*

In practical experiments, the dwell time is usually determined from the frequency bandwidth and the number of readouts along the frequency encoding direction designated in the protocol.

Definition 3.4.6 (bandwidth per pixel). *Let T_{ADC} denote the duration of the readout by the ADC, which is similarly determined by the number of frequency encodings N_{fe} and the dwell time $\Delta\tau$. Then the bandwidth per pixel BW of an MRI acquisition is defined by the relation*

$$BW = \frac{1}{T_{ADC}} = \frac{1}{N_{fe}\Delta\tau} \quad [\text{Hz/Pixel}]. \quad (3.67)$$

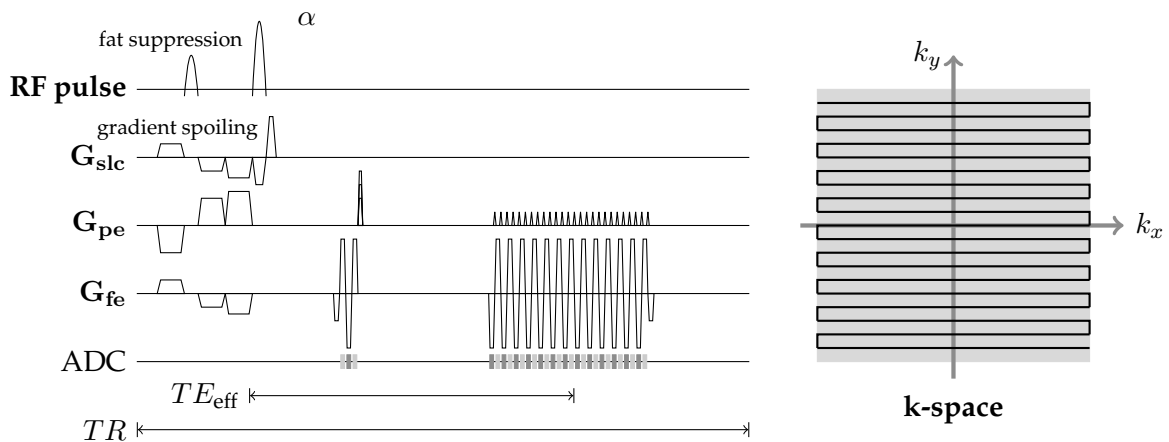


Figure 3.2: The pulse sequence diagram of a single-shot Echo Planar Imaging sequence is shown. The sequence consists of initial fat suppression and subsequent RF pulse excitation with arbitrary flip angle α_{fa} . Thereafter, three navigator echoes are collected. A preparation gradient is then used to traverse to the k-space position selected as the starting point for the echo train readout. The readouts of single lines of k-space alternate according to positive and negative readout gradients. In between, blip gradients are inserted to move to the next k-space line. The traveled path following a single RF excitation is illustrated on the right.

3.4.2. Echo Planar Imaging (EPI) sequence

Echo Planar Imaging [Mansfield, 1977, Ordidge et al., 1982, Schmitt et al., 1998] provides the advantage of fast dynamic imaging, since multiple phase encoding steps are performed after a single RF pulse excitation. In *single-shot GE-EPI*, the complete designated k-space data set required for the reconstruction of one MR image is collected within one TR . Thereby, small gradient moments referred to as *blip* gradients are used to realize the increments of Δk_y in phase encoding [Johnson and Hutchison, 1985]. A single-shot GR-EPI is illustrated in Fig. 3.2.

The great advantage of the short time of image acquisition is the fast repetition rate at which a series of images are acquired as required for dynamic MRI (Chapter 5). Hence, EPI is beneficial by achieving reasonable spatial and temporal resolution. Thereby, EPI exhibits robustness to effects of physiological motion simply due to the speed of acquisition. High temporal resolution, however, comes at the expense of well-known artifacts of EPI due to the long readout period and fast switching of high gradient amplitudes. Most notable are image blurring, susceptibility, chemical shift and eddy current artifacts [Fischer and Ladebeck, 1998]. An overview over imaging relevant concepts in EPI is given below.

Timing in EPI and ramp sampling

Whereas the phase encoding in GE sequences is performed in intervals of TR , it reduces to the chosen *echo spacing* T_{es} in EPI: $\Delta\tau_{pe} = T_{es}$. By covering the k-space plane following one RF pulse excitation, the overall time of image acquisition for N_{pe} phase encoding steps is given by $T_{ACQS} = N_{pe}T_{es} + T_{pre}$, including a time interval T_{pre} required for the typical acquisition of navigator echoes, as explained below. Since the repetition time TR comprises the acquisition of one image in single-shot EPI, TR directly determines the temporal resolution in serial image acquisitions.

Increasing N_{pe} to enhance spatial resolution serving the Nyquist-Shannon sampling theorem and decreasing TR to improve temporal resolution yields therefore opposite boundaries:

$$\begin{aligned}
k_x^{\max} &= N_{\text{fe}} \Delta k_x = \frac{2\pi N_{\text{fe}}}{F_o V_x}, & \text{where} & & N_{\text{fe}} \Delta \tau \leq T_{\text{es}}, \\
k_y^{\max} &= N_{\text{pe}} \Delta k_y = \frac{2\pi N_{\text{pe}}}{F_o V_y}, & \text{where} & & N_{\text{pe}} T_{\text{es}} + T_{\text{pre}} \leq TR.
\end{aligned} \tag{3.68}$$

In many cases, the realization of the chosen echo spacing, the bandwidth per pixel and the frequency encoding extent necessarily requires signal to be sampled during ramp up and ramp down times of the readout gradients. This is referred to as *ramp sampling*. The sampling during linearly increasing (ramp up) or decreasing (ramp down) readout gradients results in not equidistantly spaced k-space positions to be sampled. The therefore higher density at the beginning and ending of each acquired k-space line needs to be accounted for in the reconstruction process. To this end, *regridding* onto the equidistantly spaced Cartesian grid as well as *density compensation* to account for the varying densities is usually performed. This is achieved based on convolution with a convolution kernel and subsequent multiplication with a scaling factor. For more details refer to [Schmitt et al., 1998].

Contrast in EPI

Due to multiple signal rephasing, the definition of TE requires a slight adjustment.

Definition 3.4.7 (effective TE). *The effective echo time TE_{eff} is defined as the time interval beginning at the center of the RF excitation pulse and until the accumulated area under the frequency encoding gradient as well as the phase encoding gradient is zero. TE_{eff} thus corresponds to the time at which the (nominal) k-space origin is read out.*

In single-shot EPI, the minimal achievable effective TE is limited by the number of phase encoding steps N_{pe} as well as the echo spacing T_{es} :

$$TE_{\text{eff}} \geq \left(\frac{N_{\text{pe}}}{2} + 0.5 \right) T_{\text{es}} + T_{\text{pre}}. \tag{3.69}$$

Bandwidth in the phase encoding direction

If several phase encoding steps are performed within the same TR , the *phase encoding sampling interval* $\Delta\tau_{\text{pe}} > 0$ can be defined in analogy with the dwell time in the frequency encoding direction. The large *bandwidth in the phase encoding direction* of EPI has great influences and describes the outcome of many artifacts.

Definition 3.4.8 (bandwidth in phase encoding direction). *If several phase encoding steps are sampled within the same TR , let $\Delta\tau_{\text{pe}} > 0$ denote the time interval between two successive phase encoding steps. Let N_{pe} be the total number of phase encoding steps. The **bandwidth in phase encoding direction** BW_{pe} is defined analogous to the bandwidth per pixel in frequency encoding direction by*

$$BW_{\text{pe}} = \frac{1}{N_{\text{pe}} \Delta\tau_{\text{pe}}} \quad [\text{Hz/Pixel}]. \tag{3.70}$$

Remark 3.4.9. *To emphasize the difference between the bandwidth in frequency and phase encoding direction, the first is then likewise denoted by $BW_{\text{fe}} := BW$.*

Remark 3.4.10. In the previous GE sequence example, the phase encoding sampling interval appears to be zero in terms of imaging behavior, since phase encoding steps are acquired at the same time point within a TR cycle. Therefore, the definition is given solely for multiple phase encoding steps within the same TR.

Point spread function and spatial resolution

Section 3.3.2 contains the derivation of the PSF of Fourier imaging acquisitions. It characterizes the limits in spatial resolution from finite data acquisition (Thm 3.3.14). Spatial resolution is thereby proportional to the measured k-space extent. In EPI, limits of the maximum k-space sampling are related to the timing parameters, as shown in (3.68). This implicitly limits spatial resolution.

In EPI, there is another influence compromising spatial resolution that cannot be neglected: T_2^* -decay. Whereas T_2^* -decay is less severe in the frequency encoding direction, due to the short time intervals, it becomes apparent along the blipped phase-encoding direction of single-shot EPI. Here, T_2^* -decay imposes a noticeable difference in signal amplitudes between the k_y data sampled in time intervals of T_{es} over a total time interval of $N_{pe}T_{es}$. Therefore, without loss of generality, only the k_y -dimension is considered in the derivation below.

Theorem 3.4.11. Let $\delta(r - r_0)$ denote a point source at $r_0 \in V$. Assume T_2^* -values to be spatially constant, i.e. $T_2^*(r) = T_2^*$, for all $r \in V$. Consider finite k-space sampling along the phase encoding direction k_y in an EPI scenario of

- (i) a constant gradient $G_y = \frac{2\pi}{\gamma F_0 V_y T_{ACQS}}$ over the acquisition interval $\left[-\frac{T_{ACQS}}{2}, \frac{T_{ACQS}}{2}\right]$
- (ii) a trajectory $\left\{ k_y(t) := \gamma G_y t \mid t \in \left[-\frac{T_{ACQS}}{2}, \frac{T_{ACQS}}{2}\right] \right\}$, such that the origin is sampled at $t = 0$ (i.e. TE at $t = 0$) and $k_y\left(\frac{T_{ACQS}}{2}\right) = \frac{1}{2} \frac{2\pi}{F_0 V_y} = -k_y\left(-\frac{T_{ACQS}}{2}\right)$.

Then the continuous point spread function of EPI serves the following relation:

$$\text{PSF}_{r_0}(r) \propto T_{ACQS} \text{sinc}(\gamma G_y T_{ACQS}(r - r_0)/2) * \Re \left(\frac{1}{\left(\frac{1}{\gamma G_y T_2^*}\right) + ir} \right).$$

Proof. Let $\chi_{\mathcal{K}_T}$ be the characteristic function such that $\chi_{\mathcal{K}_T}(k_y(t)) = 1$ for $k_y(t) \in \left\{ k_y(t) \mid t \in \left[-\frac{T_{ACQS}}{2}, \frac{T_{ACQS}}{2}\right] \right\}$ and zero otherwise. Let $r_0 \in V$ and consider the delta distribution $\delta(r - r_0)$. With Fourier encoding and the inverse Fourier transform for image reconstruction follows:

$$\begin{aligned} \text{PSF}_{r_0}(r) &= \mathcal{FT}^{-1} \left\{ \chi_{\mathcal{K}_T}(k_y(t)) \int_V \delta(\hat{r} - r_0) \exp\left(-\frac{t}{T_2^*}\right) \exp(-ik_y(t)\hat{r}) d\hat{r} \right\} \\ &= \mathcal{FT}^{-1} \left\{ \chi_{\mathcal{K}_T}(k_y(t)) \exp\left(-\frac{t}{T_2^*}\right) \exp(-ik_y(t)r_0) \right\} \\ &\stackrel{\text{Convolution}}{\stackrel{\text{Thm}}{=}} \mathcal{FT}^{-1} \left\{ \exp\left(-\frac{t}{T_2^*}\right) \right\} * \mathcal{FT}^{-1} \left\{ \chi_{\mathcal{K}_T}(k_y(t)) \exp(-ik_y(t)r_0) \right\}. \end{aligned} \quad (3.71)$$

For the right part of the convolution follows with generalization of Thm 3.3.14:

$$\mathcal{FT}^{-1} \left\{ \chi_{\mathcal{K}_T}(k_y(t)) \exp(-ik_y(t)r_0) \right\} \stackrel{(i)+(ii)}{=} T_{ACQS} \text{sinc}(\gamma G_y T_{ACQS}(r - r_0)/2), \quad (3.72)$$

where the gradient momentum of the acquisition $\gamma G_y T_{\text{ACQS}}$ is used instead of k_{max} . For the left part of the convolution, it follows

$$\mathcal{FT}^{-1} \left\{ \exp \left(-\frac{t}{T_2^*} \right) \right\} \stackrel{(ii)}{=} \frac{1}{2\pi} \int_{\mathcal{K}_T} \exp \left(-\frac{k(t)}{\gamma G_y T_2^*} \right) \exp(ik(t)r) dk(t) \quad (3.73)$$

[Farzaneh et al., 1990]
 $\propto \Re \left(\frac{1}{\left(\frac{1}{\gamma G_y T_2^*} \right) + ir} \right)$.

□

Hence, the impact in image space from T_2^* -decay can be described by a *Lorentzian*. Since the effect of T_2^* -decay is not symmetric around the k-space center $k = 0$, the PSF describing its filter effect possess a non-zero imaginary component. The description by a Lorentzian follows from symmetric extension of the exponential decay function. The combined influence on spatial resolution due to finite sampling and T_2^* -decay is specified by two filter functions, i.e. by a sinc and a Lorentzian.

In order to understand the difference of the effect due to T_2^* -decay on phase versus frequency encoding direction, pixel sizes are often related to the respective pixel bandwidth, e.g. [Haacke, 1987, Farzaneh et al., 1990]. Accordingly, the bandwidth of the Lorentzian, which is the inverse of the decay time, is used to describe the effect of T_2^* -decay on spatial resolution instead of the *FWHM*. Whenever the bandwidth of the Lorentzian is in the range of the pixel bandwidth or exceeds it, spatial resolution is decreased. Again, a trade-off between parameters arises: Increasing the echo spacing T_{es} enhances *SNR* due to the possibility of decreasing the bandwidth in readout direction, whereas it decreases spatial resolution along the phase-encoding direction, since the time of acquisition increases. Consequences are image blurring and decreased pixel intensities.

Off-resonance effects

Spatial encoding relies entirely on controlling the spatial Larmor frequency variations. The implicitly assumed premise is the spatially constant relation $\omega_0 = -\gamma B_0$, such that a unique mapping between location and Larmor frequencies is provided by the gradients. However, this premise is violated by varying chemical surroundings of the spins or by susceptibility differences between different types of tissue. In the following, *off-resonance effects* are modeled and *chemical shift* and *susceptibility artifacts* are described.

Off-resonance artifacts are exacerbated in EPI due to the low phase encoding bandwidth. In the case of single-shot EPI, the bandwidth per pixel in frequency and phase-encoding direction are given by

$$\text{BW}_{\text{fe}} = \frac{1}{N_{\text{fe}} \Delta \tau} \quad \text{and} \quad \text{BW}_{\text{pe}} = \frac{1}{N_{\text{pe}} T_{\text{es}}}. \quad (3.74)$$

For instance, in an EPI acquisition with an echo spacing of $T_{\text{es}} = 750 \mu\text{s}$ and $N_{\text{fe}} \times N_{\text{pe}} = 128 \times 128$ data samples, the following bandwidths per pixel result:

$$\text{BW}_{\text{fe}} \geq 1333 \text{ Hz} \quad \text{and} \quad \text{BW}_{\text{pe}} \approx 10.42 \text{ Hz}. \quad (3.75)$$

Chemical shift artifact and fat suppression

Let ω_0 be the Larmor frequency that is incorporated as a reference frequency in the MR acquisition. If the frequency ω deviates from ω_0 for some spins, the frequency difference is referred

to as an *off-resonance*. The off-resonance $\Delta\omega_{cs}$ due to different molecular structures is called *chemical shift*. It can be described by a scaling of the Larmor equation: $\Delta\omega_{cs} = \gamma\sigma_{cs}B_0$.

The off-resonances $\Delta\omega_{cs}$ result in an additional phase factor in signal encoding, which leads to the following signal equation:

$$s(t) \propto \int_V m_{\perp}(\mathbf{r}, 0) \exp(-i\mathbf{k}(t) \cdot \mathbf{r}) \underbrace{\exp(-it\Delta\omega_{cs})}_{\substack{\text{phase modulation} \\ \text{due to chemical shift}}} d\mathbf{r}. \quad (3.76)$$

According to the *Fourier shift theorem*, e.g. [Jähne, 2013], the multiplication by the additional phase leads to a shift in the Fourier reconstructed image. The spatially constant off-resonances $\Delta\omega_{cs}$ therefore lead to an image shift of the signal contribution, hence, *chemical shift artifact*.

A prominent example is the difference between water and fat molecules. The relative shift in Larmor frequencies between hydrogen protons bound in water versus fat molecules is expressed by the scaling $\sigma_{cs} = 3.33$ parts per million. At a 3T MR system, this results in a frequency shift of 420 Hz. The additional phase leads to a shift in pixels of

$$\begin{aligned} \Delta x_{cs} &= \frac{\Delta\omega_{cs}}{BW_{fe}} \leq \frac{420 \text{ Hz}}{1333 \text{ Hz/pixel}} \approx 0.32 \text{ pixel} \\ \Delta y_{cs} &= \frac{\Delta\omega_{cs}}{BW_{pe}} = \frac{420 \text{ Hz}}{10.42 \text{ Hz/pixel}} \approx 40 \text{ pixels}. \end{aligned} \quad (3.77)$$

Thus, the image arising from hydrogen protons bounded in fat molecules is shifted by approximately 40 pixels in the y -dimension (according to the phase encoding direction) with respect to the image derived from water molecules.

In order to avoid a shifted fat image, one usually suppresses the fat signal by spectrally-selective excitation of only hydrogen atoms bound in fat molecules. This is possible by tuning a 90° excitation pulse to the shifted Larmor frequency in absence of any spatial encoding gradients. The fat signal is then dephased by gradient modulations. Since the longitudinal magnetization relaxes comparably slow, an excitation directly after the suppression of the fat signal yields an approximately fat-free signal in the subsequent acquisition.

The described fat saturation procedure can be incorporated as a preceding module in any sequence. For EPI, fat suppression for in vivo applications at 3T is mandatory. The diagram of Fig. 3.2 illustrates also a fat saturation module.

Susceptibility artifacts and the time of image acquisition

Another source for off-resonance effects are spatially dependent field inhomogeneities $\Delta B_0(\mathbf{r})$. These differences arise for instance due to the different *susceptibilities* of tissues. Although a *magnetic field shim procedure* is applied for each subject prior to the actual acquisition to establish best possible homogeneity of the main magnetic field, strong susceptibility differences induce discontinuities which cannot be sufficiently compensated. Furthermore, susceptibility differences induced on a mesoscopic scale cannot be assessed by a shimming procedure at all.

Artifacts of local field inhomogeneities that arise due to susceptibility differences at intersections of tissue compartments are referred to as *susceptibility artifacts*. Among the effects are geometric distortion, spatially varying intensities as well as complete signal loss. Problematic regions are for instance air-tissue interfaces such as the frontal sinus next to the orbitofrontal cortex.

The off-resonances $\Delta B_0(\mathbf{r})$ again imply an additional phase factor in the encoding process:

$$s(t) \propto \int_V m_{\perp}(\mathbf{r}, 0) \exp(-i\mathbf{k}(t) \cdot \mathbf{r}) \underbrace{\exp(-it\gamma\Delta B_0(\mathbf{r}))}_{\substack{\text{phase modulation} \\ \text{due to } B_0 \text{ inhomogeneities}}} d\mathbf{r}. \quad (3.78)$$

The additional phase again leads to a shift in the Fourier reconstructed image. However, in the case of spatially varying off-resonances, these shifts depend on their location. Therefore, the image is locally distorted and intensities are concomitantly altered.

Assume (i) and (ii) as in Thm. 3.4.11. The local distortion $\Delta \mathbf{r}_s$ depends on the local deviation of the field inhomogeneity $\Delta B_0(\mathbf{r})$ and on the time of acquisition T_{ACQS} :

$$\Delta \mathbf{r}_s \stackrel{(ii)}{\propto} \frac{\Delta B_0(\mathbf{r})}{G_y} \stackrel{(i)}{\propto} \Delta B_0(\mathbf{r}) T_{\text{ACQS}}. \quad (3.79)$$

The local field inhomogeneities act over the complete time of image acquisition. Hence, the effect is severe in EPI due to the low bandwidth in phase encoding direction, i.e.

$$\Delta \mathbf{r}_s \propto \Delta B_0(\mathbf{r}) N_{\text{pe}} T_{\text{es}} = \frac{\Delta B_0(\mathbf{r})}{\text{BW}_{\text{pe}}}. \quad (3.80)$$

The field inhomogeneities $\Delta B_0(\mathbf{r})$ likewise act as unwanted additional gradient moments. Therefore, different spatial information as intended is acquired. This results in spatial shifts and signal attenuation. Since field inhomogeneities depend on the spatial position, different local displacements sum up to geometric distortions. For a detailed analysis, refer to [Deichmann et al., 2002].

Geometric distortion, signal losses and also the loss in nominal spatial resolution (described in context of the PSF) are related to the overall time of image acquisition in EPI. Artifacts improve when the readout time is reduced. Nevertheless, the echo spacing and number of samples, which effect readout times, are correlated with SNR and spatial resolution.

Nyquist $\frac{N}{2}$ -ghosts

The multiple dephasings and rephasings of the excited signal performed by the frequency encoding gradient G_{fe} , imposes strong hardware requirements in quickly switching gradient fields. Small delays in reversing the readout directions, however, are unavoidable. The delays translate into small shifts along the readout direction alternating according to the blip procedure, e.g. in all odd phase encoding steps the readout is shifted compared to all even numbers of phase encoding steps.

Assume a k-space shift of $\Delta \mathbf{k}_0$ due to temporal delay and field modulations. Then the phase encoded readout is additionally multiplied by $\exp(i\mathbf{k}_n \cdot \mathbf{r} \pm \Delta \mathbf{k}_0 \cdot \mathbf{r})$, for odd numbers of phase encoding steps. The resulting encoding can be viewed as two separate sets of encodings which are then superimposed in the reconstruction.

Each such k-space set, however, is sampled at intervals of $2\Delta k_y$ along the phase encoding direction. The step size Δk_y was chosen such as to just fulfill the Nyquist sampling criterion (Def. 3.3.9). Consequently, the step size of $2\Delta k_y$ does not serve the Nyquist criterion anymore and results in a halved FoV. Spatial encoding of signal contributions outside the halved FoV hence folds over. This effect of sub-Nyquist sampling is explained in more detail in Sec. 3.6. Denoting $FoV_y = N$ explains the name of Nyquist $\frac{N}{2}$ -ghosts.

Shifted ghost images, arising from alternating line variation in the EPI acquisition pattern, are commonly corrected using additional *navigator echoes* [Bruder et al., 1992,

Goertler and Schmitt, 1992, Glover et al., 1992, Heid, 1997], after signal excitation and prior to the actual train of readouts. These are several readout traversals without any phase encoding to estimate the differences in encoding for a phase correction. In Fig. 3.2, the acquisition of three navigator echoes are shown, as used in the approach of [Heid, 1997].

3.4.3. Summary of Echo Planar Imaging

EPI allows for rapid image acquisition and repetition of measurements at a high temporal frame rate. However, the high temporal resolution in EPI comes at the cost of low image resolution and entails acquisition specific artifacts. Artifacts arise due to the long readout period following a single excitation, the fast switching of high gradient amplitudes and the limited bandwidth in the phase encoding direction. Therefore, the higher the number of phase encoding steps, the more severe the spatial blurring becomes or the influence from susceptibility, chemical shift and eddy current artifacts. Since spatial resolution is related to the highest k-space information acquired, this limits the spatial fidelity and resolution of EPI.

3.5. Partial-Fourier sampling and image reconstruction

Phase encoding for two-dimensional imaging is time-expensive. One approach to reduce the number of phase encoding steps without decreasing k_y^{\max} is given by *Partial-Fourier sampling*, where k-space is acquired asymmetrically. Considerations are restricted to the one-dimensional phase encoding direction in the following.

Asymmetric k-space sampling of e.g. $\left\{ d_n \mid -M\Delta k \leq n \leq \frac{N_{\text{smp}}}{2}\Delta k \right\}$, where $M < \frac{N_{\text{smp}}}{2}$, relies on the assumption of Hermitian symmetry in k-space. With Hermitian symmetry, data samples d_n of e.g. $n \geq 0$ (for the case of $M = 0$) would suffice to construct all samples d_n with $n < 0$ using the relation

$$d_{-n} = d_n^* \quad (3.81)$$

This is however only provided for the Fourier transform of a real-valued function. In GE based MRI, Hermitian symmetry is violated, for instance due to phase variations induced by inhomogeneities over the course of signal acquisition.

In order to still reconstruct omitted data points d_n with $n < M$, the assumption is made that phases in the image domain vary smoothly. Phase variations can then be estimated by the central part of k-space. Acquiring e.g. 5/8-7/8 of the designated k-space extent, the omitted part can either be set to zero or more advanced reconstruction algorithms are applied as described in Sec. 3.5.1.

The savings due to k-space undersampling are captured by the *reduction factor* R , which is, e.g. for 5/8-Partial-Fourier, given by

$$R = \frac{N_{\text{pe}}^{\text{full}}}{N_{\text{pe}}^{\text{PF}}} = 8/5, \quad (3.82)$$

where $N_{\text{pe}}^{\text{PF}}$ and $N_{\text{pe}}^{\text{full}}$ refer to the number of phase encoding steps in Partial-Fourier versus the full acquisition, respectively.

Discrete Fourier transform performed on the data while setting the omitted 3/8-1/8 to zero yields a Fourier reconstructed image according to (3.42). To distinguish this reconstruction from the solution presented below, it is referred to as a *zero-filled* reconstruction.

Definition 3.5.1 (zero-filling). Assume a k -space region of finite extent to be designated that is symmetric around the k -space center and that is discretized into grid positions corresponding to Nyquist-sampled intervals. If signal is sampled only for some of the grid positions and remaining values are set to zero, this is referred to as **zero-filled data** or **zero-filling**. It is denoted by \mathbf{d}^{zf} and $\mathbf{d}^{\text{zf},2D}$, for a representation in vector or matrix form, respectively. Fourier reconstruction of zero-filled data is termed **zero-filled (Fourier) reconstruction** here.

An example of a Partial-Fourier k -space sampling pattern as well as the respective zero-filled reconstruction is depicted in Fig. 3.3.

3.5.1. Constrained phase reconstruction in Partial-Fourier sampling

As proposed by [Haacke et al., 1990], image reconstruction of Partial-Fourier sampled signal can be improved by introducing a phase constraint in the optimization problem, based on a phase estimate $\hat{\phi}$. This extends (3.42) to the following problem:

$$\begin{aligned} I^\dagger &= \operatorname{argmin}_{I \in \mathcal{L}^2(\Omega, \mathbb{C})} \|I\|_{\mathcal{L}^2}^2, \quad \text{subject to} \\ \tilde{\mathcal{S}} \{ \mathcal{FT} \{ I \} \} &= d \quad (\text{data consistency}) \\ \arg \{ I(r) \} &= \hat{\phi}(r) \quad (\text{phase constraint}), \end{aligned} \quad (3.83)$$

where \arg denotes the operation of deriving the phase of a complex number.

The phase estimate $\hat{\phi}$ is obtained by zero-filled reconstruction. Typically a filter is additionally applied to avoid Gibbs ringing artifacts [Gibbs, 1898]. The optimization problem can be solved using the *projection onto convex sets (POCS)* algorithm [Youla and Webb, 1982] as shown in [Haacke et al., 1990, Liang and Lauterbur, 2000].

Definition 3.5.2. The set Ω is convex, if and only if $\lambda x + (1 - \lambda)y \in \Omega$ for each $x, y \in \Omega$ and for each λ with $0 \leq \lambda \leq 1$.

The *phase constraint* is captured by projection P_1 onto the convex set Ω_1 defined by:

$$\begin{aligned} P_1 : \{ I(y_q) \} &\rightarrow \Omega_1 := \left\{ I(y_q) \mid \arg(I(y_q)) = \hat{\phi}(y_q) \right\} \\ I(y_q) &\mapsto |I(y_q)| \exp\left(i\hat{\phi}(x)\right) \end{aligned} \quad (3.84)$$

P_1 projects onto Ω_1 by definition. Convexity of Ω_1 follows directly from calculating $\lambda I_1(y_q) + (1 - \lambda)I_2(y_q)$ for two arbitrary images $I_1(y_q), I_2(y_q) \in \Omega_1$.

The *data consistency* for an asymmetric sampling pattern, $0 < M < N_{\text{smp}}/2$, is captured by projection P_2 onto the convex set Ω_2 defined by:

$$\begin{aligned} P_2 : \{ I(y_q) \} &\rightarrow \Omega_2 := \left\{ I(y_q) \mid \mathcal{DFT} \{ I(y_q) \} = d_n, n \in \left\{ -M, \dots, \frac{N_{\text{smp}}}{2} - 1 \right\} \right\} \\ I(y_q) &\mapsto (\mathcal{DFT}^{-1} \circ \mathcal{R} \circ \mathcal{DFT}) (I(x)), \end{aligned} \quad (3.85)$$

where $\mathcal{R}(\hat{d}_n) = d_n$, for $n \in \left\{ -M, \dots, \frac{N_{\text{smp}}}{2} - 1 \right\}$,

and $\mathcal{R}(\hat{d}_n) = \hat{d}_n$ otherwise.

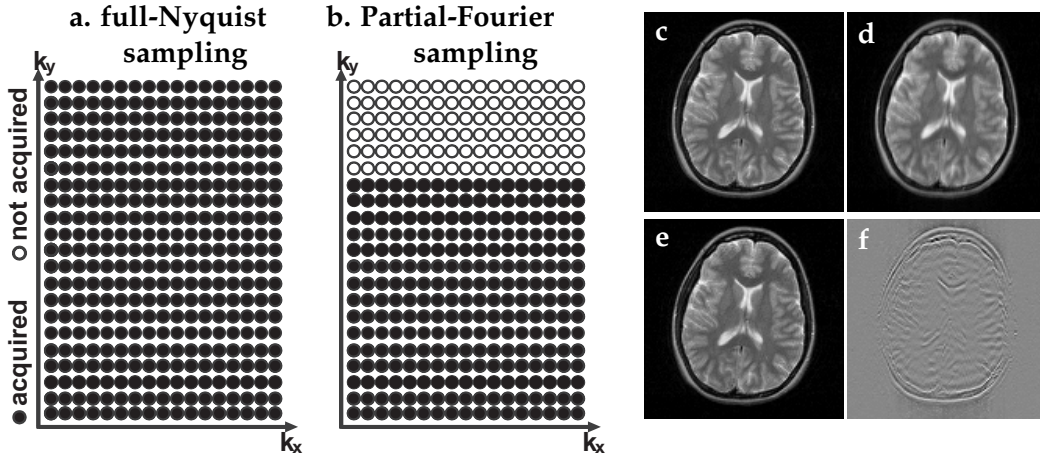


Figure 3.3: A full-Nyquist k -space sampling pattern (a) and a Partial-Fourier sampling pattern (b) are illustrated. Corresponding (zero-filled) Fourier reconstructions are demonstrated in (c) and (d). Image reconstruction of the Partial-Fourier k -space sampling using the POCS algorithm with 4 iterations is depicted in (e). A difference map between the zero-filled Fourier reconstruction of (d) and the POCS reconstruction of (e), both based on the same Partial-Fourier sampling pattern, is shown in (f).

Convexity of Ω_2 follows using the linearity of the discrete Fourier transform. Furthermore, P_2 is a projection onto Ω_2 by definition of \mathcal{R} and due to discrete Fourier inversion.

The POCS algorithm is applied by iterative projection onto $\Omega_{1,2} := \Omega_1 \cap \Omega_2$ by $P := P_1 \{ P_2 \{ \cdot \} \}$ such that $I_{k+1}(y_q) = P(I_k(y_q))$. The zero-filled Fourier reconstructed image is commonly used as an initial image $I_0(y_q)$. Practical experiences suggest that four iterations suffice for convergence, e.g. [Liang et al., 1992, McGibney et al., 1993]. Figure 3.3 depicts reconstructions from 5/8-Partial-Fourier sampled data, with Fourier reconstruction with zero-filling and using the described POCS algorithm. With Partial-Fourier, a maximum speed-up of a factor of 2 (Half-Fourier) is possible, realistic values are in the range of 1.14 – 1.6, which corresponds to 7/8-5/8 Partial-Fourier sampling.

3.6. Sub-Nyquist sampling

Another approach to reduce the number of phase encoding steps without decreasing k_y^{\max} is given by *sub-Nyquist sampling*, where k -space along k_y is acquired in larger steps of $R\Delta k_y$ for a reduction factor R .

The Theorem 3.3.7 of support-limited functions (Nyquist-Shannon) dictates maximal k -space sampling intervals Δk_x and Δk_y for artifact-free image reconstruction of the underlying spatial-support limited image function, e.g. $\Omega_x \leq FoV_x$ and $\Omega_y \leq FoV_y$. Sub-Nyquist sampling of only every R^{th} phase encoding increases the k -space interval Δk_y to $R\Delta k_y$ and thus, violates the Nyquist-Shannon criterion.

Lemma 3.3.3 (ii) reveals how the Fourier transform of the Dirac comb with intervals of Δk_y results in a Dirac comb with intervals $FoV_y = \frac{2\pi}{\Delta k_y}$ of periodic replica. Hence, sampling in intervals of $R\Delta k_y$ leads to a reduced field of view $\frac{FoV_y}{R}$. The spatial interval of uniquely encoded locations is decreased. If the support is larger than the reduced FOV, signal from both

ends of the support overlap according to (3.43). These signal overlaps are referred to as *fold-over artifacts*. An example of sub-Nyquist sampling with reduction factor $R = 3$ and corresponding images are depicted in Fig. 3.4.

Figure 3.4 further shows a sampling pattern which combines Nyquist-sampling (Δk_y) in the central k-space part and sub-Nyquist sampling ($R\Delta k_y$) in the periphery of k-space. In this case, fold-over artifacts occur only for the higher spatial frequencies, whereas the contrast is not affected. More than $1/R$ th of k-space is sampled, therefore, the *net reduction factor* (R_{net}) is lower. The general reduction is computed by the ratio of phase encoding steps in the full- over the sub-Nyquist-sampling scenario, i.e.

$$R_{\text{net}} = \frac{N_{\text{pe}}^{\text{full}}}{N_{\text{pe}}^{\text{sub}}}. \quad (3.86)$$

The essential ingredient in obtaining images without fold-over artifacts from sub-Nyquist sampled acquisitions is the usage of sensitivity information from multiple receive coils. The sensitivities thereby complement the missing information of omitted phase encoding steps. As multiple coils are an inevitable part of these methods, the term *parallel imaging* has been manifested. In the next chapter, parallel imaging reconstruction of sub-Nyquist sampled data is discussed.

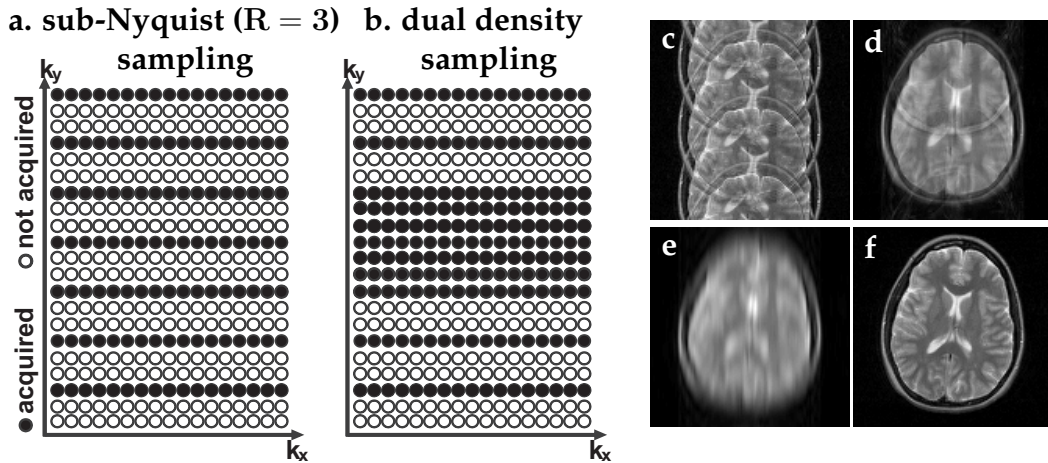


Figure 3.4: A sub-Nyquist k-space sampling pattern with reduction factor $R = 3$ is illustrated in (a) and incorporating a full-Nyquist-sampled k-space central area in (b). Corresponding zero-filled Fourier reconstructions are depicted in (c) and (d), respectively. The reconstructions exhibit the typical fold-over artifacts that arise in Fourier reconstruction of sub-Nyquist sampled k-space data. For comparison, Fourier reconstructions from Nyquist-sampled data are shown for (e) only the inner part of the dual density pattern and (f) a full-Nyquist-sampled data set covering the full k-space extent of this scenario. Whereas sub-Nyquist sampling leads to fold-over artifacts (c,d), the reduction of numbers of phase encoding steps of full-Nyquist sampled data results in reduced spatial resolution along the phase encoding direction (e).

Chapter 4

Parallel imaging

Phase encoding of Fourier imaging is a step-wise procedure performed with gradient field variations. Fourier image reconstruction requires Nyquist-sampled phase encoding to allow for an artifact-free reconstruction. For Cartesian trajectories, the time of acquisition with gradient encoding is directly proportional to the number of phase encoding steps. In single-shot EPI, T_2^* sets boundaries on the number of phase encoding steps, which consequently limits spatial resolution.

This chapter explains the possibilities of parallel imaging to reduce acquisition times and/or increase spatial resolution. Hybrid spatial encoding is presented, which relies simultaneously on gradient encoding and *sensitivity encoding* by multiple receive coils. Imaging with multiple receive coils is introduced in Sec. 4.1 and a short overview over the historic evolution of parallel imaging is given in Sec. 4.2. The two most prominent parallel imaging reconstruction approaches, SENSE [Pruessmann et al., 1999] and SMASH/GRAPPA [Sodickson and Manning, 1997, Griswold et al., 2002], are outlined in Secs. 4.3 - 4.5. Parallel imaging reconstruction reveals noise variances non-uniform over the image extent that are quantified by the *coil geometry (g)-factor* as is derived in Sec. 4.6. A discussion of previous research of parallel imaging in the context of EPI in Sec. 4.7 concludes this chapter.

4.1. Multiple receive coils: Imaging in parallel

[Roemer et al., 1990] presented an implementation of receive coil arrays for *parallel* signal reception in MRI. By imaging in parallel with multiple coils, the close proximity of individual coils to the imaged object allows for enhanced SNR while covering a large imaging region. In this section, the three most prominent coil combination methods are briefly stated.

Acquiring coil data in parallel adds another parameter to the data samples that can be used in the image reconstruction. Denote the coil sensitivity of coil α at location \mathbf{r} by $c_\alpha(\mathbf{r})$. Then data samples (cf. 3.16) for a parallel imaging acquisition are modeled by

$$\begin{aligned} d_{n,\alpha} &= \int_V c_\alpha(\mathbf{r}) m_\perp(\mathbf{r}, 0) \exp(-i\mathbf{k}_n \cdot \mathbf{r}) d\mathbf{r}, \\ &\text{for each k-space sample } n \in \{1, \dots, N_{\text{smpl}}\}, \\ &\text{for each coil } \alpha \in \{1, \dots, N_{\text{coils}}\}. \end{aligned} \tag{4.1}$$

Hence, an individual coil image \hat{I}_α is obtained for each coil element $\alpha = 1, \dots, N_{\text{coils}}$ of the utilized coil array. Individual coil images are combined based on calculated weighting factors

$p_\alpha(\mathbf{x}_m)$, for each coil α , and each pixel $\mathbf{x}_m, m = 1, \dots, N_{\text{pix}}$, by

$$\hat{I}(\mathbf{x}_m) = \sum_{\alpha=1}^{N_{\text{coils}}} p_\alpha(\mathbf{x}_m) \hat{I}_\alpha(\mathbf{x}_m). \quad (4.2)$$

The *Roemer combination* [Roemer et al., 1990] combines the N_{coils} images with optimal SNR (cf. [Roemer et al., 1990, Hayes and Roemer, 1990, Bernstein et al., 2004]) by

$$\hat{I}(\mathbf{x}_m) = \frac{\sum_{\alpha,\beta} c_\alpha^*(\mathbf{x}_m) (\Psi_{\text{coils}})_{\alpha,\beta}^{-1} \hat{I}_\beta(\mathbf{x}_m)}{\sum_{\alpha,\beta} c_\alpha^*(\mathbf{x}_m) (\Psi_{\text{coils}})_{\alpha,\beta}^{-1} c_\beta(\mathbf{x}_m)}, \quad (4.3)$$

where Ψ_{coils} denotes the noise covariance matrix of the coils (Def. 4.6.2). Whereas the noise covariance matrix can be simply measured from a pre-scan, correct estimates of sensitivity values are more complex to derive. The Roemer combination, however, relies on the correctness of the estimated coil sensitivity values.

The *root Sum of Squares (rSoS) combination* [Roemer et al., 1990] is independent of the estimation of coil sensitivity values. It is derived by

$$\hat{I}(\mathbf{x}_m) = \sqrt{\sum_{\alpha=1}^{N_{\text{coils}}} \left(\frac{|I_\alpha(\mathbf{x}_m)|}{(\Psi_{\text{coils}})_{\alpha\alpha}} \right)^2}. \quad (4.4)$$

The rSoS combination follows the idea of the Roemer combination, but with estimated coil sensitivity information based on the relative spatial varying signal contribution of each coil image. This combination is almost optimal for high SNR coil image contributions [Roemer et al., 1990, Walsh et al., 2000]. In the case of low SNR and assuming spatially Gaussian noise to be uncorrelated between coils, an increase of noise compared to Roemer combination is perceived [Constantinides et al., 1997, Walsh et al., 2000].

The *adaptive combination* [Walsh et al., 2000] formulates the combination problem in terms of matched filter of stochastic processes. The objective is to find the combination vector \mathbf{p} of weightings $p_\alpha, \alpha = 1, \dots, N_{\text{coils}}$, which maximizes the ratio between expectation values of signal and noise processes. It is derived by eigen-decomposition of the signal covariance matrix of the coils multiplied with the inverse noise covariance matrix. The SNR optimal combination vector is found to be the eigenvector corresponding to the highest eigenvalue. Both matrices are estimated from a region within the images, hence, explicit knowledge of coil sensitivities is not required. The SNR is in similar ranges as for Roemer combinations.

Remark 4.1.1. Analogous to the considerations made in [Henkelman, 1985] (see Sec. 3.3.3), an extension to arrays of receive coils exists to address the bias in SNR estimations of magnitude images [Constantinides et al., 1997].

Acquisitions with multiple coils are beneficial to improve the SNR of Nyquist-sampled MRI. Nevertheless, the additional spatial information also allows to complement Fourier encoding by gradients in the case of sub-Nyquist sampling. The origin of the idea to partially substitute gradient encoding with parallel imaging is briefly introduced in the next section.

4.2. Short history of parallel imaging

Theoretical concepts for accelerating the image acquisition by omitting phase-encoding steps and enhancing the encoding procedure by the information of multiple receive coils can already be found in the literature of the late 80's, as outlined in [Schoenberg et al., 2007].

[Hyde et al., 1986] proposed a very direct usage of coil sensitivity information. In their method, the spatial support of two coils is separated completely. Therefore, two images are obtained when projecting image information onto the two distinct supports. This allows for acquisition with half the field of view, which consequently halves the acquisition time for a fixed image resolution. The approach is very intuitive in showing how coil sensitivity information can complement spatial encoding.

Parallel Imaging with Localized Sensitivities (PILS) [Griswold et al., 2000] illustrates the same approach in a more general context. It is based on coil sensitivity's center and widths without explicit knowledge of coil sensitivity values itself. However, the necessity of strictly localized coil sensitivity patterns hardly holds in general applications.

The first description of a **k-space based parallel imaging** proposal can be found in [Carlson, 1987], and was further consolidated in [Carlson and Minemura, 1993]. The sub-Nyquist sampling is resolved by linearly combining raw data of two imaging coils: one homogeneous receive channel and one varying linearly in phase direction. Revisiting the essential idea of coil combination to estimate higher frequencies in k-space led to *simultaneous acquisition of spatial harmonics (SMASH)* [Sodickson and Manning, 1997], which was the first successful *in vivo* application of parallel imaging. A series of enhancements of SMASH followed [Bydder et al., 2002, Jakob et al., 1998, Heidemann et al., 2001]. Among these, the most robust method nowadays widely used is *generalized autocalibrating partially parallel acquisitions (GRAPPA)* [Griswold et al., 2002].

First algorithms that invert the coil sensitivities in the image space were presented by [Hutchinson and Raff, 1988, Kwiat et al., 1991, Kwiat and Einav, 1995]. In their approaches, essentially all phase-encoding steps are omitted and substituted by a similar number of coils. A concept which was later pursued in [Lin et al., 2006] and led to *MR-Encephalography* with one coil per voxel [Hennig et al., 2007]. As counterpart to the k-space algorithms, image domain based reconstructions were proposed by [Kelton et al., 1989] and enhanced by [Ra and Rim, 1993], who presented first results in a phantom. With *sensitivity encoding (SENSE)*, [Pruessmann et al., 1999] presented the first robust implementation of **image domain based parallel imaging reconstruction**. In their method, they describe the image domain procedure of *unaliasing* the sub-Nyquist sampled Fourier reconstructed image, to resolve the fold-over artifacts (*aliasing*).

Parallel imaging is often parted into k-space and image space based methods, of which GRAPPA [Griswold et al., 2002] and SENSE [Pruessmann et al., 1999] constitute the main representatives. Nevertheless, both methods can be performed in both domains as will be discussed in Sec. 4.5.2 and Sec. 6.1. Both methods are nowadays broadly applied in clinical routine and both are applicable to accelerate image acquisition of various MRI scenarios. One advantageous aspect of GRAPPA is the robustness due to the data-driven approach which does not rely on accurate determination of coil sensitivities of the multiple receive coils. Following a description of the general inverse problem in parallel imaging, both GRAPPA and SENSE will be briefly described.

4.3. Sensitivity encoding and the inverse problem in parallel imaging

The concepts of *hybrid* or *sensitivity encoding* are described more generally below. Original descriptions of sensitivity encoding are presented in [Pruessmann et al., 1999] and further dis-

ussions are given in [Pruessmann, 2006, Sodickson and McKenzie, 2001].

Reformatting the signal model of (4.1), parallel imaging data collection can be described analogously to Def. 3.2.4 by hybrid Fourier encoding kernel functions.

Definition 4.3.1. Denote the set of coils by $\mathcal{C} := \{1, \dots, N_{\text{coils}}\}$ and the coil sensitivity of coil α at spatial position \mathbf{r} by $c_\alpha(\mathbf{r})$. A general **coil sensitivity and Fourier encoding kernel** is defined by

$$\begin{aligned} E_c &: \mathcal{K} \times \mathcal{C} \times V \rightarrow \mathbb{C} \\ E_c &: (\mathbf{k}, \alpha, \mathbf{r}) \mapsto c_\alpha(\mathbf{r}) \exp(-i\mathbf{k} \cdot \mathbf{r}). \end{aligned} \quad (4.5)$$

The **parallel imaging MR signal** is expressed by incorporating the hybrid encoding:

$$d_{n,\alpha} = \int_V m_\perp(\mathbf{r}, 0) E_c(\mathbf{k}_n, \alpha, \mathbf{r}) d\mathbf{r}, \text{ for each } \mathbf{k}_n \in \mathcal{K}_{\text{smp}}, \text{ and each coil } \alpha \in \mathcal{C}. \quad (4.6)$$

The general inverse problem in parallel imaging is captured based on the - in the least squares sense - optimal approximation of the data consistency constraint:

$$\begin{aligned} I^\dagger &= \operatorname{argmin}_{I \in \mathcal{L}^2(\Omega, \mathbb{C})} \|I\|_{\mathcal{L}^2}^2 \text{ subject to } \min_{I \in \mathcal{L}^2(\Omega, \mathbb{C})} \|\mathbf{d} - \check{E}\{I\}\|_2^2, \\ \text{where } d_{n,\alpha} &= \langle m_\perp(\cdot, 0) | c_\alpha^*(\cdot) \exp(i\mathbf{k}_n \cdot \cdot) \rangle_{\mathcal{L}^2}, \\ \text{and } (\check{E}I)_{(n,\alpha)} &= \langle I | c_\alpha^*(\cdot) \exp(i\mathbf{k}_n \cdot \cdot) \rangle_{\mathcal{L}^2}. \end{aligned} \quad (4.7)$$

When a vector is formed from the $N_{\text{smp}}N_{\text{coils}}$ complex values, the linear encoding operator defines a mapping $\check{E} : \mathcal{L}^2(\Omega, \mathbb{C}) \rightarrow \mathbb{C}^{N_{\text{smp}}N_{\text{coils}}}$. Likewise, the sampled dataset along the k-space trajectory and for all coils is stacked into a vector $\mathbf{d} \in \mathbb{C}^{N_{\text{smp}}N_{\text{coils}}}$. This justifies the ℓ_2 -norm.

As for the Fourier encoding kernel, the sensitivity encoding kernel is defined continuously on \mathcal{K} and V . However, finite k-space sampling is performed along discrete points \mathbf{k}_n of the trajectory \mathcal{K}_{smp} of cardinality $N_{\text{smp}} = N_{\text{fe}}N_{\text{pe}}$. With N_{coils} , the encoding kernel is therefore evaluated ($N_{\text{smp}}N_{\text{coils}}$)-times.

In the reconstruction process, a discrete representation of the underlying object with $N_{\text{pix}} = N_xN_y$ pixels (for $\mathcal{D} = 2$) is sought. In pure Fourier imaging, the PSF is given by a sinc-function and the inverse of its FWHM describes the limit on spatial resolution (Sec. 3.3.2). The number of pixels according to the sampled data, $N_{\text{pix}} = N_{\text{smp}}$, is the best image resolution (Def. 3.3.21) for this limit. The inverse discrete Fourier transform (Def. 3.3.22) as a reconstruction at a given number of pixels determines the *spatial response*, i.e. how individual pixels reflect local magnetization densities. Note that this is different compared to the PSF, as the latter explains how single point sources propagate into reconstructed pixels.

In sensitivity encoding, however, samples are collected for each coil, wherefore the number of pixels is not necessarily bounded from above by N_{smp} . Likewise, the *spatial response* exhibits more degrees of freedom. In fact, it is determined together with the reconstruction process. Therefore, parallel imaging generally allows for modeling the discretized image reconstruction according to the number of pixels as well as the desired spatial response. In the original paper, [Pruessmann et al., 1999] describe two scenarios: the *strong* and the *weak approach*.

Let N_{pix} denote the number of reconstructed pixels. In accordance with the linear encoding operator \check{E} , consider a linear reconstruction operator that maps the data vector $\mathbf{d} \in \mathbb{C}^{N_{\text{smp}}N_{\text{coils}}}$ to a vector of reconstructed pixels $\hat{\mathbf{I}} \in \mathbb{C}^{N_{\text{pix}}}$. Hence, the reconstruction operator is characterized by a matrix $\check{F} \in \mathbb{C}^{N_{\text{pix}} \times N_{\text{smp}}N_{\text{coils}}}$. Then the concatenation defines a mapping

$$\check{F}\check{E} : \mathcal{L}^2(\Omega, \mathbb{C}) \rightarrow \mathbb{C}^{N_{\text{pix}}}. \quad (4.8)$$

Considering this mapping for individual pixels defines the *spatial response function*. Applying this mapping to a point source describes the point spread function. If the object space is also discretized into N'_{pix} voxels, (4.8) can be characterized by a matrix in $\mathbb{C}^{N_{\text{pix}} \times N'_{\text{pix}}}$.

In the *strong approach*, \check{F} - and thus the reconstructed image - is determined by fitting (4.8) to the desired voxel shape. The strong approach aims for unbiased but not necessarily efficient reconstruction. Since noise minimization is not an objective in this approach, noise amplification can be strong.

For the *weak approach*, assume the object space to be discretized into N_{pix} voxels corresponding to the number of pixels chosen for the reconstruction. The encoding operator is then described by the matrix $\check{E} \in \mathbb{C}^{(N_{\text{smp}} N_{\text{coils}}) \times N_{\text{pix}}}$ with elements

$$\check{E}_{(n,\alpha),m} = \int_V \delta(\mathbf{r} - \mathbf{r}_m) E_c(\mathbf{k}_n, \alpha, \mathbf{r}) d\mathbf{r} = c_\alpha(\mathbf{r}_m) \exp(-i\mathbf{k}_n \cdot \mathbf{r}_m). \quad (4.9)$$

In the weak approach, the operation $\check{F}\check{E}$ is solely constrained by matching one reconstructed pixel with one spatial counterpart. This is described by the *orthonormality relation*:

$$\check{F}\check{E} = \mathbb{1}_{N_{\text{pix}}}. \quad (4.10)$$

Throughout this work, the weak approach is assumed, as it complements Fourier reconstruction as presented in the previous chapter. [Sánchez-González et al., 2006] pointed out that if N_{pix} approaches infinity, the weak and strong approach become essentially identical.

Since the orthonormality relation is much less restrictive than the constraint of the strong approach, the gained degrees of freedom are used to additionally minimize noise in the reconstructed image. Image reconstruction in the weak approach based on sensitivity encoding is achieved by finding the image reconstruction matrix \check{F}^\dagger according to

$$\check{F}^\dagger = \underset{\check{F} \in \mathbb{C}^{N_{\text{pix}} \times N_{\text{smp}} N_{\text{coils}}}}{\text{argmin}} \quad \check{F}\Psi\check{F}^H, \text{ subject to } \check{F}\check{E} - \mathbb{1}_{N_{\text{pix}}} = 0, \quad (4.11)$$

where H indicates the Hermitian transpose and Ψ denotes the sample noise covariance matrix of the $N_{\text{smp}} N_{\text{coils}}$ data samples (see Def. 4.6.1). Image noise is thereby minimized (see Sec. 4.6, Prop. 4.6.5).

Assume $N_{\text{smp}} N_{\text{coils}} \geq N_{\text{pix}}$. If \check{E} is injective, \check{F}^\dagger is given by the *Moore-Penrose pseudo inverse* [Moore, 1920, Penrose, 1955]

$$\check{F}^\dagger = (\check{E}^H \Psi^{-1} \check{E})^{-1} \check{E}^H \Psi^{-1} =: \check{E}^+. \quad (4.12)$$

Therefore, SENSE reconstruction in the weak approach generally comprises the derivation of the pseudo-inverse of the encoding matrix \check{E}^+ and subsequent application to the sampled data set:

$$\check{E}^+ \mathbf{d} = \check{F}^\dagger \mathbf{d} =: \hat{\mathbf{I}}^\dagger. \quad (4.13)$$

Remark 4.3.2. *The minimization problem of (4.11) leads to the same solution (cf. 4.13) as the general weighted minimum norm solution as part of regression analysis of (4.7) when assuming the same discretization.*

Direct inversion of the encoding matrix is computationally expensive. In case of Cartesian undersampling, the problem can be sub-divided into a set of smaller inversion problems as will be briefly discussed in the next section. In case of Non-Cartesian sampling scenarios, the inverse problem is commonly solved using iterative methods such as *conjugate gradients* [Hestenes and Stiefel, 1952] as described in [Pruessmann et al., 2001].

4.3.1. Cartesian SENSE: unfolding in image space

SENSE is referred to as *image space based*, since the algorithm can be viewed as an *unfolding process* in the image domain. The algorithm requires the coil sensitivity information to be determined before the inverse problem for image reconstruction is formed. Cartesian SENSE based on regular undersampling with reduction factor R is briefly discussed below, in order to discuss parallels with GRAPPA reconstruction in Sec. 6.1.

In Cartesian SENSE, $N_{\text{pix}} := RN_{\text{smp}}$ is typically chosen. The general encoding matrix (4.9) can be expressed by two consecutive operations: first, the *folding matrix* $\check{C}^{\text{fold}} \in \mathbb{C}^{N_{\text{pix}}N_{\text{coils}} \times N_{\text{pix}}}$ that superimposes contributions from regions of the same encoding weighted by the local sensitivity. Second, the *discrete Fourier transform matrix* $\check{F} \in \mathbb{C}^{RN_{\text{smp}}N_{\text{coils}} \times N_{\text{pix}}N_{\text{coils}}}$ that performs a discrete Fourier transform into k-space. Figure 4.1 illustrates the two operations.

In a Cartesian sampling pattern with reduction factor R , spatial encoding is periodically repeated in intervals of FoV/R . The folding matrix weights local contributions with the local sensitivity of each coil and adds contributions which are in the distances of FoV/R . The latter describes how spatial contributions are *folded* on top of each other due to the non-unique gradient encoding. Elements of \check{C}^{fold} are defined by

$$\check{C}_{(n:=(n_p, n_q), \beta), (m:=(m_p, m_q))}^{\text{fold}} = c_{\beta}(\mathbf{r}_m) \delta_{(n_p, n_q), (m_p, m_q \bmod N_y/R)}, \quad (4.14)$$

where $\delta_{a,b}$ denotes a Kronecker delta, which is equal to 1, if $a = b$ and 0 otherwise. The notation *mod* refers to the modulus derivation and $N_y/R \in \mathbb{Z}$ is assumed for simplicity.

The discrete Fourier transform matrix is a block-diagonal square-matrix, where each block represents a discrete Fourier transform $\mathcal{DFT}\{\cdot\} \in \mathbb{C}^{N_{\text{pix}} \times N_{\text{pix}}}$. Its elements are defined by

$$\check{F}_{(n, \alpha), (m, \beta)} = \exp(-i\mathbf{k}_n \cdot \mathbf{r}_m) \delta_{\alpha, \beta}. \quad (4.15)$$

Due to orthogonality of Fourier kernel based row and column vectors, \check{F} is unitary, hence $\check{F}^{-1} = \check{F}^H$.

With the given encoding operations, the discretization of the object space and the weak approach, the application of \check{F}^{-1} allows one to describe the image reconstruction problem in the discretized image space. By the definition of \check{F} chosen here, this requires to form a data vector \mathbf{d}^{zf} , where unacquired k-space positions on the regular grid of Nyquist-sampled stepsizes are zero-filled (see Def. 3.5.1) before \check{F}^{-1} is applied.

$$\hat{\mathbf{I}}^{\dagger} = \underset{\mathbf{I} \in \mathbb{C}^{N_{\text{pix}}}}{\text{argmin}} \left\| \check{F}^{-1} \mathbf{d}^{\text{zf}} - \check{C}^{\text{fold}} \mathbf{I} \right\|_2^2 \quad (4.16)$$

Remark 4.3.3. *Cartesian SENSE is described here for zero-filled data, as it is used as such for the comparison with standard GRAPPA in Sec. 6.1. Note that with the formulation in terms of zero-filled data, the folded image $\check{F}^{-1} \mathbf{d}^{\text{zf}}$ essentially contains the same information R -times. This is opposed to practical implementations of Cartesian SENSE, where data is clearly not zero-filled to not increase the computational burden. The matrix \check{F} is described in $\mathbb{C}^{N_{\text{smp}}N_{\text{coils}} \times N_{\text{smp}}N_{\text{coils}}}$ instead. Besides this difference, the same argumentation applies.*

The image reconstruction in Cartesian SENSE begins with the derivation of \check{C}^{fold} and the zero-filled reconstruction $\check{F}^{-1} \mathbf{d}^{\text{zf}}$. Then, (4.16) is solved for the image vector $\hat{\mathbf{I}}^{\dagger}$. With the previous arguments, the latter is given by the Moore-Penrose pseudo inverse of \check{C}^{fold} . Due to

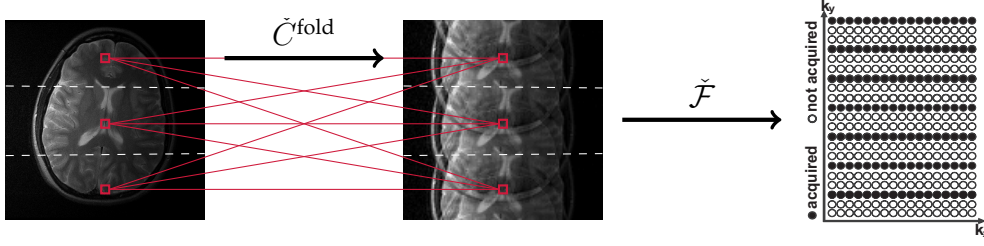


Figure 4.1: Since unique spatial encoding is periodically repeated in intervals of FoV/R (white dashed lines), the folding matrix \check{C}^{fold} folds the local contributions of the same encoding on top of each other, weighted by the sensitivity at the respective local contribution. Thus, \check{C}^{fold} forms N_{pix} spatial contributions to N_{pix}/R folded magnetization values R -times. The discrete Fourier transform matrix \check{F} transfers the magnetization values into its k -space representation. The R -fold replication corresponds with zero-filling k -space.

the structure of \check{C}^{fold} , it allows for subdivision into separately solvable sub-problems, one for each folded pixel $(\check{F}^{-1} \mathbf{d}^{\text{zf}})_p$, $p = 1, \dots, N_{\text{pix}}/R$. Assuming $N_{\text{coils}} \geq R$ and provided that the coil geometry facilitates linearly independent coil information, the corresponding sub-matrix $\check{C}_p^{\text{fold}} \in \mathbb{C}^{N_{\text{coils}} \times R}$ is injective and the solution yields

$$\mathbf{C}_p^{\text{unfold}} := (\check{C}_p^{\text{fold}})^+ := \left(\left(\check{C}_p^{\text{fold}} \right)^H \Psi_{\text{coils}}^{-1} \check{C}_p^{\text{fold}} \right)^{-1} \check{C}_p^{\text{fold}H} \Psi_{\text{coils}}^{-1}. \quad (4.17)$$

In Cartesian SENSE, the problem of deriving \check{E}^+ is thus segmented into several smaller sub-problems of reduced dimensionality, which allows for efficient calculation of the pseudo-inverse [Pruessmann et al., 1999].

4.4. Estimation of spatial harmonics: from SMASH to GRAPPA

Original motivation and developments of k -space based parallel imaging methods are briefly described below. A more detailed discussion of differences between the methods covered is provided by [Blaimer et al., 2004].

Whereas the sensitivity encoding kernel consists of a combination of gradient encoding and coil sensitivities, [Sodickson and Manning, 1997] presented - in their earlier method SMASH - the aim to emulate unacquired gradient encodings by weighted linear combinations of sensitivities of all coils $\{c_\beta, \beta \in \mathcal{C}\}$. To this end, weighing factors w_β are estimated such that

$$\sum_{\beta \in \mathcal{C}} w_\beta c_\beta \approx \exp(-in\Delta k_y), \quad (4.18)$$

for each unacquired phase encoding step $n\Delta k_y$, $n = 1, \dots, R - 1$ of a reduction factor R . The fitted spatial harmonics are used to perform k -space shifts of $n\Delta k_y$, in order to estimate missing samples based on the nearest acquired k -space samples of all coils. If $d_{(k_x, k_y), \beta}$ denotes the sample acquired for the k -space coordinates (k_x, k_y) and with the coil $\beta \in \mathcal{C}$, then the unacquired sample $d_{(k_x, k_y + n\Delta k_y)}$ of all coils combined is estimated by

$$\begin{aligned} \sum_{\beta \in \mathcal{C}} w_\beta d_{(k_x, k_y), \beta} &\approx \int_V m_\perp(\mathbf{r}, 0) \sum_{\beta \in \mathcal{C}} w_\beta c_\beta(\mathbf{r}) \exp(-i(k_x, k_y) \cdot \mathbf{r}) d\mathbf{r} \\ &\approx \int_V m_\perp(\mathbf{r}, 0) \exp(-i(k_x, k_y + n\Delta k_y) \cdot \mathbf{r}) d\mathbf{r} = d_{(k_x, k_y + n\Delta k_y)}. \end{aligned} \quad (4.19)$$

Unfortunately, this approach is limited by a poor robustness of the fitting procedure and by very specific requirements on the coil array geometry.

[Jakob et al., 1998] suggested in their method AUTO-SMASH to acquire an additional *auto-calibration signal (ACS)* line for each spatial harmonic to recreate. Thus, $R - 1$ additional lines at k-space distances of $n\Delta k_y$, $n = 1, \dots, R - 1$ are acquired. Instead of pure coil sensitivities, the ACS is then used to estimate weighting factors w_β such that

$$\sum_{\beta \in \mathcal{C}} w_\beta d_{(k_x, k_y), \beta}^{ACS} \approx \sum_{\beta \in \mathcal{C}} d_{(k_x, k_y + n\Delta k_y), \beta}^{ACS}. \quad (4.20)$$

In VD-AUTO-SMASH [Heidemann et al., 2001], the $R - 1$ ACS lines were extended to a range of Nyquist-sampled ACS data to increase the number of equations used in the fitting procedure, which improves robustness. The name *variable density (VD)* relates to the different sampling densities of Δk_y in the central k-space area and $R\Delta k_y$ in the outer k-space part. Unfortunately, the additional Nyquist-sampled ACS data increase the acquisition time. However, it can be directly included in the reconstruction.

Essential robustness was added by extension of the set of k-space sources and the usage of distinct targets in the fitting procedure, as refined in *generalized autocalibrating partially parallel acquisitions (GRAPPA)* [Griswold et al., 2002]. In GRAPPA, weights are determined individually for each target coil by weighted contributions from several k-space neighbors and all source coils:

$$\sum_{\beta \in \mathcal{C}} \sum_{(k_x, k_y)} w_{(k_x, k_y), \beta} d_{(k_x, k_y), \beta}^{ACS} \approx d_{(k_x, k_y + n\Delta k_y), \alpha}^{ACS}, \quad \text{for each target coil } \alpha \in \mathcal{C}. \quad (4.21)$$

The neighborhood of k-space samples that are incorporated in the fit and reconstruction is usually chosen much smaller than the actual acquired number of frequency encodings N_{fe} and the ACS phase encoding range. Therefore, multiple neighborhoods can be collected that overall further increases the robustness. The more general concept of *in vivo sensitivities* and standard GRAPPA reconstruction is described in the next section.

4.5. In vivo sensitivities and the inverse problem of weight calibration

In GRAPPA, the coil sensitivity information is used indirectly by deriving weights from the ACS data of all coils. Therefore, it also relies on coil sensitivities that provide - at best - independent spatial information each. Analogous to the sensitivity encoding kernels, *in vivo sensitivity kernels* are defined.

Definition 4.5.1. Given the set of coils $\mathcal{C} := \{1, \dots, N_{coils}\}$ with sensitivities $c_\alpha(\mathbf{r})$ of coil α at spatial position \mathbf{r} , a general *in vivo sensitivity and Fourier encoding kernel* is defined by

$$\begin{aligned} E_{ACS} &: \mathcal{K} \times \mathcal{C} \times V \rightarrow \mathbb{C} \\ E_{ACS} &: (\mathbf{k}, \alpha, \mathbf{r}) \mapsto m_\perp(\mathbf{r}, 0) c_\alpha(\mathbf{r}) \exp(-i\mathbf{k} \cdot \mathbf{r}). \end{aligned} \quad (4.22)$$

The *in vivo sensitivities* are thereby defined as $\hat{c}_\alpha(\mathbf{r}) = m_\perp(\mathbf{r}, 0) c_\alpha(\mathbf{r})$. The *parallel imaging MR signal* then reduces to

$$d_{n, \alpha} = \int_V E_{ACS}(\mathbf{k}_n, \alpha, \mathbf{r}) d\mathbf{r}, \quad \text{for each } \mathbf{k}_n \in \mathcal{K}_{smp}, \text{ and each coil } \alpha \in \mathcal{C}. \quad (4.23)$$

Remark 4.5.2. *The term in vivo sensitivities was introduced for instance in [Samsonov et al., 2006].*

The in vivo sensitivity encoding allows for a description of the weight derivation of GRAPPA similar to Sec. 4.3. As typical for standard GRAPPA, a Cartesian sampling pattern is assumed. Two terms become important in the description of GRAPPA and will be frequently used: a *k-space neighborhood* and the *kernel geometry*.

Definition 4.5.3 (k-space neighborhood). *A **k-space neighborhood** $\mathcal{K}_{smp}^\varepsilon(\mathbf{k}_0)$ of a k-space point \mathbf{k}_0 is an open ball around \mathbf{k}_0 that contains k-space sampling points in distances of less than or equal to ε .*

Definition 4.5.4 (kernel geometry). *Within a k-space neighborhood, a **kernel geometry** designates **source points** and **target points** by relative k-space distances within the neighborhood.*

For standard GRAPPA, the k-space neighborhoods of 2D-imaging are determined by a rectangular of lengths $B_{fe}\Delta k$ and $B_{pe}R\Delta k$ along the frequency and phase encoding direction. Hereby, B_{fe} and B_{pe} denote the number of acquired samples in the respective direction and are chosen prior to the reconstruction process. For each spatial harmonic $m\Delta k$, $m = 1, \dots, R-1$ to recover, one fixed kernel geometry is typically used in all k-space neighborhoods (for standard GRAPPA). The $R-1$ different kernel geometries in terms of relative k-space distances are illustrated for $R = 2$ in Fig. 4.2. Note that for standard GRAPPA, the $R-1$ different kernel geometries comprise the same sources (but different targets) in each k-space neighborhood.

Missing data samples (*targets*) are restored by linear combination of acquired samples (*sources*) as designated by the kernel geometry within the neighborhoods. To this end, the relative weightings from sources to targets need to be derived. It is assumed in GRAPPA that relative weightings of the fixed kernel geometry are irrespective of the k-space neighborhood (*shift invariance*). In the ACS data, sources as well as targets are given. Assuming the relative weighting to be shift invariant in k-space, the ACS data allows for the estimation of these based on a number of example source-to-target relations. Therefore, all possible placements of the kernel geometry within the range of the Nyquist-sampled ACS are collected and a linear equation is formed.

For each neighborhood that is fully contained in the ACS data, $B_{fe}B_{pe}N_{coils}$ sources are collected according to the kernel geometry. Let N_{fe}^{ACS} and N_{pe}^{ACS} denote the number of frequency and phase encoding steps of the ACS. Then the $B_{fe}B_{pe}N_{coils}$ sources can be collected $(N_{pe}^{ACS} - R(B_{pe} - 1))(N_{fe}^{ACS} - B_{fe} - 1)$ -times within the ACS, according to all possibilities for a neighborhood to be fully contained in the k-space extent of the ACS.

In analogy to the encoding matrix of (4.9), an *in vivo encoding matrix* $\check{D}^{ACS} \in \mathbb{C}^{(B_{fe}B_{pe}N_{coils}) \times (N_{pe}^{ACS} - R(B_{pe} - 1))(N_{fe}^{ACS} - B_{fe} - 1)}$ is defined with elements given by

$$\check{D}_{(n,\beta),p}^{ACS} = \int_V \hat{c}_\beta(\mathbf{r}) \exp(-i\mathbf{k}_{n,p} \cdot \mathbf{r}) d\mathbf{r}. \quad (4.24)$$

The number of columns of \check{D}^{ACS} increases with the number of possible placements of the kernel geometry within the ACS data. Note that all entries of \check{D}^{ACS} are actual acquired data samples.

For each neighborhood that is fully contained in the ACS data, $(R-1)N_{coils}$ targets are collected in accordance with the $R-1$ fixed kernel geometries. For each target harmonic $m = 1, \dots, R-1$ and each target coil $\alpha = 1, \dots, N_{coils}$, let $\mathbf{d}_{m,\alpha}^{ACS} \in \mathbb{C}^{1 \times (N_{pe}^{ACS} - R(B_{pe} - 1))(N_{fe}^{ACS} - B_{fe} - 1)}$ denote the row vector of corresponding target samples within the ACS data. A linear relation between sources and targets is assumed to be given by

$$\hat{\mathbf{w}}_{m,\alpha} \check{D}^{ACS} = \mathbf{d}_{m,\alpha}^{ACS}, \quad (4.25)$$

where the weights $\hat{\mathbf{w}}_{m,\alpha} \in \mathbb{C}^{1 \times (B_{te} B_{pe} N_{coils})}$ are unknown. The task of finding the reconstruction weights $\hat{\mathbf{w}}_{m,\alpha}$ for each target coil $\alpha = 1, \dots, N_{coils}$ and each spatial harmonic indexed by $m = 1, \dots, R - 1$ establishes the inverse problem of weight calibration.

Definition 4.5.5 (inverse problem of weight calibration). *With the notation as above, the **inverse problem of weight calibration** in k-space kernel based parallel imaging is given by*

$$\hat{\mathbf{w}}_{m,\alpha}^\dagger = \underset{\hat{\mathbf{w}}_{m,\alpha}}{\operatorname{argmin}} \left\| \mathbf{d}_{m,\alpha}^{ACS} - \hat{\mathbf{w}}_{m,\alpha} \check{D}^{ACS} \right\|_2^2, \quad (4.26)$$

for each target relation $m = 1, \dots, R - 1$ and each target coil $\alpha = 1, \dots, N_{coils}$. The matrix \check{D}^{ACS} defined as above is referred to as the **in vivo encoding matrix**.

Under the assumption that \check{D}^{ACS} is surjective, the Moore-Penrose pseudo inverse is given by

$$\check{D}^{ACS,+} := \check{D}^{ACS,H} \left(\check{D}^{ACS} \check{D}^{ACS,H} \right)^{-1}. \quad (4.27)$$

The solution of (4.26) is then obtained using the Moore-Penrose pseudo inverse by

$$\hat{\mathbf{w}}_{m,\alpha}^\dagger = \mathbf{d}_{m,\alpha}^{ACS} \check{D}^{ACS,+}. \quad (4.28)$$

The derived weights are used as coefficients in the linear combination of acquired data samples to restore missing data samples in neighborhoods outside the ACS data. The GRAPPA image reconstruction process is briefly described below.

4.5.1. GRAPPA: estimation in k-space

GRAPPA exploits *local correlations* in k-space and relies on *shift invariance* of these. A pre-defined GRAPPA kernel geometry is chosen according to the incorporated k-space neighborhood, source-to-target relations and the reduction factor R . A k-space undersampling pattern of $R = 3$ with incorporated ACS data and respective GRAPPA kernel geometry are displayed in Fig. 4.2. Based on a Cartesian k-space sampling pattern, Nyquist-sampled datasets are reconstructed from the undersampled data in two steps:

1. calibration of the reconstruction weights given an ACS dataset
2. estimation of omitted k-space data by weighted linear combination of neighboring acquired data.

Hence, at first, k-space relations between target points and their surrounding neighborhood are learned. Thereafter, the relations are applied to estimate missing data samples as weighted linear combination of acquired k-space neighborhood data.

Calibration of the reconstruction weights is achieved using the previously described ACS dataset, which covers a low-frequency k-space extent in Nyquist-sampled phase encoding steps. According to the GRAPPA kernel geometry, *sources* and *target* data are collected within the ACS data of each coil and in each neighborhood of k-space samples. The kernel's extent thereby governs the number of source-to-target relations that can be extracted. All collected sources and targets are assembled in the in vivo encoding matrix and a target vector. The optimal weights in the least-squares sense are obtained by solving the inverse problem as in (4.26) using the Moore-Penrose pseudo inverse of the in vivo encoding matrix.

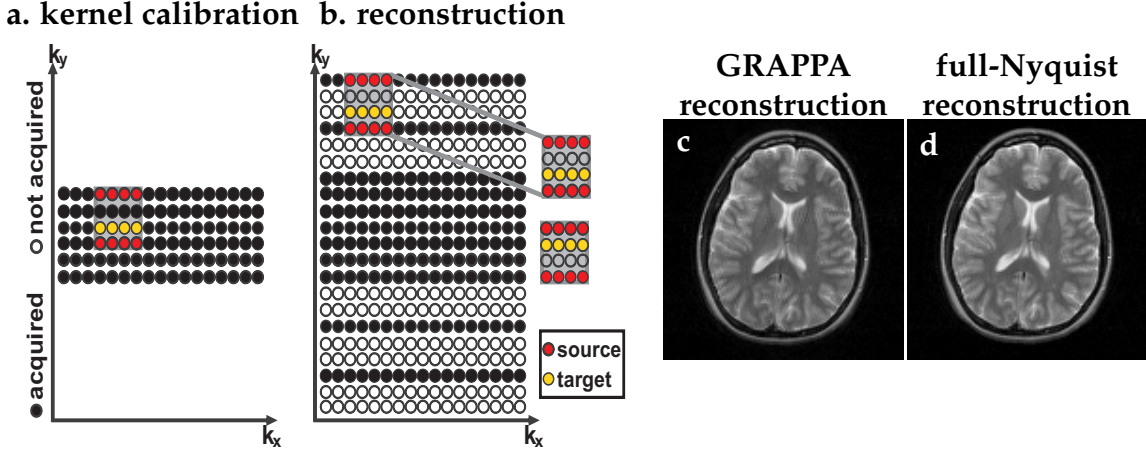


Figure 4.2: The two steps of GRAPPA reconstruction are illustrated in (a) and (b). First, reconstruction weights are calibrated according to the chosen GRAPPA kernel geometry and based on the full-Nyquist sampled ACS data (a). Second, learned weights are applied in linear combination of acquired neighborhood samples to reconstruct omitted k -space data on the Cartesian grid (b). Note that all coils are incorporated in the reconstruction (not shown). The corresponding GRAPPA reconstruction of the same example as shown in Fig. 5.2 is depicted in (c), along with full-Nyquist sampled reconstruction for comparison (d).

Estimation of omitted k -space data is performed by linear combination of neighboring acquired k -space data of all coils weighted by the reconstruction weights in accordance with the GRAPPA kernel geometry. Conventional GRAPPA essentially uses the same $B_{fe}B_{pe}N_{\text{coils}}$ source samples to reconstruct $R - 1$ target samples of one coil and repeats the process of linear combination for all possible kernel placements. This is simplified by forming one *convolution kernel* $w_{\alpha,\beta}^{2D} \in \mathbb{C}^{B_{fe} \times RB_{pe}}$ for each target coil α and each source coil β that combines the $R - 1$ relative kernel geometries. The latter is formed by shifting different geometries to a mutual target center. The central target point is set to 1 to remain acquired samples. The process of forming the convolution kernel is explained in more details in [Breuer et al., 2009]. It is furthermore described for k -t-GRAPPA in Sec. 6.2.2.

Let $d_{\beta}^{\text{zf},2D}$ be the zero-filled acquired undersampled data of coil β in matrix representation. The localized linear combination can be expressed as a convolution of weights and undersampled data in k -space for each coil and adding the contribution of each coil:

$$\hat{d}_{\alpha}^{\text{sub},2D} = \sum_{\beta \in \mathcal{C}} w_{\alpha,\beta}^{2D} * d_{\beta}^{\text{zf},2D}. \quad (4.29)$$

Hence, a Nyquist-sampled Cartesian k -space dataset $\hat{d}_{\alpha}^{\text{sub},2D}$ is estimated for each coil. Fourier reconstruction and subsequent coil combination (see Sec. 4.1) yields the final image.

SMASH-like k -space based parallel imaging reconstruction methods rely on the fundamental assumption of the *k -space locality principle*, as it was termed in [Yeh et al., 2005]. Further, the assumption of *shift invariance of k -space relations* is employed. The validity of the k -space locality principle and shift invariance is partly discussed in [Yeh et al., 2005, Kholmovski and Parker, 2006, Samsonov et al., 2006, Liu et al., 2007, Samsonov, 2008, Zhang et al., 2011, Schultz, 2013].

4.5.2. GRAPPA in image space

The reconstruction process in GRAPPA consists of a convolution in k-space (cf. 4.29), followed by coil-wise Fourier reconstruction of the estimated full datasets. Let $\mathcal{DFT}_{x,y}^{-1}\{\cdot\}$ denote the discrete Fourier transform along both spatial dimensions. Then by linearity of the discrete Fourier transform and the convolution theorem follows

$$\begin{aligned} \hat{I}_\alpha^{\text{sub}} &:= \mathcal{DFT}_{x,y}^{-1}\left\{\hat{d}_\alpha^{\text{sub},2\text{D}}\right\} = \sum_{\beta \in \mathcal{C}} \mathcal{DFT}_{x,y}^{-1}\left\{w_{\alpha,\beta}^{2\text{D}} * d_\beta^{\text{zf},2\text{D}}\right\} \\ &= \sum_{\beta \in \mathcal{C}} \mathcal{DFT}_{x,y}^{-1}\left\{w_{\alpha,\beta}^{2\text{D}}\right\} \odot \mathcal{DFT}_{x,y}^{-1}\left\{d_\beta^{\text{zf},2\text{D}}\right\} \\ &= \sum_{\beta \in \mathcal{C}} W_{\alpha,\beta}^{2\text{D}} \odot I_\beta^{\text{fold}}, \end{aligned} \quad (4.30)$$

where \odot refers to element-wise multiplication of the two matrices $W_{\alpha,\beta}^{2\text{D}}$ and I_β^{fold} . The latter denote the discrete Fourier transform of the convolution kernel $w_{\alpha,\beta}^{2\text{D}}$ and the zero-filled Fourier reconstruction of $d_\beta^{\text{zf},2\text{D}}$, respectively. This yields an image space based representation of the GRAPPA algorithm as developed by [Wang et al., 2005a, Brau et al., 2008, Breuer et al., 2009]. The coil images obtained can be combined according to any of the in Sec. 4.1 described coil combination methods.

4.6. SNR in parallel imaging

As derived in Sec. 3.3.3, image noise variance in Fourier image reconstructions is pixel-wise uncorrelated and the average SNR is inversely proportional to the spatial resolution. In parallel imaging, however, image noise variance exhibits spatial correlations. Moreover, the average SNR is decreased by the reduced number of data samples, as well as affected by the properties of the incorporated receive coil array. In the following, differences are highlighted and the *coil's geometry factor* (*g-factor*) is introduced.

The omission of parts of k-space while keeping spatial resolution parameters (e.g. field of view and pixel size) fixed generally results in a loss in SNR. This can be understood by considering the opposite: R -times *oversampling* instead of R -times *undersampling*. For oversampling, an artifact-free Fourier reconstruction is obtained (if Δk fulfills the Nyquist-Shannon criterion, so does $\Delta k/R$). However, R -times the number of measurements - each containing information about every spatial position to reconstruct - are provided for the Fourier reconstruction. This improves the image noise variance of each pixel by \sqrt{R} for R -times oversampling.

In parallel imaging, another SNR compromising factor arises despite the general SNR loss due to reduced data acquisition. The image reconstruction process further affects SNR and entails noise correlation between image pixels. In order to investigate the correlations imposed by the reconstruction process, the *sample noise covariance matrix* as well as the *image noise covariance matrix* are defined. For MRI acquisitions with multiple coils $\alpha = 1, \dots, N_{\text{coils}}$, assume the noise samples acquired in each coil α to be described by a stationary stochastic Gaussian white noise process $\{\varepsilon_d(\mathbf{k}_k, \alpha)\}_{k_k \in \mathcal{K}_{\text{smp}}}$.

Definition 4.6.1. The *sample noise covariance matrix* and the *image noise covariance matrix* are defined by $\Psi \in \mathbb{C}^{N_{\text{smp}}N_{\text{coils}} \times N_{\text{smp}}N_{\text{coils}}}$ and $\hat{\Psi} \in \mathbb{C}^{N_{\text{pix}} \times N_{\text{pix}}}$, respectively, such that

$$\Psi_{(k,\alpha),(l,\beta)} = \sigma^2(\varepsilon_d(\mathbf{k}_k, \alpha), \varepsilon_d(\mathbf{k}_l, \beta)) \quad \text{and} \quad \hat{\Psi}_{pq} = \sigma^2(\varepsilon_I(\mathbf{x}_p), \varepsilon_I(\mathbf{x}_q)),$$

for each $k, l = 1, \dots, N_{\text{smp}}$, $\alpha, \beta = 1, \dots, N_{\text{coils}}$, as well as for each pixel position, $p, q = 1, \dots, N_{\text{pix}}$, where $\mathbf{x}_p := (x_p, y_p)^T$ refers to the vector of location on the image grid.

Definition 4.6.2. In the same manner as in Def. 4.6.1, the *receive coil covariance matrix* is defined by $\Psi_{\text{coils}} \in \mathbb{C}^{N_{\text{coils}} \times N_{\text{coils}}}$ with elements of $\sigma^2(\varepsilon_d(\mathbf{0}, \alpha), \varepsilon_d(\mathbf{0}, \beta))$.

Remark 4.6.3. Entries of the receive coil covariance matrix are practically derived by sampling of pure receive noise achieved in the absence of any gradient encoding by zero-flip angle acquisitions.

Proposition 4.6.4. The sample noise covariance matrix in parallel imaging yields a block-diagonal matrix of form $\Psi = \Psi_{\text{coils}} \otimes \mathbf{1}_{N_{\text{smp}}}$, where \otimes refers to the Kronecker product and $\mathbf{1}_{N_{\text{smp}}} \in \mathbb{C}^{N_{\text{smp}} \times N_{\text{smp}}}$ denotes the identity matrix.

Proof. Since variances are finite and different k-space locations are uncorrelated (Def. 3.3.25 (i) and (iii)), it follows that

$$\Psi_{(k,\alpha),(l,\beta)} \stackrel{(iii)}{=} \delta_{kl} \sigma^2(\varepsilon_d(\mathbf{k}_k, \alpha), \varepsilon_d(\mathbf{k}_l, \beta)) \stackrel{(ii)}{=} \delta_{kl} \sigma^2(\varepsilon_d(\mathbf{0}, \alpha), \varepsilon_d(\mathbf{0}, \beta)). \quad (4.31)$$

Therefore, Ψ can be arranged into a block-diagonal matrix of N_{smp} blocks of the receive coil covariance matrix Ψ_{coils} , hence $\Psi = \Psi_{\text{coils}} \otimes \mathbf{1}_{N_{\text{smp}}}$. \square

For an empirical evaluation of the variation of SNR in parallel imaging, a large number of measurement repetitions is required to reliably estimate the spatial noise distribution. Approaches to capture the varying noise level - avoiding the often not feasible measurement repetitions - range from: noise statistics based on pseudo replica [Robson et al., 2008] to SNR scaled reconstruction [Kellman and McVeigh, 2005] to the recently proposed region of interest analysis by [Hansen et al., 2015]. In Cartesian parallel imaging acquisitions, an analytical formula to determine the non-uniform variation of noise and SNR in SENSE reconstructions is given in terms of the pixel-wise *coil geometry factor* (*g-factor*) [Pruessmann et al., 1999].

4.6.1. The SENSE g-factor

The image reconstruction process governs the transfer of data noise into image noise. In SENSE, image reconstruction consists of finding the reconstruction matrix \check{F} according to the desired spatial response. In order to investigate image noise, the effect of \check{F} onto sample noise is regarded. The ratio between full- and sub-Nyquist-sampled acquisitions guides the definition of the *coil geometry factor* (*g-factor*) [Pruessmann et al., 1999].

Proposition 4.6.5. For the reconstruction matrix $\check{F} \in \mathbb{C}^{N_{\text{pix}} \times N_{\text{smp}}N_{\text{coils}}}$, the image noise covariance matrix is obtained by $\hat{\Psi} = \check{F}\Psi\check{F}^H$.

Proof. Let $p, q \in \{1, \dots, N_{\text{pix}}\}$. In an unbiased reconstruction with zero-mean of the image noise, the respective image noise (co-)variance is given by

$$\sigma^2(\varepsilon_I(\mathbf{x}_p), \varepsilon_I(\mathbf{x}_q)) = \mathbb{E}[\varepsilon_I(\mathbf{x}_p)\varepsilon_I^*(\mathbf{x}_q)] \quad (4.32)$$

- which relates to the data noise (co-)variances by reconstruction matrix \check{F} -

$$= \mathbb{E} \left[\left(\sum_{\alpha,k} \check{F}_{p,(\alpha,k)} \varepsilon_d(\mathbf{k}_k, \alpha) \right) \left(\sum_{\beta,l} \check{F}_{q,(\beta,l)} \varepsilon_d(\mathbf{k}_l, \beta) \right)^* \right]. \quad (4.33)$$

By linearity of deriving the mean, this is equal to

$$= \sum_{\alpha,k} \sum_{\beta,l} \check{F}_{p,(\alpha,k)} \mathbb{E}[\varepsilon_d(\mathbf{k}_k, \alpha) \varepsilon_d^*(\mathbf{k}_l, \beta)] (\check{F}_{q,(\beta,l)})^*, \quad (4.34)$$

which using Prop. 4.6.4 becomes

$$= \sum_{\alpha,\beta,k} \check{F}_{p,(\alpha,k)} \sigma^2(\varepsilon_d(\mathbf{k}_k, \alpha), \varepsilon_d(\mathbf{k}_k, \beta)) (\check{F}_{q,(\beta,k)})^* \quad (4.35)$$

$$= \sum_{\alpha,\beta,k} \check{F}_{p,(\alpha,k)} (\Psi)_{\alpha,\beta} (\check{F}_{q,(\beta,k)})^*. \quad (4.36)$$

Hence, for the overall image noise covariance matrix follows

$$\hat{\Psi} = \check{F} \Psi \check{F}^H, \quad (4.37)$$

which concludes the proof. \square

The result of Prop. 4.6.5 justifies the formulation of the inverse problem of sensitivity encoding while minimizing the image noise variances as presented in (4.11). For the weak approach presented in (4.11), the image noise covariance matrix can be expressed solely based on the encoding matrix and the sample noise covariance matrix.

Proposition 4.6.6. *In the weak approach, where the spatial response is sought to be a delta distribution, the Moore-Penrose pseudo inverse solution (cf. 4.12) implies $\hat{\Psi} = (\check{E}^H \Psi^{-1} \check{E})^{-1}$ (cf. [Pruessmann et al., 1999]).*

Proof. In the weak approach, the solution of the inverse problem of (4.12) is given by

$$\check{F}^\dagger = (\check{E}^H \Psi^{-1} \check{E})^{-1} \check{E}^H \Psi^{-1}. \quad (4.38)$$

Hence, for the image noise covariance matrix follows

$$\hat{\Psi} = \check{F}^\dagger \Psi (\check{F}^\dagger)^H \quad (4.39)$$

$$= (\check{E}^H \Psi^{-1} \check{E})^{-1} \check{E}^H \Psi^{-1} \Psi \left((\check{E}^H \Psi^{-1} \check{E})^{-1} \check{E}^H \Psi^{-1} \right)^H. \quad (4.40)$$

Reducing $\Psi^{-1} \Psi = \mathbb{1}_{N_{\text{smpl}} N_{\text{coils}}}$ in the equality and reformatting the Hermitian transpose implies further that

$$\hat{\Psi} = (\check{E}^H \Psi^{-1} \check{E})^{-1} \left((\check{E}^H \Psi^{-1} \check{E})^{-1} \check{E}^H \Psi^{-1} \check{E} \right)^H = (\check{E}^H \Psi^{-1} \check{E})^{-1}. \quad (4.41)$$

\square

The sensitivity encoding kernel functions presented in Def. 4.3.1, which constitute elements of the encoding matrix \tilde{E} , are not orthogonal. Hence, the inverse problem (cf. 4.11) is ill-conditioned, leading to noise enhancements imposed by the reconstruction matrix \tilde{F} [Pruessmann et al., 1999, Pruessmann, 2006]. Since the reconstruction matrix \tilde{F} is generally not unitary, spatially varying image noise with spatial correlations occurs. The ratio between a full- and sub-Nyquist-sampled acquisition reveals characteristics of parallel imaging.

Proposition 4.6.7. *Let $\hat{\Psi}^{\text{full}} \in \mathbb{C}^{N_{\text{pix}} \times N_{\text{pix}}}$ and $\hat{\Psi}^{\text{sub}} \in \mathbb{C}^{N_{\text{pix}} \times N_{\text{pix}}}$ denote the image noise covariance matrices of the full- and sub-Nyquist-sampled scenario. Then, for each $p = 1, \dots, N_{\text{pix}}$, the following holds:*

$$\frac{\sqrt{\hat{\Psi}^{\text{sub}}_{pp}}}{\sqrt{\hat{\Psi}^{\text{full}}_{pp}}} = \sqrt{R} \sqrt{\left[\left(\check{C}_p^{\text{fold}H} \Psi_{\text{coils}}^{-1} \check{C}_p^{\text{fold}} \right)^{-1} \right]_{pp} \left[\left(\check{C}_p^{\text{fold}H} \Psi_{\text{coils}}^{-1} \check{C}_p^{\text{fold}} \right) \right]_{pp}}.$$

Proof. Let $p \in \{1, \dots, N_{\text{pix}}\}$. Relevant for the reconstruction of pixel information at pixel position p in the sub-Nyquist sampled acquisition is the unfolding process governed by

$$C_p^{\text{unfold}} \hat{\mathbf{I}}_p^{\text{fold}} = \left(\check{C}_p^{\text{fold}H} \Psi_{\text{coils}}^{-1} \check{C}_p^{\text{fold}} \right)^{-1} \check{C}_p^{\text{fold}H} \Psi_{\text{coils}}^{-1} \hat{\mathbf{I}}_p^{\text{fold}}. \quad (4.42)$$

An inverse discrete Fourier transform is performed, as outlined for the derivation of (4.16). Therefore, with the respective scaling according to the zero-filled data and with the result of Prop. 4.6.6 follows for the image noise covariance matrix:

$$\sqrt{\hat{\Psi}_{p,p}^{\text{sub}}} = \frac{1}{\sqrt{N_{\text{smp}}}} \sqrt{\left[\left(\check{C}_p^{\text{fold}H} \Psi_{\text{coils}}^{-1} \check{C}_p^{\text{fold}} \right)^{-1} \right]_{p,p}} \quad (4.43)$$

In a full-Nyquist-sampled acquisition, the matrix corresponding to C_p^{unfold} is a single vector of coil sensitivities ($\in \mathbb{C}^{N_{\text{coils}}}$), projecting the modeled magnetization value onto each coil: hence, effectively, $C_p^{\text{full,unfold}} = C_p^{\text{unfold}}$. According to Prop. 4.6.6, the respective image noise covariance matrix then yields

$$\sqrt{\hat{\Psi}_{p,p}^{\text{full}}} = \frac{1}{\sqrt{N_{\text{smp}} R}} \sqrt{\left[\left(\check{C}_p^{\text{fold}H} \Psi_{\text{coils}}^{-1} \check{C}_p^{\text{fold}} \right)^{-1} \right]_{p,p}}. \quad (4.44)$$

Therefore, the ratio between both is derived by

$$\frac{\sqrt{\hat{\Psi}_{pp}^{\text{sub}}}}{\sqrt{\hat{\Psi}_{pp}^{\text{full}}}} = \sqrt{R} \sqrt{\left[\left(\check{C}_p^{\text{fold}H} \Psi_{\text{coils}}^{-1} \check{C}_p^{\text{fold}} \right)^{-1} \right]_{p,p} \left[\left(\check{C}_p^{\text{fold}H} \Psi_{\text{coils}}^{-1} \check{C}_p^{\text{fold}} \right) \right]_{p,p}}, \quad (4.45)$$

which concludes the proof. \square

Proposition 4.6.7 depicts the general loss of SNR due to undersampling by reduction factor R , as well as the SENSE reconstruction dependent additional variation for each pixel. The latter thereby highly depends on the (dis-)similarities between coil sensitivities of different coils and is thus referred to as the *coil's geometry factor (g-factor)*.

Definition 4.6.8 (g-factor). *The coil geometry factor (g-factor) captures the additional pixel-dependent image noise standard deviation differences arising in a sub-Nyquist-sampled acquisition compared to full-Nyquist sampling. The g-factor is defined pixel-wise by*

$$g_{\mathbf{x}_p} = \frac{\text{SNR}_{\mathbf{x}_p}^{\text{full}}}{\sqrt{R} \text{SNR}_{\mathbf{x}_p}^{\text{sub}}}, \quad \text{for each } p = 1, \dots, N_{\text{pix}}.$$

Corollary 4.6.9 (SENSE g-factor). *Assuming artifact-free image reconstruction, the g-factor in Cartesian SENSE is given by*

$$g_{\mathbf{x}_p} = \sqrt{\left[\left(\check{C}_p^{\text{fold}H} \Psi_{\text{coils}}^{-1} \check{C}_p^{\text{fold}} \right)^{-1} \right]_{p,p} \left[\left(\check{C}_p^{\text{fold}H} \Psi_{\text{coils}}^{-1} \check{C}_p^{\text{fold}} \right) \right]_{p,p}}.$$

The validity of the SENSE g-factor of Cor. 4.6.9 follows from Prop. 4.6.7. Note that noise potentially present in the derived sensitivity data is often omitted for two reasons: 1. spatial variations in sensitivity values are assumed to vary slowly, hence low-resolution acquisitions suffice for estimation which yields benign SNR characteristics 2. noise variance can be further reduced by spatial smoothing.

4.6.2. The GRAPPA g-factor

The image reconstruction process in GRAPPA yields an estimation of Nyquist-sampled data for each coil. The respective coil images are subsequently combined according to the chosen coil combination method. In order to analyze image noise, the effect of the reconstruction weights in image space $\left\{ W_{\alpha,\beta}^{2D}, \beta = 1, \dots, N_{\text{coils}} \right\}$ for reconstruction of coil image \hat{I}_α according to (4.30) is investigated. The coil combination weightings further impact image noise in the combined image \hat{I} . Again, the ratio between a full- and sub-Nyquist-sampled image reconstructions leads to the derivation of the GRAPPA g-factor for *uncombined* as well as *combined* images [Brau et al., 2008, Breuer et al., 2009].

Assuming additive noise, let I_α^{sub} and $\varepsilon_{I_\alpha}^{\text{sub}} := \varepsilon_I^{\text{sub}}(\cdot, \alpha)$ depict the pure image and noise part, respectively, of the reconstructed image $\hat{I}_\alpha^{\text{sub}}$ of coil α . Then the reconstruction in image space (cf. 4.30) relates the resulting image noise $\varepsilon_{I_\alpha}^{\text{sub}}$ to the zero-filled Fourier reconstruction of data noise $\varepsilon_{I_\beta}^{\text{fold}} := \varepsilon_I^{\text{fold}}(\cdot, \beta)$ by

$$\hat{I}_\alpha^{\text{sub}} = I_\alpha^{\text{sub}} + \varepsilon_{I_\alpha}^{\text{sub}} = \sum_{\beta \in \mathcal{C}} W_{\alpha,\beta}^{2D} \odot \left(I_\beta^{\text{fold}} + \varepsilon_{I_\beta}^{\text{fold}} \right). \quad (4.46)$$

Definition 4.6.10. *Analogous to Def. 4.6.2, define the receive coil covariance matrix in image space by $\hat{\Psi}_{\text{coils}} \in \mathbb{C}^{N_{\text{coils}} \times N_{\text{coils}}}$ with elements $\left(\hat{\Psi}_{\text{coils}} \right)_{\beta\gamma} := \sigma^2(\varepsilon_I^{\text{fold}}(\mathbf{x}_p, \beta), \varepsilon_I^{\text{fold}}(\mathbf{x}_p, \gamma))$.*

Proposition 4.6.11. *Let $\left\{ W_{\alpha,\beta}^{2D} \in \mathbb{C}^{N_x \times N_y}, \beta = 1, \dots, N_{\text{coils}} \right\}$ be the set of GRAPPA weights in image space for target coil α . Let $p \in \{1, \dots, N_{\text{pix}}\}$ and let $\hat{\Psi}_{\text{coils}} \in \mathbb{C}^{N_{\text{coils}} \times N_{\text{coils}}}$ be the receive coil covariance matrix in image space. Given the image pixel $\mathbf{x}_p = (x_p, y_p)$, define the matrix $W_{\mathbf{x}_p} \in \mathbb{C}^{N_{\text{coils}} \times N_{\text{coils}}}$ by $(W_{\mathbf{x}_p})_{\alpha\beta} = W_{\alpha,\beta}^{2D}(x_p, y_p)$. Then the image noise variance of the image pixel is derived by*

$$\sigma^2(\varepsilon_I^{\text{sub}}(\mathbf{x}_p, \alpha)) = \left| W_{\mathbf{x}_p} \hat{\Psi}_{\text{coils}} W_{\mathbf{x}_p}^H \right|_{\alpha\alpha}.$$

Proof. Let $p \in \{1, \dots, N_{\text{pix}}\}$. Assume an unbiased image reconstruction to provide a zero-mean of image noise. According to (4.46), the image noise variance of the corresponding pixel $\mathbf{x}_p = (x_p, y_p)$ yields

$$\sigma^2(\varepsilon_I^{\text{sub}}(\mathbf{x}_p, \alpha)) = \mathbb{E}[\varepsilon_I(\mathbf{x}_p, \alpha) \varepsilon_I(\mathbf{x}_p, \alpha)^*] \quad (4.47)$$

- which relates to the data noise variance introduced by the GRAPPA image space weights $W_{\alpha,\beta}^{2D}$
-

$$= \mathbb{E} \left[\left(\sum_{\beta} W_{\alpha,\beta}^{2D}(\mathbf{x}_p) \varepsilon_I^{\text{fold}}(\mathbf{x}_p, \beta) \right) \left(\sum_{\gamma} W_{\alpha,\gamma}^{2D}(\mathbf{x}_p) \varepsilon_I^{\text{fold}}(\mathbf{x}_p, \gamma) \right)^* \right]. \quad (4.48)$$

By linearity of deriving the mean, this is equal to

$$= \sum_{\beta} \sum_{\gamma} W_{\alpha,\beta}^{2D}(\mathbf{x}_p) \mathbb{E} \left[\varepsilon_I^{\text{fold}}(\mathbf{x}_p, \beta) \varepsilon_I^{\text{fold}}(\mathbf{x}_p, \gamma)^* \right] W_{\alpha,\gamma}^{2D}(\mathbf{x}_p)^*, \quad (4.49)$$

which using Prop. 3.3.27 and Prop. 4.6.4 becomes

$$= \sum_{\beta,\gamma} W_{\alpha,\beta}^{2D}(\mathbf{x}_p) \left(\hat{\Psi}_{coils} \right)_{\beta,\gamma} W_{\alpha,\gamma}^{2D}(\mathbf{x}_p)^* \quad (4.50)$$

$$= \left| W_{\mathbf{x}_p} \hat{\Psi}_{coils} W_{\mathbf{x}_p}^H \right|_{\alpha\alpha}. \quad (4.51)$$

which concludes the proof. \square

Remark 4.6.12. Please note that in order to provide uniform argumentation for SENSE and GRAPPA, the proof of Prop. 4.6.11 differs significantly from the reasoning presented in [Breuer et al., 2009]. The same line of argument is further utilized in Chapter 6.

Proposition 4.6.13. Let $\sigma^2 \left(\varepsilon_I^{\text{full}}(\mathbf{x}_p, \alpha) \right)$ and $\sigma^2 \left(\varepsilon_I^{\text{sub}}(\mathbf{x}_p, \alpha) \right)$ denote the image noise variance of pixel \mathbf{x}_p and coil α for the full- and sub-Nyquist-sampled scenario. Then

$$\frac{\sigma \left(\varepsilon_I^{\text{sub}}(\mathbf{x}_p, \alpha) \right)}{\sigma \left(\varepsilon_I^{\text{full}}(\mathbf{x}_p, \alpha) \right)} = \sqrt{R} \frac{\sqrt{\left| W_{\mathbf{x}_p} \hat{\Psi}_{coils} W_{\mathbf{x}_p}^H \right|_{\alpha\alpha}}}{\sqrt{\left| \hat{\Psi}_{coils} \right|_{\alpha\alpha}}},$$

for each $p = 1, \dots, N_{\text{pix}}$ and for each $\alpha = 1, \dots, N_{\text{coils}}$.

Proof. Let $p \in \{1, \dots, N_{\text{pix}}\}$. Following Prop. 4.6.11, the standard deviation in case of the undersampled acquisition is given by

$$\sqrt{\left| W_{\mathbf{x}_p} \hat{\Psi}_{coils} W_{\mathbf{x}_p}^H \right|_{\alpha\alpha}}, \quad (4.52)$$

where $\hat{\Psi}_{coils}$ arises from the undersampling scenario. In case of full Nyquist-sampled acquisition with Fourier reconstruction, the R -times increased sampling and solely incorporating Fourier reconstruction leads to

$$\sigma \left(\varepsilon_I^{\text{full}}(\mathbf{x}_p, \alpha) \right) = \frac{1}{\sqrt{R}} \sqrt{\left| \hat{\Psi}_{coils} \right|_{\alpha\alpha}}. \quad (4.53)$$

Therefore, the image noise standard deviation in pixel \mathbf{x}_p is derived by

$$\frac{\sigma \left(\varepsilon_I^{\text{sub}}(\mathbf{x}_p, \alpha) \right)}{\sigma \left(\varepsilon_I^{\text{full}}(\mathbf{x}_p, \alpha) \right)} = \sqrt{R} \frac{\sqrt{\left| W_{\mathbf{x}_p} \hat{\Psi}_{coils} W_{\mathbf{x}_p}^H \right|_{\alpha\alpha}}}{\sqrt{\left| \hat{\Psi}_{coils} \right|_{\alpha\alpha}}}. \quad (4.54)$$

\square

The *uncombined GRAPPA g-factor* in accordance with Def. 4.6.8 follows from Prop. 4.6.13.

Corollary 4.6.14 (uncombined GRAPPA g-factor). *Assuming artifact-free image reconstruction, the uncombined g-factor in Cartesian GRAPPA is defined by*

$$g_{\mathbf{x}_p, \alpha} = \frac{\sqrt{\left| W_{\mathbf{x}_p} \hat{\Psi}_{coils} W_{\mathbf{x}_p}^H \right|_{\alpha\alpha}}}{\sqrt{\left| \hat{\Psi}_{coils} \right|_{\alpha\alpha}}}.$$

Coil combination of the individual coil images is performed according to the method of choice, e.g. Roemer combination, combination by root sum of squares or adaptive combination (Sec. 4.1). Let $\{p_\alpha^{2D}, \alpha = 1, \dots, N_{coils}\}$ denote the coil weightings according to the chosen coil combination method. The combined reconstructed image is then described by

$$\hat{f}^{sub} = \sum_{\alpha \in \mathcal{C}} p_\alpha^{2D} \odot \left(\sum_{\beta \in \mathcal{C}} W_{\alpha, \beta}^{2D} \odot \hat{f}_\beta^{fold} \right). \quad (4.55)$$

Hence, the coil combination weighting simply extends the GRAPPA weighting. Analogous to Cor. 4.6.14, the combined GRAPPA g-factor is obtained.

Corollary 4.6.15 (GRAPPA g-factor). *Assuming artifact-free image reconstruction, the combined g-factor in Cartesian GRAPPA is defined by*

$$g_{\mathbf{x}_p} = \frac{\sqrt{\left| \left(\mathbf{p}_{\mathbf{x}_p}^T W_{\mathbf{x}_p} \right) \hat{\Psi}_{coils} \left(\mathbf{p}_{\mathbf{x}_p}^T W_{\mathbf{x}_p}^H \right) \right|}}{\sqrt{\left| \left(\mathbf{p}_{\mathbf{x}_p}^T \mathbf{1} \right) \hat{\Psi}_{coils} \left(\mathbf{p}_{\mathbf{x}_p}^T \mathbf{1} \right) \right|}},$$

where $\mathbf{p}_{\mathbf{x}_p}$ is the vector of respective coil weightings and $\mathbf{1}$ denotes a vector of ones.

Note that the potential of noise arising in the derived reconstruction weights is commonly omitted, since the weights are derived in a least-squares-optimization based on a sufficiently high number of training relations. As a result the noise level of the weights is very low and the noise in the weights can often be ignored.

4.6.3. Summary of g-factors

The g-factor framework facilitates the analytical derivation of image noise variance in standard parallel imaging scenarios, e.g. SENSE and GRAPPA reconstructions. Whereas image SNR in Fourier reconstruction depends solely on the k-space extent covered and is mutually uncorrelated, the image SNR in parallel imaging depends furthermore on the pixel-wise g-factor. As a consequence, image SNR in parallel imaging varies spatially and is correlated across pixels.

4.7. Parallel imaging and sub-Nyquist sampled EPI

Echo planar imaging (EPI) suffers from a number of artifacts. Among these are signal cancellations and geometric distortions due to differences in in-plane susceptibilities as well as an

inherent image blurring due to relaxation effects (cf. Sec. 3.4.2). A main reason for artifacts in EPI is the long readout period with a low bandwidth in the phase encoding direction. Parallel imaging offers a reduction of readout times with faster k-space velocity in the phase encoding direction. Therefore, it has the potential to alleviate in-plane susceptibility artifacts, geometric distortion and image blurring in EPI.

With sub-Nyquist-sampling along the phase encoding direction at reduction factor R , the same k-space extent is traversed R -times faster with larger blip gradients. Consequently, the echo train length is R -times shorter. Figure 4.3 illustrates how the timing of full- and sub-Nyquist sampling along the blipped phase encoding direction relates to signal magnitudes governed by T_2^* -decay.

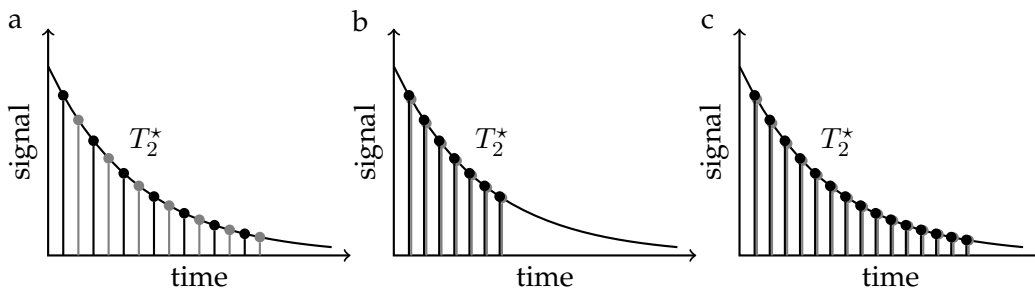


Figure 4.3: Parallel imaging achieves reduced readout lengths in EPI while maintaining or even increasing spatial resolution. Compared to a full-Nyquist-sampled scenario (a) with fixed echo spacing, either the same k-space extent is reached within an R th part of the readout time (b) or the R -fold range is covered in the same time interval (c). R is equal to 2 in the example. (A similar illustration is shown in [Griswold et al., 1999].)

Previous research on sub-Nyquist sampled EPI

Relatively early, the beneficial effects - besides g-factor penalties - of parallel imaging for EPI acquisitions were studied based on simulations, phantom and in vivo measurements using the SMASH approach [Griswold et al., 1999]. Increased spatial resolution and decreased geometric distortion were observed in sub-Nyquist-sampling ($R = 2$) scenarios with doubled matrix sizes. Notwithstanding, the decrease in SNR was noted as well. Interestingly, potential implications of parallel imaging for EPI were also already discussed in [Carlson and Minemura, 1993].

Main principles stated in [Griswold et al., 1999] directly apply for single-shot MRI scenarios incorporating other parallel imaging methods, of which various have been investigated. Possibilities to enhance EPI using SENSE have been explored in a range of applications, comprising diffusion-weighted imaging [Bammer et al., 2001, Bammer et al., 2002] and functional MRI (fMRI) measurements [Golay et al., 2000, de Zwart et al., 2002, Preibisch et al., 2003, Schmidt et al., 2005]. Opportunities for GRAPPA in the context of EPI have been considered for continuous arterial spin labeling (ASL) [Wang et al., 2005b], in dynamic susceptibility contrast (DSC) perfusion imaging [Newbould et al., 2006], and in fMRI experiments [Lütcke et al., 2006, Mintzopoulos et al., 2008, Preibisch et al., 2008]. A comparison between GRAPPA and SENSE in EPI acquisitions was performed by [Skare et al., 2007, Preibisch et al., 2008], in which GRAPPA was observed to provide more robustness against effects of motion and off-resonances. Recently, further developments on increasing motion robustness in EPI with GRAPPA were presented [Baron and Beaulieu, 2016].

Limitations reported for sub-Nyquist sampled parallel EPI

With sub-Nyquist-sampled parallel EPI, an improvement of spatial resolution and a reduction of geometric distortion was noticeable in the various parallel imaging methods. However, the benign effects of the shortened readout was accompanied by a substantial loss in image SNR, due to the parallel imaging reconstruction inherent g-factor penalty. This loss of SNR is further exacerbated at higher reduction factors. The latter are essential to achieve a notable decrease of inherent EPI artifacts. In previous applications of parallel imaging, reduction factors less or equal to $R = 4$ were utilized, in the majority of cases, a reduction factor of $R = 2$ or $R = 3$ was used. The SNR loss for $R = 3$ often already exceeded acceptable limits [Lütcke et al., 2006, Preibisch et al., 2008]. Furthermore, dependencies of the type of trajectory onto the imaging performance were observed [Skare et al., 2007], as well as how the parallel imaging method is employed in the reconstruction scheme [Preibisch et al., 2008, Schmiedeskamp et al., 2012].

Time-resolved parallel imaging methods of dynamic MRI have the potential to resolve the SNR limitations of standard parallel imaging in EPI. Dynamic MRI is discussed in the subsequent chapter and EPI is described for its clinical application of cerebral perfusion. The more benign g-factors for time-resolved parallel imaging methods are content of Chapter 6. The g-factor as derived in Sec. 4.6 thereby constitutes the basis for the time-resolved considerations. Chapter 7 then demonstrates the investigations of time-resolved parallel imaging in k-t-sub-Nyquist sampled EPI.

Chapter 5

Dynamic magnetic resonance imaging

For spatial encoding, a set of Fourier coefficients is sampled to obtain a single image. In order to capture dynamic changes of the imaged object, the image acquisition process has to be repeated to obtain a series of snapshot images. *Dynamic MRI* comprises monitoring signal evolution over time by acquisition of a series of images. The purpose is to capture physiological motion, functional changes or for instance, the dynamics of the arrival and passage of an injection of contrast agent.

In this chapter, the concepts of (static) image acquisitions are extended to the serial measurements of dynamic MRI. The concept of sampling in k-t-space (Sec. 5.1) and Fourier reconstruction of time series of images (Sec. 5.2) is described. Sub-Nyquist sampling patterns are extended to k-t-sub-Nyquist sampling patterns in k-t-space (Sec. 5.3). The *time-resolved* data acquisition can be likewise combined with *time-resolved* parallel imaging, as is described in Sec. 5.4. Whereas the coil sensitivity domain enhances spatial encoding, the additional dimension of time frames enriches reconstruction based on exploiting temporal correlations. An overview of *time-resolved parallel imaging* approaches is briefly stated and the core method of this thesis, k-t-GRAPPA [Huang et al., 2005, Jung et al., 2008, Jung et al., 2011], is described. The application of EPI for dynamic MRI in the clinical context of *dynamic susceptibility contrast* (DSC) weighted cerebral perfusion imaging concludes this chapter (Sec. 5.5).

5.1. Concept and sampling of k-t-space

For dynamic MRI, the concept of k-space is extended by the domain of imaged time frames and is then referred to as *k-t-space* [Xiang and Henkelman, 1993].

The time-dependent MR signal $s(t)$ can be described - independent of time - in terms of k-space locations. In *static* MRI, a single image is acquired over a certain time interval by collecting a set of Fourier samples. During this time interval, the object-motion and internal dynamics are assumed to be approximately static and only relaxation influences are considered in the contrast mechanism.

In *dynamic* MRI, k-space data sets for several temporal stages of the object are collected in a serial order. A beating heart, for instance, is thereby captured in a series of snapshot images. The repeated acquisition of images is described by *outer* time frames $t = 1, \dots, N_{\text{time}}$ of the t^{th} time interval of image acquisition. This extends data samples from multiple coil elements

(cf. 3.16/4.1), as follows:

$$d_{n,t,\alpha} = \int_V c_\alpha(\mathbf{r}) m_\perp(\mathbf{r}, 0, t) \exp(-i\mathbf{k}_n \cdot \mathbf{r}) d\mathbf{r},$$

(5.1)

for each k-space sample $n \in \{1, \dots, N_{\text{smp}}\}$,
for each coil $\alpha \in \{1, \dots, N_{\text{coils}}\}$,
for each time frame $t \in \{1, \dots, N_{\text{time}}\}$.

Figure 5.1 illustrates how the time-dependent MR signal $\tilde{s}(\mathbf{k}) \equiv s(t)$ (cf. 3.12) is repeatedly sampled along the different k-space positions. All samples within one *inner* temporal acquisition window are assigned to the same k-space data set. The time series of all k-space data sets reflect the temporal evolution according to *outer* time frames. Thereby, the set of sampled k-space coordinates in comparing two time frames do not have to be identical. Following the concept of k-space, sampling in *k-t-space* then simply yields a partition of the trajectory into equivalence classes.

Definition 5.1.1 (sampling in k-t-space). Let $\{\mathbf{k}_n := \mathbf{k}(t_n)\}_{n=1}^{N_{\text{smp}}^{\text{total}}}$ be a set of visited k-space points of $N_{\text{smp}}^{\text{total}}$ samples over the time interval $[\tau_1, \tau_{N_{\text{time}}+1}]$ of acquisition. Consider a partition $\tau_1 < \tau_2 < \dots < \tau_{N_{\text{time}}+1}$ which divides the overall acquisition time into N_{time} time intervals. Relating sampled k-space points within the same time interval accordingly facilitates the following definition

$$\mathcal{K}_{\text{smp}} \times \mathcal{T} := \{(\mathbf{k}_{n_t}, t) \mid t = 1, \dots, N_{\text{time}} \text{ and } n_t \in [\tau_t, \tau_{t+1}]\},$$

(5.2)

where \mathcal{T} denotes the set of time frames. The set $\mathcal{K}_{\text{smp}} \times \mathcal{T}$ denotes the **sampling in k-t-space**.

Remark 5.1.2. The sampling of consecutive time frames is described here as strictly sequential. In cardiac dynamic MRI, however, k-space acquisitions are often segmented. Thereby, samples of the same time frame are acquired with intermissions, in which samples of other time frames are collected. Due to the periodicity of the beating heart, different k-space samples can be binned according to their relative acquisition time within the cardiac cycle. Definition 5.1.1 maintains meaningful, when time frames correspond to different heart phases of the cardiac cycle.

Sampling in k-t-space allows to define the *temporal resolution* as the sampling rate of time frames.

Definition 5.1.3 (temporal resolution). Consider the partition $\tau_1 < \dots < \tau_{N_{\text{time}}+1}$ of the total acquisition time interval $[\tau_1, \tau_{N_{\text{time}}+1}]$ of a dynamic MRI scenario as in Def. 5.1.1. Let Δt be the minimum length such that $\tau_{t+1} - \tau_t \leq \Delta t$, for all $t = 1, \dots, N_{\text{time}}$. Then the **temporal resolution** is defined with respect to Δt .

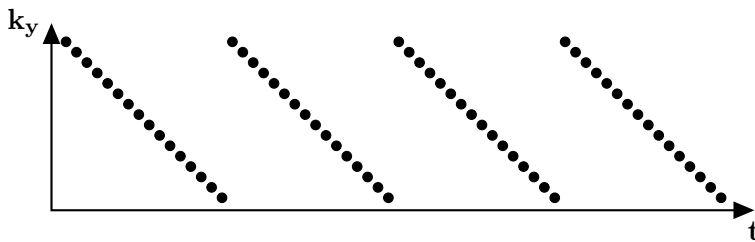


Figure 5.1: In dynamic MRI, the time-resolved MR signal is divided into equivalence classes to represent k-space sets with respect to different time frames.

Strictly speaking, the k-t-space concept requires motion to occur only between and not within time frames. In general this is not true and motion during the acquisition of one time frame (i.e. *intra-frame motion*), may lead to *motion artifacts*. Various approaches to correct for motion during the measurement exist ranging from simple averaging to cardiac triggering and prospective motion correction schemes, e.g. [Wood and Henkelman, 1986, Zaitsev et al., 2006, Maclaren et al., 2013]. A logical approach to better capture the *inter-frame motion* and to mitigate motion artifacts due to intra-frame motion is to increase the temporal resolution.

5.2. Fourier image reconstruction in dynamic MRI

Fourier reconstruction can be performed individually for each time frame. The limitations discussed in Sec. 3.3 directly apply. Yet, another practical limitation arises in dynamic MRI due to the idiosyncrasy of the encoding process and spatial resolution: a trade-off between spatial and temporal resolution. The more Fourier coefficients are acquired (for enhanced spatial resolution), the longer the intervals for repetition become, i.e. the lower the temporal resolution is. This extends the list of practical limitations of Fourier encoding and Fourier reconstruction in dynamic MRI by:

1. discrete (or frequency band-limited) data sampling
2. finite data sampling
3. negative correlation of signal-to-noise and spatial resolution
4. negative correlation of spatial and temporal resolution

Increasing temporal resolution imposes limitations on the spatial resolution. Increasing spatial resolution necessitates a longer readout. Hence, increasing spatial resolution without violating the Nyquist theorem necessarily decreases the temporal resolution.

The time frames acquired in the dynamic MRI measurement form a discrete set. This requires the object's dynamics to be frequency band-limited (analogous to Thm 3.3.7), as to fulfill the Nyquist-Shannon criterion in the temporal domain. Therefore, in full-Nyquist-sampled dynamic Fourier encoding, the object's spatial extent and the frequency band of motion dictates the sampling scheme. In most applications, one cannot determine the sampling rate of time frames that is sufficient to obtain unaliased temporal information. Nevertheless, great similarity between neighboring time frames suggests a high redundancy in full-Nyquist sampling k-t-space data. This potentially allows for reduced data acquisition, when making correct assumptions in the reconstruction process.

5.3. Sub-Nyquist sampling in k-t-space

In the following, patterns for regular Cartesian sub-Nyquist sampling in k-t-space are discussed. Assuming k-space undersampling for each time frame by reduction factor R , the pattern can be shifted in consecutive time frames by $\Delta s \cdot \frac{2\pi}{FOV}$ (Thm. 3.3.7), for $\Delta s \in \{1, \dots, R-1\}$, in order to ensure the sampling of each k-space position on the Cartesian grid once within R consecutive time frames. Note that the temporal resolution as defined in Def. 5.1.3 of the k-space data sets is maintained, although the sampling intervals of each single k-space position is increased by R .

Examples of resulting k-t-undersampling patterns for different shifts at a reduction factor of $R = 5$ are depicted in Fig. 5.2. The third illustration in Fig. 5.2 has been shown to be a more benign sampling pattern [Tsao et al., 2003a] by solving the Euclidean packing problem. For better visibility, the frequency encoding direction is omitted and only time frames against phase encodings are shown. In the presented examples, a variable density acquisition with Nyquist sampled k-space center is displayed.

The regular k-t-space undersampling presented in Fig. 5.2 corresponds to patterns applied in this work, leaving open the choice of reduction factor as well as the usage of variable density sampling. How to exploit the correlations due to the additional time domain in combination with parallel imaging is discussed in the following section.

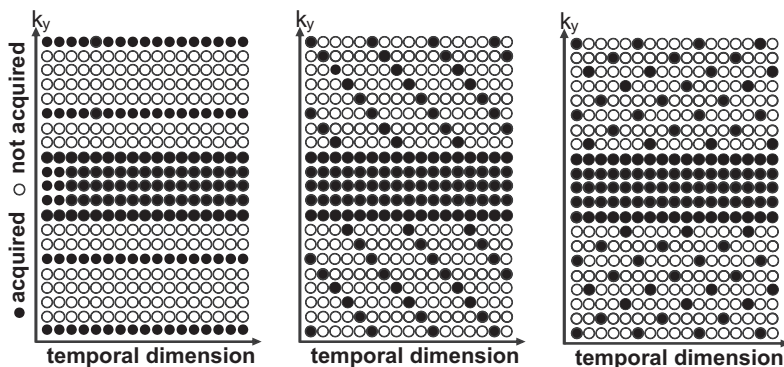


Figure 5.2: Variants of k-t-undersampling patterns at reduction factor $R = 5$ are depicted. The k_x -dimension - not displayed - lies perpendicular to the page. The k-space sampling pattern is shifted by $\Delta s = 0$ (left), $\Delta s = 1$ (middle) and $\Delta s = 2$ (right) for consecutive time frames.

5.4. Time-resolved parallel imaging

The k-t-sub-Nyquist sampled data of multiple receive coils in k-t-space is the basis of various approaches to solve the image reconstruction problem using sensitivity encoding as well as temporal correlations. A brief literature overview is given below (Sec. 5.4.1), followed by the presentation of k-t-GRAPPA (Sec. 5.4.2).

5.4.1. Literature overview: Time-resolved parallel imaging

Early implementations of utilizing correlations along the temporal domain were described as *view sharing techniques* [Riederer et al., 1988], or as *keyhole methods* [Van Vaals et al., 1993, Jones et al., 1993]. The latter comprises the acquisition of one Nyquist-sampled time frame followed by only updates in form of low-resolution data. However, the missing updates of high spatial frequency data constitutes the major drawback of keyhole methods [Hu, 1994]. Ideas to use random sampling patterns or to use block interpolation between time frames were introduced to address this problem [Parrish and Hu, 1995, Doyle et al., 1995].

Using the extended data information in the overall k-t-space was consolidated by considering the temporal frequency response of the imaged time series, as for instance in the *UNFOLD method* (UNaliasing by Fourier-encoding the Overlaps using the temporaL Dimension) by [Madore et al., 1999]. UNFOLD exploits the limited temporal bandwidth of many applications in dynamic MRI which entails a dense support in x-f-space (as the Fourier counterpart of the k-t-domain) of the spatio-temporal frequencies. Hence, by shifting the undersampling pattern along the temporal domain, the aliasing in the folded spatial information is spread along the temporal frequency domain according to the respective temporal frequency of the periodically

repeated undersampling patterns. The underlying true magnetization representation occurs around the zeroth temporal frequency component. Assuming the region of support in x - f -space to be known, the unaliased data can be simply extracted by a filter procedure [Tsao, 2002]. However, the UNFOLD approach depends on precise knowledge of the region of support and the undersampling induced replica to be strictly distinguishable. This limits the practicability of UNFOLD, since especially when moving to higher reduction factors, overlapping domains can hardly be avoided.

Based on the shifted sub-Nyquist-sampled data in the UNFOLD scheme, the view sharing technique can be applied using a *Sliding Window* approach as described in [d’Arcy et al., 2002]. Hereby, R consecutive sub-Nyquist-sampled k -space data sets are additively combined into a single full-Nyquist-sampled data set. The advantage of this procedure is that high spatial frequency information is also updated and that it does not rely on the knowledge of the region of support. The disadvantages, however, comprise the occurrence of artifacts due to mismatched k -space acquisitions and a decrease in temporal resolution by R .

All of the methods described so far exploit only temporal correlations. Each k -space data point is reconstructed independently of other k -space data points, as opposed to e.g. parallel imaging which also uses spatial correlations. The group of *time-resolved parallel imaging* approaches comprise methods which employ in addition to spatial also temporal correlations in the image reconstruction process.

A first approach of enhancing parallel imaging with temporal information originated in [Kellman et al., 2001a, Kellman et al., 2001b] and [Madore, 2001, Madore, 2002]. In *TSENSE*, [Kellman et al., 2001a] suggested to perform SENSE based on the shifted sub-Nyquist sampling followed by temporal filtering in x - f -space with the UNFOLD approach to reduce residual aliasing artifacts at reduction factor $R = 2$. The possibilities of artifact-suppression of UNFOLD to aid parallel imaging to achieve higher reduction factors was elaborated in *UNFOLD-SENSE* [Madore, 2002]. Additionally presented in [Kellman et al., 2001a], is an algorithm for adaptive estimations of sensitivities from temporally filtered sub-Nyquist-sampled time frames in a prior step. This idea was extended by acquisition of ACS data in *SHRUG* [Madore, 2004], where the GRAPPA-like autocalibration signal serves as a basis for sensitivity estimation.

The requirement of actual knowledge of the region of support was replaced with learning the needed temporal frequency information from a set of *training data* by [Tsao et al., 2003a]. In *k-t-BLAST* and *k-t-SENSE* [Tsao et al., 2003a], reconstruction is enhanced by the signal covariance matrix as estimated from the training data. Thereby, the training data set at low spatial resolution is assumed to sufficiently represent temporal variations within the time-resolved imaging scenario. Relative signal magnitudes are estimated and incorporated within the optimization problem as to balance data consistency with the estimated relative contribution. *k-t-SENSE* extends the idea of *k-t-BLAST* by incorporating coil sensitivities as well.

Subsequent to *SHRUG* and in analogy to *TSENSE*, *TGRAPPA* [Breuer et al., 2005b] enhances GRAPPA based parallel imaging reconstruction by exploiting the additional, temporal domain. In *TGRAPPA*, dynamic updates of the estimated GRAPPA reconstruction weights are obtained by additively combining the - in total - R adjacent time frames to form a Nyquist-sampled data set serving as temporally filtered ACS data for kernel calibration. Whereas *SHRUG* incorporated the acquisition of ACS data as part of every time frame, *TGRAPPA* solely works with the shifted sub-Nyquist-sampled data sets. As in *TSENSE* or *UNFOLD-SENSE*, the time domain is utilized to support the actual parallel imaging reconstruction. Further, the methods *KL-TSENSE* and *KL-TGRAPPA* [Ding et al., 2011] introduce an optimal linear filter employing the Karhunen-Loeve transform for estimating coil sensitivities or ACS data to improve *TSENSE* and *TGRAPPA*, respectively.

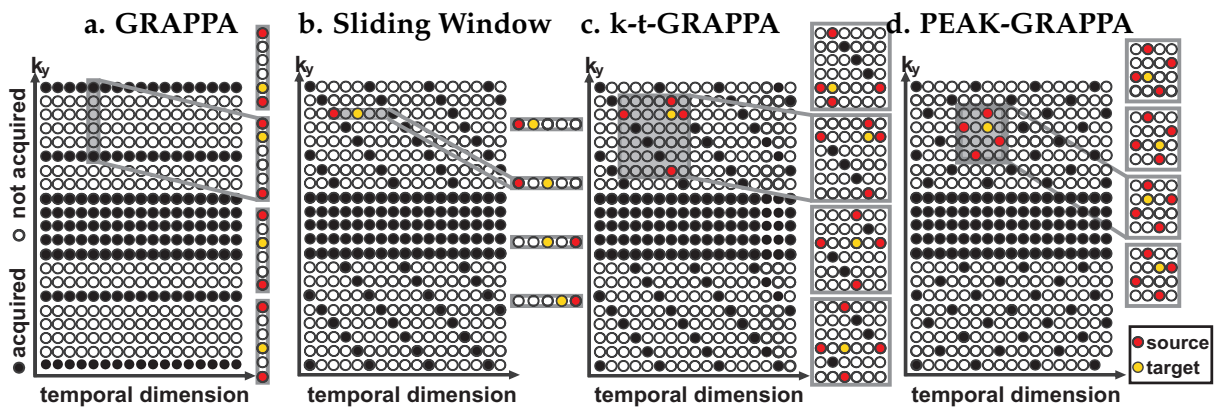


Figure 5.3: Four different reconstruction kernels approaches are illustrated for a reduction factor of $R = 5$: (a) non-time-resolved kernels for GRAPPA, (b) the only time-resolved SW kernels, and (c) time-resolved kernels for k - t -GRAPPA, as well as (d) for PEAK-GRAPPA.

As a further development of TGRAPPA, time-resolved GRAPPA based reconstruction kernels were proposed in k - t -GRAPPA [Huang et al., 2005]. Analogous to k - t -SENSE, k - t -GRAPPA is the k - t -space based counterpart which jointly utilizes spatio-temporal correlations in the reconstruction process. A practical analysis on the optimality of kernel geometries led to *parallel MRI with extended and averaged GRAPPA kernels (PEAK-GRAPPA)* [Jung et al., 2008, Jung et al., 2011].

A completely different methodological approach to consider the temporal domain in the image reconstruction is given by the concept of *partial separability (PS)* in the context of MRI, introduced by [Liang, 2007, Haldar and Liang, 2010]. Thereby, k - t -space data is mapped onto a data space of reduced dimensionality, in order to remove low variance information to enhance signal information. The mapping is based on the Karhunen-Loeve transform. Similarly in k - t -PCA [Pedersen et al., 2009], the principal components of the variation based on training data are derived and the estimated signal covariances based on the principal components are incorporated in the reconstruction process, as a further development of k - t -SENSE. These methods build a transition and directly merge into iterative approaches based on regularization using assumptions about the spatial and temporal correlations.

Central to the present work is the time-resolved GRAPPA based approach of k - t -GRAPPA and its optimization PEAK-GRAPPA. As both k - t -GRAPPA and PEAK-GRAPPA follow the same methodological idea, both methods are jointly referred to as k - t -GRAPPA. At higher reduction factors, an optimized PEAK-GRAPPA sampling pattern and reconstruction kernel is used, unless the original k - t -GRAPPA approach and PEAK-GRAPPA are explicitly compared with each other. k - t -GRAPPA is described in further detail in the subsequent section.

Time-resolved GRAPPA based parallel imaging facilitates reduced data acquisition while providing a robustness and a benign SNR behavior. Note that time-resolved parallel imaging methods were developed in the context of cardiac dynamic MRI which still constitutes its main application.

5.4.2. k-t-GRAPPA

k-t-GRAPPA exploits correlations in k-space as well as in the temporal domain. A *time-resolved* GRAPPA kernel geometry is defined comprising k-space neighbors as well as temporal adjacent data points. The number of targets and the kernel geometry depend on the k-t-undersampling pattern with respect to reduction factor R . Figure 5.3 depicts different undersampling patterns in k-t-space with defined kernel structures illustrated for k-t-GRAPPA as well as for the PEAK-GRAPPA kernels. A kernel geometry is defined for each of the $R - 1$ relative target spatial harmonics, as further drafted in Fig. 5.3. As for conventional GRAPPA, k-t-GRAPPA reconstruction consists of two steps:

1. calibration of the reconstruction weights given the Nyquist-sampled ACS data set
2. estimation of unacquired k-space data in each time frame by weighted linear combination of data at neighboring k-space locations and time points.

Calibration of the reconstruction weights is performed using the ACS data set. The ACS data is also time-resolved in k-t-GRAPPA, as opposed to conventional GRAPPA (Sec. 4.5.1). The ACS data is usually acquired by fully sampling the k-space center for each time frame, but can also be derived by adding R adjacent time frames as described in [Huang et al., 2005]. Source and target data points are collected in accordance with the chosen time-resolved GRAPPA kernel geometry. The GRAPPA kernel thereby incorporates B_{fe} , B_{pe} and B_t acquired samples as sources, along the two encoding dimensions and the temporal domain. The optimal weights in the least-squares sense to relate sources and targets in k-t-space are derived using the Moore-Penrose pseudo inverse. This solves the inverse problem of weight calibration (cf. 4.26). Whereas only source points within the same time frame are considered in conventional GRAPPA, source points are collected in three dimensions (frequency/phase encoding and time) for 2D-slice imaging with k-t-GRAPPA.

The *estimation of omitted k-space data* can be expressed as a convolution of the weights with the undersampled data. In the case of k-t-GRAPPA, a series of images is reconstructed based on the time-enhanced kernel geometries. Let $w_{\alpha,\beta}^{3D} \in \mathbb{C}^{B_{fe} \times R B_{pe} \times B_t}$ denote the weights (combined to a convolution kernel) in k-t-space for target coil α and source coil β . Let $d_{\beta}^{zf,3D}$ be the zero-filled acquired undersampled data of coil β in the same representation. A time series of reconstructed data for each coil is obtained by convolution of $w_{\alpha,\beta}^{3D}$ with $d_{\beta}^{zf,3D}$, i.e.

$$\hat{d}_{\alpha}^{sub,3D} = \sum_{\beta \in \mathcal{C}} w_{\alpha,\beta}^{3D} * d_{\beta}^{zf,3D}. \quad (5.3)$$

The final series of reconstructed images is obtained by Fourier reconstruction along the k-space dimensions and subsequent coil combination using either rSoS, Roemer or Walsh combination (Sec. 4.1). Thus, for coil combination weightings p_{α}^{3D} , for coils $\alpha = 1, \dots, N_{coils}$, image reconstruction yields

$$\hat{f}^{sub,3D} = \sum_{\alpha=1}^{N_c} p_{\alpha}^{3D} \odot \left(\mathcal{DFT}_{x,y}^{-1} \left\{ \hat{d}_{\alpha}^{sub,3D} \right\} \right). \quad (5.4)$$

Finite acquisition requires explicit treatment of k-space borders, as well as the first and last time frames, since the kernel structure necessarily exceeds the domain of acquired data samples. Usually, the source domain is artificially enlarged by either zero-filling or by assuming a periodic boundary condition.

The k-t-GRAPPA approach is - like GRAPPA - purely data-driven and does not require the derivation of sensitivity values. It relies on the k-space locality principle and k-space shift-invariance of the reconstruction weights. Furthermore, temporal correlations are assumed. As opposed to methods such as UNFOLD (see Sec. 5.4.1), k-t-GRAPPA does not require direct knowledge about the support of temporal frequencies.

Excluding correlations along the time dimension, k-t-GRAPPA becomes identical to conventional GRAPPA and the analogy to a Sliding Window (SW) approach is found by neglecting spatial correlations. However, k-t-GRAPPA cannot be expressed as a concatenation of those two methods, since the three-dimensional convolution kernel cannot be separated into a k-space and a temporal kernel. Since SW can be analogously formulated as based on a convolution kernel, differences between all methods k-t-GRAPPA, conventional GRAPPA and SW are pinned down to the different kernel dimensionality and the usage of coil sensitivities, as illustrated in Fig. 5.3. Note that the different coils are not shown in Fig. 5.3.

With k-t-GRAPPA, higher reduction factors can be achieved compared to conventional parallel imaging which act on each time frame separately. Both methods exhibit an improved noise behavior in comparison to conventional GRAPPA [Huang et al., 2005, Bauer et al., 2013]. [Jung and Kozerke, 2009] demonstrated significant differences in the noise treatment in cardiac applications of k-t-SENSE and k-t-GRAPPA. Whereas the k-space based method k-t-GRAPPA exhibits smooth noise enhancement over the range of images, k-t-SENSE shows greater noise enhancement in the area of motion and less noise in static areas. However, these are heuristic observations and are not supported by a theoretical analysis so far.

Summary of (time-resolved) parallel imaging

Parallel imaging, where spatial encoding is supplemented by locally varying coil sensitivity information, facilitates k-space sampling to the sub-Nyquist-regime with a reduction factor R , while maintaining image resolution. The omission of time-consuming phase encoding steps directly reduces the total acquisition time at a given spatial resolution. The reduction in scan time comes at the expense of a loss in SNR, arising from the reduced data aggregation as well as an additional penalty described by the g-factor. The noise amplification limits the applicability of parallel imaging methods such as GRAPPA and SENSE when moving to higher reduction factors.

In dynamic MRI, increasing spatial resolution of Fourier encoding limits the temporal resolution and vice versa. Dynamic MRI allows to extend parallel imaging by additionally exploiting correlations in the time domain. Here, undersampling in k-t-space with time-resolved parallel imaging provides the potential to improve the spatio-temporal resolution.

In the next chapter, a theoretical framework for a noise analysis of k-t-GRAPPA is developed which is equivalent to the g-factor formulation for conventional GRAPPA. The presented analysis was published in [Ramb et al., 2015a]. Furthermore, parameters shaping the different - yet similar - noise behavior of the GRAPPA versus the SENSE approach are investigated. The presented framework bridges noise analyses between image and k-space based as well as non-time-resolved and time-resolved parallel imaging methods.

5.5. Clinical applications of dynamic echo planar imaging

Echo planar imaging (EPI) is applied in diverse scientific and clinical context ranging from measurements of cerebral perfusion or diffusion, to angiography or myocardial perfusion, to investigations of brain activities referred to as functional MRI. In particular in the clinical context, EPI is still the most common imaging technique to achieve fast multi-slice coverage capturing functional morphological changes in the clinical context. In the scope of this thesis, EPI is applied for - but not limited to - dynamic susceptibility contrast (DSC) weighted cerebral perfusion imaging.

5.5.1. Dynamic susceptibility contrast weighted cerebral perfusion imaging

Cerebral perfusion MRI is nowadays part of the clinical routine in the assessment and diagnosis of tumoral, vascular or inflammatory diseases of the brain. Decreased perfusion is observed in patients with acute stroke (review of perfusion MRI in stroke patients in [Copen et al., 2011]), whereas increased perfusion is often perceived in brain tumors, due to enhanced capillary density and permeability. An overview of MR perfusion imaging in brain tumors can be found in [Covarrubias et al., 2004]. In both cases, the additional evaluation of the physiology, as targeted by cerebral perfusion MRI, provides more differentiated information to support the clinical diagnosis.

In the diagnosis and treatment of brain tumors, it is important to correctly grade the malignancy of the tumors. Whereas conventional anatomic MRI allows for a depiction with great detail, it does not reveal the tumor grade of the affected tissue. In all cases, a stereotactic or open biopsy has to be performed for histological estimation. It is therefore essential to identify the most aggressive tumorous area for sampling. Cerebral perfusion MRI has the potential to assist precise localization as well as detailed delineation of tumorous tissue.

For dynamic susceptibility contrasted (DSC) weighting, paramagnetic gadolinium (Gd) based contrast agent is injected into the vasculature system [Rosen et al., 1990, Rosen et al., 1991a, Rosen et al., 1991b]. The volume of contrast agent - referred to as bolus - is transported via the cardiopulmonary circulation to the brain. The interaction of paramagnetic Gd-chelate with its surrounding magnetized tissue induces susceptibility differences (Sec. 3.4.2) between the vessel structure and the adjacent tissue. This implies a shortening of T_2^* -decay rates and a strong signal decrease. Thus, the actual dynamic susceptibility contrast consists of a signal decrease, when the contrast agent arrives at the observed tissue, followed by a signal recovery when the contrast agent is washed out.

Dynamic susceptibility contrast is used in the context of cerebral perfusion measurements to derive hemodynamic parameters that support the classification of the state of perfused tissue. The shape and the amplitude of the signal dip depend on the amount and the magnetic properties of the contrast agent, as well as the distribution and density of the vessel structure and the TE [Fisel et al., 1991, Boxerman et al., 1995, Weisskoff et al., 1994, Østergaard, 2005]. Findings further imply that spin echo measurements are to some extent sensitive to the vessel sizes, which is not the case for GE based measurements. A review of main principles of DSC weighted cerebral perfusion as well as main methodologies are presented in [Østergaard, 2005, Østergaard et al., 1996b, Østergaard et al., 1996a]. Main concepts are briefly summarized here. Since GE based imaging is incorporated in this work, it is solely referred to T_2^* -decay rates in the following.

A central assumption in the derivation of perfusion parameters from DSC weighted acquisitions is the linkage of dynamic changes of $R_2^* = 1/T_2^*$ decay rates, $\Delta R_2^*(t)$, to the temporal variation of contrast agent concentration in the tissue, $C_t(t)$, as part of the tracer kinetic approach:

$$C_t(t) \propto \Delta R_2^*(t). \quad (5.5)$$

Experimental findings based on injections of different doses substantiate a close linear relationship between the amplitude of the dip and the concentration during the passage of contrast agent [Simonsen et al., 1999]. Based on this assumption, the monitored signal drop can be translated into a time-dependent indicator for contrast agent concentration within the proximity of the respective spatial origin. The concentration curve is derived based on an estimate of the mean baseline magnitude signal \hat{s}_0 and calculating ΔR_2^* by

$$C_t(t) \propto \Delta R_2^*(t) := -\ln\left(\frac{s(t)}{\hat{s}_0}\right)/TE, \quad (5.6)$$

The baseline signal \hat{s}_0 is usually estimated over the time interval after the signal has reached a steady state and before the arrival of contrast agent.

In DSC weighted cerebral perfusion measurements, the first passage of the bolus is dynamically imaged. EPI thereby typically serves as a fast imaging method to capture the contrast agent passage. The concentration time curve is then estimated for each pixel. The spatio-temporal resolution of the acquisition sets boundaries within this process. Figure 5.4 shows an example of reconstructed magnitudes and concentration time curve. The *time to peak*, the *bolus arrival time*, the *FWHM* and the *area under the curve* serve as indicators and can be directly deduced from the concentration curve. With further calculations, various perfusion parameters can be obtained such as **cerebral blood volume (CBV)**, cerebral blood flow (CBF) or mean transit time (MTT), of which CBV is the main concern in this work. For a detailed overview over perfusion parameters refer to [Østergaard et al., 1996b].

Cerebral blood volume (CBV)

A common model to derive CBV is given by the area under the concentration curve normalized to the first moment of the input concentration - referred to as arterial input function - for each pixel. Correct derivation of the arterial input function to obtain quantitative CBV values has been - and still is - a diversely discussed issue, e.g. [Calamante et al., 2002, van Osch et al., 2003, Kellner et al., 2013]. An estimate of relative CBV can be obtained by

$$CBV \propto \int \Delta R_2^*(t) dt. \quad (5.7)$$

This equation still holds without the normalization by the arterial input function. Integration is usually performed either solely over the first bolus passage or including the typical second bolus recirculation.

Careful consideration is required when integration is performed over the complete concentration curve and in the case of a non-intact blood-brain barrier. The latter is an epiphenomenon in some brain diseases. With a broken blood-brain barrier, contrast agent enters surrounding tissue compartments. Unexpected distributions of contrast agent into the tissue impairs the derivation of CBV, since T_1 is thereby artificially altered. This effect is termed T_1 leakage. Approaches to correct for T_1 leakage are manifold, ranging from mitigating the effect due to large TR and/or small flip angle acquisition, to retrospective correction based on acquisitions of multiple echoes, to post-processing methods using linear fits to estimate the rate

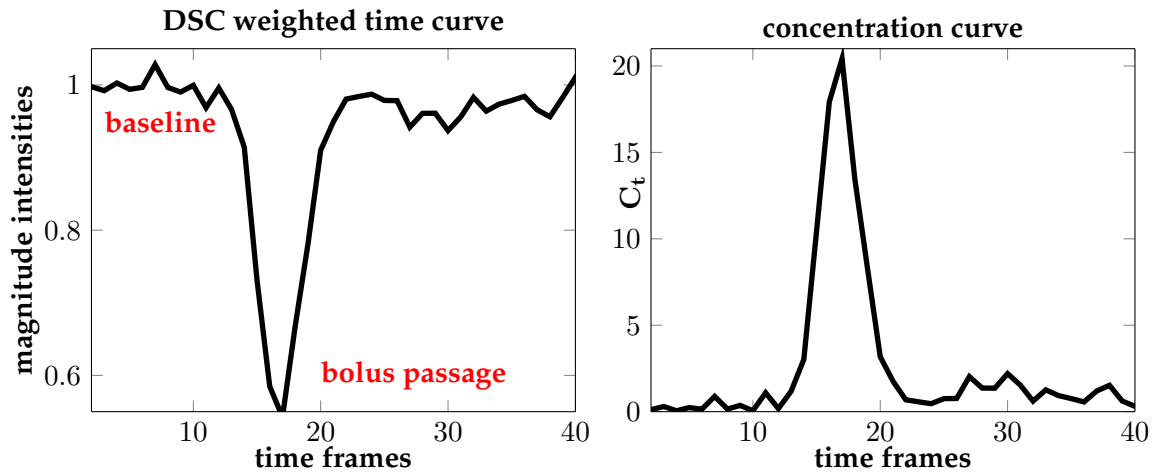


Figure 5.4: Time series of a single pixel as part of a DSC weighted cerebral perfusion measurement are shown: signal magnitudes (left) and the corresponding concentration curve (right). The baseline signal is reached in steady state and before bolus arrival. The subsequent bolus passage induces the typical signal dip of DSC weighted imaging.

of falsification, to doubled administration of contrast agent, e.g. [Schmiedeskamp et al., 2012, Boxerman et al., 2006, Hu et al., 2010, Paulson and Schmainda, 2008]. The considerations presented below therefore comprise the integration of solely the first bolus passage. Moreover, the repetition time TR is chosen to be as minimal as possible, yet large enough to avoid T_1 leakage corruption.

In the Chapter 7, k-t-sub-Nyquist sampled EPI is performed in the context of DSC-weighted cerebral perfusion measurements. The investigation of k-t-sub-Nyquist sampled EPI is motivated by the gained degrees of freedom in improving spatio-temporal resolution for clinical applications. This is particularly desirable for tumor assessment for an easier delineation of affected tissue.

Contributions of this thesis

Chapters 2-5 covered the MR imaging process from signal formation to Fourier encoding and parallel imaging reconstruction. The connection with more general concepts was described in Chapter 1. In contrast to most works on the subject of MRI, a mathematical language was emphasized - in particular in the description of Fourier imaging. Among the own contributions in these chapters is the equivalent theoretical expression of g-factors for SENSE and GRAPPA, as derived in Chapter 4.

The author's contribution in the following parts into two main topics that are united under the umbrella of k-t-sub-Nyquist sampled time-resolved parallel imaging. Chapters 6 and 7 are each dedicated to one of the topics. Chapter 6 is again sub-divided into two parts of complementary contents. Each contribution is presented in the form that is common practice for the MR community: *Theory, Methods, Results, Discussion*. The author's publications and conference contributions are listed on page 159.

Chapter 6 contains the developments towards a unified framework for parallel imaging methods. A derivation of SENSE in a framework identical to the GRAPPA formulation is provided and explored in a simulated data set. To this end, the two hybrid methods extended GRAPPA and truncated SENSE are introduced. With the shown transition from GRAPPA to SENSE, the presented work sheds light on the relationship between the two most prominent standard parallel imaging methods and sets a theoretical basis for a more unified framework.

Transitioning from static to dynamic MRI, a g-factor formalism for k-t-GRAPPA is furthermore presented in Chapter 6. Analytical approaches to derive g-factors were previously available only for standard parallel imaging methods, but not for time-resolved parallel imaging methods. The presented analysis comprises spatially non-uniform image noise and temporal frequency responses, which are investigated in a cardiac application. Static and dynamic parallel MRI methods are thereby connected. The influence of exploiting spatial versus temporal correlations is furthermore revealed in the transition from k-t-GRAPPA to Sliding Window reconstruction. In a cooperation with the Institute for Biomedical Engineering, University and ETH Zürich, Switzerland, [Binter et al., 2016], g-factors were also derived for k-t-SENSE, which complements the work towards a unified general framework for parallel imaging.

With the confirmed benign g-factors of k-t-GRAPPA at high reduction factors, a central contribution of this thesis was to transition k-t-GRAPPA concepts into the context of brain imaging, which is the content of Chapter 7. Therefore, a k-t-sub-Nyquist sampled EPI sequence (k-t-EPI) with three different acquisition strategies was implemented. EPI has been and is still a target of vivid research. The introduction of k-t-GRAPPA into EPI has not been previously reported. k-t-EPI is investigated and applied in the context of dynamic susceptibility contrast weighted cerebral perfusion measurements. In a close cooperation with the Department of Neuroradiology of the University Medical Center in Freiburg, k-t-EPI was applied in several patient measurements to assess the cerebral blood volume at higher spatial resolution than the current clinical protocol provides.

Towards a unified general framework for parallel imaging

Parallel imaging allows for faster image acquisition based on hybrid Fourier and sensitivity encoding. The most prominent parallel imaging methods are Cartesian SENSE and GRAPPA. Time-resolved parallel imaging techniques, such as k-t-GRAPPA, further exploit correlations in x-f-space to achieve a similar task in dynamic MRI. The aim of this chapter is to develop the foundation of a unified theoretical framework for parallel imaging of static and dynamic MRI.

In Sec. 6.1, an equivalent expression for Cartesian SENSE as for GRAPPA is derived. Based on the shared framework, differences and similarities are investigated. The transition from GRAPPA to Cartesian SENSE is shown by extending the support in k-space of the GRAPPA convolution kernel. The effect of the extension in GRAPPA - and likewise truncation of SENSE - is observed based on g-factor calculations.

In Sec. 6.2, a bridge is built between conventional GRAPPA of static MRI and k-t-GRAPPA used in dynamic MRI. To this end, an analytical noise analysis framework for k-t-GRAPPA is developed on the basis of the g-factor formulation for conventional GRAPPA. The subsequent analysis of k-t-GRAPPA and GRAPPA in a cardiac application confirms the more benign SNR behavior of k-t-GRAPPA. Furthermore, the transition from k-t-GRAPPA to Sliding Window is revealed by step-wise virtual compression of coil elements in the reconstruction process.

The g-factor analysis for an extended GRAPPA algorithm was partly presented in [Ramb and Schultz, 2013]. The derived g-factor framework for k-t-GRAPPA was published in [Ramb et al., 2013c], including some of the figures. Parts of this work have also been presented as conference contributions [Ramb et al., 2013a, Ramb et al., 2013b, Ramb et al., 2014a]. Complementary considerations for image space based time-resolved parallel imaging methods were published in a cooperation [Binter et al., 2016].

6.1. Static imaging with SENSE and GRAPPA: differences and similarities

Cartesian SENSE and GRAPPA both solve the general image reconstruction problem in parallel imaging based on undersampled data acquisition. However, both methods approach this problem differently. In this section, similarities and differences are investigated. To this end, SENSE is expressed in an equivalent formulation as GRAPPA in image space and can then be transformed into a k-space formulation equivalent to GRAPPA in k-space (Sec. 6.1.1). *ExtGRAPPA* and *trSENSE* are introduced to aid a transition between both methods (Sec. 6.1.2). Within the same framework, the effects of different parameters onto g-factor noise are analyzed (Sec. 6.1.3) and discussed (Sec. 6.1.4). Parts of this work were presented in [Ramb and Schultz, 2013]. Facets of the relationship between GRAPPA to SENSE are also discussed in [Yeh et al., 2005, Sodickson and McKenzie, 2001, Schultz, 2013], however, in a different formal approach.

6.1.1. Theory: from SENSE to GRAPPA

In this section, an expression for Cartesian SENSE reconstruction (see Sec. 4.3.1) similar to the standard GRAPPA reconstruction (see Secs. 4.5.1 and 4.5.2) is derived.

In Cartesian SENSE, the Moore-Penrose pseudo inverse $C_p^{\text{unfold}} \in \mathbb{C}^{R \times N_{\text{coils}}}$ (cf. 4.17) is computed for each *aliased* or *folded* spatial position in the Fourier reconstructed image of the zero-filled undersampled data of all coils, denoted by $\check{\mathcal{F}}^{-1} \mathbf{d}^{\text{zf}} \in \mathbb{C}^{N_{\text{pix}} N_{\text{coils}}}$ (cf. 4.16). Let $\hat{\mathbf{I}}^{\text{fold}} := \check{\mathcal{F}}^{-1} \mathbf{d}^{\text{zf}}$ represent the vector in image space that contains the folded contributions. In order to express the unfolding operation by a single matrix multiplication, a single unfolding matrix $C^{\text{unfold}} \in \mathbb{C}^{N_{\text{pix}} \times N_{\text{coils}} N_{\text{pix}}}$ is formed. It consists of a block-diagonal matrix with blocks C_p^{unfold} , for each $p = 1, \dots, N_{\text{smp}}$, which is column-wise R -times repeated. The *unfolded* image vector $\hat{\mathbf{I}} \in \mathbb{C}^{N_{\text{pix}}}$ is then derived - analogous to (4.13) - by

$$\hat{\mathbf{I}} := \frac{1}{R} C^{\text{unfold}} \hat{\mathbf{I}}^{\text{fold}}, \quad (6.1)$$

where the factor $1/R$ arises, since $\hat{\mathbf{I}}^{\text{fold}}$ contains R replica of the same information (see Remark 4.3.3). This reconstructed image is already coil combined.

In order to obtain the image of a single coil, coil sensitivities of each coil α are described by a diagonal matrix $C_\alpha \in \mathbb{C}^{N_{\text{pix}} \times N_{\text{pix}}}$ such that

$$(C_\alpha)_{n,m} := c_\alpha(\mathbf{r}_m) \delta_{n,m}. \quad (6.2)$$

Multiplication by C_α then provides the reconstructed image weighted by coil α :

$$\hat{\mathbf{I}}_\alpha := C_\alpha \hat{\mathbf{I}} = \frac{1}{R} C_\alpha C^{\text{unfold}} \hat{\mathbf{I}}^{\text{fold}}. \quad (6.3)$$

Define the matrix $C_\beta^{\text{all}} \in \mathbb{C}^{N_{\text{pix}} \times N_{\text{pix}} N_{\text{coils}}}$ which extends the definition of (6.2) to including all coils, where coil sensitivity weightings are only non-zero for contributions from the indexed coil β . Analogous to deriving $\hat{\mathbf{I}}_\alpha$, define then $\hat{\mathbf{I}}_\beta^{\text{fold}} := C_\beta^{\text{all}} \hat{\mathbf{I}}^{\text{fold}}$ as the aliased image corresponding to coil β (R -times replicated). Matrix multiplication can be equivalently expressed as element-wise multiplication of each coil weighted image and subsequent addition, hence

$$\hat{\mathbf{I}}_\alpha = \frac{1}{R} \sum_{\beta \in \mathcal{C}} C_\alpha C_\beta^{\text{unfold}} \hat{\mathbf{I}}_\beta^{\text{fold}}. \quad (6.4)$$

In this notation, the matrix $C_\alpha C_\beta^{\text{unfold}} \in \mathbb{C}^{N_{\text{pix}} \times N_{\text{pix}}}$ is a square-matrix which performs a part of the unfolding process only based on coil β and projects the result onto target coil α .

Two observations are made: first, by the definition of $\hat{\mathbf{I}}^{\text{fold}}$, each row of $C_\alpha C_\beta^{\text{unfold}}$ necessarily contains the same unfolding information R -times. Thus, one of the R folded pixel values in each case suffices to reconstruct the respective R unfolded pixel values. Second, each folded pixel position $p = 1, \dots, N_{\text{pix}}$ (including the R replica) contributes to the same unfolded pixel position. Hence, the diagonal of $C_\alpha C_\beta^{\text{unfold}}$ connects each folded pixel position with the same pixel position in the unfolded image. Based on the two observations, the diagonal elements $\text{diag}(C_\alpha C_\beta^{\text{unfold}})$ are formed into a vector $\tilde{\mathbf{c}}_{\alpha,\beta} \in \mathbb{C}^{N_{\text{pix}}}$ and (6.4) simplifies to

$$\hat{\mathbf{I}}_\alpha = \sum_{\beta \in \mathcal{C}} \tilde{\mathbf{c}}_{\alpha,\beta} \odot \hat{\mathbf{I}}_\beta^{\text{fold}}, \quad (6.5)$$

where \odot is again used to emphasize element-wise multiplication of the two vectors. By simple rearranging the vectors $\tilde{\mathbf{c}}_{\alpha,\beta}$, $\hat{\mathbf{I}}_{\beta}^{\text{fold}}$ and $\hat{\mathbf{I}}_{\alpha}^{\dagger} \in \mathbb{C}^{N_{\text{pix}}}$ into two-dimensional representations $\tilde{C}_{\alpha,\beta}$, I_{β}^{fold} and $\hat{I}_{\alpha}^{\text{sub}} \in \mathbb{C}^{N_x \times N_y}$, an equivalent expression of (6.5) is given by

$$\hat{I}_{\alpha}^{\text{sub}} = \sum_{\beta \in \mathcal{C}} \tilde{C}_{\alpha,\beta} \odot I_{\beta}^{\text{fold}}. \quad (6.6)$$

This representation of Cartesian SENSE facilitates direct comparison with the image space GRAPPA formulation of Sec. 4.5.2 (cf. 4.30).

Cartesian SENSE reconstruction of the coil image of coil α thus is determined by $\tilde{C}_{\alpha,\beta}$ for each coil β . With linearity of the discrete Fourier transform and the Fourier convolution theorem, (6.6) can be transformed to

$$\hat{d}_{\alpha}^{\text{sub},2D} = \sum_{\beta \in \mathcal{C}} \mathcal{DFT}_{x,y} \left\{ \tilde{C}_{\alpha,\beta} \right\} * d_{\beta}^{\text{zf},2D}, \quad (6.7)$$

where $\mathcal{DFT}_{x,y} \{ \}$ denotes the 2-dimensional discrete Fourier transform along the two spatial dimensions and using the notation as introduced in Sec. 4.5.2. This representation yields a k-space formula for Cartesian SENSE in analogy to the k-space algorithm of GRAPPA (cf. 4.29).

The equations of (6.6) and (6.7) reveal the following observations:

1. Cartesian SENSE reconstruction can be approached as a convolution in k-space, of which fully sampled coil data is obtained.
2. The convolution kernel comprises linear combinations of coil sensitivities.
(*sensitivity image weights*)
3. The local unfolding in the image domain yields generally a global convolution in k-space.
(*full extent*)

Similarly, for GRAPPA, the equations of (4.29) and (4.30) demonstrate:

1. Cartesian GRAPPA reconstruction can be approached as a multiplication in image space.
2. The convolution kernel comprises linear combinations of in vivo sensitivities.
(*ACS image weights*)
3. The support of the convolution kernel is postulated to consist of a small neighborhood structure in k-space. (*truncated extent*)

Note that it is not a real difference that either the calibration scan precedes the actual measurement (typical for the coil sensitivities estimation of SENSE) or that it is part of the scan (ACS data acquisition for GRAPPA). For GRAPPA, both variants can be applied and are often referred to as *extra ACS* or *inplace ACS*, respectively. Also for SENSE, coil sensitivities can be acquired in an extra scan or as part of the measurement, the latter led to the nomenclature of *modified SENSE (mSENSE)* [Wang et al., 2001].

With the derived expressions, both approaches can be described precisely with the same terminology. Therefore, different influences as part of the image reconstruction process can be isolated to distinguish their effects on the reconstructed image. Two fundamental differences between SENSE and GRAPPA are the usage of 'pure' (estimated from acquisitions and

smoothed, object influences are removed) coil sensitivities in SENSE versus in-vivo sensitivities (weighted with the object) in GRAPPA, as well as the truncated support of convolution kernels in GRAPPA versus the full k-space extent in SENSE. These two opposed parameters between SENSE and GRAPPA can now be targeted in a separate analysis. Differences in the outcome in terms of g-factor maps are investigated below.

6.1.2. Methods: truncated SENSE and extended GRAPPA

An *extGRAPPA* (GRAPPA with extended kernel) reconstruction was achieved by extending the kernel sizes in the GRAPPA reconstruction. The algorithm was based on (4.29), where the kernel extent is given according to the chosen neighborhood size $B_{fe} \times B_{pe}$. If B_{fe} and B_{pe} approach N_{fe}^{ACS} and N_{pe}^{ACS}/R , respectively, the number of possible kernel placements within the ACS data reduces to one (cf. Sec. 4.5). This leads to a poor robustness of the fitting procedure. In order to still obtain enough k-space neighborhood samples, the calibration data were therefore artificially enlarged by periodically repeating samples along both dimensions. The isolated effect of ‘pure’ versus in vivo sensitivities at full kernel extent were compared between SENSE and extGRAPPA at the maximal kernel extent $B_{fe} = N_x$ and $B_{pe} = N_y/R$.

A *trSENSE* (SENSE with truncation of the k-space extent of the coil sensitivity data) reconstruction was obtained by truncating the k-space representation of the coil sensitivities used in the unfolding process. Truncating the extent allows to compare ‘pure’ coil sensitivities versus in vivo sensitivities at truncated kernel extent. Table 6.1 illustrates how the two hybrid methods extGRAPPA and trSENSE relate to conventional GRAPPA and SENSE.

The influence of full or truncated kernel extent and the image weights based on coil sensitivities or ACS data was investigated using GRAPPA, *extGRAPPA*, *trSENSE* and SENSE image reconstruction in the same setting. All reconstructions were performed based on a simulated data set of the *Shepp-Logan phantom* of size 64×64 with 8 coil channels. Simulated coil-channels were assumed to be arranged equidistantly in a circle around the object. Gaussian noise was added in k-space such that the receive coil covariance matrix was given by $\Psi_{coils} = 0.1 \cdot \mathbb{1}_{N_{coils}}$. Undersampling at a reduction factor $R = 4$ was simulated. Low resolution in the phantom data was necessary to reduce computational burden and storage capacity due to the direct full matrix approach for SENSE and the image weight calibration based on the ACS data at full kernel extent for extGRAPPA.

An implementation of GRAPPA following the weight calibration of (4.28) and reconstruction in image space of (4.30) served as a basis for GRAPPA and extGRAPPA. The transition from GRAPPA to extGRAPPA was obtained by extending the kernel sizes $B_{fe} \times B_{pe}$ employed in image weight calibration. Sizes were step-wise increased until a full extent of $B_{fe} \times B_{pe} = N_x \times N_y/R$ was reached. The weights used in the reconstruction were derived by shifting

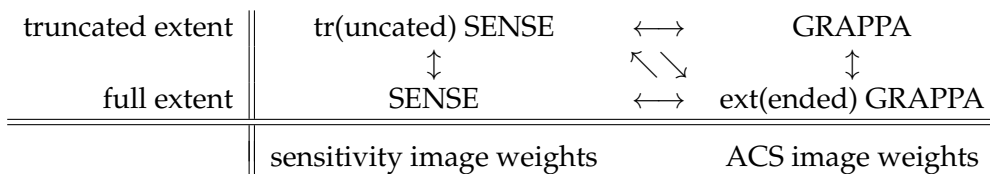


Table 6.1: coil sensitivities and a full kernel extent is incorporated in SENSE, whereas GRAPPA employs in vivo sensitivities and a truncated reconstruction kernel. In order to investigate these two fundamental differences of GRAPPA and SENSE separately, two hybrid methods, i.e. extended GRAPPA and truncated SENSE, are introduced.

the kernel geometry over the ACS data and further circularly beyond the extent of ACS data. The latter ensured enough k-space neighborhood samples also at large kernel extents. After calibration of the ACS image weights $W_{\alpha,\beta}^{2D}$, coil-wise image reconstruction was performed in image space (cf. 4.30). Coil-wise reconstructions were combined into a single image using rSoS (cf. 4.4).

An implementation of SENSE according to (6.1)-(6.6) was the foundation for evaluation of equivalence of the formulation. Based on the sensitivity weights $\tilde{C}_{\alpha,\beta}$, the transition from SENSE to trSENSE was performed. Truncation of the extent of coil sensitivity image weights for trSENSE was performed using a 2-dimensional Gaussian filter constructed from two Gaussian distributions with standard deviations $\sigma_{fe} = B_{fe}$ and $\sigma_{pe} = B_{pe}R$, respectively. The filter was then applied in the k-space representation of $\tilde{C}_{\alpha,\beta}$. For conventional SENSE, the full extent ($N_x \times N_y$) of sensitivity image weights were used. Coil-wise images were obtained based on (6.6). Again, a single reconstructed image was obtained by rSoS combination (cf. 4.4).

The equivalent reconstruction schemes of (tr)SENSE and (ext)GRAPPA, i.e.

$$\hat{I}_{\alpha}^{\text{sub}} = \sum_{\beta \in \mathcal{C}} \tilde{C}_{\alpha,\beta} \odot I_{\beta}^{\text{fold}} \quad \text{and} \quad \hat{I}_{\alpha}^{\text{sub}} = \sum_{\beta \in \mathcal{C}} W_{\alpha,\beta}^{2D} \odot I_{\beta}^{\text{fold}}, \quad (6.8)$$

facilitated the direct comparison of the sensitivity image weights $\tilde{C}_{\alpha,\beta}$ of (tr)SENSE with the ACS image space weights $W_{\alpha,\beta}^{2D}$ of (ext)GRAPPA. Noise enhancement in all four variants was analyzed with the g-factor as in Cor. 4.6.15, i.e.

$$g_{\mathbf{x}_p} = \frac{\sqrt{\left| \left(\mathbf{p}_{\mathbf{x}_p}^T \tilde{C}_{\mathbf{x}_p} \right) \hat{\Psi}_{\text{coils}} \left(\mathbf{p}_{\mathbf{x}_p}^T \tilde{C}_{\mathbf{x}_p}^H \right) \right|}}{\sqrt{\left| \left(\mathbf{p}_{\mathbf{x}_p}^T \mathbf{1} \right) \hat{\Psi}_{\text{coils}} \left(\mathbf{p}_{\mathbf{x}_p}^T \mathbf{1} \right) \right|}} \quad \text{and} \quad g_{\mathbf{x}_p} = \frac{\sqrt{\left| \left(\mathbf{p}_{\mathbf{x}_p}^T W_{\mathbf{x}_p} \right) \hat{\Psi}_{\text{coils}} \left(\mathbf{p}_{\mathbf{x}_p}^T W_{\mathbf{x}_p}^H \right) \right|}}{\sqrt{\left| \left(\mathbf{p}_{\mathbf{x}_p}^T \mathbf{1} \right) \hat{\Psi}_{\text{coils}} \left(\mathbf{p}_{\mathbf{x}_p}^T \mathbf{1} \right) \right|}}, \quad (6.9)$$

where the matrix $\tilde{C}_{\mathbf{x}_p} \in \mathbb{C}^{N_{\text{coils}} \times N_{\text{coils}}}$ is defined by $\left(\tilde{C}_{\mathbf{x}_p} \right)_{\alpha\beta} = \tilde{C}_{\alpha,\beta}(x_p, y_p)$.

6.1.3. Results: influences of kernel extent and weight calibration

Figure 6.1 depicts image reconstructions for SENSE and trSENSE with (truncated) sensitivity weights in comparison to GRAPPA and extGRAPPA with ACS calibrated weights. The arrangement of the sub-figures corresponds with the axes of Table 6.1. The g-factor maps demonstrate the influence of image weight variations on noise amplifications in the reconstructed image.

The two left columns in Fig. 6.1 display (tr)SENSE reconstructions and g-factor maps obtained using sensitivity image weights at truncations in k-space of different extent. Whereas SENSE performs artifact-free unfolding in the presented scenario, truncating the extent of image weights from measured coil sensitivities introduces artifacts when limiting the representation in k-space. The g-factor map of SENSE exhibits the typical division of the image into R compartments with sharp edges at compartment boundaries. This sharp delineation softens when decreasing the kernel extent. Nevertheless, g-factor values only describe the noise influence due to coil arrangement and the process of image reconstruction. With the truncation, artifacts arising in the form of unaliased object edges are not accounted for in the g-factor analysis.

The two right columns in Fig. 6.1 illustrate (ext)GRAPPA reconstruction and g-factor maps using image weights derived by circular weight calibration with varying neighborhood sizes based on the ACS data. For extGRAPPA, extending the kernel size is very robust and an artifact-free image is obtained in each scenario. The g-factor maps exhibit considerable influence on kernel sizes. At small kernel extents, smooth variations of the GRAPPA g-factor noise are observed. When extending the kernel, these smooth variations are sharpened. At full extent, strictly delimited compartments very similar to the SENSE g-factor appear for the GRAPPA g-factor. The GRAPPA g-factors exhibit a high noise level in this case.

The observations are in accordance with the SNR optimality of SENSE, a property that is expected from theory if correct coil sensitivities are provided. The latter is the case in the simulated scenario presented here. Interestingly, at large - yet not full - kernel extent, the highest g-factors of extGRAPPA are found, indicating an ill-conditioned weight calibration problem. Note that g-factors values in this case exceed the range of color-coding displayed. The average value in the central part is 10.32. The assessment of a series of different kernel sizes for (ext)GRAPPA suggests that a smaller kernel size results in a more benign reconstruction in terms of g-factor noise. However, it should not be too small, since the the smallest kernel of $B_{fe} \times B_{pe} = 3 \times 2$ shows again increased g-factors.

In Fig. 6.2, the image weights of one target and source coil corresponding to the reconstructions of Fig. 6.1 are depicted. The change in image weights exhibits alteration from smooth variations to sharp - yet noise affected - compartment weighting. This demonstrates how GRAPPA reconstruction becomes very similar to SENSE. The findings indicate that it is the differences in kernel extents which truly distinguishes between the two approaches.

6.1.4. Discussion

The findings indicate that extGRAPPA at full kernel extent is very similar to SENSE reconstruction. Based on the true underlying coil sensitivities, extGRAPPA exhibits comparably higher noise influences in the weight determination, but nevertheless approaches the SENSE reconstruction in terms of g-factor maps. For extGRAPPA at full kernel extent, the derived weights as well as the g-factor maps exhibit the same sharp compartments as for SENSE. Observations suggest that in truncating SENSE, spatial maps of reconstruction weights and g-factors accordingly contain smoother edges. This investigation implies that truncation of the kernel extent is the actual difference between both methods in terms of signal and noise transfer. The imaged object as part of the ACS data and presence of noise do not significantly contribute to sharpening of contours in image weights and g-factor maps.

The different kernel sizes of extGRAPPA reconstructions reveal an interesting behavior in terms of g-factors. The most benign g-factor map is obtained at a small kernel size, which is nevertheless not too small to not convey any information. Compared to the results of this small kernel size, the g-factor maps are severely increased for the almost maximum kernel extent. This suggests that there is indeed a gain in truncating the kernel sizes for GRAPPA. Since the object influences the derivation of weights by the in vivo sensitivities including all coils, the optimal kernel size most likely depends on the respective object to be imaged.

This is opposed to SENSE, where pure coil sensitivities determine the reconstruction weighting. Although the g-factor maps suggest an improvement of the noise influences due to the coil arrangement, a larger truncation of the kernel extent introduces artifacts for SENSE. This demonstrates that g-factor maps do not reflect systematic errors of the reconstruction. It further shows that SENSE cannot be improved by a kernel truncation. SENSE relies on the

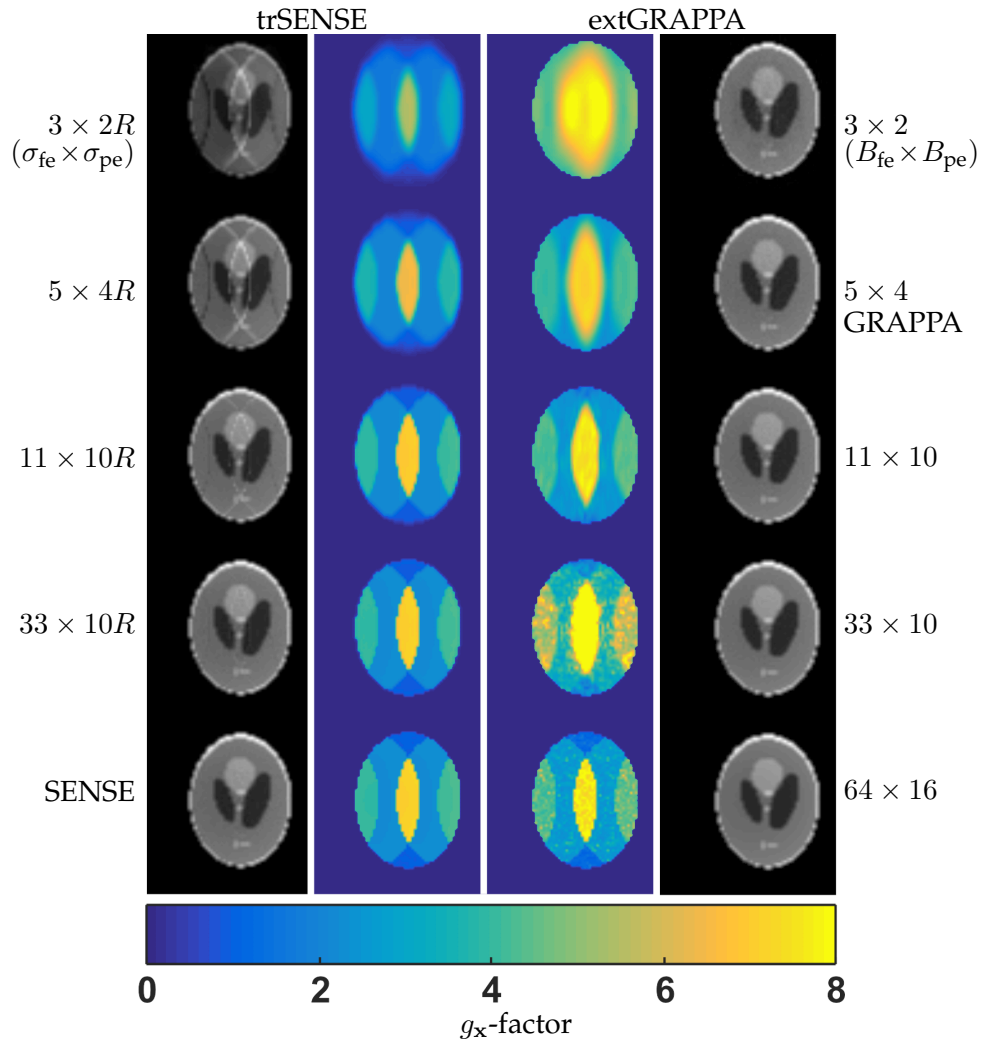


Figure 6.1: Combined reconstructed images and g -factor maps of variations of (tr)SENSE and (ext)GRAPPA reconstructions at reduction factor $R = 4$ of the Shepp-Logan phantom are depicted. Whereas sensitivity image weights were used on all reconstructions on the left, reconstruction images on the right were obtained using weights that were calibrated based on ACS data. The kernel extent incorporated step-wise increases from top to bottom.

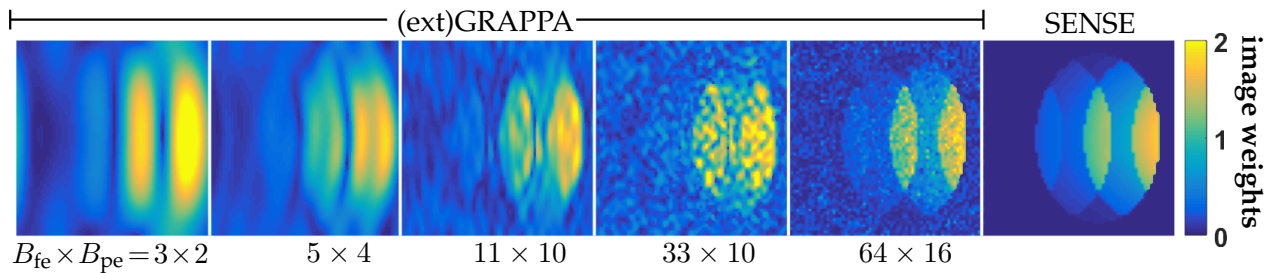


Figure 6.2: The absolute value of the image weights of target coil $\alpha = 1$ and source coil $\beta = 1$ are displayed as employed in the five (ext)GRAPPA and one SENSE image reconstruction results of Fig. 6.1.

correctness of coil sensitivity values, whereas the data-driven method GRAPPA depends on the in vivo coil sensitivity and object influences, in combination with the kernel geometry and weight calibration procedure.

6.2. From static to dynamic MRI: Generalized framework for k-t-based methods

Time-resolved parallel imaging methods (as covered in Chapter 5) additionally exploit temporal correlations, in order to improve spatio-temporal resolution of dynamic MRI. These methods achieve advantageous SNR at higher reduction factors relative to frame-by-frame reconstruction, as observed in the measurements. Experimental findings further suggest great differences in the noise outcome depending on the type of k-t-method, such as for instance between k-t-SENSE and k-t-GRAPPA [Jung and Kozerke, 2009]. The findings indicate: Whereas k-t-GRAPPA exhibits spatially smooth noise influences, k-t-SENSE displays greater noise enhancement in the area of motion and less noise in static areas.

Analytical frameworks for deriving the pixel-wise g-factor are available for SENSE [Pruessmann et al., 1999], GRAPPA [Brau et al., 2008, Breuer et al., 2009] and PARS (parallel MRI with adaptive radius in k-space) [Yeh et al., 2005]. These methods are applicable only to individual single image acquisitions for a slice or volume.

In the following, an analytical framework is developed to analyze the signal and noise transfer in k-t-GRAPPA reconstructions. To this end, an extension of the g-factor for k-t-space kernel based time-resolved parallel imaging methods is formulated (Sec. 6.2.1). The proposed theoretical framework is used to analyze the noise behavior and temporal fidelity of k-t-GRAPPA in comparison with conventional GRAPPA (non-time-resolved, solely parallel imaging) and Sliding Window (time-resolved, without parallel imaging) reconstruction in an in vivo cardiac measurement (Secs. 6.2.2 and 6.2.3). The formulations in the same theoretical setting allows to delineate causes and effects of differences between these methods, which is discussed in Sec. 6.2.4. Previous heuristic observations of a more benign SNR behavior are thereby explained in a common theoretical framework. Parts of this work have been published [Ramb et al., 2015a] and were presented as conference contributions [Ramb et al., 2013a, Ramb et al., 2013b, Ramb et al., 2014a].

6.2.1. Theory: k-t-GRAPPA and g-factors in x-f-space

The development of an analytical framework for the analysis of signal and noise transfer comprises the following steps: first, the k-t-GRAPPA reconstruction in x-f-space is introduced, to obtain weights which act like a transfer function. Second, the expression in x-f-space is used to extend the g-factor of conventional GRAPPA to the domain of temporal frequencies. Third, the g-factor formalism in x-f-space is transferred into a temporally averaged g-factor expression in image space which facilitates the comparison with known GRAPPA g-factor maps.

Along with the investigation of noise transfer, the signal behavior governed by the reconstruction is further considered. In this endeavor, k-t-GRAPPA weights in x-f-space are utilized to formulate the signal transfer between sub-Nyquist and full-Nyquist sampled scenarios. If the reference depicting the underlying truth is given, the temporal fidelity with respect to different reduction factors can be rated.

k-t-GRAPPA in x-f-space

Analogous to GRAPPA in image space (Sec. 4.5.2), k-t-GRAPPA can be formulated in x-f-space when assuming a circular boundary condition for all spatio-temporal dimensions. In cardiac MRI, this is valid due to the periodic movement of the heart. Hence, reconstruction in x-f-space solves the treatment of first and last time frames by employing circular neighbors in the reconstruction.

The reconstruction process in k-t-GRAPPA comprises the convolution in k-t-space (cf. 5.3) and subsequent Fourier reconstruction of individual coil images of the derived full data set. In order to perform k-t-GRAPPA in x-f-space, the data - sampled in k-t-space - is transformed into equivalent x-f-space based representation. After omitted data samples are restored in x-f-space, the data is expressed in x-t-space to obtain the time series of magnitude images. The derivation of this process is described below.

Let $d_{\beta}^{\text{zf},3\text{D}}$ be the zero-filled sub-Nyquist sampled three-dimensional data of coil $\beta = 1, \dots, N_{\text{coils}}$. Let $w_{\alpha,\beta}^{\text{3D}} \in \mathbb{C}^{B_{\text{fe}} \times RB_{\text{pe}} \times B_t}$ denote the three-dimensional convolution kernel of reconstruction weights for target coil α and source coils $\beta = 1, \dots, N_{\text{coils}}$. Repeating (5.3) here, the omitted data of coil α is reconstructed from the k-t-sub-Nyquist sampled data by

$$\hat{d}_{\alpha}^{\text{sub},3\text{D}} = \sum_{\beta \in \mathcal{C}} w_{\alpha,\beta}^{\text{3D}} * d_{\beta}^{\text{zf},3\text{D}}. \quad (6.10)$$

Let $\mathcal{DFT}_{x,y}^{-1}\{\cdot\}$ and $\mathcal{DFT}_{x,y,t}^{-1}\{\cdot\}$ be the inverse discrete Fourier transforms along both spatial dimensions and additionally along the temporal domain, respectively. Likewise, let $\mathcal{DFT}_t\{\cdot\}$ refer to the discrete Fourier transform solely along the domain of time frames. For the series of images $\hat{I}_{\alpha}^{\text{sub},3\text{D}}$ Fourier reconstructed from restored data $\hat{d}_{\alpha}^{\text{sub},3\text{D}}$, the convolution theorem implies the following

$$\begin{aligned} \hat{I}_{\alpha}^{\text{sub},3\text{D}} &= \mathcal{DFT}_{x,y}^{-1}\left\{\hat{d}_{\alpha}^{\text{sub},3\text{D}}\right\} = \mathcal{DFT}_t\left\{\mathcal{DFT}_{x,y,t}^{-1}\left\{\sum_{\beta \in \mathcal{C}} w_{\alpha,\beta}^{\text{3D}} * d_{\beta}^{\text{zf},3\text{D}}\right\}\right\} \\ &= \mathcal{DFT}_t\left\{\sum_{\beta \in \mathcal{C}} \mathcal{DFT}_{x,y,t}^{-1}\left\{w_{\alpha,\beta}^{\text{3D}} * d_{\beta}^{\text{zf},3\text{D}}\right\}\right\} \\ &= \mathcal{DFT}_t\left\{\sum_{\beta \in \mathcal{C}} \tilde{W}_{\alpha,\beta}^{\text{3D}} \odot \tilde{I}_{\beta}^{\text{fold},3\text{D}}\right\}, \end{aligned} \quad (6.11)$$

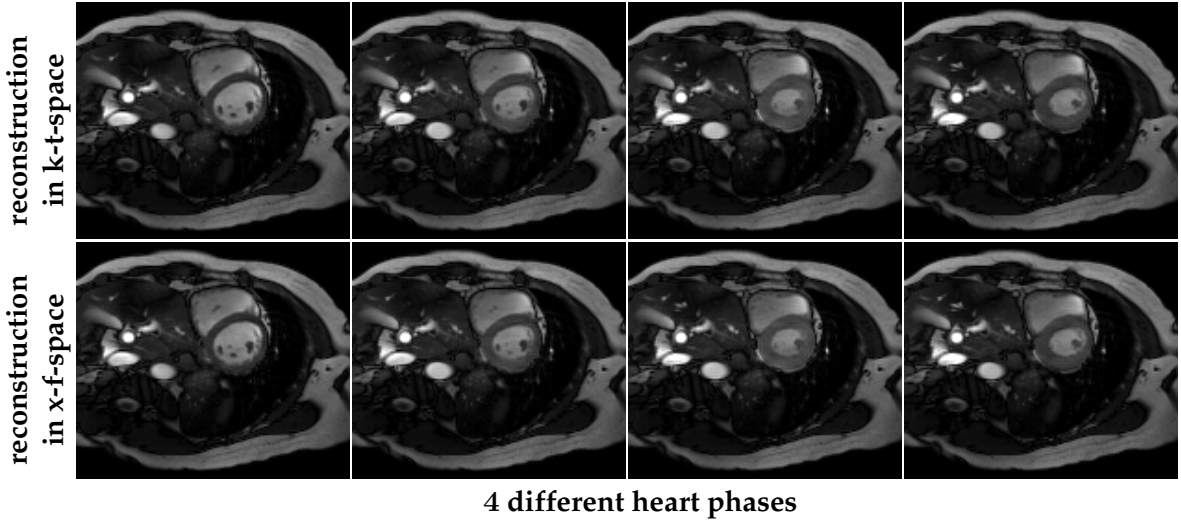


Figure 6.3: Four time frames resulting from PEAK-GRAPPA reconstruction of k - t -undersampled cardiac data at reduction factor $R = 5$ are shown. The equivalent reconstruction between k - t -GRAPPA in k - t -space (first row) and in x - f -space (second row) is illustrated.

where $\tilde{W}_{\alpha,\beta}^{3D} \in \mathbb{C}^{N_x \times N_y \times N_{\text{time}}}$ and $\tilde{I}_{\beta}^{\text{fold},3D} \in \mathbb{C}^{N_x \times N_y \times N_{\text{time}}}$ denote the results of the discrete Fourier transform along both spatial and the temporal dimension of reconstruction weights and data samples, respectively. The notation \odot refers again to element-wise multiplication. After element-wise multiplication and the summation of contributions from different coils in x - f -space, the final series of images in x - t -space is obtained by an additional Fourier transform along the temporal dimension to transition from the temporal frequency domain to time frames.

Altogether, (6.11) yields a representation of the k - t -GRAPPA algorithm in x - f -space. The reconstructed coil images are again combined according to the method of choice (Sec. 4.1). For coil combination weightings p_{α}^{3D} , for coils $\alpha = 1, \dots, N_{\text{coils}}$, the time series of images is given by

$$\hat{I}_{\text{sub},3D} = \sum_{\alpha=1}^{N_c} p_{\alpha}^{3D} \odot \left(\mathcal{DFT}_t \left\{ \sum_{\beta \in \mathcal{C}} \tilde{W}_{\alpha,\beta}^{3D} \odot \tilde{I}_{\beta}^{\text{fold},3D} \right\} \right). \quad (6.12)$$

Figure 6.3 depicts four time frames of reconstructed images based on the same cardiac k - t -space data, but reconstructed in k - t -space (cf. 5.4) versus in x - f -space (cf. 6.12).

The reconstruction weights in x - f -space establish the transfer from sub- to full-Nyquist-sampled data. Therefore, applying the reconstruction weights to pure receive coil noise reveals the noise transfer as part of the image reconstruction process. This, as well as the PSF when using the weights on a signal point source, will be discussed in the subsequent sections.

The k - t -GRAPPA g -factor in x - f -space

As for conventional GRAPPA, coil geometry- (g) -factor considerations are derived based on the measured receive coil covariance matrix and the reconstruction weights estimated from the ACS data. For k - t -GRAPPA, where reconstruction weights comprise k -space neighbors as well as neighboring time frames, the pixel-wise g -factor is extended to the range of temporal frequencies. These obtained $g_{\mathbf{x}_p, f}$ -factors refer to the spatial position $\mathbf{x}_p := (x_p, y_p)$ and the

resolved temporal frequencies f , as defined below.

Assume an additive noise term $\tilde{\varepsilon}_{I_\alpha}^{\text{sub},3D}$ to corrupt the otherwise noise-free reconstructed image data in x-f-space $\tilde{I}_\alpha^{\text{sub},3D}$. The relation between the noise affected reconstruction in x-f-space and the Gaussian noise process in the data domain is determined by the reconstruction weights. These act on the zero-filled Fourier reconstruction $\tilde{I}_\beta^{\text{fold},3D}$ with noise term $\tilde{\varepsilon}_{I_\beta}^{\text{fold},3D}$. The relation is described by

$$\tilde{I}_\alpha^{\text{sub},3D} + \tilde{\varepsilon}_{I_\alpha}^{\text{sub},3D} = \sum_{\beta \in \mathcal{C}} \tilde{W}_{\alpha,\beta}^{3D} \odot \left(\tilde{I}_\beta^{\text{fold},3D} + \tilde{\varepsilon}_{I_\beta}^{\text{fold},3D} \right). \quad (6.13)$$

Definition 6.2.1 (resolved temporal frequencies). *Based on the temporal resolution Δt and the number of time frames N_{time} , define the set of **resolved temporal frequencies** in accordance with the Nyquist-Shannon sampling theorem by $\mathcal{F}_{\Delta t} := \left\{ -\frac{1}{2\Delta t}, \dots, \frac{1}{2\Delta t} - \frac{1}{N_{\text{time}}\Delta t} \right\}$.*

Proposition 6.2.2. *Let $\left\{ \tilde{W}_{\alpha,\beta}^{3D} \in \mathbb{C}^{N_x \times N_y \times N_{\text{time}}}, \beta = 1, \dots, N_{\text{coils}} \right\}$ be the set of k-t-GRAPPA weights in x-f-space for the target coil α . Let $\hat{\Psi}_{\text{coils}} \in \mathbb{C}^{N_{\text{coils}} \times N_{\text{coils}}}$ denote the receive coil covariance matrix in image space. For each image pixel $\mathbf{x}_p = (x_p, y_p)$ with $p \in \{1, \dots, N_{\text{pix}}\}$ and each resolved temporal frequency $f \in \mathcal{F}_{\Delta t}$, define the matrix $W_{\mathbf{x}_p f} \in \mathbb{C}^{N_{\text{coils}} \times N_{\text{coils}}}$ by $(W_{\mathbf{x}_p f})_{\alpha\beta} = \tilde{W}_{\alpha,\beta}^{3D}(\mathbf{x}_p, f)$. Then, the image noise variance of the image pixel \mathbf{x}_p at the temporal frequency f and for coil α is given by*

$$\sigma^2(\tilde{\varepsilon}_{I_\alpha}^{\text{sub}}(\mathbf{x}_p, f, \alpha)) = \left| W_{\mathbf{x}_p f} \hat{\Psi}_{\text{coils}} W_{\mathbf{x}_p f}^H \right|_{\alpha\alpha}.$$

Proof. Let $p \in \{1, \dots, N_{\text{pix}}\}$ and $f \in \mathcal{F}_{\Delta t}$. Assume unbiased image reconstruction providing image noise with zero mean. The expression of (6.13) implies the following for the image noise variance at (\mathbf{x}_p, f) :

$$\begin{aligned} \sigma^2 \left(\tilde{\varepsilon}_{I_\alpha}^{\text{sub}}(\mathbf{x}_p, f, \alpha) \right) &= \mathbb{E} \left[\tilde{\varepsilon}_{I_\alpha}^{\text{sub}}(\mathbf{x}_p, f, \alpha) \tilde{\varepsilon}_{I_\alpha}^{\text{sub}}(\mathbf{x}_p, f, \alpha)^* \right] \\ &= \mathbb{E} \left[\left(\sum_{\beta} \tilde{W}_{\alpha,\beta}^{3D}(\mathbf{x}_p, f) \varepsilon_I^{\text{fold}}(\mathbf{x}_p, f, \beta) \right) \left(\sum_{\gamma} \tilde{W}_{\alpha,\gamma}^{3D}(\mathbf{x}_p, f) \varepsilon_I^{\text{fold}}(\mathbf{x}_p, f, \gamma) \right)^* \right]. \end{aligned} \quad (6.14)$$

$$(6.15)$$

With linearity of the mean the equality follows to

$$\sigma^2 \left(\tilde{\varepsilon}_{I_\alpha}^{\text{sub}}(\mathbf{x}_p, f, \alpha) \right) = \sum_{\beta} \sum_{\gamma} \tilde{W}_{\alpha,\beta}^{3D}(\mathbf{x}_p, f) \mathbb{E} \left[\varepsilon_I^{\text{fold}}(\mathbf{x}_p, f, \beta) \varepsilon_I^{\text{fold}}(\mathbf{x}_p, f, \gamma)^* \right] \tilde{W}_{\alpha,\gamma}^{3D}(\mathbf{x}_p, f)^*. \quad (6.16)$$

Using Prop. 3.3.27 and Prop. 4.6.4, this simplifies to

$$\sigma^2 \left(\tilde{\varepsilon}_{I_\alpha}^{\text{sub}}(\mathbf{x}_p, f, \alpha) \right) = \sum_{\beta,\gamma} \tilde{W}_{\alpha,\beta}^{3D}(\mathbf{x}_p, f) \left(\hat{\Psi}_{\text{coils}} \right)_{\beta,\gamma} \tilde{W}_{\alpha,\gamma}^{3D}(\mathbf{x}_p, f)^* \quad (6.17)$$

$$= \left| W_{\mathbf{x}_p f} \hat{\Psi}_{\text{coils}} W_{\mathbf{x}_p f}^H \right|_{\alpha\alpha}. \quad (6.18)$$

□

Proposition 6.2.2 demonstrates how noise variances solely depend on the coil covariance matrix $\hat{\Psi}_{coils} \in \mathbb{C}^{N_{coils} \times N_{coils}}$ and the reconstruction weights in x-f-space $W_{\mathbf{x}_p f} \in \mathbb{C}^{N_{coils} \times N_{coils}}$. As for conventional GRAPPA, the relation between sub-Nyquist and full-Nyquist sampled image noise reflects the additional g-factor.

Proposition 6.2.3. *For each pixel \mathbf{x}_p , $p \in \{1, \dots, N_{pix}\}$ and each resolved temporal frequency $f \in \mathcal{F}_{\Delta t}$, consider the corresponding standard deviation of image noise, $\sigma(\tilde{\varepsilon}_I^{full}(\mathbf{x}_p, f, \alpha))$ and $\sigma(\tilde{\varepsilon}_I^{sub}(\mathbf{x}_p, f, \alpha))$, of the full- and sub-Nyquist-sampled image acquisition scenario in x-f-space. Then*

$$\frac{\sigma(\tilde{\varepsilon}_I^{sub}(\mathbf{x}_p, f, \alpha))}{\sigma(\tilde{\varepsilon}_I^{full}(\mathbf{x}_p, f, \alpha))} = \sqrt{R} \frac{\sqrt{|W_{\mathbf{x}_p f} \hat{\Psi}_{coils} W_{\mathbf{x}_p f}^H|_{\alpha\alpha}}}{\sqrt{|\hat{\Psi}_{coils}|_{\alpha\alpha}}}.$$

Proof. Let $p \in \{1, \dots, N_{pix}\}$ and let $f \in \mathcal{F}_{\Delta t}$. In the corresponding Fourier reconstruction from full-Nyquist sampled data, the standard deviation of noise is reduced by the square root of the reduction factor R in comparison with the sub-Nyquist sampled scenario:

$$\sigma_{\mathbf{x}_p f}(\tilde{\varepsilon}_\alpha^{full}) = \frac{1}{\sqrt{R}} \cdot \sqrt{|\hat{\Psi}_{coils}|_{\alpha\alpha}}. \quad (6.19)$$

With the result of Prop. 6.2.2 then directly follows

$$\frac{\sigma(\tilde{\varepsilon}_I^{sub}(\mathbf{x}_p, f, \alpha))}{\sigma(\tilde{\varepsilon}_I^{full}(\mathbf{x}_p, f, \alpha))} = \sqrt{R} \frac{\sqrt{|W_{\mathbf{x}_p f} \hat{\Psi}_{coils} W_{\mathbf{x}_p f}^H|_{\alpha\alpha}}}{\sqrt{|\hat{\Psi}_{coils}|_{\alpha\alpha}}}, \quad (6.20)$$

which concludes the proof. \square

Corollary 6.2.4 (uncombined k-t-GRAPPA g-factor in x-f-space). *Based on an artifact-free image reconstruction, the **uncombined g-factor in x-f-space of k-t-GRAPPA** (or of similar time-resolved GRAPPA kernel based methods) is defined by*

$$g_{\mathbf{x}_p f, \alpha} = \frac{\sqrt{|W_{\mathbf{x}_p f} \hat{\Psi}_{coils} W_{\mathbf{x}_p f}^H|_{\alpha\alpha}}}{\sqrt{|\hat{\Psi}_{coils}|_{\alpha\alpha}}}.$$

Corollary 6.2.5 (k-t-GRAPPA g-factor in x-f-space). *Assuming artifact-free image reconstruction, the **combined g-factor in x-f-space of k-t-GRAPPA** or any time-resolved GRAPPA kernel based method is defined by*

$$g_{\mathbf{x}_p f} = \frac{\sqrt{|(\tilde{\mathbf{p}}_{\mathbf{x}_p f}^T W_{\mathbf{x}_p f}) \hat{\Psi}_{coils} (\tilde{\mathbf{p}}_{\mathbf{x}_p f}^T W_{\mathbf{x}_p f}^H)|}}{\sqrt{|(\tilde{\mathbf{p}}_{\mathbf{x}_p f}^T \mathbf{1}) \hat{\Psi}_{coils} (\tilde{\mathbf{p}}_{\mathbf{x}_p f}^T \mathbf{1})|}},$$

where $\tilde{\mathbf{p}}_{\mathbf{x}_p f}$ denotes the vector of coil combination weightings in x-f-space according to the choice of coil combination method.

Corollaries 6.2.4 and 6.2.5 provide an analytical description of the noise propagation between full- and k-t-sub-Nyquist sampled acquisition scenarios with Fourier and k-t-GRAPPA based reconstructions, respectively. The generality of the concept allows for an application to any time-resolved kernel based reconstruction scenario. The expression in x-f-space reflects spatial variations of noise contributions for each temporal frequency separately. Hence, the filter response is likewise revealed. This facilitates the comparison with approaches that interpolate only in the temporal domain such as *Sliding Window (SW)*. For comparison with non-time-resolved methods such as conventional GRAPPA, the subsequent section covers how temporally averaged g-factors are derived combining the contributions in x-f-space.

The temporal average g-factor

The proposed $g_{x,f}$ -factor is pixel-wise derived over the range of resolved temporal frequencies. By *Parseval's theorem*, the total noise contribution in the temporal domain is described by the integral of the squared frequency contributions. Therefore, g-factor contributions of individual temporal frequencies can be combined accordingly into a pixel-by-pixel g-factor map of the average temporal domain contributions.

Definition 6.2.6 (total g-factor of k-t-GRAPPA). Let $\{g_{x_p,f} \mid p = 1, \dots, N_{pix}, f \in \mathcal{F}_{\Delta t}\}$ denote the set of pixel- and frequency-wise combined g-factors in x-f-space of a k-t-GRAPPA reconstruction scenario. The **total g-factor of k-t-GRAPPA** capturing temporally averaged pixel-by-pixel g-factor values is defined by

$$g_{x_p}^{avg} := \sqrt{\frac{1}{N_{time}} \sum_f (g_{x_p,f})^2}.$$

That this is indeed a meaningful definition is substantiated by comparison with the statistical evaluation based on a series of pseudo-replica reconstruction in the Sec. 6.2.2. Total g-factor values solely depend on the reconstructed pixel position and can be directly compared to g-factor maps of conventional GRAPPA or SENSE reconstructions. In order to distinguish between the spatial g-factor maps derived from time-resolved versus non-time-resolved methods, the notation $g_{x_p}^{avg}$ instead of g_{x_p} is used.

The temporal point spread function

The reconstruction weights in x-f-space establish the transfer from sub- to full-Nyquist-sampled k-t-space data. Therefore, applying the reconstruction weights to a signal point source reveals the *temporal point spread function*. The implications for the temporal signal variations are characterized in the filter response over the range of temporal frequencies.

Let $\delta_{enc} \in \mathbb{C}^{N_{coils} \times N_{time}}$ such that $(\delta_{enc})_{\alpha,t} := \delta_{t,t_0}$, where δ_{t,t_0} denotes the Kronecker delta. Then δ_{enc} corresponds to a point source in the temporal domain that is of spatially constant magnitude in all coils. Denote its respective representation in x-f-space by $\tilde{\delta}_{enc}$. The signal magnitude arising in the reconstruction process is captured by

$$m_{x_p,\alpha}^{sub}(f) := \left| W_{x_p,f} \cdot \tilde{\delta}_{enc} \right|_{\alpha,f}, \quad (6.21)$$

for each coil $\alpha = 1, \dots, N_{coils}$ and based on expressing the reconstruction weights $W_{x_p,f}$ as in Prop. 6.2.2. In the corresponding Nyquist sampled scenario, the signal magnitude - likewise denoted by $m_{x_p,\alpha}^{full}(f)$ - is the input itself. The magnitude transfer function expressing the decay in temporal frequency bandwidth is captured in the subsequent definition.

Definition 6.2.7 (temporal point spread function). *The magnitude signal transfer over the range of resolved temporal frequencies is defined for each pixel $\mathbf{x}_p, p = 1, \dots, N_{pix}$ and each coil $\alpha = 1, \dots, N_{coils}$ by the following ratio:*

$$tPSF_{\mathbf{x}_p, \alpha}(f) := \frac{m_{\mathbf{x}_p, \alpha}^{sub}(f)}{m_{\mathbf{x}_p, \alpha}^{full}(f)} = \frac{|W_{\mathbf{x}_p f} \cdot \tilde{\delta}_{enc}|_{\alpha, f}}{|\tilde{\delta}_{enc}|_{\alpha, f}}.$$

Denoting the vector of coil combination weightings in x - f -space by $\tilde{\mathbf{p}}_{\mathbf{x}_p f}$, the combined signal transfer is captured by

$$tPSF_{\mathbf{x}_p}(f) := \frac{m_{\mathbf{x}_p}^{sub}(f)}{m_{\mathbf{x}_p}^{full}(f)} = \frac{|\tilde{\mathbf{p}}_{\mathbf{x}_p f}^T \cdot W_{\mathbf{x}_p f} \cdot \tilde{\delta}_{enc}|}{|\tilde{\mathbf{p}}_{\mathbf{x}_p f}^T \cdot \tilde{\delta}_{enc}|}.$$

The function is termed **temporal point spread function (tPSF)**, since it reflects the relative response to a temporal point source.

Temporal fidelity

A finite temporal frequency response indicates a loss in temporal fidelity. In case a fully sampled reference acquisition is available, the loss in temporal fidelity can be investigated by the absolute value of differences.

Definition 6.2.8 (temporal root mean square error). *The **temporal root mean square error (tRMSE)** is defined by the square root of the cumulative difference between the reconstruction result and the reference depicting the underlying truth. It is defined for each pixel $\mathbf{x}_p, p = 1, \dots, N_{pix}$ by*

$$tRMSE(\mathbf{x}_p) := \sqrt{\frac{1}{N_{time}} \sum_{t=1}^{N_{time}} |\hat{f}_t^{sub, 3D} - f_t^{full, 3D}|^2}.$$

The tRMSE demonstrates any temporal bias introduced in the reconstruction as the counterpart to the analysis of noise variances in the image values.

With Corollaries 6.2.4 and 6.2.5, as well as with Def. 6.2.6, a framework for the analysis of noise transfer in k-t-methods is derived. Furthermore, Def. 6.2.7 facilitates to express the signal transfer due to extending the kernel to the temporal domain. Provided a reference exists, the bias is addressed by Def. 6.2.8.

6.2.2. Methods: signal and noise transfer analysis in cardiac MRI

An in vivo short axis cardiac acquisition was performed on a Philips Ingenia 3T scanner using a receive coil array with 28 coil elements. A bSSFP (Sec. 3.4.1) was utilized to acquire Nyquist-sampled images during a 20 s breath-hold acquisition to capture 42 different heart phases (see Remark 5.1.2). The measurement was performed in a healthy volunteer. Informed consent was obtained prior to the acquisition. Coil sensitivity maps were acquired and estimated in a separate scan in advance. The following sequence parameters were used:

parameter	value
TE	1.58 ms
TR	3.15 ms
flip angle α_{fa}	40°
slice thickness	8 mm
matrix size	148 × 132
BW	1316 Hz/Px
number of time frames	42
spatial resolution	2 × 2 × 8 mm ³
temporal resolution	21.6 ms

The duration of one heart cycle was approximately 907 ms. Hence, the 42 images of heart phases provide a temporal resolution of 21.6 ms and temporal frequencies in units of 1.1 Hz. The total covered bandwidth of temporal frequencies in the Nyquist-sampled acquisition was approximately 46 Hz.

Undersampling in k-t-space was retrospectively mimicked for reduction factors ranging from $R = 3$ to $R = 5, 7$ and 9 and following the different patterns of k-t-GRAPPA, PEAK-GRAPPA, GRAPPA and SW (Figs. 5.2 and 5.3). The number of ACS lines was thereby set to 11. However, ACS data was only used for weight calibration and not subsequently added in the reconstructed images, in order to investigate pure reconstruction performance.

Note that retrospective undersampling in the case of the gradient echo based bSSFP acquisitions is justified since signal is sampled in a steady state and with independent excitation for each phase encoding step. Therefore, sampling schemes can be freely varied. This is opposed to applying undersampling to image acquisitions comprising several readouts within one excitation interval, such as EPI. In these cases, varied sampling schemes lead to a modification of the acquisition itself and therefore directly affects the imaging behavior.

In the case of k-t-undersampling, the sampling frequency with respect to single k-space positions decreases. For a reduction by $R = 5$ and $R = 7$, the sample number per k-space position reduces to 8 and 6 data points, respectively, of the corresponding time series. As a consequence, the temporal frequency bandwidth lessens to about 8.8 Hz and 6.6 Hz, respectively.

Computation of weights in x-f-space

The reconstruction weights in x-f-space were derived in three steps: First, the kernel geometries of the $R - 1$ relative target structures were combined into a single convolution kernel. This was achieved by shifting the individual patterns of sources and targets according to a mutual target center. Individual weights were additively overlaid and the one central target point of the combined kernel was set to 1. The convolution kernel for SW thereby simply consists of R entries of unity which was replicated to fit the number of receive coils of the reconstruction.

Second, the convolution kernel was flipped in the $k_x - k_y$ - as well as the temporal dimension, and furthermore extended in size by zero-filling to match the size of the acquired zero-filled data in k-t-space. The first and second step is illustrated for k-t-GRAPPA, PEAK-GRAPPA and SW at reduction factor $R = 5$ in Fig. 6.4. Small arrows visualize the reversed order on account of flipping the orientation of the combined convolution kernel.

Third, the inverse discrete Fourier transform $\mathcal{DFT}_{x,y,t}^{-1}\{\cdot\}$ was applied along both spatial dimensions as well as the temporal domain to transfer the augmented, combined convolution kernel into x-f-space. The such obtained weights in x-f-space are of size $\tilde{W}_{\alpha,\beta}^{3D} \in \mathbb{C}^{N_x \times N_y \times N_{time}}$, for each target and source coil, $\alpha, \beta = 1, \dots, N_{coils}$.

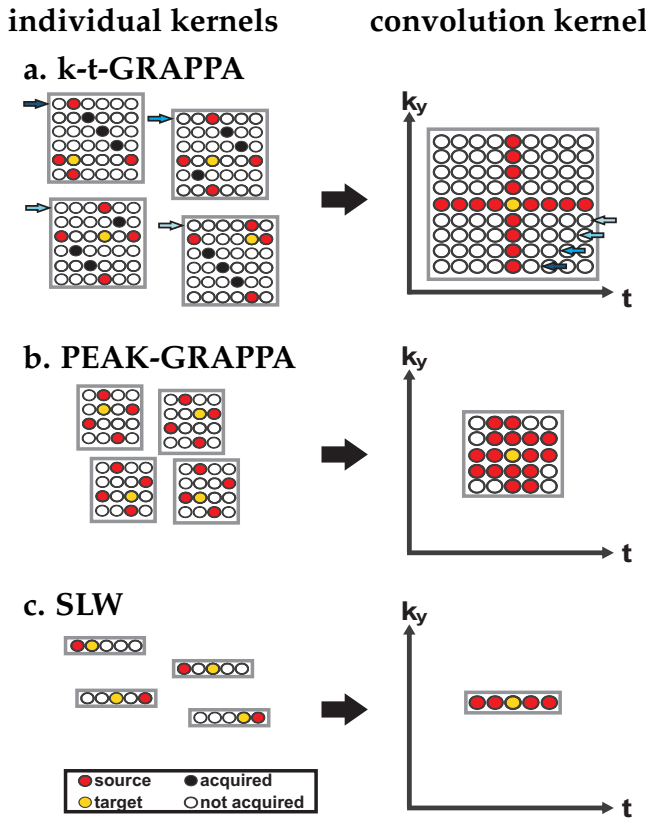


Figure 6.4: In order to obtain the combined convolution kernel, the individual reconstruction kernels corresponding to $R - 1$ relative target relations for reduction factor R are shifted with respect to a mutual kernel center and flipped in k -space and temporal dimensions (blue arrows). This process is illustrated for a. k - t -GRAPPA, b. PEAK-GRAPPA and c. SW for reduction factor $R = 5$. Sources indicate weighting factors from that relative position. Whereas weights are learned from the ACS data for k - t -GRAPPA and PEAK-GRAPPA, all weights are of value 1 in case of SW.

Computation of g_{xf} -factors, g_x^{avg} -factors and tPSF

The same algorithm for calculation of combined g_{xf} -factors (Cor. 6.2.5), temporal average g_x^{avg} -factors (Def. 6.2.6) and tPSF (Def. 6.2.7) was used for k - t -GRAPPA, PEAK-GRAPPA and SW. For conventional GRAPPA, the g_x -factor algorithm was performed according to Cor. 4.6.15 using weights in image space derived frame-by-frame.

Results of the g_{xf} -factor analysis were reformatted into a series of spatial maps discretized over temporal frequencies, of which single image columns were extracted for a depiction over the frequency bandwidth. Spatial maps of g_x^{avg} -factors, depicting the overall noise distribution, were directly compared with g_x -factor maps derived for conventional GRAPPA. Filter response curves were extracted from the derived tPSF values of single pixel and compared with corresponding g_{xf} -factor curves.

In the presented scenario, a Nyquist-sampled reference is available, since k - t -sub-Nyquist sampling was only mimicked. Hence, tRMSE values (Def. 6.2.8) could be calculated and compared with the g -factor results. Moreover, the number of coils - the crucial part of parallel imaging - was reduced by grouping coil elements into virtual coil arrays according to [Buehrer et al., 2007]. Temporal average g_x^{avg} -factors and tRMSE were then derived for the reduced coil scenario while the receive coil covariance matrix was set to the identity matrix.

Statistical validation based on pseudo-replica images

All analytically derived results were statistically validated based on a series of pseudo-replica image reconstructions according to the procedure suggested in [Robson et al., 2008]. To this end, several sets of 256 pseudo measurement repetitions were generated by replicating k - t -space data from the Nyquist-sampled original k - t -data and adding Gaussian distributed

noise to each. Respectively one set - per reconstruction method considered - of pseudo-replicated k-t-space data was undersampled and reconstructed according to k-t-GRAPPA, PEAK-GRAPPA and SW. A further set of pseudo-replica was not undersampled and solely Fourier reconstructed. From such *pseudo* repetitions of acquisition and reconstruction, each with different noise impacts, the standard deviations in the cases of sub-Nyquist and full-Nyquist sampling were derived, denoted by $\hat{\sigma}_{xf}^{\text{sub}}$ and $\hat{\sigma}_{xf}^{\text{full}}$, respectively. Thereof, estimates for the statistical noise distribution, i.e. *statistical g-factors*, were computed in the x-f-space as well as a temporal mean in x-t-space according to

$$\hat{g}_{xf} := \frac{\hat{\sigma}_{xf}^{\text{sub}}}{\hat{\sigma}_{xf}^{\text{full}} \sqrt{R}} \quad \text{and} \quad \hat{g}_x^{\text{avg}} := \frac{1}{N_{\text{time}}} \sum_{t=1}^{N_{\text{time}}} \left(\frac{\hat{\sigma}_{xt}^{\text{sub}}}{\hat{\sigma}_{xt}^{\text{full}} \sqrt{R}} \right). \quad (6.22)$$

The statistical g-factors in x-f-space (\hat{g}_{xf}) were directly compared to analytically derived g_{xf} -factors in x-f-space. The temporal mean of statistical g-factors in x-t-space (\hat{g}_x^{avg}) were compared to the temporal frequency combined g_x^{avg} -factors (Def. 6.2.6). The latter in particular emphasizes that g_x^{avg} -factors represent temporally averaged noise distributions in the case of time-resolved parallel imaging. Analytical g_x^{avg} -factors as well as statistical g-factors in x-t-space allow to evaluate the noise performance of k-t-methods with respect to g_x -factor maps of non-time-resolved conventional parallel imaging procedures.

6.2.3. Results: signal and noise transfer in a cardiac application

Figure 6.5 depicts analytically derived g_{xf} -factor maps next to statistically estimated \hat{g}_{xf} -factor maps for SW, k-t-GRAPPA and PEAK-GRAPPA at $R = 5$. The contribution in static as well as moving tissue with respect to each individual temporal frequency is demonstrated. Analytical and statistical results are in excellent agreement.

Two fundamental observations can be derived from the g_{xf} -factor maps of Fig. 6.5: First, incorporating the coil domain as part of the reconstruction process implies spatially varying g-factors (k-t-GRAPPA, PEAK-GRAPPA), whereas constant contributions over image space are obtained in the only-time-resolved method (SW). Second, the g_{xf} -factor maps of higher temporal frequencies exhibit larger values in moving tissue whereas contributions quickly decrease in the area of static tissue for k-t-GRAPPA and PEAK-GRAPPA.

All g_{xf} -factor maps demonstrate: While the zeroth temporal frequency component exhibits values slightly exceeding 1, g-factors lower than 1 appear in higher temporal frequency maps. This indicates a filtering effect of noise contributions at higher temporal frequencies. The theoretical results of g-factors below 1 is striking, since the g_x -factor is necessarily greater or equal to 1 ([Pruessmann et al., 1999]) for non-time-resolved methods such as SENSE.

Characteristic frequency response

Figure 6.6 depicts the analytical and statistical g-factors for mimicked reduction factors of $R = 5$ and $R = 7$. Rather than the complete spatial maps as in Fig. 6.5, only a single image column is shown, but over the complete range of resolved temporal frequencies. The display demonstrates the different frequency responses to moving tissue between the three time-resolved reconstruction methods. Also, effects that result from increasing the reduction factor are visualized.

In the SW approach, the spatially invariant frequency responses exhibit dark stripes over the domain of temporal frequencies. The number and repetition of these stop-bands increase

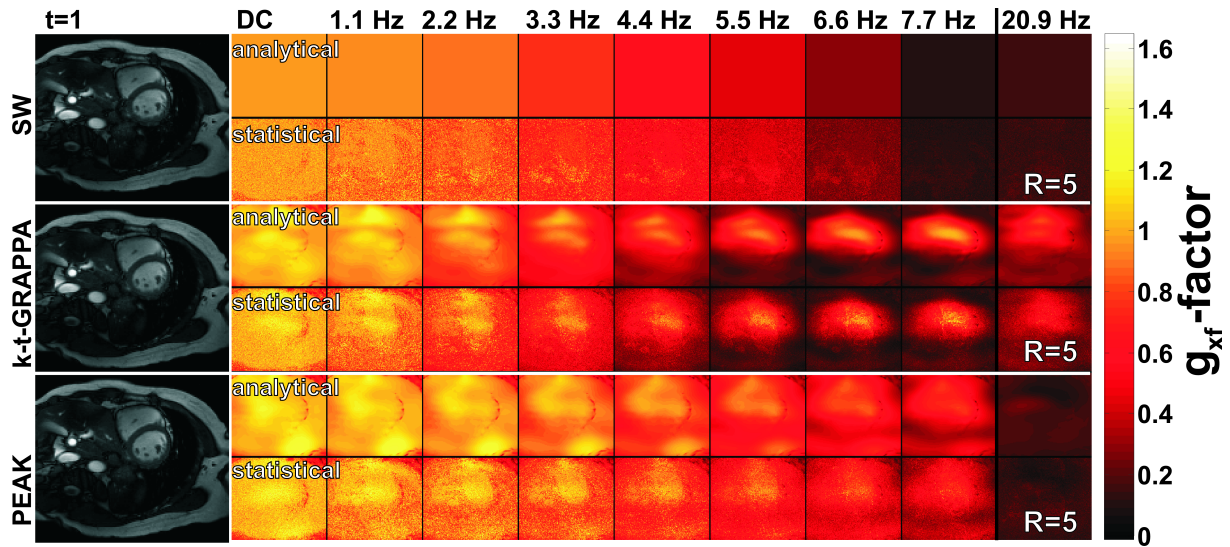


Figure 6.5: Analytically derived g_{xf} -factors as well as statistical \hat{g}_{xf} -factors derived from the series of pseudo-replica at reduction factor $R = 5$, for SW, k-t-GRAPPA and PEAK-GRAPPA. A single reconstructed magnitude image is displayed for spatial reference of moving and static tissue. Spatial g -factor maps are displayed for temporal frequencies of 0 Hz, 1.1 Hz, 2.2 Hz, . . . , 7.7 Hz and 20.9 Hz. Units of 1.1 Hz result from the overall measurement duration of the heart cycle.

at higher reduction factors. These stop-bands indicate a suppression of contributions from the respective temporal frequencies.

A similar response is observed for k-t-GRAPPA in the area of static tissue. However, in the region of the beating heart, values remain around 1 over the complete frequency bandwidth. The latter appears in both reduction factors.

PEAK-GRAPPA provides generally smooth g -factor variations in the spatial as well as the temporal frequency domain, which is visible in both Figs. 6.5 and 6.6. As for k-t-GRAPPA, contributions differ in static tissue compared to motion affected regions. However, a smoother transition between both static and dynamic areas is observed.

Variations with respect to the higher reduction factor are relatively small. For all three methods, the decay of values in static tissue when moving to higher temporal frequencies occurs at a lower temporal frequency for the higher reduction factor $R = 7$, as compared to the results for $R = 5$.

Frequency combined and temporal average g -factors

Figure 6.7 demonstrates temporal frequency combined g_x^{avg} -factors (Def. 6.2.6) in comparison with temporal average \hat{g}_{xt} -factors (cf. 6.22) derived from the pseudo-replica images in the temporal domain for SW, k-t-GRAPPA and PEAK-GRAPPA. The shown g -factor maps yield the combined g_{xf} -factors displayed in Fig. 6.6 for both reduction factors $R = 5$ and $R = 7$. The excellent agreement substantiates how temporal frequency combination of g_{xf} -factor maps represents temporally averaged g -factor noise in the time domain in the case of time-resolved reconstruction methods.

Furthermore, g_x -factors (Cor. 4.6.15) for conventional GRAPPA at reduction $R = 3$ are depicted. Despite the lower reduction factor, the values highly exceed the g -factors obtained in time-resolved methods. The strong noise amplification is demonstrated by values greatly

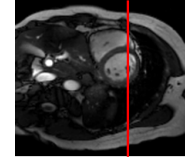
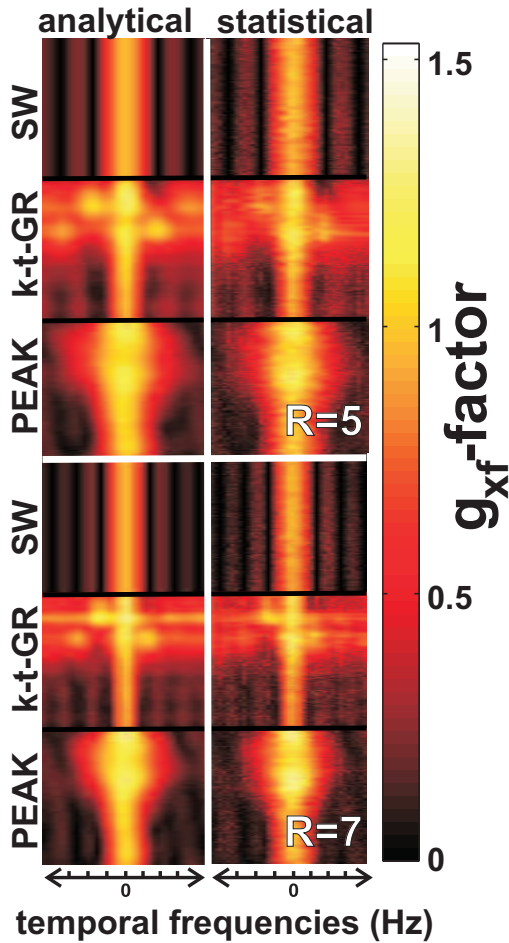


Figure 6.6: Analytical g_{xf} -factors and statistical \hat{g}_{xf} -factors are depicted for one imaged column (red line in the magnitude image) and over the complete range of sampled temporal frequencies for Sliding Window (SW), k-t-GRAPPA (k-t-GR) and PEAK-GRAPPA (PEAK). Results for two different reduction factors $R = 5$ and $R = 7$ are shown. The selected image column contains pixels of the moving heart as well as of static tissue. The respective differences in g-factor responses of the three methods are demonstrated. Temporal frequencies are aligned, wherefore differences between both reduction factors can be compared as well.

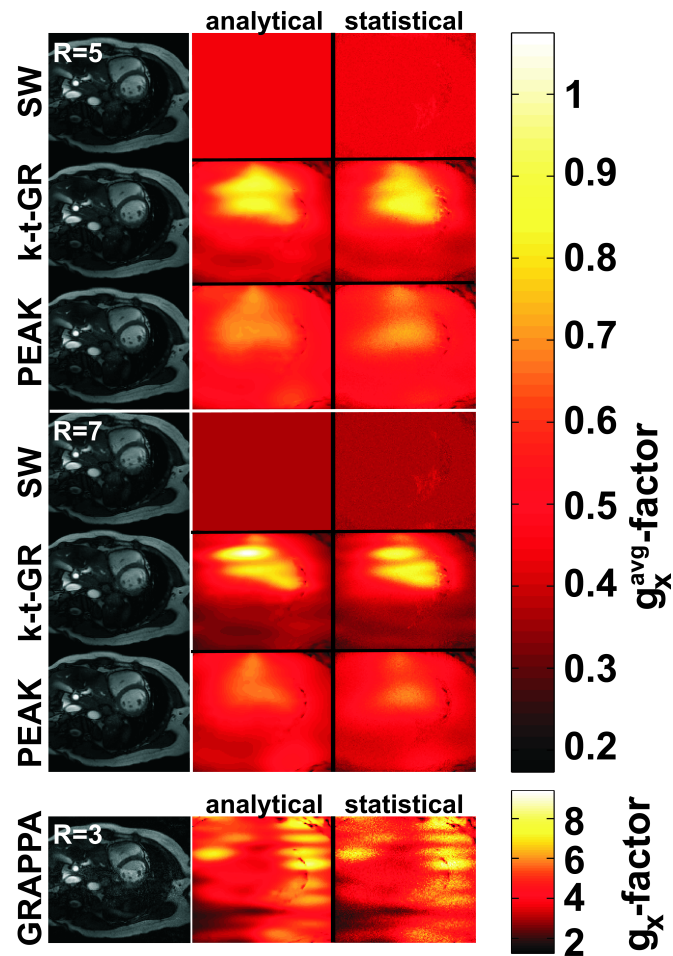
larger than 1 and confirms high noise penalties for GRAPPA at reduction factors above $R = 3$ known from practical observations. The maximum and spatially averaged g_x -factor values of GRAPPA at $R = 3$ are 8.52 and 4.68, respectively. The maximum and spatially averaged values for all four methods are collected in Table 6.2.

The g_x -factors are spatially invariant for SW. Consequently, the total noise contribution in the temporal domain is independent of pixel position as well. The maximum and average g_x -factor value for SW is 0.45 at $R = 5$. At the higher reduction of $R = 7$, the average g_x -factor decreases to 0.38 (cf. Table 6.2).

For k-t-GRAPPA and PEAK-GRAPPA, differences of g_x -factors in moving versus static tissue lead to spatially varying g_x^{avg} -factors. Total noise contributions are higher in the region of the moving heart. At $R = 5$, maximum values are 0.92 for k-t-GRAPPA and 0.72 for PEAK-GRAPPA (cf. Table 6.2). At $R = 7$, the maximum value of k-t-GRAPPA slightly exceeds 1, whereas it is moderately decreased to 0.69 in the case of PEAK-GRAPPA. Average values of k-t-GRAPPA and PEAK-GRAPPA are in a similar range for both reduction factors. In both cases, the average values slightly decrease for the higher reduction of $R = 7$.

Visual inspection of Fig. 6.7 further suggests that k-t-GRAPPA performs similar to SW in imaging of static tissue, with a strong enhancement in the area of the heart. In the case of PEAK-GRAPPA, the relative g-factor increase in pixels containing motion is much less than for k-t-GRAPPA. Maps of g_x^{avg} -factors for PEAK-GRAPPA exhibit smooth spatial variations with only a minor variation between both reduction factors.

Figure 6.7: Temporal average g -factor noise distributions are displayed for Sliding Window (SW), k -t-GRAPPA (k -t-GR) and PEAK-GRAPPA (PEAK) at reduction factors $R = 5$ and $R = 7$, as well as for conventional GRAPPA reconstruction at reduction factor $R = 3$. GRAPPA g -factors are plotted with separate scaling, since values highly exceed the g -factors of the three time-resolved methods. Maps of $g_{\mathbf{x}}^{\text{avg}}$ -factors obtained from frequency combination of the analytical $g_{\mathbf{x}f}$ -factors are shown next to temporal averages of the statistically derived $\hat{g}_{\mathbf{x}t}$ -factors. Both maps are in very good agreement. For k -t-GRAPPA and PEAK-GRAPPA, the total noise contributions in moving tissue are higher than in static tissue.



method		g_x^{avg} -factors	g_x^{avg} -factors
		maximum	mean
GRAPPA	$R = 3$	8.52	4.68 ± 1.22
SW	$R = 5$	0.45	0.45
	$R = 7$	0.38	0.38
k-t-GRAPPA	$R = 5$	0.92	0.53 ± 0.14
	$R = 7$	1.07	0.46 ± 0.16
PEAK-GRAPPA	$R = 5$	0.72	0.56 ± 0.08
	$R = 7$	0.69	0.49 ± 0.08

Table 6.2: The table contains maximum values and mean values of the g_x^{avg} -factors depicted in Fig. 6.7 for GRAPPA (reduction factor $R = 3$), SW, k-t-GRAPPA and PEAK-GRAPPA (reduction factors $R = 5$ and $R = 7$).

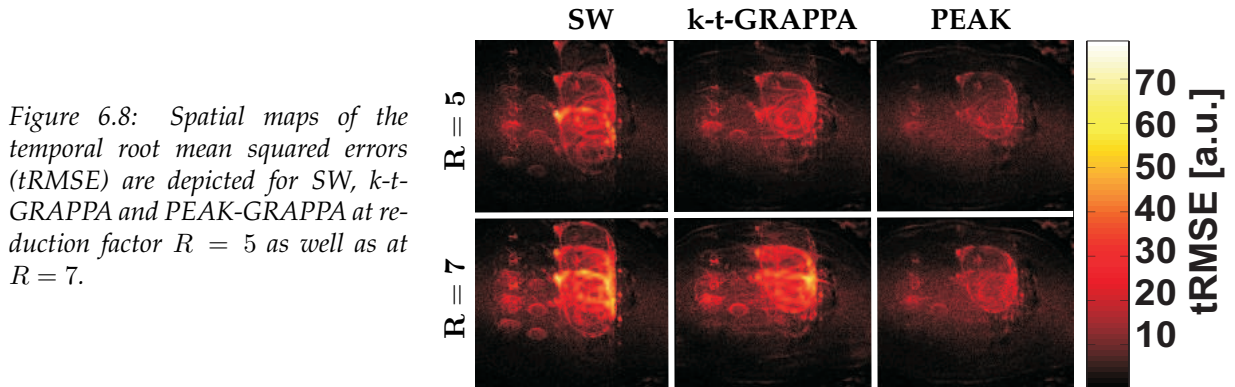


Figure 6.8: Spatial maps of the temporal root mean squared errors (tRMSE) are depicted for SW, k-t-GRAPPA and PEAK-GRAPPA at reduction factor $R = 5$ as well as at $R = 7$.

The temporal average g_x^{avg} -factor maps of Fig. 6.7 confirm an advantageous noise behavior when exploiting temporal correlations in image reconstruction. In the same acquisition scenario, k-t-kernel based reconstructions outperform purely k-space based kernel reconstruction in terms of g-factor results. Nevertheless, as g-factor values further decrease at the higher reduction for all three time-resolved methods, the trade-off between noise suppression and reconstruction fidelity requires further consideration.

Noise variances and temporal bias

Figure 6.8 addresses the systematic reconstruction error which is assessed in comparison with the Nyquist-sampled reference. The tRMSE values determine the temporal bias of the reconstruction and hence yield a counterpart to the investigation of noise variances. Comparison of the spatial maps of Figs. 6.7 and 6.8 demonstrate: whereas temporal average g_x^{avg} -factors decrease for the higher reduction factor, systematic errors in the reconstruction increase. In all three time-resolved methods, tRMSE errors are related to moving tissue.

For SW, unresolved fold-over artifacts become apparent in the form of ghosts of the moving heart. SW reconstruction exhibits the largest tRMSE values at both reduction factors, which are listed as part of the maximum and mean values of Table 6.3. The mean tRMSE, however, is only slightly higher than for k-t-GRAPPA. Also for k-t-GRAPPA, a strong increase in the maximum tRMSE values is observed for the higher reduction factor of $R = 7$ (cf. Table 6.3).

For PEAK-GRAPPA, the spatial maps of tRMSE reveal temporal bias mostly at the heart

method		tRMSE	
		maximum	mean
SW	$R = 5$	78.56	6.62 ± 6.39
	$R = 7$	76.76	8.41 ± 9.12
k-t-GRAPPA	$R = 5$	45.13	6.08 ± 5.11
	$R = 7$	72.10	8.17 ± 8.35
PEAK-GRAPPA	$R = 5$	25.45	5.33 ± 3.40
	$R = 7$	32.57	6.19 ± 4.38

Table 6.3: The table lists maximum and mean tRMSE values derived from the spatial maps depicted in Fig. 6.8 for SW, k-t-GRAPPA and PEAK-GRAPPA at reduction factors $R = 5$ and 7.

contours (cf. Fig. 6.8). Maximum tRMSE are much lower for PEAK-GRAPPA than for k-t-GRAPPA and SW (cf. Table 6.3). Furthermore, the increase of the tRMSE when moving from a reduction factor $R = 5$ to a factor of $R = 7$ is relatively low. The relative increase between reduction factor $R = 5$ and $R = 7$ is approximately 1.6 for k-t-GRAPPA and yields 1.3 in the case of PEAK-GRAPPA. Nevertheless, resulting maximum values at $R = 7$ are 72.10 in k-t-GRAPPA versus 32.57 in PEAK-GRAPPA. Between all three methods and both reduction factors, average tRMSE values are the lowest for PEAK-GRAPPA. Both tRMSE maps and maximum/average tRMSE values suggest that PEAK-GRAPPA provides the highest temporal fidelity in the comparison.

Temporal fidelity as visible in the magnitude images

For visualization of the effects onto temporal resolution, the depiction of a single image column over the range of acquired time frames is provided in Fig. 6.9. The figure illustrates two main influences that compromise temporal fidelity: temporal smoothing and noise enhancement. For conventional GRAPPA reconstruction, the strong noise enhancement - despite the lower reduction factor - is visible. The high noise level decreases the temporal quality. Temporal smoothing, however, is not observed.

For SW, temporal smoothing appears at both reduction factors and is more severe at the higher reduction. Artificial structures appear during contraction of the heart. Noise influences seem to be minor and are not visible in areas of static tissue.

A similar behavior is observed for k-t-GRAPPA in static tissue. At $R = 5$, image quality is comparably improved in moving tissue and artifacts as arising in SW are not present. A slight noise enhancement during systole is hinted for k-t-GRAPPA at $R = 5$. At $R = 7$, however, strong artifacts and noise influences are revealed.

PEAK-GRAPPA exhibits a benign noise behavior without artificial image alterations. Very slight spatial smoothing is indicated within tissue compartments, however without considerably compromising the temporal quality at $R = 5$. For the higher reduction of $R = 7$, smoothing and noise influences increase in visibility. Nevertheless, even at $R = 7$, high image quality is noticeable for the PEAK-GRAPPA reconstruction.

Figure 6.10 illustrates how single pixel magnitudes of different methods evolve over the course of time frames. Signal contributions within two pixels are displayed: one pixel located in the blood pool of the heart and one pixel within the area of fat tissue. Whereas the latter displays constant contributions from static tissue, the first reflects parts of the myocardium during later time frames and returns to blood pool depiction thereafter. This becomes visible

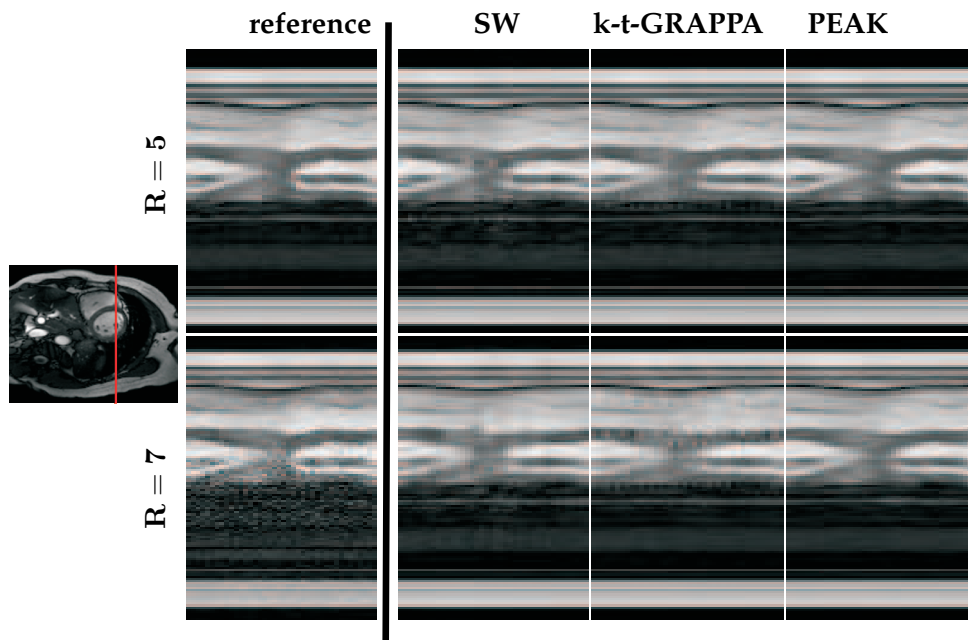


Figure 6.9: Magnitude signal of the same image column as in Fig. 6.6 is displayed over the range of acquired time frames. The Nyquist-sampled reference, GRAPPA reconstruction for reduction $R = 3$, as well as SW, k-t-GRAPPA and PEAK-GRAPPA for reduction factors $R = 5$ and $R = 7$ are shown. The selected image column comprises static tissue as well as the moving heart chambers.

in the signal drop of magnitudes of the two upper plots of Fig. 6.10. Whereas SW, k-t-GRAPPA and PEAK-GRAPPA are in excellent accordance with the reference in the case of the static pixel for both reduction factors (two lower plots), major differences become visible in the case of the moving tissue. A reduced drop of the main signal dip is visible for the reduction factor $R = 7$, in particular for SW and k-t-GRAPPA reconstruction.

Pixel-dependent signal and noise transfer

Figures 6.11 and 6.12 depict the frequency response according to g_{xf} -factors (Fig. 6.11) and the reconstruction of a delta input signal (Fig. 6.12) for the same two pixels as described above. Different frequency filtering characteristics become evident. For SW, a main lobe - whose width is usually determined by the **full width at half maximum (FWHM)** - and several side-lobes separated by zero-crossings are visible. The results follow the known theory, but are expressed in the framework presented here. Therefore, characteristics detected for k-t-GRAPPA and PEAK-GRAPPA can be directly compared to a known frequency response.

Both k-t-GRAPPA and PEAK-GRAPPA exhibit contributions from all resolved temporal frequencies. In both, frequency responses vary spatially as a result of parallel imaging reconstruction. For k-t-GRAPPA, large contributions of high temporal frequencies are observed. A fast decay is given for the pixel in static tissue, high frequency contributions, however, remain large. PEAK-GRAPPA exhibits a smooth decay over the range of temporal frequencies. In all considered cases, the FWHM is the widest for PEAK-GRAPPA.

The **tPSF** obtained from reconstruction of a delta input signal using the in vivo calibrated weights in x-f-space confirm the characteristics revealed in the frequency resolved g_{xf} -factors. k-t-GRAPPA provides a similar **FWHM** as SW reconstruction, however, without completely

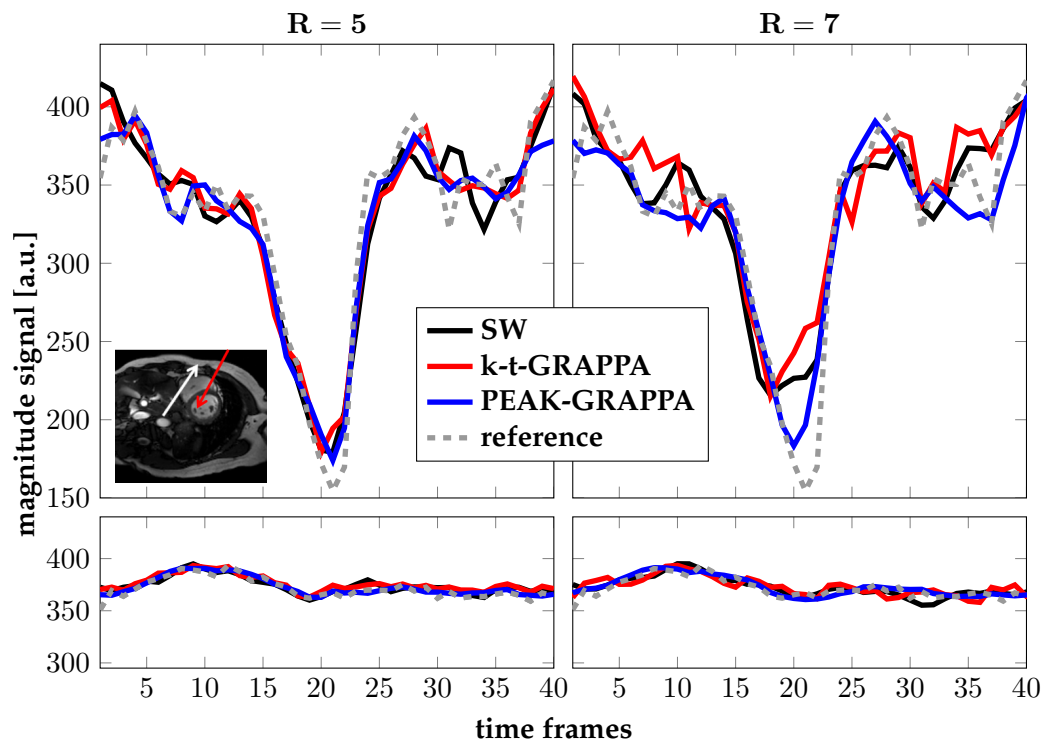


Figure 6.10: The temporal evolution of the magnitude signal for two individual pixels is depicted for all considered time-resolved reconstruction methods and two reduction factors. Dotted time curves show the Nyquist-sampled reconstruction for reference. One pixel is located within the blood pool (red arrow) and depicts the myocardium during systole. The other pixel reflects magnitude signal in the static area of fat tissue (white arrow).

suppressing any temporal frequency. In the higher temporal frequency range, k-t-GRAPPA reaches a plateau. PEAK-GRAPPA provides monotonous decay except for a slight increase at the higher temporal frequency components in some cases. The FWHM of PEAK-GRAPPA exceeds the one obtained in SW and k-t-GRAPPA for both reduction factors.

The two main observations from Figs. 6.11 and 6.12 are: first, time-resolved parallel imaging results in frequency responses which depend on the spatial position. Second, the temporal frequency responses for the time-resolved parallel imaging scenarios shown here cover the overall range of frequency components. Third, PEAK-GRAPPA provides the most benign frequency filtering characteristics between the three considered methods.

The influence of the number of coil elements

All previous findings of the three time-resolved methods indicate the main difference to be the usage of the coil domain (parallel imaging) or excluding it (SW) in the reconstruction process - in addition to the temporal domain. The effect on the numbers of coil elements and the transfer between time-resolved parallel imaging and SW is addressed in Figs 6.13 and 6.14, respectively.

Figure 6.13 shows spatially averaged g_x^{avg} -factors and tRMSE values for different numbers of coil elements virtually compressed. Since the coil domain is not relevant in SW reconstruct-

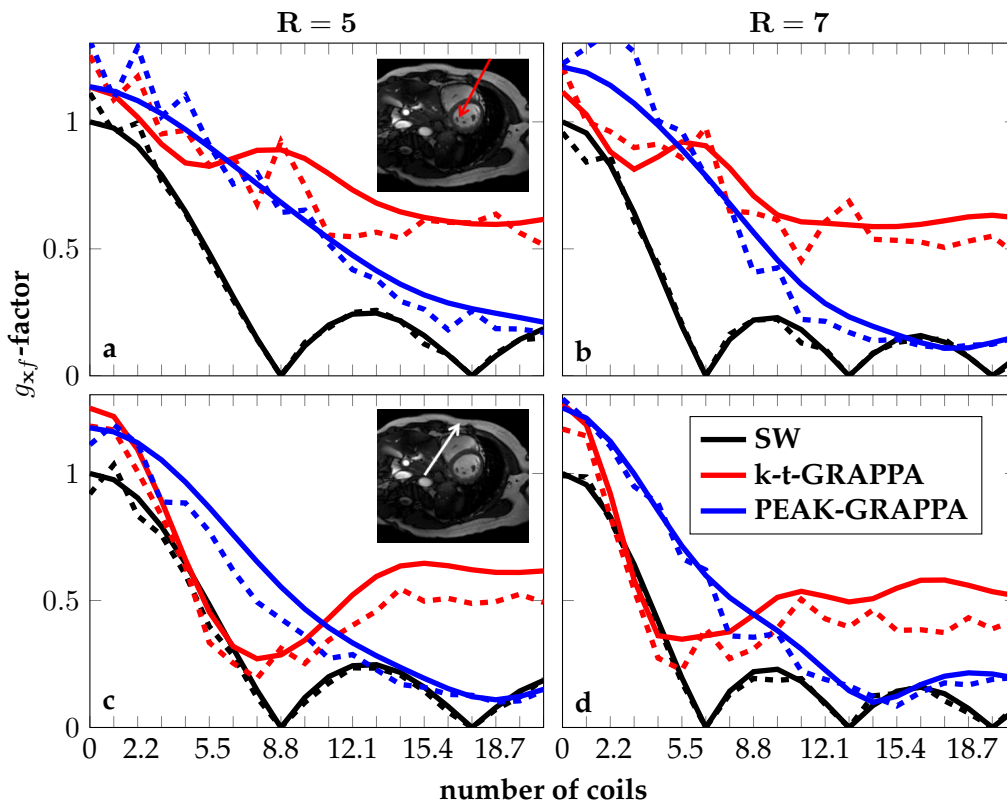


Figure 6.11: The g_{xf} -factor values for the same two pixels as shown in Fig. 6.10 are plotted over the zeroth and all positive temporal frequencies for SW, k-t-GRAPPA and PEAK-GRAPPA. Values for the pixel depicting moving tissue are contained in (a,b) and static tissue contributions from fat tissue is depicted in (c,d). The columns correspond to reduction factor $R = 5$ (a,c) and $R = 7$ (b,d). Whereas solid lines illustrate analytically derived g_{xf} -factors, dotted lines demonstrate the respective result from the pseudo-replica evaluation.

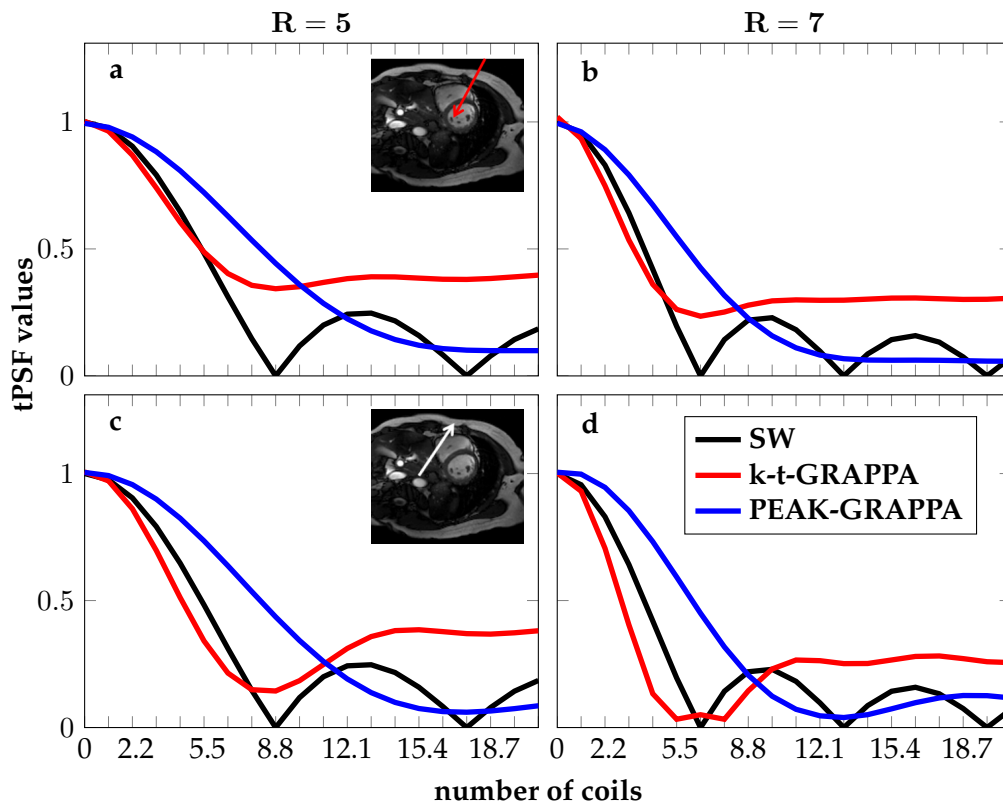


Figure 6.12: Analogous to Fig. 6.11, $tPSF$ values of the two pixels are shown as obtained from SW, k -t-GRAPPA and PEAK-GRAPPA. The plots depict reconstructed values, which were derived by applying the *in vivo* calibrated weights to a delta input signal in x - f -space. $tPSF$ values differ only slightly between the moving tissue pixel (a,b) and the static one (c,d). Quicker decay occurs when moving from the reduction factor $R = 5$ (a,c) to $R = 7$ (b,d).

tion, spatially averaged g_x^{avg} -factors are constant in all coil scenarios. k -t-GRAPPA and PEAK-GRAPPA, however, rely on variations provided by multiple coils and the coil geometry. When only a single coil element is used, k -t-GRAPPA and PEAK-GRAPPA incorporate only temporal correlations in the reconstruction process. Both methods then act similar to SW, but with *in vivo* calibrated temporal interpolation kernels. With a single coil, the kernel extent along the temporal domain determines the averaging of neighboring time frames. The extent is the widest for k -t-GRAPPA (see Fig. 5.3), therefore, decreasing noise variances is the highest for k -t-GRAPPA in the single-coil scenario.

Comparing mean g_x^{avg} -factors and mean tRMSE values versus the number of incorporated coils discloses the influence of time-resolved parallel imaging: mean tRMSE decreases while g_x^{avg} -factors increase. For the scenarios of only one or two coil elements, calculation of tRMSE in comparison with the reconstructed Nyquist-sampled reference is affected by the reduced coverage of the few coil elements.

In the cases of two and more coil elements, PEAK-GRAPPA provides the highest g_x^{avg} -factors (nevertheless below 1) and lowest tRMSE values for both reduction factors in terms of spatial averages shown here (comprising moving and static tissue). The simultaneous depiction of noise and fidelity factors demonstrates again the antagonistic behavior of noise variances and temporal bias in k -t-GRAPPA and PEAK-GRAPPA, however, with respect to exploiting spatial correlations based on multiple receiver coils.

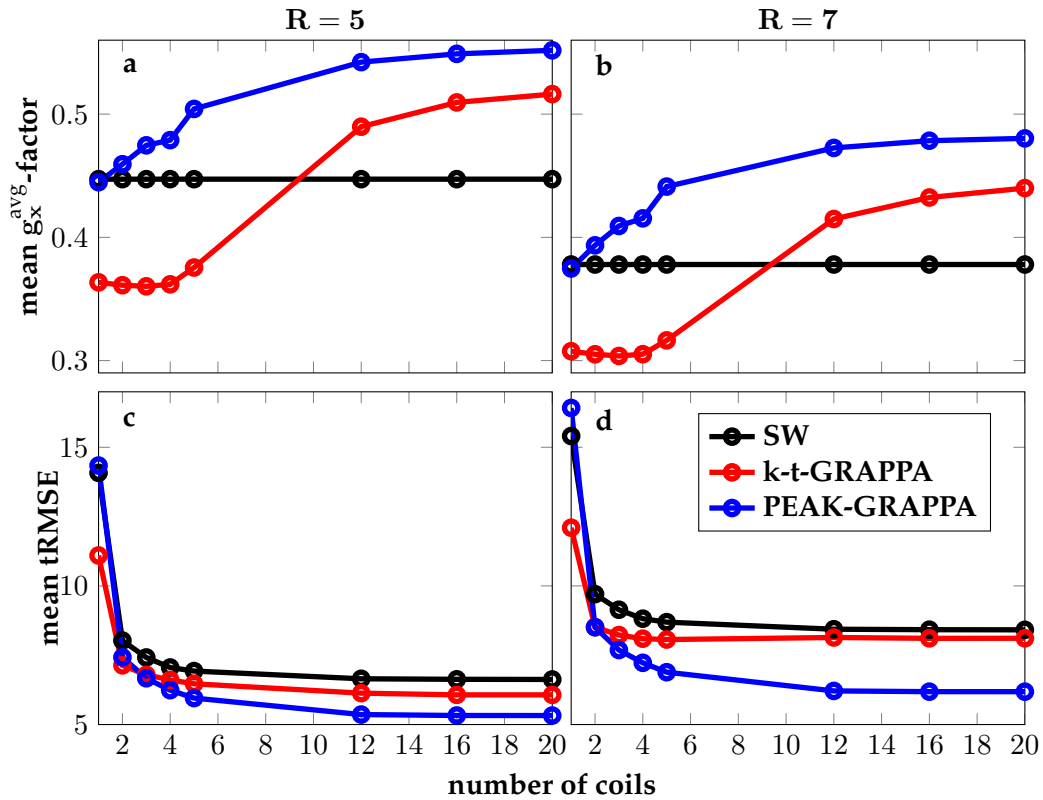


Figure 6.13: Spatially averaged g_x^{avg} -factors (a,b) and spatially averaged tRMSE values (c,d) are depicted with respect to a range of reduced numbers of coils. The pixel-wise g_x^{avg} -factors and tRMSE values were additionally spatially averaged to obtain a single value for each scenario. Derived values are accentuated by a circular marker and are connected to guide the eye.

Figure 6.14 illustrates a step-wise reduction of using coil sensitivity information in the time-resolved parallel imaging reconstruction until a single-coil scenario is reached. This corresponds to the step-wise reduction of the parallel imaging influence to pure temporal interpolation. Along the two axes showing coil elements and temporal frequencies, the transition in the characteristics of the temporal frequency responses is reflected. This includes the decrease of spatial variations when moving to reduced coil scenarios as well as the emergence of side lobes along the higher frequency range.

6.2.4. Discussion

The presented signal and noise transfer analysis of a retrospectively k-t-sub-Nyquist sampled in vivo cardiac acquisition comprises the evaluation of image noise as well as characteristics in the temporal frequency response with respect to spatial position and in various reduction factors. The utilized $g_{x,f}$ -factor analyses provides a generalization of the known GRAPPA g-factor formalism for time-resolved methods such as k-t-GRAPPA and PEAK-GRAPPA. Pixel-wise noise variances are quantified in x-f-space where contributions are considered over the range of resolved temporal frequencies. Thereby, method-specific frequency responses indicating temporal frequency filtering are revealed.

Furthermore, temporal average g_x^{avg} -factor maps are derived by frequency combination of

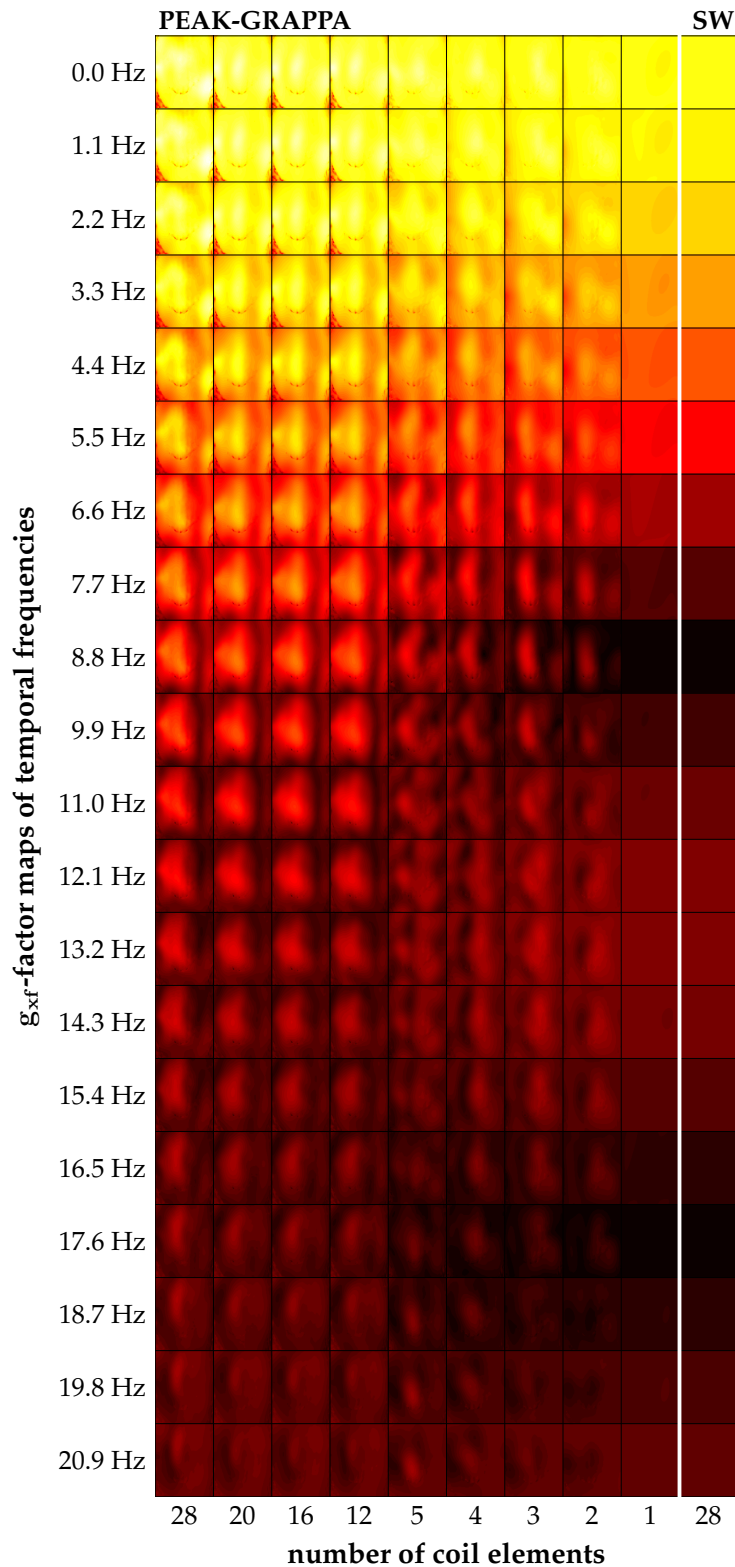
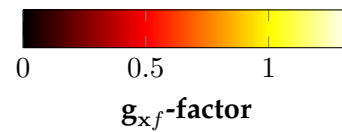


Figure 6.14: Spatial maps of g_{xf} -factors are depicted beginning with the zeroth temporal frequency and ranging over all positive resolved temporal frequency (from top to bottom row). Virtual coil scenarios of varying numbers of coil elements are demonstrated for PEAK-GRAPPA, beginning with the original scenario of 28 coil elements and reductions to 20, 16, 12, 5, 4, 3, 2 and 1 coil elements (from left to right column). Maps of g_{xf} -factors in the case of SW (including the original 28 coil elements) is shown next to the single-coil-scenario of PEAK-GRAPPA. The transfer from incorporating coil sensitivities in addition to the temporal domain (time-resolved parallel imaging with PEAK-GRAPPA) to only utilizing the temporal domain (SW) is illustrated. The reduction factor applied is $R = 5$ in all cases shown.



g_{xf} -factors. This provides a measure directly comparable to the known g_x -factor metric of non-time-resolved parallel imaging methods. The presented tools facilitate theoretical analyses where previously solely heuristic observations from practical settings could be derived. Furthermore, the presented theory confirms noise reduction at the expense of temporal smoothing in a general framework.

The analytically derived g_{xf} - and g_x^{avg} -factors are validated using statistically derived relative noise variances based on the concept introduced in [Robson et al., 2008]. Whereas g_{xf} -factors are compared to relative standard variations between sub- and full-Nyquist-sampled pseudo-replica reconstruction in x-f-space. The frequency combined g_x^{avg} -factors are evaluated based on temporal averaged relative standard variations derived from pseudo-replica images in x-t-space. In all cases, analytical and statistical results are in excellent agreement (Figs. 6.5, 6.6 and 6.7 as well as Fig. 6.11).

Temporal frequency filtering characteristics

The temporal frequency domain reflects method-dependent temporal frequency responses in the signal and noise transfer (Figs. 6.5, 6.6, 6.11 and 6.12). Temporal frequency filtering is revealed by g_{xf} -factor values below 1 in all time-resolved methods considered. Furthermore, delta input analyses captured by the tPSF here are used to determine method-dependent filtering characteristics (Fig. 6.12). Similar to the approach presented here, modulation transfer functions were proposed in [Chao et al., 2010] for the assessment of temporal frequency properties in UNFOLD-SENSE [Madore, 2002] and variants of k-t-SENSE. Based on the depiction in x-f-space as well as the tPSF analysis, typical filter characteristics can be investigated.

The three time-resolved methods considered all exhibit properties of a low-pass filter with decreasing FWHM at higher reduction. The frequency response is spatially constant in the case of SW, and depends on the spatial position in the case of the two time-resolved parallel imaging methods. This is a new insight for these methods. The frequency response analysis of k-t-GRAPPA and PEAK-GRAPPA allows to directly relate the revealed characteristics to the known frequency filtering behavior of SW. The SW convolution kernel is shaped as a box and hence, leads to a frequency response that is described by the absolute values of the sinc function. FWHM of the main lobe is one marker of filter effects. The several side-lobes and zero-crossings indicates leakage effects. The FWHM of the main lobe decreases with increasing kernel extent. The non-trivial shapes of three-dimensional convolution kernels for k-t-GRAPPA and PEAK-GRAPPA reveal different responses in tissues of static versus motion affected areas. The investigation illustrates how the frequency response of k-t-GRAPPA is similar to SW in the case of static tissue, however, covering all temporal frequencies, and increases in permeability in moving tissue. PEAK-GRAPPA exhibits benign filtering behavior by providing the widest FWHM - in comparison with SW and k-t-GRAPPA - as well as no side-lobes and by presenting almost monotonous decay over the range of temporal frequencies.

The temporal frequency filtering behavior is directly linked to the kernel geometry and relies on the sampling pattern as well. The wider FWHM and smooth variations for PEAK-GRAPPA are explained by the smaller extent in k-t-space of the convolution kernel and the smooth variations in weighting factors. The latter is evoked by the increased density in the optimized sampling pattern while the first is implied by the chosen kernel geometry. Both time-resolved parallel imaging methods exhibit the capability to distinguish between areas of moving and static tissue in the temporal filtering process evoked by the usage of in vivo coil sensitivities.

g-Factors

The derivation of g_x^{avg} -factor maps demonstrates an advantageous noise behavior for the time-resolved methods considered (Fig. 6.7 and Table 6.2). Values below 1 indicate a noise reduction besides the additional penalty arising due to undersampling by reduction factor R . The temporal average contributions facilitate the comparison of time-resolved parallel imaging with the known g-factor metric of non-time-resolved parallel imaging methods [Pruessmann et al., 1999, Brau et al., 2008, Breuer et al., 2009]. The comparison confirms the improved SNR performance of k-t-GRAPPA and PEAK-GRAPPA versus conventional GRAPPA in a theoretical framework.

However, the improved SNR is accompanied by a signal reduction in the domain of temporal frequencies of which temporal blurring can possibly arise. Whether temporal blurring is induced relies on the temporal frequency filter response of the reconstruction method as well as the bandwidth of temporal variations present in the monitored dynamics. Sampling of discrete time frames itself imposes the requirement on band-limited support in the temporal frequency domain. This is further affected by k-t-sub-Nyquist sampling and time-resolved parallel imaging reconstruction. Nevertheless, k-t-sub-Nyquist sampling facilitates in some cases to increase the repetition rate of data acquisition. The overall effect on temporal blurring is therefore dependent on many factors and needs to be considered with respect to the concrete application.

The presented cardiac scenario is based on full-Nyquist sampled data to compare the effect of k-t-sub-Nyquist sampling in different scenarios and with respect to a common reference. However, if k-t-sub-Nyquist sampling would have been applied in the presented cardiac measurement, the overall acquisition time would have been drastically reduced which provides increased patient comfort and more scan efficiency in the clinical context. Reduced measurement times are furthermore beneficial in decreasing the potential for patient motion to compromise the depiction fidelity. Regardless of acquisition times, the presented analysis shows that temporal fidelity is of good quality for k-t-GRAPPA and PEAK-GRAPPA at $R = 5$. It is also in an acceptable range for PEAK-GRAPPA at $R = 7$ (Figs. 6.9 and 6.10).

tRMSE

The tRMSE analysis is a cumulative indicator of temporal fidelity (Fig. 6.8 and Table 6.3, as well as Fig. 6.13). The g_x^{avg} -factors and tRMSE values together demonstrate the counterparts of temporal bias and noise variances in the time-resolved methods. Considering noise behavior solely cannot be the only predictor for a performance evaluation of reconstruction methods. Accuracy of temporal evolutions in particular yields an important criterion in time-resolved reconstruction methods.

In SW, where weights are not calibrated on in vivo coil sensitivity data and k-space neighbors are not incorporated in the reconstruction, temporal frequency filtering is applied regardless of the degree of motion present in the time series of individual spatial positions. The applied filter is independent of the position within the image as well as the number of coils utilized in the data acquisition. A high noise reduction is obtained by temporally averaging k-t-space data according to the extent of the interpolation kernel. Thereby, high tRMSE values arise which further increase for higher reduction factors.

For k-t-GRAPPA and PEAK-GRAPPA, temporal frequency filtering appears attenuated in imaged areas of higher dynamics. Consequently, lower tRMSE values than in SW are obtained,

however, with lessened noise reduction. In comparing SW, k-t-GRAPPA and PEAK-GRAPPA, the latter achieves the lowest tRMSE in all scenarios (Fig. 6.8 and Table 6.3, as well as Fig. 6.13), but shows the least noise suppression of the three time-resolved methods (Fig. 6.7 and Table 6.2).

Generality of the framework

The generality of the presented concepts facilitates its application to any k-t convolution kernel based reconstruction method of which weights are derived in advance. An extension to the third spatial dimension follows directly, which facilitates application in time-resolved volume imaging. The extension of the g-factor concept allows for *inter*-method and *intra*-method comparison. Inter-method comparison is established between time-resolved and non-time-resolved methods, e.g. k-t-GRAPPA and GRAPPA, as well as between time-resolved parallel imaging and purely time-resolved methods, e.g. k-t-GRAPPA and SW. Intra-method comparison, as for instance between k-t-GRAPPA and PEAK-GRAPPA, is useful to evaluate the effect of different parameters on noise transfer.

The concept presented here in x-f-space may also be applied to non-time-resolved methods. However, in order to compute $g_{x,f}$ -factors in the case of serial image acquisition and non-time-resolved image reconstruction of each time frame, one set of temporal average weights need to be derived. This might impose a minor modification to the original reconstruction process, if different sets of weights were initially incorporated over the domain of time frames. In the case of non-time-resolved GRAPPA, the described algorithms can be directly applied, if GRAPPA weights are derived only once and are repeatedly applied. If weights are calibrated frame-by-frame, a temporal average would be required to derive an overall convolution kernel.

A parallel imaging method in volume imaging and based on sub-Nyquist-sampling in two directions is introduced in CAIPIRINHA [Breuer et al., 2005a]. Although non-time-resolved 3-dimensional (in space) CAIPIRINHA scenarios provide a three dimensional sub-Nyquist sampling pattern similar to time-resolved 2-dimensional k-t-GRAPPA reconstructions, there is a clear difference between incorporating a further spatial versus the temporal dimension. The presented analysis demonstrates how incorporation of the temporal domain has a completely different influence.

The influence of the number of coils

The considerations of virtual coil element reduction (Figs. 6.13 and 6.14) demonstrate transitions between the parallel imaging influence and the usage of temporal correlations in the context of fidelity (tRMSE) and g-factors. When the number of coils is reduced, parallel imaging reconstruction is successively suppressed until convergence to the SW approach is obtained. Weighting along the temporal domain is prioritized when the complementary coil information diminishes. The strong weighting of the temporal domain supports greater noise reduction. At the same time, however, artifacts and temporal smoothing is introduced. The contrary findings of tRMSE and g-factors when compressing the coil array support the observation (Fig. 6.13).

Further, the cumulative analysis presented here does not reflect any improvements after a number of 12 coil elements is reached and when moving to higher numbers of coil elements. Note that the reduced coil array scenarios assume the identity as receiver covariance matrices, hence, are assumed to be fully decorrelated, in the g_x^{avg} -factor computation. Nevertheless, stagnation of improvement with respect to increasing the number of coil elements was similarly

reported in other studies, for instance [Schnell et al., 2014].

The spatially dependent filtering characteristics for PEAK-GRAPPA are benign in terms of the almost monotonous decay over temporal frequencies as well as the increased noise suppression in static tissue versus the greater permeability in areas of moving tissue. The transition from time-resolved parallel imaging to purely temporal interpolation demonstrates that by incorporating the coil sensitivities in the reconstruction process, leakage is avoided and the FWHM filter behavior is spatially adjusted (Fig. 6.14).

Conclusion

The presented cardiac application and previous discussions of parallel imaging discloses the following relations of incorporating different domains:

1. With ACS weight calibration, the usage of coil sensitivities as part of the reconstruction process entails regional noise increases, but also guides the reconstruction process to restore depiction fidelity in sub-Nyquist sampling scenarios
2. By incorporating temporal correlations, a noise amplification due to sub-Nyquist sampling is reduced at the expense of temporal fidelity.
3. With a combination of assessing coil sensitivity as well as temporal information, a spatially varying noise transfer as well as spatially variable temporal frequency filtering is evoked.

The main gain of extending the existing g-factor formulation to the set of time-resolved parallel imaging reconstruction methods is the establishment of a shared framework for the analysis. Given a common basis, performances can be evaluated and compared: performances between various acquisition schemes and method-specific parameters such as the convolution kernel, the size and sampling strategy of ACS data, performances of time-resolved versus non-time-resolved parallel imaging methods, and last but not least, performance comparison with other established approaches in time-resolved parallel imaging, e.g. k-t-SENSE [Tsao et al., 2003a] and k-t-PCA [Pedersen et al., 2009]. The latter is established in particular due to the complementary extension of g-factor considerations for image space based time-resolved parallel imaging methods [Binter et al., 2016].

6.3. Summary of the g-factor analysis in (time-resolved) parallel imaging

In this chapter, theory and methods towards a unified general framework for parallel imaging methods were presented. The aim was to shed light on the comparison of and the transition between non-time-resolved and time-resolved parallel imaging methods. To this end, a GRAPPA based formulation of SENSE was derived and variants of both methods - termed trSENSE and extGRAPPA - were investigated.

Furthermore, a general g-factor framework for time-resolved parallel imaging was derived and demonstrated in a cardiac application. All analyses shown are generally applicable to any (k-t)-kernel based parallel imaging reconstruction method. The application presented revealed the different implications of incorporating information from the coil and/or the time domain. Transitions from k-t-GRAPPA and PEAK-GRAPPA (time-resolved parallel imaging) to conventional GRAPPA (pure parallel imaging) and SW (purely time-resolved) were established.

Chapter 7

k-t-sub-Nyquist sampled parallel EPI

This chapter addresses the advantages and disadvantages of parallel imaging in EPI. A k-t-sub-Nyquist sampled parallel EPI acquisition and reconstruction scheme is proposed in order to improve spatial resolution, enhance volume coverage at a given TR and mitigate in-plane susceptibility artifacts in EPI. The developed method is applied to - but not limited to - [dynamic susceptibility contrast \(DSC\)](#) weighted cerebral perfusion imaging.

A brief introduction into the clinical motivation of cerebral perfusion imaging as well as a discussion of earlier achievements in sub-Nyquist sampled EPI is given in Sec. 7.1. Subsequently, acquisition strategies and reconstruction approaches developed within this work are presented in Sec. 7.2. The pulse sequence design of k-t-EPI consists of interleaved EPI with three different ACS acquisition strategies: *inplace*, *dynamic extra* and *extra* (Sec. 7.2.1). Image reconstruction is based on k-t-GRAPPA (Sec. 7.2.2). The strategies suggested are first evaluated based on in vivo measurements with flip angle induced temporal contrast dynamics (Sec. 7.2.3) and then successfully applied in DSC weighted cerebral perfusion measurements with contrast agent in patients (Sec. 7.2.4). Results are presented and discussed in Secs. 7.3 and 7.4.

The development and initial feasibility results of k-t-EPI - including some of the figures - were published in [[Ramb et al., 2016b](#)]. Parts of this work have been presented as conference contributions [[Ramb et al., 2014b](#), [Ramb et al., 2015b](#), [Ramb et al., 2015c](#), [Ramb et al., 2016a](#)]. Note that in using k-t-sub-Nyquist sampling patterns in EPI, the sampling scheme leads to a modification of the acquired echo train. This directly affects the imaging behavior. As a practical consequence, optimization of sampling schemes by retrospective undersampling of full Nyquist-sampled data is not an option in EPI.

7.1. Goals

Overcome SNR limitations of parallel imaging at high reduction factors in EPI

Only few, previous reports on actively employing the temporal domain in the image reconstruction process of EPI acquisition exist (see Sec. 4.7). One difficulty reported for sub-Nyquist sampled parallel EPI is the loss of SNR, inherent to parallel imaging reconstructions. Time-resolved parallel imaging methods, such as k-t-GRAPPA, exhibit more benign g-factors compared to conventional parallel imaging methods, as particularly considered in Chapter 6. EPI with k-t-SENSE was considered in the context of myocardial perfusion acquisitions [[Tsao et al., 2003b](#)]. Keyhole imaging in combination with EPI was discussed by [[Zaitsev et al., 2001](#), [Zaitsev et al., 2005](#)]. A combination of k-t-GRAPPA or PEAK-GRAPPA and EPI has not been reported previously.

The purpose of this work is to translate the beneficial SNR behavior of k-t-GRAPPA to EPI in order to achieve higher reduction factors and ultimately reduced susceptibility artifacts. Different acquisition strategies are discussed as well as the question whether the advantageous imaging behavior of k-t-based methods in the context of dynamic measurements of motion is also beneficial in the context of dynamic contrast acquisitions. The aim is to overcome previous SNR limitations of parallel imaging in EPI and to facilitate higher reduction factors.

High resolution CBV assessment in DSC weighted cerebral perfusion imaging

Dynamic susceptibility contrast (DSC) weighted cerebral perfusion MRI aids the localization and delineation of tumorous tissue. Whereas a spatial resolution of approximately 1 mm is obtained in anatomical MR images, perfusion parameters derived from EPI, such as cerebral blood volume (CBV), are constrained to lower spatial resolutions (see Sec. 5.5.1). This is due to the trade-off between readout duration, evoked artifacts and temporal resolution of cerebral perfusion MRI.

The aim is to acquire CBV maps with higher spatial resolution and improved slice coverage at a given TR . This allows for a more detailed delineation of tumor borders and to reveal different graduation of tumorous tissue. The latter is particularly desirable in assisting stereotactic surgery biopsies.

7.2. Methods

A gradient spoiled EPI sequence including fat suppression and navigator acquisition for phase correction [Heid, 1997] was modified to follow a k-t-sub-Nyquist sampling pattern. Three different approaches to perform the additional acquisition of ACS data were realized. The sequence and acquisitions strategies are referred to as *k-t-EPI* with *inplace*, *dynamic extra* or *extra ACS* (Sec. 7.2.1).

k-t-GRAPPA reconstruction was used to account for k-t-sub-Nyquist sampling (Sec. 7.2.2). Subsequent to performance evaluation measurements (Sec. 7.2.3), the most benign acquisition strategy was applied in DSC weighted cerebral perfusion measurements (Sec. 7.2.4).

7.2.1. Data acquisition strategies

Interleaved readout trajectories were implemented to compose the k-t-EPI sequence. The interleave pattern was varied according to the respective ACS acquisition strategies. Different moments of blip gradients were thereby incorporated to perform the varying step-sizes in k-space along the phase encoding direction. The amount of phase encoding steps as well as the number of repetitions at a sampling rate of TR could be adjusted also in the ACS data.

Three different possibilities to combine interleaved sub-Nyquist-sampling as well as Nyquist-sampled ACS data were investigated. The three variants are presented in Fig. 7.1 and are referred to as: 1. *inplace ACS*, 2. *dynamic extra ACS*, 3. *extra ACS* acquisition. Figure 7.1 illustrates k-space trajectories with 5 interleaves (only 3 – 4 are shown). Each interleave shown performs undersampling by R (only partly in the case of *inplace ACS*). The combination of the R adjacent interleaves yields a full Nyquist-sampled Cartesian data set. The acquisition with R interleaves relates to reduction factor of R in a k-t-sub-Nyquist sampled acquisition. Therefore, k-t-EPI acquisitions are referenced by their reduction factor R below, although the net reduction in the case of *inplace ACS* is of course lower.

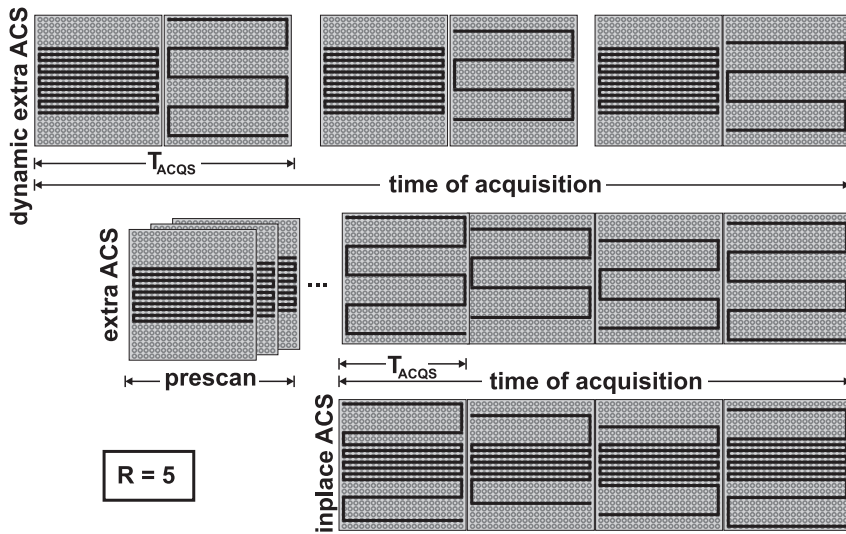


Figure 7.1: The three acquisition strategies for k - t -sub-Nyquist sampled EPI with ACS are illustrated for a single slice acquisition (T_{ACQS}). **Dynamic extra ACS:** ACS data is acquired during the actual scan, but separate from the higher resolution data, three interleaves are shown. **Extra ACS:** ACS data is acquired as part of a pre-scan. **Inplace ACS:** ACS data is acquired incorporated in the actual scan. Four interleaves are displayed for the extra and in-place ACS scenarios.

In order to reduce phase variations due to off-resonances between adjacent interleaves, **echo time shifting (ETS)** was utilized [Feinberg and Oshio, 1994]. To this end, a temporal delay was inserted before each undersampled echo train of an interleaved trajectory. This delay varied depending on the total number of interleaves and the current trajectory shift. For reduction factor R (corresponding to R interleaves) and an echo spacing of T_{es} , the different delays were $s \frac{T_{es}}{R}$, $s = 1, \dots, R - 1$. Combination of the different interleaves then exhibits a similar timing as an equivalent fully sampled trajectory. It has been shown that ETS provides more benign phase behavior in similar EPI trajectories [Zaitsev et al., 2001, Zaitsev et al., 2005]. More details on the three different ACS acquisition schemes are given below.

Acquisition of inplace ACS

In k - t -EPI with inplace ACS, the ACS lines were acquired as part of the otherwise k - t -sub-Nyquist sampled trajectory. In the periphery of the designated k -space extent, k -space traversal occurred in step sizes of $R\Delta k_y$, whereas Nyquist-sampling in step sizes of Δk_y was accomplished in the central k -space area. The two different blip gradients are depicted in the pulse sequence diagram in Fig. 7.2.

The k -space trajectory of k - t -EPI with inplace ACS consisted of three sections with 1. sub-Nyquist-sampling, 2. Nyquist-sampling and 3. again sub-Nyquist-sampling. While the second section was held constant over the entire measurement repetitions, the first and third section were shifted by $s\Delta k_y$, $s = 1, \dots, R - 1$ along the phase encoding direction. The latter evoked the k - t -sub-Nyquist sampling pattern over k - t -space confined by the k - t -space trajectory. The inplace acquired ACS data was directly inserted in the k - t -space data grid for image reconstruction.

In this particular case, ETS mitigates not only phase variations between adjacent time frames, but also compensates the two-fold k -space velocities as part of inplace ACS acquisitions. ETS was implemented by delaying the first and third section of each echo train. Intervals were prepared such that the Nyquist-sampled ACS section was acquired with the same timing and realizing the same TE in every measurement repetition.

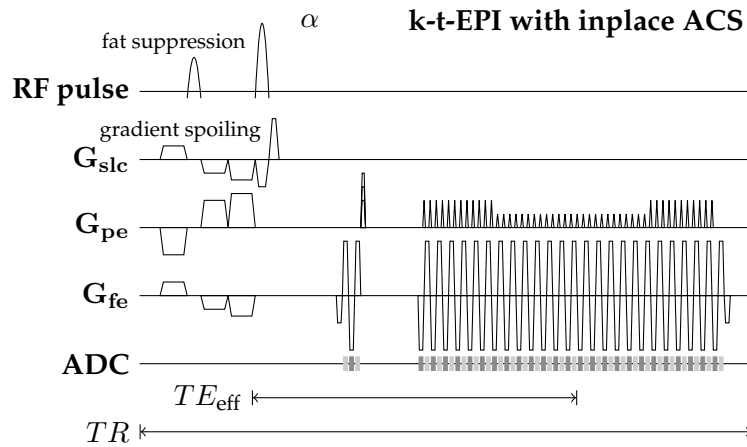


Figure 7.2: The pulse sequence diagram of a k-t-EPI trajectory with inplace ACS acquisition is shown. The readout of the dual density sampling pattern parts into three sections: first, sub-Nyquist-sampling with blip gradients that perform steps of $R\Delta k_y$ along phase encoding direction, second, the fully sampled ACS data section with Nyquist sampling (Δk_y), third, again sub-Nyquist-sampling. The variations over the measurement repetitions for a k-t-sub-Nyquist sampling pattern are realized by different phase encoding preparations that induce a series of shifts of the initial readout.

Acquisition of dynamic extra ACS

In k-t-EPI with dynamic extra ACS, the acquisition scheme consisted of two separate k-space acquisitions after the same RF pulse excitation. This is illustrated in Fig. 7.1, where the time of image acquisition T_{ACQS} embraces two sets of k-space trajectories: ACS data and sub-Nyquist-sampled imaging data. Directly subsequent to the acquisition of low resolution ACS data, the imaging measurement corresponding to the designated higher spatial resolution followed within the same echo train. The latter varied according to the k-t-undersampling pattern over the course of repetitions, whereas the ACS acquisition remained the same for each excitation. The pulse sequence diagram of Fig. 7.3 demonstrates the acquisition scheme of the two data sets that follow the same RF pulse excitation. Temporal delays for ETS were inserted after the completed ACS section and before the beginning of the imaging readout.

Acquisition of extra ACS

In k-t-EPI with extra ACS, the total amount of ACS data - including all temporal repetitions - was collected in an initial set of data acquisition. The actual k-t-sub-Nyquist sampled imaging data acquisition followed after the ACS section was completed. Figure 7.1 indicates the two-step procedure of separate prescan and the actual measurement trajectory (dots indicate the separation). The corresponding pulse sequence diagram is shown in Fig. 7.4.

The N_t^{ACS} separate echo train readouts to obtain N_t^{ACS} time frames of the low spatial resolution ACS data were realized with the same TE and TR as the actual readout. Navigator echoes for phase correction were acquired separately for both types of echo trains. Nyquist-sampled ACS readouts and k-t-sub-Nyquist sampled acquisitions were realized with a fixed step size each, Δk_y and $R\Delta k_y$, and with fixed blip gradients during the readout interval. ETS was utilized for the k-t-sub-Nyquist sampled echo train.

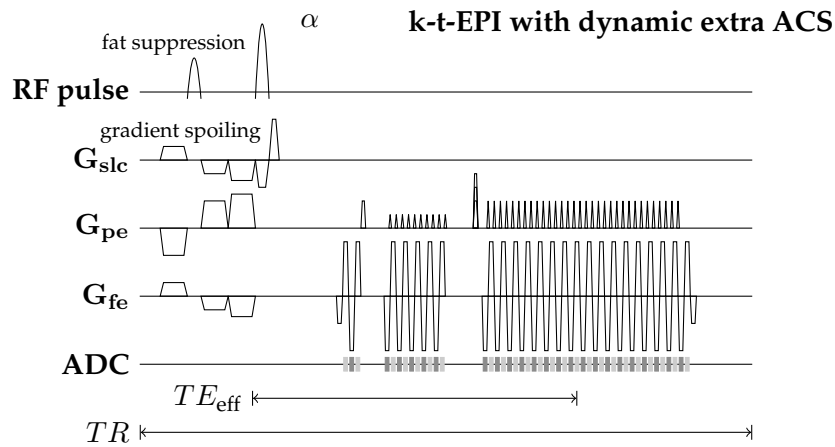


Figure 7.3: The pulse sequence diagram of a k - t -EPI with dynamic extra ACS scheme is illustrated. Directly after the acquisition of navigator echoes, the first (of two) preparation gradient prepares the initial k -space position for the sampling of low-resolution ACS data. After the ACS acquisition, the second preparation gradient is used to traverse to the k -space position of the k - t -sub-Nyquist sampled measurement. Only the latter preparation gradient varies over the measurement repetitions to achieve the k - t -pattern.

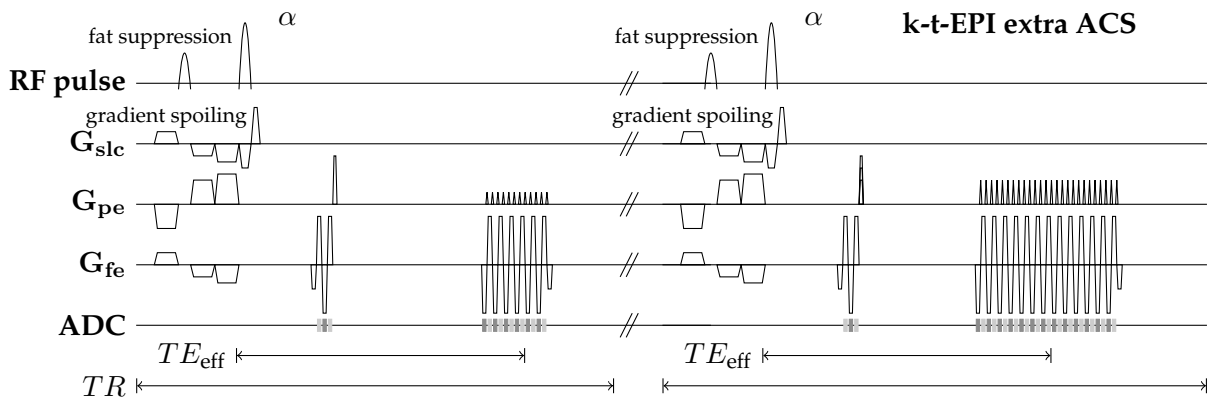


Figure 7.4: The pulse sequence diagram of k - t -EPI with extra ACS parts into two acquisition blocks, both of which can be each arbitrarily often repeated. The separation of both blocks is indicated by the small doubled slants. Whereas the echo train of the ACS data collection incorporates blips realizing Nyquist-sampled phase encoding steps of Δk_y , blip gradients that perform step sizes of $R\Delta k_y$ are utilized in the echo train of the sub-Nyquist-sampled data, according to the reduction factor R . In the latter, the shifts of the k - t -Nyquist-sampling pattern are implemented in different preparation gradients.

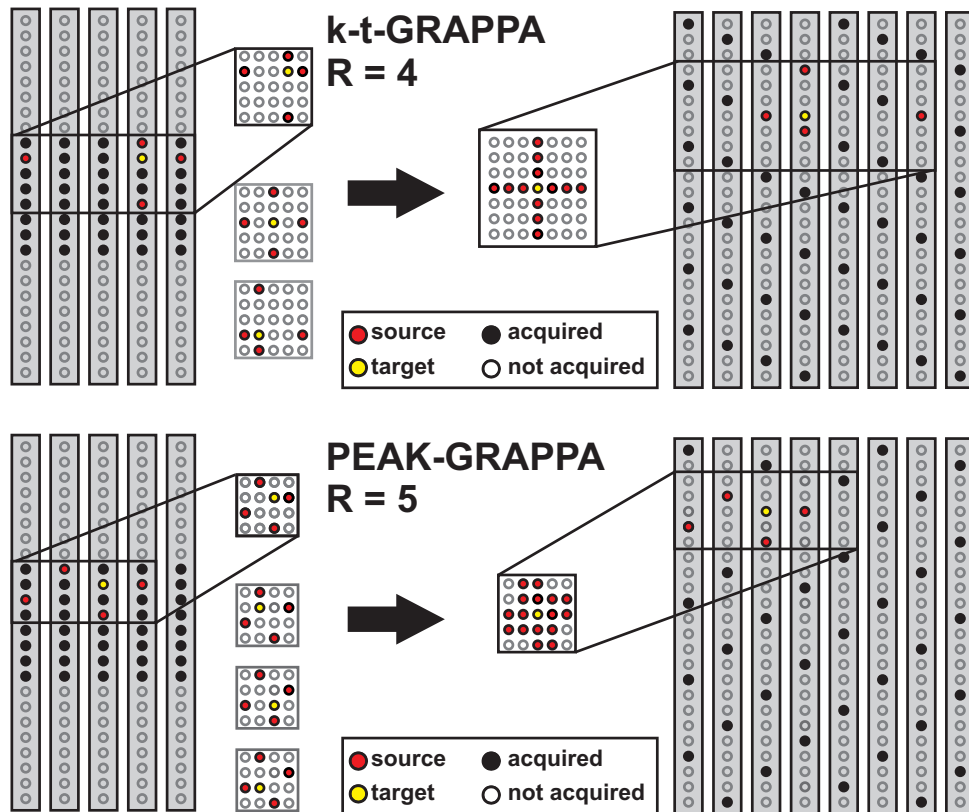


Figure 7.5: k-t-GRAPPA reconstruction is illustrated for reduction factor $R = 4$ and for the PEAK-GRAPPA pattern with $R = 5$. For the latter, the serial order of interleaves ($s = 0, 1, 2, 3, 4$) was permuted to $s = 0, 2, 4, 1, 3$. The depiction translates the k-t-space trajectories of k-t-EPI of Fig. 7.1 into the two sets of k-t-space data utilized in the two steps of the reconstruction. In the first step, reconstruction weights relating source and target data points are derived based on the ACS data and according to the reconstruction kernel geometry, shown on the left. In the second step, the reconstruction weights are combined into a single convolution kernel, which is then convolved with the k-t-sub-Nyquist sampled data, shown on the right.

Shifting in k-t-sub-Nyquist sampling

The k-t-EPI acquisitions are in accordance with the undersampling patterns used in time-resolved parallel imaging methods. Thereby, the additionally acquired ACS data allows for the usage of self-calibration methods such as k-t-GRAPPA. In all scenarios with $R > 5$, the interleaves were permuted to comply with the desired kernel geometry of PEAK-GRAPPA. Figure 7.5 illustrates the difference between serial and permuted order of interleaves.

Nyquist and Partial-Fourier sampled EPI

Nyquist sampled EPI acquisitions served as a reference. In order to achieve the designated TE , 5/8- or 6/8-Partial-Fourier had to be incorporated. Partial-Fourier sampling was performed as described in Sec. 3.5. The asymmetric sampling along the phase encoding direction was thereby reversed such that the central k-space was met after 1/8th or 2/8th of the echo train.

7.2.2. Image reconstruction for k-t-EPI

Image reconstruction for k-t-EPI acquisitions was implemented as a six steps procedure and was performed off-line in MATLAB (The Mathworks, USA). The workflow is schematically represented in Fig. 7.6. Depending on the acquisition pattern, the missing k-space data were addressed either by parallel imaging reconstruction or by the [projection onto convex sets \(POCS\)](#) algorithm. Five iterations were performed of the POCS algorithm presented in [Haacke et al., 1990]. Note that sub-Nyquist and Partial-Fourier sampling could also be applied simultaneously, as for instance shown in [Ramb et al., 2014b].

The calibration of reconstruction weights depended on the different ACS acquisition strategies. Whereas temporally averaged reconstruction weights were used in the case of the extra ACS acquisition scheme, reconstruction weights were derived for each time frame separately in the case of measurements with inplace or dynamic extra ACS. This is related to the difference that inplace and dynamic extra ACS lines contain the actual signal dynamics, while the extra ACS lines describe a different time series. For inplace ACS acquisitions, reconstructions using N_{time} sets of individually derived reconstruction weights as well as using a single set of temporally averaged weights were investigated. Since the results were very similar, the latter approach was favored in the results presented, due to faster reconstruction. For dynamic ACS acquisition, the first approach was incorporated.

Individual coil images were combined based on the adaptive procedure [Walsh et al., 2000]. All k-t-sub-Nyquist sampled measurements were additionally reconstructed using conventional GRAPPA for comparison. Note that conventional GRAPPA is directly applicable also for the k-t-space undersampling pattern.

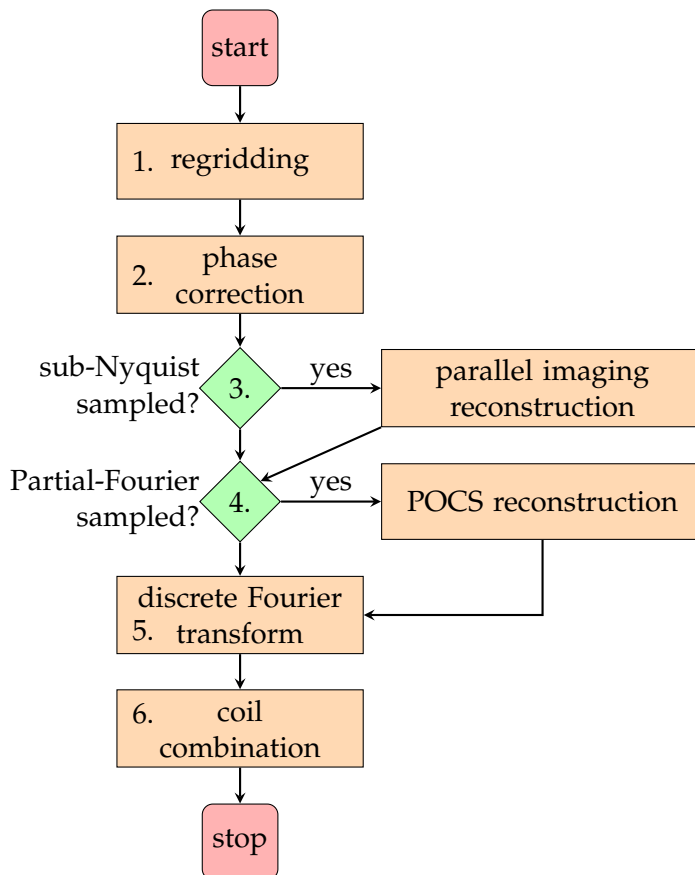


Figure 7.6: The workflow of k-t-EPI image reconstruction consists of six steps. 1. Regridding and density compensation is performed in order to account for ramp sampling (Sec. 3.4.2). 2. Phase correction is carried out based on the navigator echoes acquired (Sec. 3.4.2). If applicable, 3. parallel imaging reconstruction (Sec. 5.4.2) or 4. POCS reconstruction (Sec. 3.5) is then incorporated to reconstruct k-space data on a grid that fulfills the Nyquist theorem. The process concludes with 5. an inverse discrete Fourier transform (Def. 3.3.22) and 6. coil combination (Sec. 4.1).

parameter	value
TE	30.0 ms
TR	1500 ms
flip angle α	variations over repetitions
number of slices	1 slice
slice thickness	3.7 mm
field of view	$240 \times 240 \text{ mm}^2$
matrix size	170×170
BW	1548 Hz/Px
echo spacing	780 μs
number of time frames	120
nominal spatial resolution	$1.4 \times 1.4 \times 3.7 \text{ mm}^3$
temporal resolution	1500 ms

Table 7.1: Sequence parameters for the investigation of the k-t-sub-Nyquist sampling scenarios of k-t-EPI at various reduction factors are listed. For reference, a Nyquist-sampled EPI (with 5/8-Partial-Fourier sampling to achieve the TE of 30 ms) was acquired with similar parameters. Note that the high spatial resolution in the Nyquist-sampled EPI could be realized since only 5 slices were imaged at the given TR.

7.2.3. In vivo measurements with flip angle induced dynamics

Reconstruction quality, temporal fidelity and noise behavior was assessed in a preceding investigation based on dynamics induced by variations of the flip angle at constant TR. The flip angle variations mimicked a global bolus passage of contrast agent. The procedure allowed for a reproducible comparison of different acquisition patterns without the necessity of contrast agent administration.

In vivo measurements using k-t-EPI with different acquisition strategies were conducted on a 3T PRISMA Scanner (Siemens, Erlangen, Germany). All acquisitions with flip angle induced dynamics were obtained from the same healthy volunteer (male, 30 years) and in a single session of measurements. For each set of parameters, the same slice orientation was acquired. The scanner was equipped with a 64-channel head coil array. Among those, the 32 channels that provide the highest signal magnitude were selected for parallel reception.

Sub-Nyquist-sampling with k-t-EPI was performed at reduction factors of $R = 5$, $R = 7$ and $R = 9$, for each ACS acquisition strategy. Additionally, Nyquist-sampled EPI images were acquired for the comparison. The latter incorporated 5/8-Partial-Fourier sampling, in order to realize the designated TE of 30 ms. This TE corresponds to a standard effective echo time in clinical cerebral perfusion. Please note that additional Partial-Fourier sampling is not required in the case of k-t-sub-Nyquist sampling to realize the desired TE.

The measurement parameters are listed in Table 7.1. The parameters were chosen to match a standard clinical protocol besides an increase in spatial resolution to $1.4 \times 1.4 \times 3.7 \text{ mm}^3$. Although such a high spatial resolution is usually not accomplished in the standard EPI measurement, it was reached by imaging solely five slices. In this way, the relatively long readout of the Nyquist-sampled EPI could be realized within the given TR of 1.5 s.

The total readout length varied depending on the trajectory, the reduction factor and the number of ACS lines. The latter was chosen to provide a TE of 30 ms in all acquisitions and is listed in Table 7.2. For extra ACS, each measurement incorporated 20 temporal repetitions of the ACS acquisition. Corresponding readout lengths for the echo spacing of 780 μs are collected

acquisition strategy	R = 5	R = 7	R = 9
k-t-EPI with inplace ACS	20	21	18
k-t-EPI with dynamic extra ACS	10	14	18
k-t-EPI with extra ACS	20	21	18

Table 7.2: Choices of numbers of ACS lines for the different acquisition strategies and reduction factors.

Table 7.3: Readout lengths of the varying acquisition strategies

reduction factor	inplace ACS	(dynamic) extra ACS
$R = 5$	$50 \cdot 780\mu\text{s} = 39.00 \text{ ms}$	$34 \cdot 780\mu\text{s} = 26.52 \text{ ms}$
$R = 7$	$43 \cdot 780\mu\text{s} = 33.54 \text{ ms}$	$25 \cdot 780\mu\text{s} = 19.50 \text{ ms}$
$R = 9$	$35 \cdot 780\mu\text{s} = 27.30 \text{ ms}$	$19 \cdot 780\mu\text{s} = 14.82 \text{ ms}$
EPI reference $R = 1$	$128 \cdot 5/8 \cdot 780\mu\text{s} = 62.4 \text{ ms}$	

in Table 7.3. Among the k-t-EPI scenarios, inplace ACS requires the longest echo train due to incorporating Nyquist-sampled phase encodings at the central part of k-space. For inplace ACS, the corresponding net reductions were $R_{\text{net}} = 3.4/4.02/4.97$. However, even the longest readout time of 39 ms at $R = 5$ is lower than the time of image acquisition for the 5/8-Partial-Fourier- and Nyquist-sampled EPI of 62.4 ms.

Each acquisition consisted of 120 repetitions during which flip angles were varied only in the first part of measurement repetitions. The evolution of flip angles over repetitions was designed similar to the characteristic signal drop during bolus passage in cerebral perfusion imaging with contrast agent (see Fig. 5.4). The initial flip angle of 75° was step-wise reduced to a minimum of 7° and subsequently incremented to restore the initial flip angle: $75^\circ, 74.93^\circ, \dots, 28.91^\circ, 13.21^\circ, 7.32^\circ, 12.43^\circ, 24.24^\circ, \dots, 74.56^\circ, 75^\circ$. Relative flip angle changes range between 10 and 100% of the initial flip angle. The bolus arrival time was set to $t = 10TR$ in the sequence. The first 10 measurement repetitions comprise the transition into steady state and the baseline signal, before designed changes in the magnitude intensity occur.

The k-t-EPI data was additionally reconstructed using non-time-resolved GRAPPA for comparison. They are referred to as GRAPPA-EPI or simply as GRAPPA. The POCS reconstructed Nyquist-sampled EPI scenarios were termed POCS-EPI below. The resulting time series of images were analyzed in terms of temporal fidelity and noise.

Temporal fidelity

As the repetition with the minimal flip angle mimics the maximal signal drop during the bolus passage, an increase of magnitude values for that particular time frame indicates blurred temporal information. Therefore, the mean and standard deviation of the magnitude signal for the lowest flip angle were assessed to reveal temporal smoothing. Since also broadening of the time curve marks temporal inaccuracy, mean and standard deviation of the FWHM were estimated. All analyses were performed separately for each pixel.

The FWHM was derived based on fitting a Gaussian function - denoted by f below - with least-square deviation to the time series of each pixel. Among the three fitted parameters a, b, c , the outcome of c was used to estimate the FWHM according to the relation:

$$f(x) = a \exp\left(\frac{-(x-b)^2}{2c^2}\right) \quad \text{and} \quad \text{FWHM} = 2\sqrt{2 \ln 2}c. \quad (7.1)$$

In total, 7456 pixels were included in the estimation of mean and standard deviations of min-

imal signal magnitudes and FWHM. The pixels were selected by manually drawing a ROI inside the brain area within the image. The skull and the outer parts of the brain were not incorporated in the ROI to avoid motion artifacts. Values obtained from the Nyquist-sampled EPI were assumed to depict a ground-truth reference.

Temporal signal-to-noise ratio

Signal fluctuations of each acquisition and reconstruction type were rated using the last 80 of the 120 measurements, which were acquired without flip angle variations. The temporal signal-to-noise-ratio was assessed according to the definition below and with $N_t = 80$.

Definition 7.2.1 (temporal signal-to-noise-ratio (tSNR)). Let $\hat{d}^{sub,3D}(\mathbf{x}_p)$ denote the reconstructed k-t-space signal of combined coil contributions of pixel \mathbf{x}_p . The **temporal signal-to-noise-ratio (tSNR)** is defined for each pixel $\mathbf{x}_p, p = 1, \dots, N_{pix}$ by

$$tSNR(\mathbf{x}_p) = \frac{\overline{\hat{d}^{sub,3D}(\mathbf{x}_p)}}{\sigma(\hat{d}^{sub,3D}(\mathbf{x}_p))},$$

where the nominator and denominator are defined by the mean and standard deviation, i.e.

$$\begin{aligned} \overline{\hat{d}^{sub,3D}(\mathbf{x}_p)} &:= \frac{1}{N_t} \sum_{t=1}^{N_t} \hat{d}^{sub,3D}(\mathbf{x}_p, t) \\ \sigma(\hat{d}^{sub,3D}(\mathbf{x}_p)) &:= \sqrt{\frac{1}{N_t - 1} \sum_{t=1}^{N_t} \left| \hat{d}^{sub,3D}(\mathbf{x}_p, t) - \overline{\hat{d}^{sub,3D}(\mathbf{x}_p)} \right|^2}. \end{aligned}$$

Remark 7.2.2. The tSNR reflects temporal variations in the time series of individual pixels. It demonstrates also influences by artifacts that fluctuate over the temporal repetitions. Periodically changing artifacts due to the periodic repetition of different trajectories are likewise revealed.

Temporal average g-factor

Temporal average g-factor values were derived to capture SNR losses due to parallel imaging. In the case of k-t-GRAPPA, the total g-factor contribution was calculated following Def. 6.2.6. For the additional conventional GRAPPA reconstruction, g-factors were derived according to Cor. 4.6.15 and subsequently averaged over the range of time frames.

7.2.4. First-pass bolus perfusion in vivo measurements

Initial feasibility results of k-t-EPI in cerebral perfusion imaging were obtained in two repeated DSC weighted acquisitions, each measurement with only half of the normal contrast agent dose, and by comparing k-t-EPI with the currently standard clinical EPI protocol. The measurements were conducted on a 3T clinical scanner (Tim TRIO, Siemens, Erlangen, Germany) in six patients (two measurements per subject). The patients examined had been diagnosed with different grades of tumorous tissue found in various areas of the brain. The study was approved by the local ethical committee, and written informed consent was given prior to examination.

The two cerebral perfusion imaging scenarios were performed in the order of 1. the currently standard clinical EPI protocol and 2. the proposed k-t-EPI acquisition with in-place ACS

at reduction factor $R = 5$. The sequence parameters of both imaging protocols are depicted in Table 7.4. For DSC weighted imaging, an injection of 0.2 ml per kg body weight of 0.5 M Gadoteridol (Prohance, Bracco Imaging, Italy) was administered at a flow rate of 3 ml/s.

The serial image acquisition was performed during the injection of contrast agent and comprised 50 time frames. The same temporal resolution, effective echo time and spacing were used, in order to support the direct comparison. The echo spacing and respective reduced sampling along phase encoding direction led to the following readout times per slice:

$$\begin{aligned} 96 \cdot 780\mu\text{s} &= 74.88\text{ms}, & \text{for standard EPI, 6/8-Partial-Fourier sampling,} \\ 50 \cdot 780\mu\text{s} &= 39.00\text{ms}, & \text{for k-t-EPI, inplace ACS, } R = 5. \end{aligned}$$

The k-t-EPI sequence achieved in particular substantially higher spatial resolution with increased brain coverage. Whereas the nominal spatial resolution was $1.8 \times 1.8 \text{ mm}^2$ for the standard EPI and at the given field of view of $240 \times 240 \text{ mm}^2$, the k-t-EPI sequence provided a nominal spatial resolution of $1.4 \times 1.4 \text{ mm}^2$ with the same field of view and TR . The nominal spatial resolution is indicated, since spatial resolution can potentially be further decreased due to the asymmetric sampling in the case of Partial-Fourier sampling, or imposed by relaxation over the readout interval.

All k-t-EPI data sets were additionally reconstructed using non-time-resolved GRAPPA for comparison. Two sets of reconstructions were derived for the conventional EPI acquisition as well: first, the vendor based reconstruction and second, off-line Fourier reconstruction incorporating the POCS algorithm with 5 iterations. Whereas the first yields images as currently used in the clinical context, the latter facilitates the comparison with k-t-EPI acquisitions and reconstructions within the same reconstruction framework, where all steps are controlled. In order to distinguish the four reconstructions based on the two acquisition types, they are referred to as:

- | | | |
|-----------------|---|--------------------------------------|
| 1. standard EPI | } | conventional EPI acquisition |
| 2. POCS-EPI | | |
| 3. k-t-EPI | } | k-t-EPI with inplace ACS acquisition |
| 4. GRAPPA-EPI | | |

Assessment of CBV maps, temporal fidelity and g-factors

The **cerebral blood volume (CBV)** was determined off-line for POCS-EPI, k-t-EPI and GRAPPA-EPI and using the vendor's platform in the case of standard EPI. Off-line estimated CBV were derived according to the formulae presented in (5.6) and (5.7), which reduce in the case of discrete time series to

$$\begin{aligned} \hat{\text{CBV}}(\mathbf{x}_p) &\propto \sum_t \Delta \hat{R}_2^*(\mathbf{x}_p, t), \\ \text{where } \Delta \hat{R}_2^*(\mathbf{x}_p, t) &:= -\ln \left(\frac{\hat{I}_t^{\text{full}}(\mathbf{x}_p)}{\hat{I}_0(\mathbf{x}_p)} \right) / TE \quad \text{and} \quad \hat{I}_0(\mathbf{x}_p) := \frac{1}{N_t} \sum_{t=1}^{N_t} \hat{I}_t^{\text{full}}(\mathbf{x}_p). \end{aligned} \tag{7.2}$$

The summation was performed over the first bolus passage. For the comparison, the window selected for the display of the relative CBV maps of each method was scaled to a similar appearance.

acquisition parameters	conventional EPI	k-t-EPI, inplace ACS
TE		30.0 ms
TR		1500 ms
flip angle α_{fa}		75°
number of slices	15 slices	20 slices
slice thickness		3.7 mm
field of view		240 × 240 mm ²
matrix size	128 × 128	170 × 170
BW	1548 Hz/Px	1446 Hz/Px
echo spacing		780 μ s
phase undersampling	6/8 Partial-Fourier	$R = 5, 20$ ACS lines
number of phase encoding steps	$N_{pe} = 96$	$N_{pe} = 50$
number of time frames		50
nominal spatial resolution	$1.8 \times 1.8 \times 3.7 \text{ mm}^3$	$1.4 \times 1.4 \times 3.7 \text{ mm}^3$
temporal resolution		1500 ms

Table 7.4: The table contains acquisition parameters of the first-pass DSC weighted cerebral perfusion measurements of the standard clinical protocol (conventional EPI) and the proposed k-t-EPI acquisition with inplace ACS at reduction factor $R = 5$.

Average temporal signal evolutions between POCS-EPI, k-t-EPI and GRAPPA-EPI were compared based on two designated ROIs, in order to find differences in temporal fidelity. To this end, time series of magnitudes were normalized to individual baselines for each pixel. Mean and standard deviation were computed. The FWHM was furthermore estimated by the same fitting procedure as presented in (7.1) and according to least-square deviation for each reconstructed pixel separately. Its mean and standard deviation were compared between POCS-EPI, k-t-EPI and GRAPPA-EPI.

For the assessment of SNR losses as an inherent penalty in parallel imaging, temporally averaged g-factors were derived in the case of k-t-EPI and GRAPPA-EPI.

7.3. Results

Based on the in vivo measurements with flip angle induced dynamics, individual reconstruction results are examined from various aspects in Sec. 7.3.1. Initial results in DSC weighted cerebral perfusion are shown in Sec. 7.3.2.

7.3.1. Measurements with flip angle induced dynamics

Figure 7.7 presents the same time frame of the series of magnitude images for the various k-t-EPI acquisitions with flip angle induced dynamics. A time frame in steady state is chosen and before flip angle variations occur. The k-t-EPI scenarios are demonstrated for the three ACS acquisition schemes (inplace, dynamic extra and extra ACS) at three different reductions ($R = 5, 7$ and 9). The measurements confirm the feasibility of highly undersampled EPI with high depiction quality.

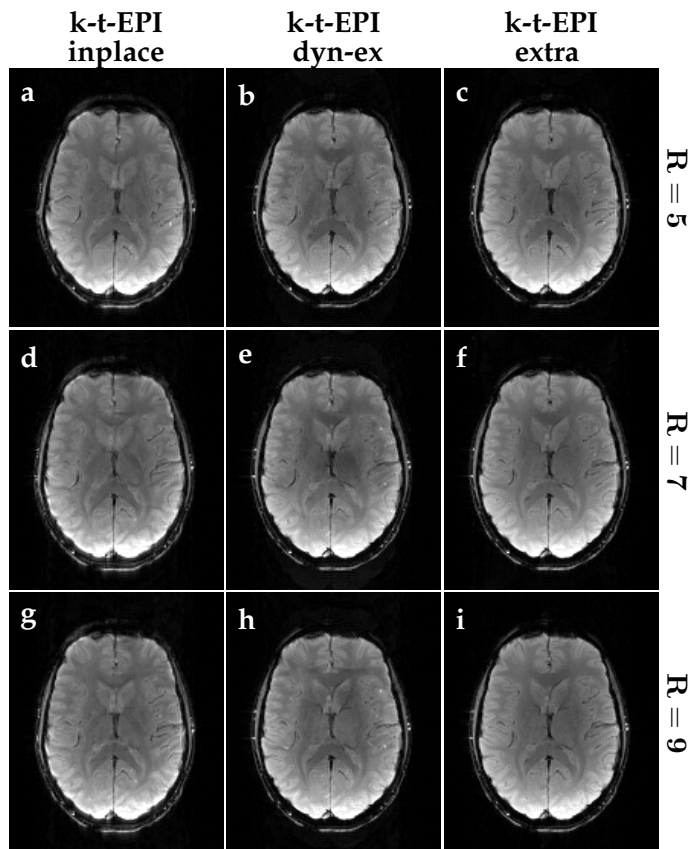
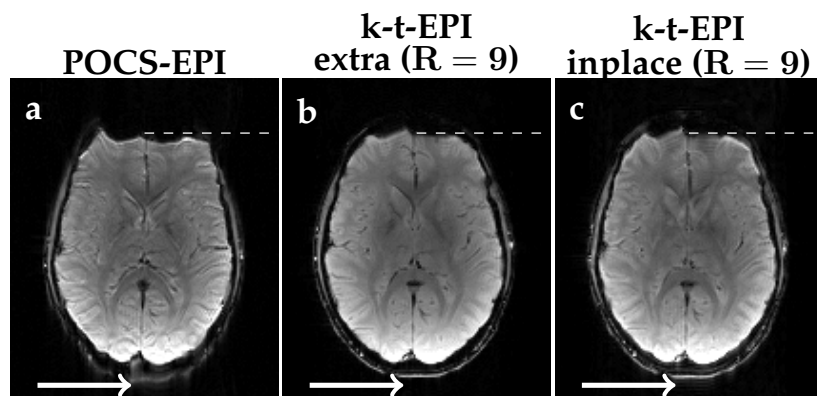


Figure 7.7: Reconstructed magnitude images of the same slice and time frame are displayed for the three k - t -EPI imaging scenarios at different reduction factors: (a,b,c) $R = 5$, (d,e,f) $R = 7$ and (g,h,i) $R = 9$. The different ACS schemes are sorted into columns: (a,d,g) inplace ACS, (b,e,h) dynamic extra (dyn-ex) ACS and (c,f,i) extra ACS.

Figure 7.8: Transverse slice reconstructions are shown for (a) POCS-EPI (Nyquist-sampled, $R = 1$ and 5/8-Partial Fourier) and (b,c) two scenarios of k - t -EPI at $R = 9$. White arrows and dashed lines indicate artifacts due to different in-plane susceptibilities. These are improved in k - t -EPI.



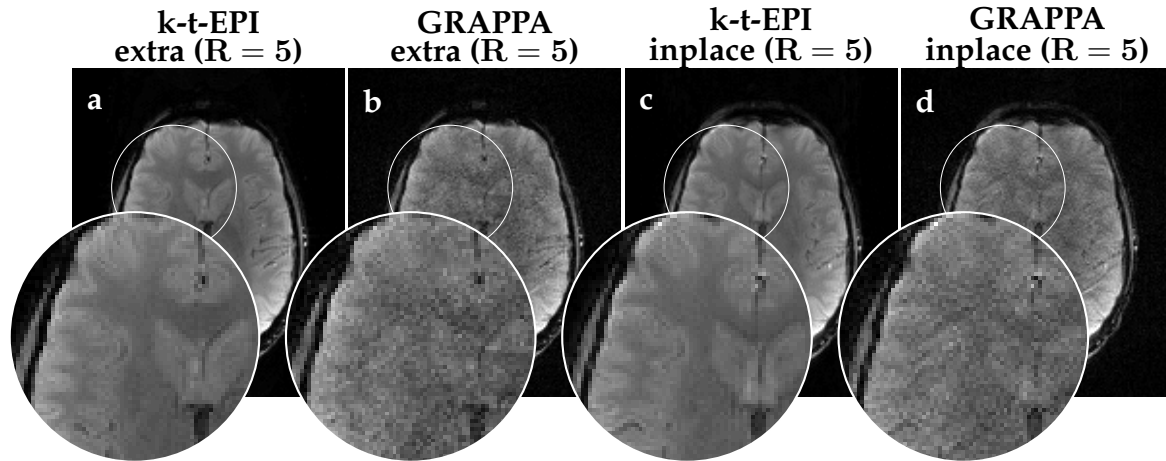


Figure 7.9: Magnitude images are presented for k-t-EPI acquisition at $R = 5$ with (a,b) extra ACS and (c,d) inplace ACS scheme. Magnifications of the brain area indicated are used to disclose the different noise levels between (a,c) k-t-GRAPPA and (b,d) additional GRAPPA reconstruction of the same data sets.

In-plane susceptibilities and noise

As stressed by the dashed lines and white arrows in Fig. 7.8, POCS-EPI is affected by in-plane susceptibility artifacts that lead to a signal loss in the orbito-frontal cortex. This loss is mitigated in the k-t-sub-Nyquist sampled acquisitions due to the shorter readout duration per slice. Figure 7.8 emphasizes particularly the improvement of in-plane susceptibility artifacts in k-t-EPI at $R = 9$ as opposed to POCS-EPI. At $R = 9$, the shortest readout duration of the considered scenarios is provided with extra or dynamic extra ACS.

In-plane susceptibility artifacts are likewise moderated in the additional GRAPPA reconstructions, since the same sub-Nyquist sampled data is the basis. However, starting at $R = 5$, GRAPPA reconstructions are corrupted by severe noise amplification, which is observed in all scenarios. This effect is highlighted in Fig. 7.9. The depiction discloses a substantial loss in image quality of the GRAPPA reconstructions, already at $R = 5$. More fine details are resolved in the k-t-EPI images. White matter and gray are in particular easier to distinguish.

Temporal fidelity

Figure 7.10 reveals the signal drop induced by flip angle variations. An image column of the transverse slice is displayed over the range of time frames acquired. The POCS-EPI acquisition serves as a reference. Excellent agreement is found for k-t-EPI with inplace ACS acquisition at all reduction factors, as well as for the GRAPPA reconstructions. The latter is expected, since conventional GRAPPA does not incorporate neighboring time frames in the reconstruction process. However, the high noise level is visible over all time frames for the GRAPPA reconstruction.

Slightly reduced temporal fidelity is suspected in k-t-EPI with dynamic extra ACS acquisition, with no noticeable increase at the higher reductions. At reduction factor $R = 9$, however, temporal fidelity appears degraded by residual aliasing artifacts. Severe temporal blurring occurs at reconstructions based on extra ACS acquisitions. The width of the signal dip is already slightly broadened at $R = 5$, which increases in severity when moving to higher reductions. Strongest blurring is found for extra ACS at $R = 9$. Although extra ACS provided high robustness against in-plane susceptibility artifacts, the findings suggests to exclude this acquisition scenario for DSC weighted cerebral perfusion measurements.

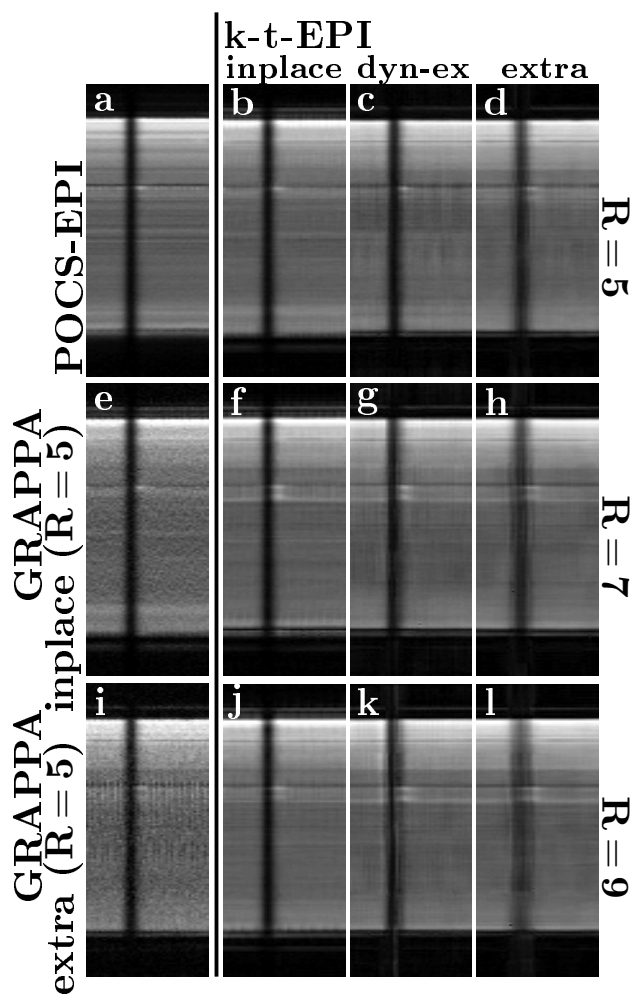


Figure 7.10: Reconstructed magnitude values of an image column are displayed along the series of time frames acquired. The spatial position of the column is indicated in the additional transverse slice representation. Reconstructions correspond to the magnitude images of Fig. 7.7-7.9, and comprise (a) POCS-EPI, (b-d,f-h,j-l) k-t-EPI for the three acquisition strategies and the three reduction factors, as well as additional GRAPPA reconstruction for $R = 5$ with (e) inlace and (i) extra ACS acquisition.

A closer consideration of the temporal depiction quality is given in Fig. 7.11, where the time series of individual pixels are regarded. Figure 7.11a compares different acquisition strategies at $R = 5$, while Fig. 7.11b shows the time series for different reduction factors for the same acquisition type (inlace ACS). Figure 7.11a discloses how the extra ACS scheme leads to a reduction of the signal depth. Both inlace and dynamic ACS acquisition reflect the same magnitude response as the POCS-EPI reference. Time series obtained from GRAPPA reconstruction exhibit signal fluctuations, in particular during constant flip angle application. Figure 7.11b demonstrates excellent temporal fidelity for the inlace ACS acquisition scheme and k-t-based reconstruction kernels during the variation of flip angles and at all three reduction factors. Shortly before the first flip angle decrease occurs, as well as shortly after the last increase, increased magnitude values are observed for reduction factors $R = 7$ and $R = 9$. However, the cause cannot be clearly deduced from the current display, since the slightly different effective spatial resolutions could also cause variations.

Whereas time series of solely one pixel location is considered in Fig. 7.11, a cumulative evaluation is presented in Fig. 7.12 and Table 7.5. Figure 7.12 addresses the temporal fidelity with respect to the depth of signal decrease (Fig. 7.12a and b) and the FWHM of the mimicked bolus passage (Fig. 7.12c and d) in the various k-t-sub-Nyquist-sampled scenarios.

Differences of the three acquisition strategies with respect to increasing reductions are shown in Fig. 7.12a and c. A loss of depth and width of the virtual bolus passage is evident

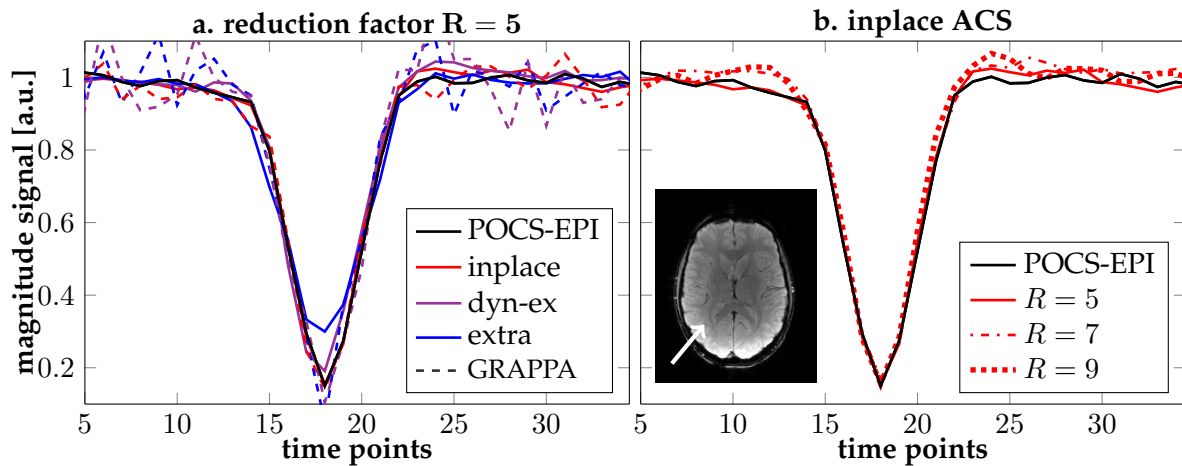


Figure 7.11: Magnitude values for a single pixel - as specified by the white arrow in the transverse slice image - are plotted over the range of time frames. Different scenarios are grouped. For the same reduction factor $R = 5$, reconstructed time series of k - t -EPI of the inplace, dynamic extra (*dyn-ex*) and extra ACS scheme are shown in (a), and in comparison with the POCS-EPI for reference. Additional GRAPPA reconstructions of the same three data sets (indicated by the same colors) are drawn using dashed lines. Results of all reduction factors, but solely from the inplace ACS acquisition scheme (red), are brought together in (b). For reference, POCS-EPI is again included. GRAPPA reconstructions are not inserted in (b).

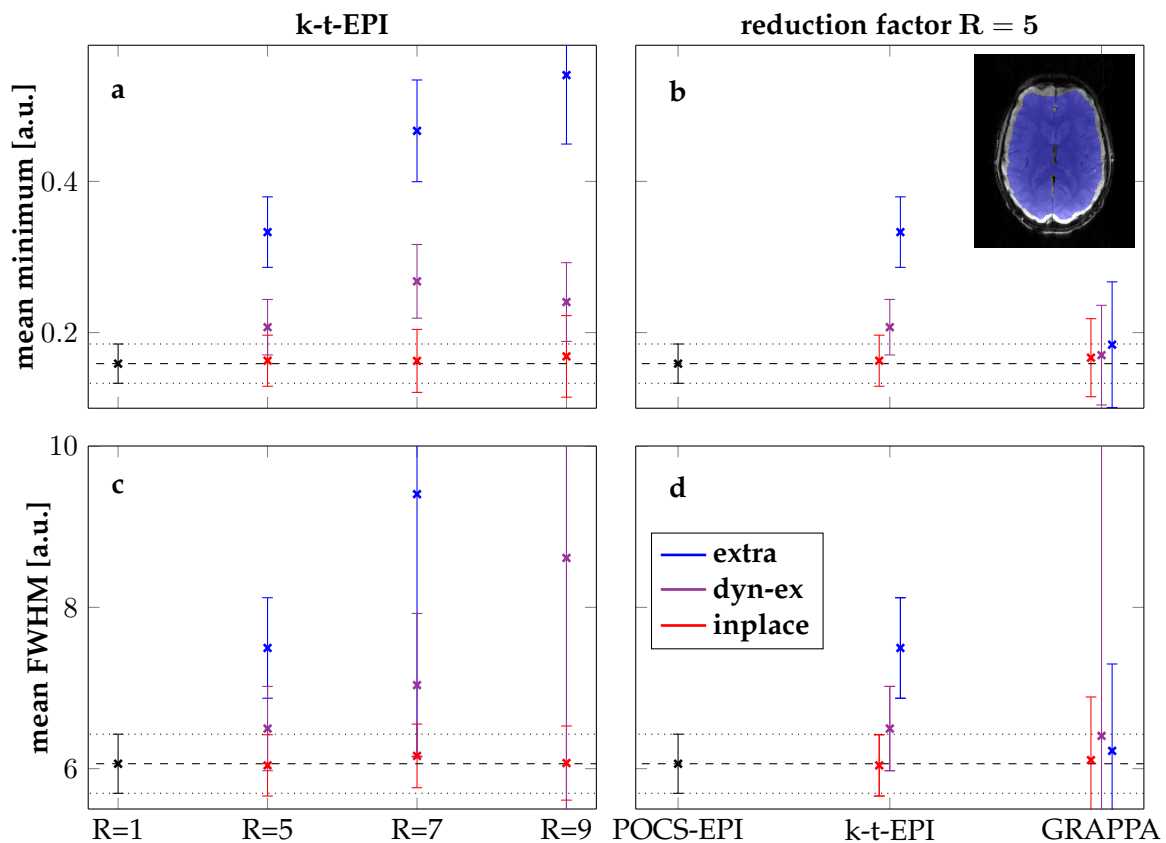


Figure 7.12: Mean values and standard deviation for the statistical evaluation of 7456 pixel (blue ROI in the magnitude image) are presented. Intensities of the time frame corresponding to RF pulse excitation with the lowest flip angle are investigated in (a,b). A cumulative analysis of the estimated FWHM values is depicted in (c,d). The exhaustive analysis is shown in Table 7.5.

method		minimum	FWHM	tSNR
POCS-EPI	$R = 1$	0.16 ± 0.03	6.06 ± 0.37	48.01 ± 15.69
k-t-EPI inplace ACS	$R = 5$	0.16 ± 0.03	6.04 ± 0.38	47.99 ± 15.49
	$R = 7$	0.16 ± 0.04	6.16 ± 0.4	43.32 ± 13.40
	$R = 9$	0.17 ± 0.05	6.07 ± 0.5	45.91 ± 14.90
GRAPPA-EPI inplace ACS	$R = 5$	0.17 ± 0.05	6.12 ± 0.78	12.29 ± 4.32
	$R = 7$	0.17 ± 0.07	8.42 ± 15.11	5.73 ± 2.68
	$R = 9$	n.a.	n.a.	n.a.
k-t-EPI dyn-ex ACS	$R = 5$	0.21 ± 0.04	6.5 ± 0.52	34.20 ± 14.49
	$R = 7$	0.27 ± 0.05	7.04 ± 0.89	33.14 ± 13.61
	$R = 9$	0.24 ± 0.05	8.61 ± 3.75	35.39 ± 14.54
GRAPPA-EPI dyn-ex ACS	$R = 5$	0.17 ± 0.07	6.41 ± 4.56	7.51 ± 2.47
	$R = 7$	0.31 ± 0.14	10.49 ± 23.44	4.26 ± 2.20
	$R = 9$	n.a.	n.a.	n.a.
k-t-EPI extra ACS	$R = 5$	0.33 ± 0.05	7.5 ± 0.62	46.44 ± 19.57
	$R = 7$	0.47 ± 0.07	9.4 ± 3.25	39.94 ± 18.16
	$R = 9$	0.54 ± 0.09	23.24 ± 37.72	33.45 ± 14.44
GRAPPA-EPI extra ACS	$R = 5$	0.18 ± 0.08	6.22 ± 1.08	11.01 ± 4.69
	$R = 7$	0.32 ± 0.2	10.22 ± 33.28	5.17 ± 2.73
	$R = 9$	n.a.	n.a.	n.a.

Table 7.5: Mean and standard deviations of the minimum signal and FWHM estimated for all imaging strategies are displayed. A subset of which is contained in Fig. 7.12. Average tSNR values and corresponding standard deviations are furthermore listed. The estimation was performed over the 7456 pixels highlighted by the blue ROI in Fig. 7.12.

in k-t-EPI with extra ACS acquisitions and k-t-kernel based reconstructions. Temporal fidelity decreases severely when moving to higher reduction factors. Also for the dynamic extra ACS scheme, the depth and width as observed in the POCS-EPI reference are not reached on average. Whereas values are in a closer range at reduction factor $R = 5$, in particular FWHM values are considerably increased at reduction factor $R = 9$. High temporal fidelity with unbiased mean values are achieved with k-t-EPI and inplace ACS acquisition. Deviations occur in a slightly larger interval, however still within an acceptable range. Increases with respect to higher reduction factors are minor.

Figure 7.12b and c reveals different behaviors of time-resolved k-t-GRAPPA versus non-time-resolved GRAPPA reconstruction of the three acquisition strategies. Whereas mean values diverge substantially between the three ACS scenarios in the case of k-t-kernel based reconstructions, differences are much smaller for conventional GRAPPA. Nevertheless, both confirm the closest agreement with POCS-EPI in the case of inplace ACS. It is striking that GRAPPA exhibits greater standard deviations than each time-resolved counterpart. It is also the standard deviation that differs strongly between the three acquisition strategies in the case of conventional GRAPPA.

Explicit values for the cumulative analysis of depth and width of the imitated bolus passage are accumulated in Table 7.5. Remaining scenarios are furthermore listed, in order to complement the selection displayed of Fig. 7.12. Only values for GRAPPA reconstructions at $R = 9$ were excluded, since evaluation was impaired by visible, strong artifacts. Please note again the close agreement between k-t-EPI with inplace ACS - at all reduction factors - and the POCS-EPI reference. Values for GRAPPA reconstructions at reduction factor $R = 7$ exceed their counterparts of k-t-GRAPPA reconstructions even in the worst-case scenario of $R = 9$ of the

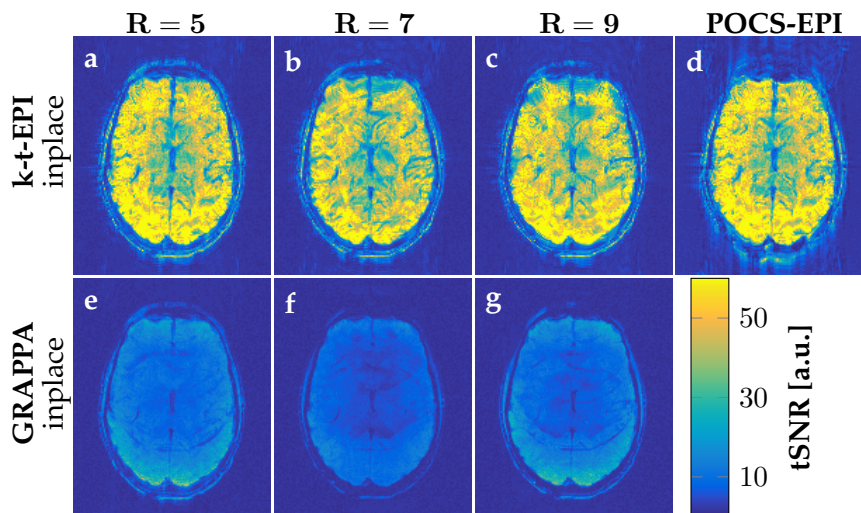


Figure 7.13: t SNR values of a transverse slice are shown for k-t-EPI with in-place ACS and additional GRAPPA reconstructions at (a,e) $R = 5$ (b,f), $R = 7$ and (c,g) $R = 9$, as well as for (d) POCS-EPI. A complementary cumulative analysis of t SNR is contained in Table 7.5.

latter.

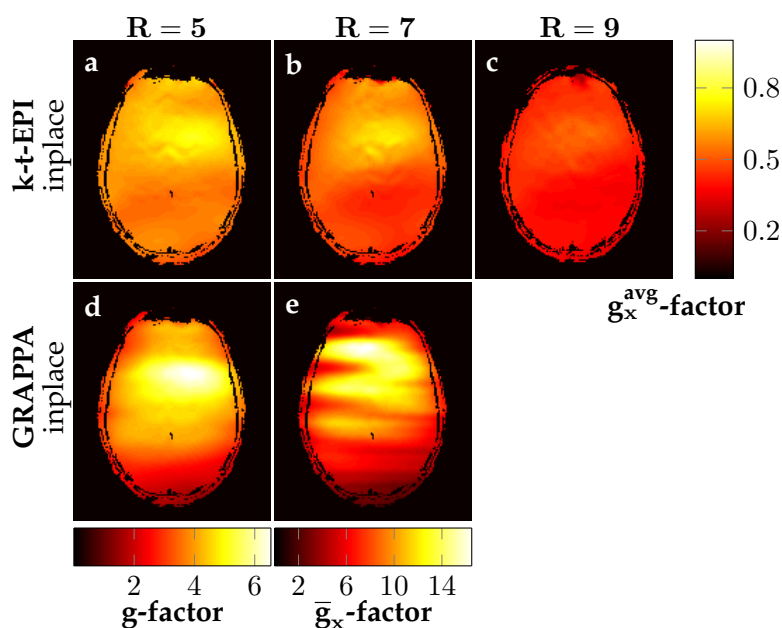
tSNR and g-factor

Based on the previous findings on temporal fidelity, k-t-EPI with in-place ACS acquisition scheme is further investigated. Figure 7.13 presents t SNR maps derived over an interval of repetitions with constant flip angle. Compared to POCS-EPI, GRAPPA reconstructions are affected by a severe loss of t SNR, whereas k-t-EPI with k-t-GRAPPA reconstruction provides the same high t SNR. Residual aliasing artifacts are visible in the t SNR maps of GRAPPA.

Cumulative t SNR values - also for the other acquisition schemes - are listed in Table 7.5. A close agreement with POCS-EPI is found for k-t-EPI with extra ACS acquisition at reduction factor $R = 5$, as well as for all in-place ACS scenarios, in the case of k-t-GRAPPA reconstruction. In the GRAPPA reconstructions ($R = 5$ and $R = 7$), t SNR losses range between 68% and 85%. Best performance is hereby found again for the in-place ACS scheme at reduction $R = 5$. In comparison, reductions between 1% and 31% are present in k-t-GRAPPA reconstructions, including also scenarios with reduction factor $R = 9$.

As a counterpart of t SNR considerations, temporal average g-factor penalties are demonstrated in Fig. 7.14. Frequency combined g_x^{avg} -factor maps, which reflect temporally averaged contributions, are provided in the case of k-t-GRAPPA. Whereas g-factor penalties decrease when moving to higher reduction factors in the case of time-resolved parallel imaging, high g-factor values are obtained in the GRAPPA reconstructions of $R = 5$ and $R = 7$. The substantially higher g-factor penalty implies severe SNR degradation. The g-factor results support the observations made in terms of t SNR. The reduced noise variances of k-t-EPI are in accordance with investigations in the context of cardiac MRI, as covered in Chapter 6. Both t SNR and g-factor maps complement the visual impression of spatio-temporal depiction quality of the various strategies. Due to its superior performance in the investigation with flip angle induced dynamics, k-t-EPI with in-place ACS acquisition scheme at $R = 5$ was selected for DSC weighted cerebral perfusion imaging in patients.

Figure 7.14: Frequency combined g_x^{avg} -factor maps are displayed for k-t-EPI at (a) $R = 5$, (b) $R = 7$ and (c) $R = 9$, all with the same color coding. Temporal average g_x -factor maps for the additional GRAPPA reconstruction are depicted for (d) $R = 5$ and (e) $R = 7$. A different scaling range is used for the latter, since values are much higher. The transverse slices correspond to the one of Fig. 7.13.



7.3.2. DSC weighted cerebral perfusion

Initial feasibility results of the application of k-t-EPI with in-place ACS at $R = 5$ in DSC weighted imaging of cerebral perfusion are demonstrated in Figures 7.15, 7.16 and 7.17. Three representative patients - out of six imaging sessions in total - are shown in order to demonstrate different aspects. Each figure corresponds to one of the three patients.

Figure 7.15 shows reconstructed magnitude images and corresponding CBV maps of a single slice. All four reconstruction scenarios - based on the two DSC weighted acquisitions at half-dose - are demonstrated: Standard EPI and POCS-EPI (conventional EPI measurement), as well as k-t-GRAPPA and GRAPPA reconstruction of the k-t-sub-Nyquist sampled EPI acquisition. The figure shows the same slice for all measurements. In total 15 slices were acquired in the conventional measurement and 20 slices in the case of k-t-EPI at $R = 5$. Improved spatial resolution in the k-t-sub-Nyquist sampled acquisition is clearly noticeable.

In Fig. 7.15, data are shown of an oligodendroglioma WHO (World Health Organization) grade II in the left temporal lobe. It corresponds to the area with high signal intensities in the left temporal lobe of the FLAIR images. Small veins draining into the left temporal lobe are visible in the magnitude images and corresponding CBV maps. These are best to delineate in k-t-EPI and are also apparent in POCS-EPI. Fine details are concealed in GRAPPA-EPI due to the presence of noise in both the magnitude image and the CBV map.

A small leptomeningeal artery in a sulcus on the right temporo-occipital lobe (magnification) is better depicted in k-t-EPI than in the standard EPI or in POCS-EPI. The GRAPPA reconstruction - coming from the same measurement data - provides this fine detail. However, the fidelity in the latter is compromised by the noise enhancement. The detail is lost in the corresponding CBV map of the GRAPPA reconstruction.

Figure 7.16 contains a similar arrangement of transverse slice images obtained in another patient with a glioblastoma multiforme WHO grade IV. Magnitudes during bolus passage as well as CBV maps are represented for standard EPI, k-t-EPI and GRAPPA-EPI. Tumor is evident in the corpus callosum and the left anterior cingulate cortex. The T_1 -weighted reference and the FLAIR image demonstrate hyperintense contrast in these areas.

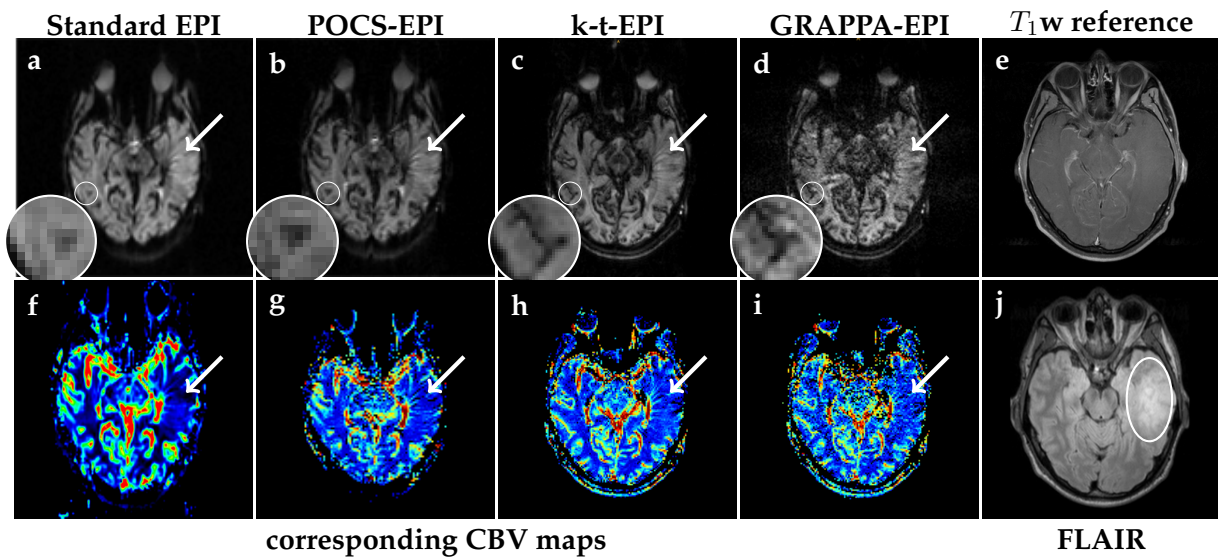


Figure 7.15: Magnitude images during bolus passage and corresponding CBV maps are displayed for (a,f) standard EPI, (b,g) POCS-EPI, as well as (c,h) for k-t-EPI (inplace ACS, $R = 5$) and (d,i) GRAPPA-EPI. The first two and the latter two are derived from the conventional EPI acquisition and the k-t-sub-Nyquist-sampled measurement, respectively. Furthermore shown is (e) a T_1 -weighted image and (j) a FLAIR acquisition. Both give evidence for a oligodendroglioma WHO grade II in the left temporal lobe (white oval). Prominent veins that pass into the left ventricle are visible in the corresponding CBV maps (white arrows). The magnifications highlight a small artery in a sulcus to emphasize the different spatial resolutions of the two acquisition, as well as different reconstruction performance of the four approaches.

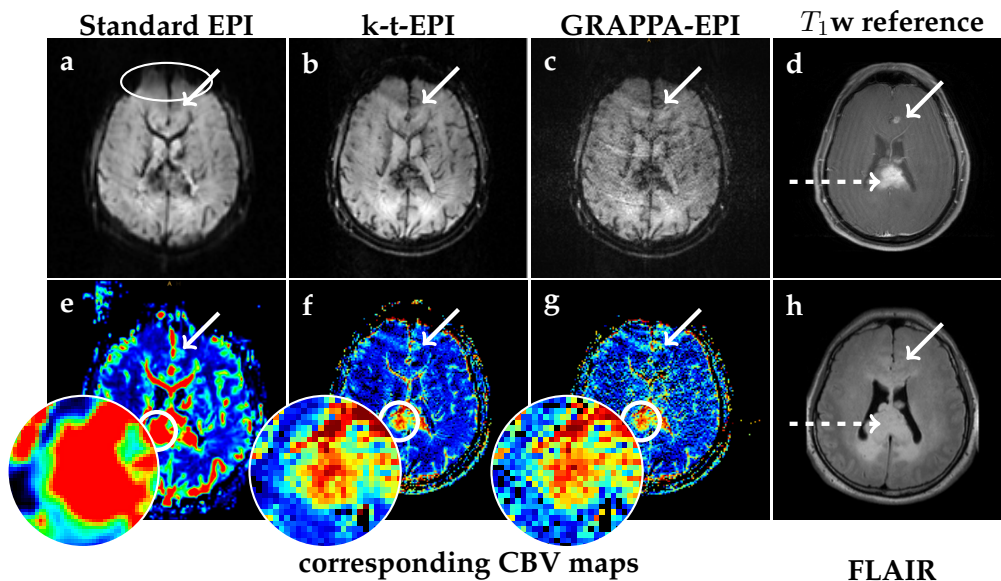


Figure 7.16: Reconstruction results of magnitude images during bolus passage and CBV maps are shown for (a,e) standard EPI, (b,f) k-t-EPI and (c,g) GRAPPA-EPI. The latter two are based on the same measurement data. The first is obtained directly from the vendor's platform. For reference, T_1 -weighted and FLAIR images are displayed in (d) and (h), respectively. A multifocal glioblastoma multiforme WHO grade IV in the corpus callosum and in the left anterior cingulate cortex (white, dashed and solid arrows) leads to increased intensities in the T_1 -weighted image and the FLAIR image. In the case of k-t-EPI acquisition, the CBV map shows finer details in the corpus callosum than in the standard EPI. (see magnification). Note that interpolation to a higher pixel grid is evident in the vendor's CBV map.

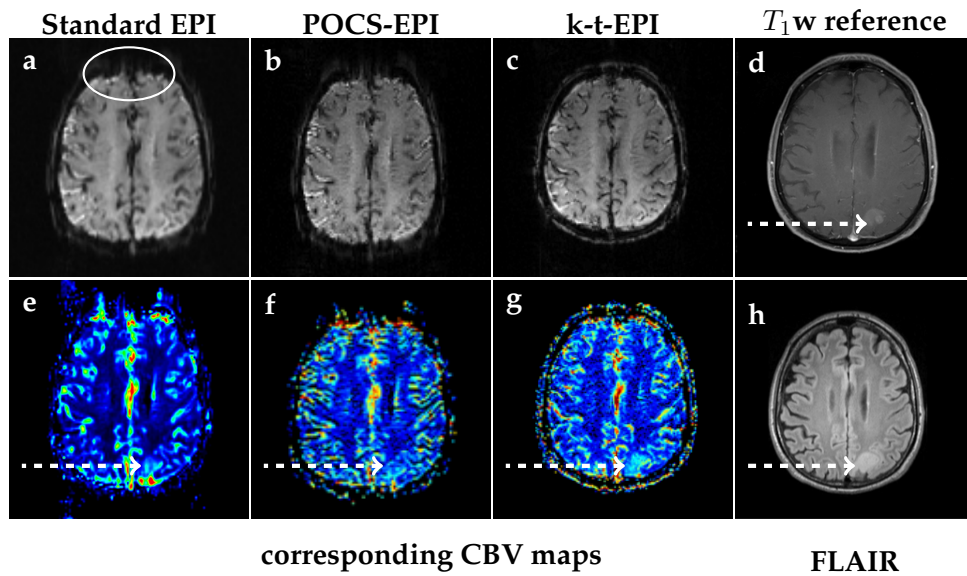


Figure 7.17: Similar as to Figs. 7.15 and 7.16, reconstructed images of a transverse slice during bolus passage are represented, together with CBV results, for (a,e) standard EPI, (b,f) POCS-EPI, as well as (c,g) k-t-EPI. The first two constitute on-line and off-line reconstructions of the same measurement data. The third is the proposed k-t-EPI scenario. Additionally, a T_1 -weighted (d) and a FLAIR image (h) is given for reference. The patient has an anaplastic oligastrocytoma WHO grade III in the left mesial parietal lobe (white, dashed arrows). The increase in CBV is best delineated in the case of k-t-EPI. In-plane susceptibility artifacts can be seen in standard EPI and POCS-EPI, but are mitigated in k-t-EPI (white, solid arrows).

The improved spatial resolution facilitates a finer depiction in k-t-EPI, in particular with respect to the small lesion in the cingulate cortex. In the case of standard EPI, the affected area is hard to distinguish from the vessels of the anterior interhemispheric fissure and it is obscured by noise in the GRAPPA-EPI scenario. Likewise, the tumorous part in the corpus callosum is easier to delimit from the ventricles in k-t-EPI than in POCS-EPI. Corresponding CBV maps of k-t-EPI hereby exhibit a more detailed gradation. Within this area, CBV values of k-t-EPI suggest the most aggressive part to be more confined and centralized compared to the findings of the standard EPI measurement. The transverse slice furthermore reveals in-plane susceptibility artifacts in the latter, which are not present in the acquisition strategy of k-t-EPI. GRAPPA-EPI shows similar CBV behavior. However, CBV maps appear again highly corrupted by noise and artifacts are visible in the magnitude image.

In Fig. 7.17, cerebral perfusion images from a third patient with an anaplastic oligastrocytoma WHO grade III in the left mesial parietal lobe are displayed. The tumor is hyperintense in the FLAIR image and abnormal contrast behavior is observed in the T_1 -weighted reference. In the standard EPI and POCS-EPI, the corresponding area is hard to determine within the CBV maps. A much better assessment of the increased CBV of the tumor is achieved based on the significantly higher spatial resolution in k-t-EPI.

The measurement data of all six patients provided a higher spatial resolution of magnitude images and in the assessment of CBV. In all cases, areas of tumorous tissue were more confined in the CBV maps. In cases of very small lesions, these were often better to locate in the high resolution maps of k-t-EPI acquisition compared to the conventional EPI.

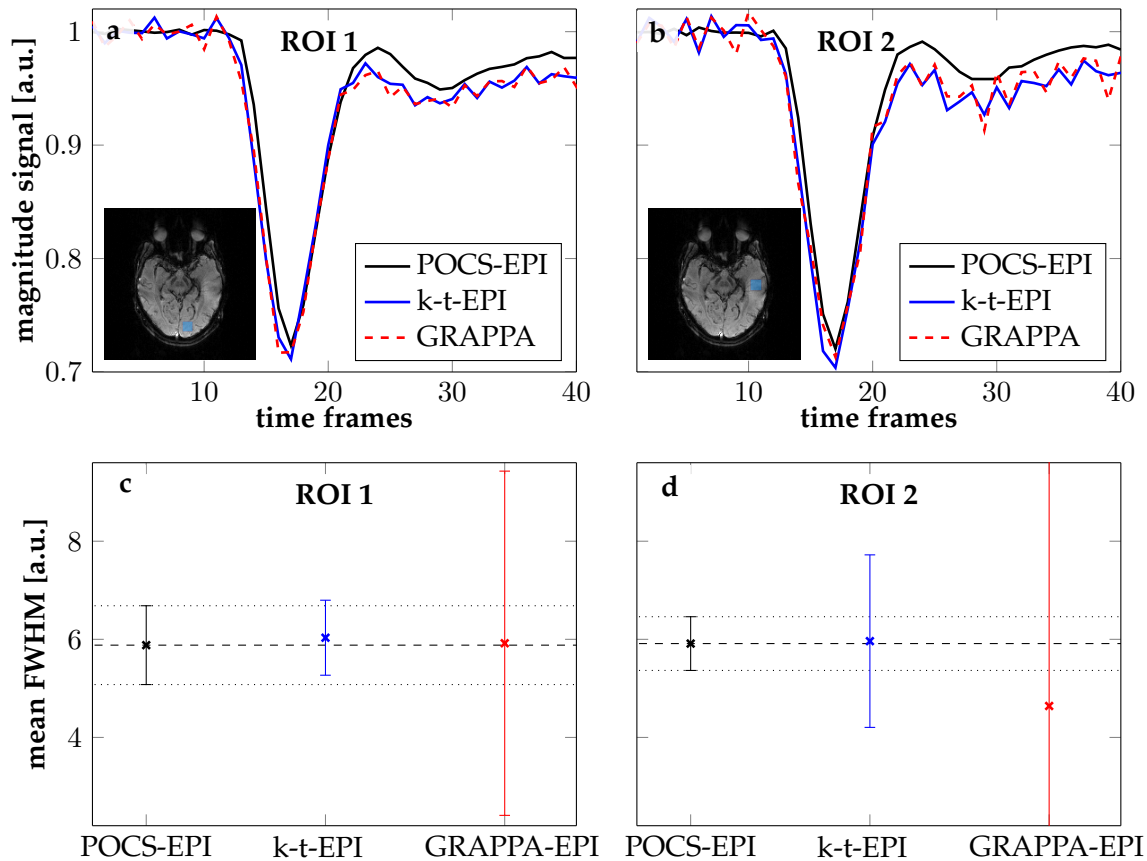


Figure 7.18: For the same patient data as in Fig. 7.15, average signal evolution are displayed in (a) and (b), for two different ROIs (corresponding to the blue box). Intensity curves were normalized to the baseline each and shifted along the time domain to account for different timings of administration of contrast agent during individual measurements. Furthermore shown are mean and standard deviations of the FWHM estimation within the same ROIs, in (c) and (d).

Temporal evolution, tSNR and g-factors

In addition to the visual representation in Fig. 7.15, an analysis based on ROIs of the same measurement is presented in Fig. 7.18 for POCS-EPI, k-t-EPI and GRAPPA-EPI. This data set is representative of the results in other patient measurements. Normalized and averaged magnitude intensity time curves for two different ROIs, as well as the cumulative mean and standard deviation of the FWHM estimation, are displayed. The three methods exhibit the same depth during maximum signal decrease, but differ slightly after the bolus passage. Note that k-t-EPI and GRAPPA-EPI were derived from the same acquisition data. As this data was acquired during the repeated administration of contrast agent, the first administration could still affect the measurement. Both k-t-EPI and GRAPPA-EPI time curves are very similar. In both, slight systematic fluctuations are present in the averaged temporal evolution. The latter indicates the origin to lie within the acquisition itself and not the reconstruction method.

Estimations of the FWHM reveal a much greater range of deviation for GRAPPA-EPI than in k-t-EPI. For the second ROI, the mean obtained in GRAPPA-EPI is even lower than in the POCS-EPI reference. Mean FWHM of k-t-EPI and POCS-EPI are in a close agreement. Standard deviations of k-t-EPI are found to be larger in some regions.

Using the example of the slice of Figure 7.19, tSNR and g-factors are assessed for two differ-

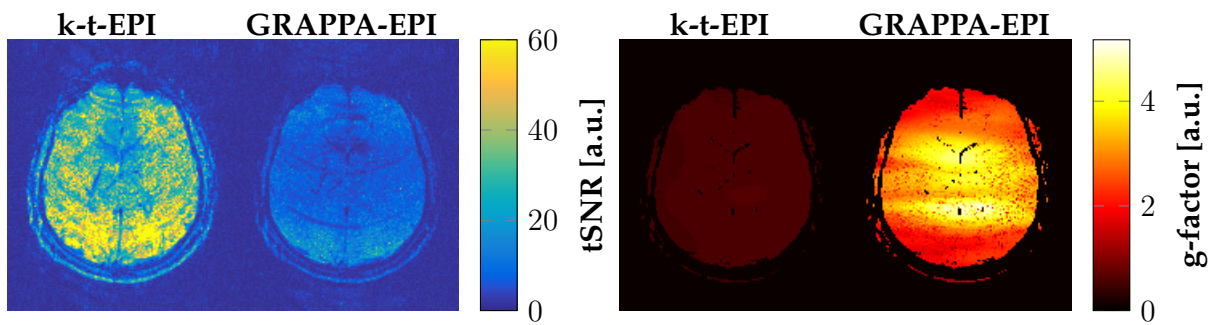


Figure 7.19: t SNR maps and temporal average g -factors for the same slice as in Fig. 7.16 are shown for the two parallel imaging reconstructions of k - t -EPI and GRAPPA-EPI. Whereas k - t -EPI provides high t SNR and low g -factor penalty, t SNR is reduced and g -factor noise amplified in GRAPPA-EPI.

ent parallel imaging reconstruction scenarios as part of k - t -EPI and GRAPPA-EPI in Fig. 7.19. As expected from the analysis based on dynamics induced by flip angle variation, k - t -EPI produces higher t SNR and lower g -factor penalty than GRAPPA-EPI. The g -factor map of GRAPPA-EPI exhibits the typical increase in the central part of the reconstruction due to reduced sensitivities. The same area has also slightly higher g -factor values in k - t -EPI, which is not visible in the same color coding as GRAPPA-EPI.

7.4. Discussion

Based on an interleaved EPI trajectory, three different acquisition strategies that facilitate k - t -undersampled EPI with ACS data acquisition were presented: k - t -EPI with inplace, extra and dynamic extra ACS. The sampling scheme allows to incorporate time-resolved parallel imaging reconstruction methods, such as k - t -GRAPPA, into EPI. In this way, the number of time-consuming phase encoding steps can be substantially reduced while maintaining or even increasing the spatial resolution. The thereby shortened echo train has a beneficial effect on suppressing in-plane susceptibility artifacts as well as geometric distortion. Previous reports on incorporating non-time-resolved parallel imaging methods, such as GRAPPA, into EPI were limited to low reduction factors. With k - t -EPI, the aim to overcome SNR limitations was reached. Higher reduction factors with a more benign SNR behavior were presented.

In order to evaluate the three acquisition strategies with respect to different reduction factors, in vivo measurements with flip angle induced dynamics were performed. The most benign acquisition scenario for DSC weighted cerebral perfusion imaging was identified: k - t -EPI with inplace ACS at reduction factor $R = 5$. It was successfully applied in DSC weighted cerebral perfusion imaging in patients. The goal of high spatial resolution CBV assessment was thereby achieved without sacrificing temporal resolution. Comparison with the standard clinical routine measurement confirms that more fine details are reproduced in the k - t -EPI measurement. Several cases were shown, where the higher resolution in CBV maps provided a substantial gain in information. Additionally, improved imaging behavior in the orbitofrontal cortex with less distortion was observed.

SNR in comparison with GRAPPA

High g-factor penalties limited the application of high reduction factors in the context of non-time-resolved parallel imaging and make time-resolved methods more favorable. However, neighboring time frames are somehow combined in the latter and temporal fidelity is therefore a great issue. These concerns are addressed in the analysis of in vivo measurements based on controlled flip angle induced dynamics, as well as in the DSC-weighted acquisitions in patients.

The substantial SNR loss in conventional GRAPPA reconstructions is effectively compensated by applying k-t-GRAPPA in EPI. Figures 7.7 and 7.9 demonstrate the improved image quality in terms of SNR. Correspondingly, DSC-weighted images during bolus passage exhibit a reduced noise level in k-t-EPI acquisitions (Figs. 7.15 - 7.17).

The improved noise behavior of k-t-EPI is confirmed in the theoretical framework of g-factors (Figs. 7.14 and 7.19). In GRAPPA reconstructions, high temporal average g-factors certify a high noise level. The findings clearly indicate that reduction factors above $R = 7$ exceed the capability of conventional GRAPPA reconstruction, despite the usage of the high number of 32 coil channels.

Since the g-factor solely reflects penalties in noise variances and not systematic errors, it cannot constitute the only metric assessed in rating the quality of reconstructions in k-t-EPI. On this account, tSNR values were assessed to reveal temporally fluctuating artifacts of the series of reconstructions. Maps of tSNR of k-t-EPI appear to be of a similar quality as for POCS-EPI (Fig. 7.13 and Table 7.5)). However, slight blurring artifacts appear also in k-t-EPI in the DSC weighted acquisition shown in Fig. 7.19. In GRAPPA reconstructions, tSNR loss is strong and maps exhibit residual artifacts.

Spatio-temporal fidelity and dependency on ACS

[Blaimer et al., 2011] reported that improved g-factors in time-resolved parallel imaging come at the expense of a loss in temporal fidelity. Accuracy in the reconstruction of dynamics was therefore thoroughly considered based on the controlled flip angle variation scheme. Visual inspection (Fig. 7.10), comparison of magnitude evolutions (Fig. 7.11 and 7.18) and an evaluation based on mean values and standard deviations (Fig. 7.12 and Table 7.5)) yielded conclusive assertions about the temporal fidelity in k-t-EPI.

Although differences in timing are not a criterion for exclusion of image reconstruction, temporal depiction fidelity demands certain aspects to be fulfilled. Reconstruction techniques that use convolution kernels in k-t-space implicitly assume shift invariant relations as defined by the kernel geometry. The acquired ACS data have to sufficiently reflect the relevant spatio-temporal correlations, in order to obtain reliable reconstruction weights. As evident in the different temporal response of the three acquisition strategies (Figs. 7.11 and 7.12), depiction fidelity highly depends on the spatio-temporal information the ACS data provides.

In the extra ACS scheme, both sets are acquired in separate RF pulse excitations with the same TR . This supports signal stability and facilitates higher amounts of ACS lines to be sampled in comparison to the other acquisition strategies. The latter increases the number of observations used in the system of equations for calibration of the weights, which seems to be beneficial at first. However, extra ACS data is acquired before the dynamics of the mimicked or actual bolus passage occur. The findings suggest that the full depth of signal decrease cannot be obtained with extra ACS acquisition and k-t-kernel based reconstruction (Fig. 7.12 and Table 7.5). Corresponding FWHM estimations likewise demonstrate a strong broadening of the

intensity variation in these scenarios. Temporal smoothing becomes worse when moving to higher reduction factors. This clearly indicates the necessity of updating ACS data to sufficiently match the spatio-temporal information of the k-t-sub-Nyquist sampled data sets.

An update of ACS data on dynamics is performed in the dynamic extra and the inplace ACS acquisitions scheme. Both schemes therefore provide ACS data that reflects the temporal variation as contained in the k-t-sub-Nyquist sampled data set. ACS data of these schemes therefore allow for the calibration of convolution kernels in k-t-space either as one single averaged kernel or as individual kernels per time frame. Whereas the first has the advantage of more equations in the derivation of the weights, the latter benefits from temporally more accurate calibration data. Procedures need to be chosen in the context of the target application.

Whereas the trajectory of the individual echo trains are the same for k-t-EPI with dynamic extra and extra ACS, two main differences in the temporal order are substantial: 1. the different temporal information content of the ACS data, as already discussed, and 2. different relaxation influences. While both sets are acquired within the same RF excitation in the dynamic extra ACS scheme, both sets are acquired in separate RF pulse excitations for the extra ACS scheme. The first implies that relaxation influences - in particular T_2^* -decay - are effective over both sets in combination, which is not the case in the latter. Whereas timing differences prevents the extra ACS to be incorporated in the images itself, contrast and off-resonance differences impedes the insertion of dynamic extra ACS data. The fixed k_y sampling steps in both acquisition schemes is generally more favorable in terms of a more benign off-resonance behavior. Furthermore, greater echo train reductions relative to the inplace ACS scheme are possible.

The range of ACS lines in the dynamic extra scheme is restricted to a relatively small number of lines, since the desired TE in the subsequent sub-Nyquist sampled echo train imposes timing limitations. The calibration of weights is therefore more affected by noise, which then propagates into the reconstructed image. In terms of temporal fidelity, decreased FWHM on the one hand indicate a smeared temporal response for dynamic extra ACS (Fig. 7.12 and Table 7.5). On the other hand, the signal depth seems less affected (Figs. 7.11 / 7.12 and Table 7.5). This suggests that artifacts could be a main reason for the corrupted temporal fidelity. An improvement of the stability in dynamic extra ACS acquisition as well as development of an advanced strategy to use the ACS data as part of the image series could potentially alleviate these issues in further works.

With the inplace ACS scheme, all data acquired is part of the reconstructed time series of images. An advantage of the acquisition strategy is the same contrast behavior in both ACS and sub-Nyquist-sampled data. In particular the main image contrast - provided by the ACS data - is acquired without g-factor penalty. Another benefit is the dynamically updated ACS data, as already mentioned. Disadvantages of the acquisition scheme arise from the varying phase encoding step sizes within the acquisition of individual images. Dual density acquisitions in EPI with two different velocities in k-space traversal are more prone to off-resonances. Difficulties arise due to the superposition of two different artifact outcomes.

In k-t-EPI with inplace ACS acquisition, excellent agreement with POCS-EPI is observed (Figs. 7.11 / 7.12 and Table 7.5). This indicates high temporal fidelity in the inplace acquisition scheme. Mean values of the induced signal intensity drop, as well as the FWHM, are in the same range as for POCS-EPI, also at the higher reduction factors.

As discussed, the three schemes reveal a high dependency on how ACS data is acquired in EPI. An interesting aspect is revealed in the comparison of a time-resolved and a non-time-resolved parallel imaging reconstruction for k-t-EPI, e.g. k-t-GRAPPA and GRAPPA, in conjunction with these acquisition dependencies. The known trade-off between the time-resolved and non-time-resolved methods lies within noise variances and depiction bias. The latter man-

ifested for instance in the investigation of g-factors and tRMSE as part of Chapter 6. Fig. 7.12b and d demonstrate for the quid quo pro of variances and bias in the three approaches of k-t-EPI: Different ACS schemes mainly affect the mean signal and not the variances in the case of k-t-GRAPPA reconstruction. In the case of GRAPPA, the different schemes affect the variance and not so much the mean signal.

Artifact assessment

Artifacts of k-t-EPI are expected to appear with periodicity of R , due to the periodic application of R different readout trajectories. The tSNR was used to reveal increased variances due to artifacts that fluctuate over the temporal repetitions. However, an appropriate procedure for the differentiation of temporally changing artifacts was not found. The combination of trajectory variations, in particular in combination with physiological noise influences, e.g. breathing or heart beat, complicates the separate assessment.

In k-t-EPI with dynamic extra and extra ACS, wave-like artifacts were sometimes perceived. Whenever these wave-like artifacts were observed, it was in regions of strong B_0 inhomogeneity and solely as part of in vivo measurements. Wave-like artifacts could indicate residual aliasing artifacts that could not be resolved due to insufficiency of the reconstruction weights to account for different off-resonance effects of the individual trajectories. Corresponding CBV maps (not shown here) did not exhibit direct effects of the artificial variation, which is presumably due to the greatly different temporal frequency of these artifacts.

Benefits of increased spatial resolution and improved SNR might outweigh wave-like artifacts that sometimes arise. However, this depends on the target application. For instance in fMRI, any artificial increase at a higher frequency could introduce temporal correlations which alter the derived general linear model dramatically. Further analysis on the outcome and occurrence of these artifacts is therefore highly required.

Since these artifacts were not observed in in-place ACS acquisition, the DSC weighted cerebral perfusion imaging scenarios presented were not affected. Nevertheless, a more distinct assessment of minor periodic fluctuations in correlation with physiological influences would be highly beneficial.

Potentials of k-t-EPI in DSC weighted cerebral perfusion

Time-resolved parallel imaging reconstruction with k-t-EPI and in-place ACS acquisition at reduction factor $R = 5$ was chosen, since it was clearly superior over the other two ACS schemes and GRAPPA reconstruction in terms of SNR and temporal fidelity. Its application in DSC weighted cerebral perfusion imaging facilitated a substantial increase in spatial resolution compared to the standard clinical EPI protocol (Figs. 7.15 - 7.17). Initial feasibility was confirmed in six patients.

Fine details, such as small arteries or venous structures are revealed in the magnitude images of k-t-EPI (Fig. 7.15). High resolution is further preserved in the subsequent CBV assessment. In comparison with the standard EPI, small lesions, as found in the cingulate cortex (Fig. 7.15) or in the parietal lobe (Fig. 7.17), are easier to delineate in the high resolution CBV maps of k-t-EPI.

High spatial resolution provides the potential of more precise delineation of tumor borders. This is supported by the intrinsically finer pixel depiction, but also since partial volume effects are effectively mitigated when the imaging raster of the imaged volume is increased. Differ-

ent types of tissue - in particular vessels and tumorous tissue - are better to distinguish based on the higher spatial resolution CBV maps provided by k-t-EPI. Figure 7.16 demonstrates the small lesion in the cingulate cortex to be much better resolved in the k-t-EPI acquisition than in the conventional EPI. It is specifically easier to differentiate it from the vessels of the anterior interhemispheric fissure. The finer gradation of CBV values of Fig. 7.16 furthermore suggests more detailed estimates of CBV. In stereotactic biopsy surgeries, the more precise localization with more distinct intensity information would be highly beneficial to identify the most aggressive tumorous area for sampling. The enhanced information of high resolution CBV could furthermore assist the navigation in open brain surgeries. The improved spatial resolution and the more accurate geometric conformity thereby simplifies co-registration with the structural MR images for neuronavigation.

Limitations of the current investigation

Relative CBV values depend to some extent on the acquisition type and the method used for post-processing [Paulson and Schmainda, 2008]. On this account, k-t-EPI was not only compared to the vendor's CBV result - used in the clinical routine -, but also to an off-line reconstruction of the exact same post-processing framework (POCS-EPI). In this way, unknown impacts onto CBV derivation can be excluded.

Furthermore discussed in [Paulson and Schmainda, 2008], is the effect of doubled administration of contrast agent. In their study, the application of a full dose of contrast agent as a pre-load is demonstrated to exhibit statistically significant consistency in CBV results. A pre-load potentially decreases T_1 of tissue, wherefore the baseline signal appears reduced. However, this could also weaken relative effects of T_1 leakage.

Two half-dose boli were administered in the patient measurements presented. Solely two half-dose DSC weighted acquisitions allow the evaluation of k-t-EPI in direct comparison with the standard technique of the clinical routine. Two measurements with normal contrast agent dose - in either two different patients or in the same patient at two separate days - cannot be directly compared. In the acquisitions presented, confounding influences due to T_1 leakage are assumed to be low at the given TR of 1.5s. Nevertheless, the repeated contrast agent administration slightly alters the measurement.

The ROI analysis of Fig. 7.18 shows small differences in the signal response after the first-pass of bolus between the two acquisitions. Attenuated recovery of the baseline signal indicates predominant effects of T_2^* leakage according to [Paulson and Schmainda, 2008]. These were excluded in the CBV derivation presented, since integration was performed solely over the first bolus passage. Figure 7.18 further demonstrates the same maximal relative signal drop in k-t-EPI as in POCS-EPI.

It has been reported in various applications that dual or multi-echo acquisition allows for the correction of T_1 leakage effects [Schmiedeskamp et al., 2012, Zaitsev et al., 2005, Paulson and Schmainda, 2008]. The high reduction available with k-t-EPI can be directly translated into an increase of either the number of echoes fitted into one TR or the spatial resolution of individual echo acquisitions. Promising imaging scenarios as presented in [Schmiedeskamp et al., 2012] could be refined using k-t-EPI, in order to support the adjustment of T_1 leakage influences.

This work presents initial feasibility of k-t-EPI with inplace ACS for DSC weighted cerebral perfusion imaging. The two main limitations of the current study are: 1. doubled administration of half-dose contrast agent and 2. the limited number of only six subjects. Reasoning for

the first was discussed above and seems unavoidable for evaluation of the proposed methods in terms of the clinical status quo. In order to overcome the second limitation, a clinical study with a cohort of patients is required. Concrete calculation of the number of cases required would then be based on 1. the expected difference between both acquisitions, 2. a designated range for equivalence of both acquisition results, 3. an estimate of the standard deviation of both measurements, as well as 4. the designated power of the study. To avoid any bias due to the order of the two measurements with contrast agent, a pseudo-randomized order is necessary.

The cases acquired so far suggest that the high spatial resolution CBV maps achieved with k-t-EPI and inplane ACS acquisition at $R = 5$ indeed allow for a substantial gain of information for the clinical application.

Generality of the k-t-EPI concept and relation to other techniques

Here, k-t-EPI is applied to [dynamic susceptibility contrast \(DSC\)](#) weighted cerebral perfusion imaging. However, the generality of the modifications provided with k-t-EPI allow for direct application in any other EPI based dynamic MRI scenario. Among the possible applications are dynamic contrast enhanced (DCE) MRI, angiography or myocardial perfusion, as well as arterial spin labeling (ASL) or blood oxygenation level dependent (BOLD) fMRI, or diffusion MRI. These applications typically rely on EPI based readouts, where various sampling approaches provide different pros and cons.

The presented k-t-EPI trajectory could be used to enhance approaches of interleaved GE-EPI as reported for instance in the context of contrast-enhanced first-pass cardiac imaging [[Bhat et al., 2009](#)] or for DCE-weighted cardiac perfusion [[Ding et al., 1998](#)]. Likewise, it could be compared with standard two-dimensional EPI or three-dimensional approaches for ASL as done in [[Vidorrreta et al., 2013](#)]. Moreover, achievements of parallel EPI as presented in the context of diffusion or fMRI, e.g. [[Bammer et al., 2001](#), [Schmidt et al., 2005](#)], could be investigated further with the usage of k-t-EPI. Initial results of k-t-EPI in fMRI were presented as conference contributions [[Ramb et al., 2015b](#), [Ramb et al., 2015c](#)].

As k-t-EPI relies on k-t-sub-Nyquist-sampling, it does not conflict with other advanced imaging techniques related to RF excitation or multiple echo acquisitions. The potential, beneficial implications of k-t-EPI for multi-echo acquisition were already discussed in the context of T_1 leakage correction. Recently described multiband excitation [[Larkman et al., 2001b](#), [Larkman et al., 2001a](#), [Moeller et al., 2010](#)] increases the acquisition efficiency by simultaneous slice excitation. It uses sensitivity encoding to separate different slice information. In the application of k-t-EPI presented here, the echo train reduction was used to increase spatial resolution and brain coverage while maintaining temporal resolution - at given TE and TR . The multiband technique could be investigated for k-t-EPI, in order to accomplish an additional gain in temporal resolution.

Parallel imaging in three-dimensional EPI acquisitions were discussed for instance for readout-segmented EPI with GRAPPA ($R = 2$) in diffusion MRI [[Frost et al., 2014](#)], as well as for multi-shot EPI and GRAPPA ($R = 2$) in fMRI [[Lutti et al., 2013](#)]. Again, higher reductions could be reached with further development of k-t-EPI for three-dimensional slab acquisitions.

The introduction of CAIPIRINHA (sub-Nyquist sampling along two phase encoding directions) in three-dimensional EPI was very recently used in the context of fMRI at 7T [[Narsude et al., 2015](#)]. A comparison with k-t-EPI could provide further insights about effects of undersampling along different domains in EPI. Moreover, transverse slice images of k-t-EPI

benefit from mitigated in-plane susceptibility artifacts. These artifacts increase with field strength, e.g. at $7T$ [[Martino et al., 2011](#)]. Including k-t-EPI at high fields therefore offers the potential to alleviate this concern.

Chapter 8

Summary and outlook

At the core of this thesis lies the investigation of k-t-sub-Nyquist sampled time-resolved parallel MRI. With k-t-sub-Nyquist sampling, MRI measurements become more efficient, since time-consuming gradient encoding steps are omitted. Efficiency is only guaranteed, if the imaging information can be reconstructed without compromising the spatio-temporal resolution by image artifacts, noise or spatial blurring. Reconstruction from partially sampled data is the task of (time-resolved) parallel imaging and implicitly poses assumptions on the imaging data. A central question of this work was to evaluate implications of these implicit assumptions with respect to imaging acquisitions that are influenced by measurement noise and signal instabilities.

United by the motivation to respond to this central question, k-t-sub-Nyquist sampling with time-resolved parallel imaging was approached from two ends: from the theoretical and the practical end. A signal and noise transfer analysis for time-resolved parallel imaging methods was derived as one key element towards a unified theoretical framework of these methods. Furthermore, time-resolved parallel imaging was explored in the practical context of k-t-sub-Nyquist sampled EPI, where signal is sensitive to disturbances such as the off-resonance phenomena. On the one hand, a united theoretical framework is needed to evaluate and optimize different approaches. On the other hand, it cannot be considered in theory alone, as more complex influences are solely revealed in the practical realization. For this reason, both ends were pursued in this work.

The theoretical side: towards a unified framework

From SENSE to GRAPPA: Two prominent methodological approaches of parallel imaging in the case of static MRI are connected by analogous expressions, paired with the investigation of differences by their effects on g-factor outcomes. SENSE uses sensitivities at full acquisition extent as unfolding weights. GRAPPA employs ACS calibrated reconstruction weights with a truncated kernel extent. Two hybrid methods, extGRAPPA and trSENSE, demonstrate the transitions between SENSE and GRAPPA. The difference in the kernel extent mainly distinguishes between the two approaches.

From GRAPPA to k-t-GRAPPA: A generalization of the known GRAPPA g-factor for k-t-kernel based time-resolved parallel imaging methods such as k-t-GRAPPA is provided. The generalized $g_{x,f}$ -factors are derived pixel-wise and over the range of resolved temporal frequencies. Frequency combination of these quantify the temporally averaged g_x^{avg} -factors for time-resolved methods that are directly comparable to the g-factors of non-time-resolved parallel imaging methods. By the extension of the g-factor concept, non-time-resolved parallel imaging (e.g. GRAPPA) and time-resolved parallel imaging (e.g. k-t-GRAPPA) are bridged. The more benign SNR behavior of k-t-GRAPPA compared to GRAPPA is explained in a theoretical

framework. The improvement due to PEAK-GRAPPA kernels is analyzed. The antagonistic behavior between g-factors (reduced noise variances) and temporal smoothing (increased bias) in time-resolved parallel imaging is demonstrated in an in vivo cardiac application.

From k-t-GRAPPA to Sliding Window: The extended g-factor framework is likewise applicable to the Sliding Window (SW) approach. By step-wise virtual compression of coil elements, a transition from time-resolved parallel imaging (k-t-GRAPPA) to solely temporal kernels (SW) is performed. The effect onto g-factors reveals: The usage of multiple coil information as well as temporal correlations in the reconstruction process results in a spatially varying signal and noise transfer. The pixel-wise frequency response characteristics of k-t-GRAPPA are analyzed with reference to known theory. In particular the PEAK-GRAPPA kernel exhibits benign filtering characteristics for dynamic MRI.

The practical side: k-t-sub-Nyquist-sampled Parallel EPI

In k-t-EPI, the transition of k-t-GRAPPA concepts to brain imaging scenarios is performed. There are several degrees of freedom in the realization of k-t-sub-Nyquist sampled EPI with k-t-GRAPPA reconstruction. Three acquisition strategies are presented: k-t-EPI with inplace ACS, dynamic extra ACS and extra ACS. The signal behavior of EPI that is sensitive to any inconsistencies demonstrates the effects of different acquisition strategies on the image reconstruction result of time-resolved parallel imaging. The different acquisition strategies reveal the necessity that ACS data contains the underlying dynamics, whereas the kernel calibration does not need to be performed separately for each time frame. The different k-t-EPI scenarios based on dynamics induced by flip angles confirmed similar observations as obtained in the theoretical considerations, where the g-factor and tRMSE analysis demonstrated a decrease in noise variances at the expense of an increased bias.

To incorporate parallel imaging in EPI reduces the readout times per slice and increases the bandwidth of the phase encoding direction. Ultimately, this mitigates the main source of artifacts in EPI. With the presented imaging scenarios, the benign SNR behavior of time-resolved versus non-time-resolved parallel imaging reconstructions is made accessible for EPI. Higher reduction factors were achieved compared to previous applications of conventional GRAPPA in EPI. Due to the higher reduction factors, the k-t-sub-Nyquist sampled acquisitions result in considerably reduced spatial blurring and mitigated in-plane susceptibility artifacts compared to standard EPI.

EPI is diversely used in research and in the clinical context. The k-t-EPI with inplace ACS acquisition was applied to - but is not limited to - dynamic susceptibility contrast weighted cerebral perfusion imaging in tumor patients. With the higher reduction factors achievable, the k-t-sub-Nyquist sampled acquisition and k-t-GRAPPA reconstruction allows for an increase of spatial resolution and improved slice coverage at the same TR , compared to standard EPI. This facilitates the assessment of perfusion parameter maps, such as the cerebral blood volume (CBV), at a higher spatial resolution. With the derived spatial resolution of 1.4 mm at 3T, the CBV maps correspond more closely to the anatomical images, which are typically obtained with a resolution of approximately 1 mm. This provides great potential in particular in the assistance of stereotactic biopsies or open brain surgeries. In tumor imaging, the preliminary study indicated an easier delineation of tumor borders due to the increased spatial resolution.

Further developments in spatio-temporal image reconstruction

The analysis of differences in kernel based methods revealed the benefits of incorporating sensitivity information from multiple coils in combination with the temporal domain in the reconstruction process. The gained understanding in different outcomes of kernel based methods that incorporate either the domain of coils (GRAPPA) or time frames (SW) or both (k-t-GRAPPA) in the reconstruction can be used in further approaches.

[Liang, 2007, Haldar and Liang, 2010] introduced the concept of *partial separability (PS)* in the context of MRI. The *spatio-temporal image* $I \in \mathbb{C}^{N_{\text{pix}} \times N_{\text{time}}}$ is thereby expressed by

$$I(\mathbf{x}_p, t) = \sum_{l=1}^L u_l(\mathbf{x}_p) v_l(t), \quad \text{for } p = 1, \dots, N_{\text{pix}} \text{ and } t = 1, \dots, N_{\text{time}}, \quad (8.1)$$

where $u_l(\mathbf{x}_p)$ indicate the *spatial weights* and $v_l(t)$ denote the *temporal basis functions*. The temporal subspace spanned by the set $\{v_l\}_{l=1}^L$ can be obtained from a data set of high temporal resolution by singular value decomposition.

[Lustig and Pauly, 2010, Murphy et al., 2012] propose a GRAPPA kernel based iterative parallel imaging reconstruction procedure referred to as *iterative self-consistent parallel imaging reconstruction from arbitrary k-space (SPIRiT)*. In their method, the iterative reconstruction is constrained by the requirement of self-consistency of neighborhood relations in k-space, similar to GRAPPA. To this end, a SPIRiT operator is determined based on a Nyquist-sampled data set.

The ACS data in the k-t-EPI scenarios presented in this work fulfill the requirements of both high temporal resolution and Nyquist-sampling. Therefore, it allows for the derivation of a set of temporal basis functions $V \in \mathbb{C}^{L \times N_{\text{time}}}$ (in matrix form), as well as a SPIRiT operator \check{G} . Further work with k-t-EPI therefore comprises an iterative reconstruction approach that integrates temporal basis functions of the PS approach with kernel-based iterative parallel imaging of SPIRiT. The spatio-temporal image $I^\dagger \in \mathbb{C}^{N_{\text{pix}} \times N_{\text{time}}}$ is obtained by

$$I^\dagger = U^\dagger V, \quad \text{with} \quad U^\dagger = \underset{U \in \mathbb{C}^{N_{\text{pix}} \times L}}{\text{argmin}} \left\| \mathbf{d} - \check{S}(\check{F}(UV)) \right\|_2^2 + \|\check{G}(UV)\|_2^2 + \mathcal{R}(U), \quad (8.2)$$

where \check{S} is the sampling operator, \check{F} performs the discrete Fourier transform along both spatial dimensions. The additional term $\mathcal{R}(\cdot)$ describes the optional usage of regularization to promote for instance spatial-spectral sparsity. Initial results have been presented in [Ramb et al., 2016a] and a comprehensive study will be subject to future work.

List of paper and conference contributions

List of publications (full paper)

Ramb, R., Mader, I., Jung, B., Hennig, J., and Zaitsev, M. (2016). *High resolution CBV assessment with PEAK-EPI: k-t-undersampling and reconstruction in echo planar imaging*. *Magnetic Resonance in Medicine*, in press

Binter, C., **Ramb, R.**, Jung, B., and Kozerke, S. (2016). *A g-factor metric for k-t SENSE and k-t PCA based parallel imaging*. *Magnetic Resonance in Medicine*, 75(2):562–571 doi: 10.1002/mrm.25606 [[Binter et al., 2016](#)]

Ramb, R., Binter, C., Schultz, G., Assländer, J., Breuer, F., Zaitsev, M., Kozerke, S., and Jung, B. (2015). *A g-factor metric for k-t-GRAPPA and PEAKGRAPPA based parallel imaging*. *Magnetic Resonance in Medicine*, 74(1):125–135. [[Ramb et al., 2015a](#)]

Ramb, R., Eichler, M., Ing, A., Thiel, M., Weiller, C., Grebogi, C., Schwarzbauer, C., Timmer, J., and Schelter, B. (2013). *The impact of latent confounders in directed network analysis in neuroscience*. *Philosophical Transactions of the Royal Society of London A: Mathematical, Physical and Engineering Sciences*, 371(1997):20110612. [[Ramb et al., 2013c](#)]

List of conference contributions as first author

Ramb, R., Christodoulou, A. G., Mader, I., Zaitsev, M., Liang, Z.-P., and Hennig, J. (2016). *High resolution CBV assessment with PEAK-EPI and PSSPIRiT-EPI*. In *Proceedings of the 24th Annual Meeting of ISMRM, Singapore* [[Ramb et al., 2016a](#)]

Ramb, R., Levan, P., and Hennig, J. (2015). *PEAK-EPI: Feasibility and benefits of k-t-undersampled EPI acquisition and PEAK-GRAPPA reconstruction in fMRI*. In *Proceedings of the 23rd Annual Meeting of ISMRM, Toronto, Canada*, p. 3920. [[Ramb et al., 2015b](#)]

Ramb, R., Levan, P., Zaitsev, M., and Hennig, J. (2015). *Feasibility of Resting-state fMRI in the orbitofrontal cortex with less distortion using PEAKEPI*. In *Proceedings of the 22nd Annual Meeting of OHBM, Honolulu, Hawaii, USA* [[Ramb et al., 2015c](#)]

Ramb, R., Kellner, E., Dragonu, I., Testud, F., Mader, I., Hennig, J., Zaitsev, M., and Jung, B. (2014). *k-t-EPI: k-t-undersampled EPI acquisition and reconstruction in cerebral perfusion*. In *Proceedings of the 22nd Annual Meeting of ISMRM, Milano, Italy*, page p. 4370. [[Ramb et al., 2014b](#)]

Ramb, R., Binter, C., Schultz, G., Assländer, J., Breuer, F., Zaitsev, M., Kozerke, S., and Jung, B. (2014). *An analytical g-factor framework for k-t-GRAPPA/PEAK-GRAPPA*. In SFB workshop on Imaging with Modulated/Incomplete Data. [[Ramb et al., 2014a](#)]

Ramb, R., Binter, C., Breuer, F., Schultz, G., Zaitsev, M., Kozerke, S., and Jung, B. (2013). *A g-factor metric for k-t-GRAPPA reconstructions*. In Proceedings of the 21st Annual Meeting of ISMRM, Salt Lake City, USA, p. 4370. [[Ramb et al., 2013b](#)]

Ramb, R. and Schultz, G. (2013). *Extended GRAPPA and Truncated SENSE: Separating Effects in Parallel Imaging*. In Proceedings of the 30th Annual Scientific Meeting of ESMRMB, Toulouse, France. [[Ramb and Schultz, 2013](#)]

Ramb, R., Binter, C., Breuer, F., Kozerke, S., and Jung, B. (2013). *A g-factor metric for k-t-GRAPPA reconstructions*. In ISMRM workshop on Data Sampling and Image Reconstruction [[Ramb et al., 2013a](#)]

Diploma thesis

Ramb, R. (2011). *Graphical Models in Time Series: From Basic Concepts to Latent Variables*. Diplomarbeit (Diploma thesis), Philipps-Universität Marburg. [[Ramb, 2011](#)]

Bibliography

- [Bammer et al., 2002] Bammer, R., Auer, M., Keeling, S. L., Augustin, M., Stables, L. A., Prokesch, R. W., Stollberger, R., Moseley, M. E., and Fazekas, F. (2002). Diffusion tensor imaging using single-shot SENSE-EPI. *Magnetic Resonance in Medicine*, 48(1):128–136.
- [Bammer et al., 2001] Bammer, R., Keeling, S. L., Augustin, M., Pruessmann, K. P., Wolf, R., Stollberger, R., Hartung, H.-P., and Fazekas, F. (2001). Improved diffusion-weighted single-shot echo-planar imaging (EPI) in stroke using sensitivity encoding (SENSE). *Magnetic Resonance in Medicine*, 46(3):548–554.
- [Baron and Beaulieu, 2016] Baron, C. A. and Beaulieu, C. (2016). Motion robust GRAPPA for echo-planar imaging. *Magnetic Resonance in Medicine*, 75(3):1166–1174.
- [Bauer et al., 2013] Bauer, S., Markl, M., Föll, D., Russe, M., Stankovic, Z., and Jung, B. (2013). k-t GRAPPA accelerated phase contrast MRI: Improved assessment of blood flow and 3-directional myocardial motion during breath-hold. *Journal of Magnetic Resonance Imaging*, 38(5):1054–1062.
- [Bernstein et al., 2004] Bernstein, M. A., King, K. F., and Zhou, X. J. (2004). *Handbook of MRI pulse sequences*. Elsevier.
- [Bertero et al., 1985] Bertero, M., Mol, C. D., and Pike, E. R. (1985). Linear inverse problems with discrete data. I. General formulation and singular system analysis. *Inverse Problems*, 1(4):301.
- [Bhat et al., 2009] Bhat, H., Zuehlsdorff, S., Bi, X., and Li, D. (2009). Whole-heart contrast-enhanced coronary magnetic resonance angiography using gradient echo interleaved EPI. *Magnetic Resonance in Medicine*, 61(6):1388–1395.
- [Binter et al., 2016] Binter, C., Ramb, R., Jung, B., and Kozerke, S. (2016). A g-factor metric for k-t SENSE and k-t PCA based parallel imaging. *Magnetic Resonance in Medicine*, 75(2):562–571.
- [Blaimer et al., 2004] Blaimer, M., Breuer, F., Mueller, M., Heidemann, R. M., Griswold, M. A., and Jakob, P. M. (2004). SMASH, SENSE, PILS, GRAPPA: how to choose the optimal method. *Topics in Magnetic Resonance Imaging*, 15(4):223–236.
- [Blaimer et al., 2011] Blaimer, M., Ponce, I. P., Breuer, F. A., Jakob, P. M., Griswold, M. A., and Kellman, P. (2011). Temporal filtering effects in dynamic parallel MRI. *Magnetic Resonance in Medicine*, 66(1):192–198.
- [Bloch, 1946] Bloch, F. (1946). Nuclear Induction. *Physical Review*, 70:460–474.
- [Boxerman et al., 2006] Boxerman, J., Schmainda, K., and Weisskoff, R. (2006). Relative cerebral blood volume maps corrected for contrast agent extravasation significantly correlate with

- glioma tumor grade, whereas uncorrected maps do not. *American Journal of Neuroradiology*, 27(4):859–867.
- [Boxerman et al., 1995] Boxerman, J. L., Hamberg, L. M., Rosen, B. R., and Weisskoff, R. M. (1995). MR contrast due to intravascular magnetic susceptibility perturbations. *Magnetic Resonance in Medicine*, 34(4):555–566.
- [Brau et al., 2008] Brau, A. C., Beatty, P. J., Skare, S., and Bammer, R. (2008). Comparison of reconstruction accuracy and efficiency among autocalibrating data-driven parallel imaging methods. *Magnetic Resonance in Medicine*, 59:382–395.
- [Breuer et al., 2005a] Breuer, F. A., Blaimer, M., Heidemann, R. M., Mueller, M. F., Griswold, M. A., and Jakob, P. M. (2005a). Controlled aliasing in parallel imaging results in higher acceleration (CAIPIRINHA) for multi-slice imaging. *Magnetic Resonance in Medicine*, 53(3):684–691.
- [Breuer et al., 2009] Breuer, F. A., Kannengiesser, S. A., Blaimer, M., Seiberlich, N., Jakob, P. M., and Griswold, M. A. (2009). General formulation for quantitative G-factor calculation in GRAPPA reconstructions. *Magnetic Resonance in Medicine*, 62(3):739–746.
- [Breuer et al., 2005b] Breuer, F. A., Kellman, P., Griswold, M. A., and Jakob, P. M. (2005b). Dynamic autocalibrated parallel imaging using temporal GRAPPA (TGRAPPA). *Magnetic Resonance in Medicine*, 53(4):981–985.
- [Brockwell and Davis, 2013] Brockwell, P. J. and Davis, R. A. (2013). *Time series: Theory and methods*. Springer Science & Business Media.
- [Bruder et al., 1992] Bruder, H., Fischer, H., Reinfelder, H.-E., and Schmitt, F. (1992). Image reconstruction for echo planar imaging with nonequidistant k-space sampling. *Magnetic Resonance in Medicine*, 23(2):311–323.
- [Buehrer et al., 2007] Buehrer, M., Pruessmann, K. P., Boesiger, P., and Kozerke, S. (2007). Array compression for MRI with large coil arrays. *Magnetic Resonance in Medicine*, 57(6):1131–1139.
- [Bydder et al., 2002] Bydder, M., Larkman, D. J., and Hajnal, J. V. (2002). Generalized SMASH imaging. *Magnetic Resonance in Medicine*, 47(1):160–170.
- [Calamante et al., 2002] Calamante, F., Gadian, D., and Connelly, A. (2002). Quantification of perfusion using bolus tracking magnetic resonance imaging in stroke assumptions, limitations, and potential implications for clinical use. *Stroke*, 33(4):1146–1151.
- [Carlson, 1987] Carlson, J. W. (1987). An algorithm for NMR imaging reconstruction based on multiple RF receiver coils. *Journal of Magnetic Resonance (1969)*, 74(2):376–380.
- [Carlson and Minemura, 1993] Carlson, J. W. and Minemura, T. (1993). Imaging time reduction through multiple receiver coil data acquisition and image reconstruction. *Magnetic Resonance in Medicine*, 29(5):681–687.
- [Chao et al., 2010] Chao, T.-C., Chung, H.-W., Hoge, W. S., and Madore, B. (2010). A 2D MTF approach to evaluate and guide dynamic imaging developments. *Magnetic Resonance in Medicine*, 63:407–418.
- [Constantinides et al., 1997] Constantinides, C. D., Atalar, E., and McVeigh, E. R. (1997). Signal-to-noise measurements in magnitude images from NMR phased arrays. *Magnetic Resonance in Medicine*, 38(5):852–857.

- [Cooley and Tukey, 1965] Cooley, J. W. and Tukey, J. W. (1965). An Algorithm for the Machine Calculation of Complex Fourier Series. *Mathematics of Computation*, 19(90):297–301.
- [Copen et al., 2011] Copen, W. A., Schaefer, P. W., and Wu, O. (2011). MR Perfusion Imaging in Acute Ischemic Stroke. *Neuroimaging Clinics of North America*, 21(2):259–283. Stroke Imaging.
- [Covarrubias et al., 2004] Covarrubias, D. J., Rosen, B. R., and Lev, M. H. (2004). Dynamic magnetic resonance perfusion imaging of brain tumors. *The Oncologist*, 9(5):528–537.
- [d’Arcy et al., 2002] d’Arcy, J. A., Collins, D. J., Rowland, I. J., Padhani, A. R., and Leach, M. O. (2002). Applications of sliding window reconstruction with cartesian sampling for dynamic contrast enhanced MRI. *NMR in Biomedicine*, 15:174–183.
- [de Zwart et al., 2002] de Zwart, J. A., van Gelderen, P., Kellman, P., and Duyn, J. H. (2002). Application of sensitivity-encoded echo-planar imaging for blood oxygen level-dependent functional brain imaging. *Magnetic Resonance in Medicine*, 48(6):1011–1020.
- [Deichmann et al., 2002] Deichmann, R., Josephs, O., Hutton, C., Corfield, D., and Turner, R. (2002). Compensation of Susceptibility-Induced BOLD Sensitivity Losses in Echo-Planar fMRI Imaging. *Neuroimage*, 15(1):120–135.
- [Ding et al., 1998] Ding, S., Wolff, S. D., and Epstein, F. H. (1998). Improved coverage in dynamic contrast-enhanced cardiac MRI using interleaved gradient-echo EPI. *Magnetic Resonance in Medicine*, 39(4):514–519.
- [Ding et al., 2011] Ding, Y., Chung, Y.-C., Jekic, M., and Simonetti, O. P. (2011). A new approach to autocalibrated dynamic parallel imaging based on the Karhunen-Loeve transform: KL-TSENSE and KL-TGRAPPA. *Magnetic Resonance in Medicine*, 65(6):1786–1792.
- [Doyle et al., 1995] Doyle, M., Walsh, E. G., Blackwell, G. G., and Pohost, G. M. (1995). Block Regional Interpolation Scheme for k-Space (BRISK): A Rapid Cardiac Imaging Technique. *Magnetic Resonance in Medicine*, 33(2):163–170.
- [Farzaneh et al., 1990] Farzaneh, F., Riederer, S. J., and Pelc, N. J. (1990). Analysis of T2 limitations and off-resonance effects on spatial resolution and artifacts in echo planar imaging. *Magnetic Resonance in Medicine*, 14(1):123–139.
- [Feinberg and Oshio, 1994] Feinberg, D. A. and Oshio, K. (1994). Phase errors in multi-shot echo planar imaging. *Magnetic Resonance in Medicine*, 32(4):535–539.
- [Fischer and Ladebeck, 1998] Fischer, H. and Ladebeck, R. (1998). Echo-planar imaging image artifacts. In *Echo-planar imaging*, pages 179–200. Springer.
- [Fisel et al., 1991] Fisel, C. R., Ackerman, J. L., Buxton, R. B., Garrido, L., Belliveau, J. W., Rosen, B. R., and Brady, T. J. (1991). MR Contrast Due to Microscopically Heterogeneous Magnetic Susceptibility: Numerical Simulations and Applications to Cerebral Physiology. *Magnetic Resonance in Medicine*, 17(2):336–347.
- [Frost et al., 2014] Frost, R., Miller, K. L., Tijssen, R. H., Porter, D. A., and Jezzard, P. (2014). 3D Multi-slab diffusion-weighted readout-segmented EPI with real-time cardiac-reordered k-space acquisition. *Magnetic Resonance in Medicine*, 72(6):1565–1579.
- [Gallichan et al., 2011] Gallichan, D., Cocosco, C. A., Dewdney, A., Schultz, G., Welz, A., Hennig, J., and Zaitsev, M. (2011). Simultaneously driven linear and nonlinear spatial encoding fields in MRI. *Magnetic Resonance in Medicine*, 65(3):702–714.

- [Gerlach and Stern, 1922] Gerlach, W. and Stern, O. (1922). Der experimentelle Nachweis der Richtungsquantelung im Magnetfeld. *Zeitschrift für Physik A Hadrons and Nuclei*, 9(1):349–352.
- [Gibbs, 1898] Gibbs, J. W. (1898). Fourier’s series. *Nature*, 59:200.
- [Glover et al., 1992] Glover, G. H., Maier, J. K., and Vavrek, R. M. (1992). Correction of NMR data acquired by an echo-planar technique. US Patent 5,151,656.
- [Goertler and Schmitt, 1992] Goertler, G. and Schmitt, F. (1992). Method for suppressing image artifacts in a magnetic resonance imaging apparatus. US Patent 5,138,259.
- [Golay et al., 2000] Golay, X., Pruessmann, K. P., Weiger, M., Crelier, G. R., Folkers, P. J., Kollias, S. S., and Boesiger, P. (2000). PRESTO-SENSE: An ultrafast whole-brain fMRI technique. *Magnetic Resonance in Medicine*, 43(6):779–786.
- [Griswold et al., 1999] Griswold, M., Jakob, P., Chen, Q., Goldfarb, J., Manning, W., Edelman, R., and Sodickson, D. (1999). Resolution enhancement in single-shot imaging using simultaneous acquisition of spatial harmonics (SMASH). *Magnetic Resonance in Medicine*, 41(6):1236–1245.
- [Griswold et al., 2002] Griswold, M. A., Jakob, P. M., Heidemann, R. M., Nittka, M., Jellus, V., Wang, J., Kiefer, B., and Haase, A. (2002). Generalized autocalibrating partially parallel acquisitions (GRAPPA). *Magnetic Resonance in Medicine*, 47(6):1202–1210.
- [Griswold et al., 2000] Griswold, M. A., Jakob, P. M., Nittka, M., Goldfarb, J. W., and Haase, A. (2000). Partially parallel imaging with localized sensitivities (PILS). *Magnetic Resonance in Medicine*, 44(4):602–609.
- [Gudbjartsson and Patz, 1995] Gudbjartsson, H. and Patz, S. (1995). The rician distribution of noisy mri data. *Magnetic Resonance in Medicine*, 34(6):910–914.
- [Gustafson and Sigal, 2011] Gustafson, S. J. and Sigal, I. M. (2011). *Mathematical concepts of quantum mechanics*. Springer Science & Business Media.
- [Haacke, 1987] Haacke, E. M. (1987). The effects of finite sampling in spin-echo or field-echo magnetic resonance imaging. *Magnetic Resonance in Medicine*, 4(5):407–421.
- [Haacke et al., 1999] Haacke, E. M., Brown, R., Thompson, M., and Venkatesan, R. (1999). Magnetic resonance imaging: physical principles and sequence design. 1999. *New York: A John Wiley and Sons*.
- [Haacke et al., 1990] Haacke, E. M., Liang, Z.-P., and Boada, F. E. (1990). Image reconstruction using POCS, model constraints, and linear prediction theory for the removal of phase, motion, and Gibbs artifacts in magnetic resonance and ultrasound imaging. *Optical Engineering*, 29(5):555–566.
- [Haase et al., 1986] Haase, A., Frahm, J., Matthaei, D., Hancicke, W., and Merboldt, K.-D. (1986). FLASH imaging. Rapid NMR imaging using low flip-angle pulses. *Journal of Magnetic Resonance (1969)*, 67(2):258–266.
- [Hahn, 1950] Hahn, E. L. (1950). Spin Echoes. *Physical Review*, 80:580–594.
- [Haldar and Liang, 2010] Haldar, J. and Liang, Z.-P. (2010). Spatiotemporal imaging with partially separable functions: A matrix recovery approach. In *IEEE International Symposium on*

Biomedical Imaging, pages 716–719.

- [Hansen et al., 2015] Hansen, M. S., Inati, S. J., and Kellman, P. (2015). Noise propagation in region of interest measurements. *Magnetic Resonance in Medicine*, 73(3):1300–1308.
- [Hargreaves, 2012] Hargreaves, B. (2012). Rapid gradient-echo imaging. *Journal of Magnetic Resonance Imaging*, 36(6):1300–1313.
- [Hayes and Roemer, 1990] Hayes, C. E. and Roemer, P. B. (1990). Noise correlations in data simultaneously acquired from multiple surface coil arrays. *Magnetic Resonance in Medicine*, 16(2):181–191.
- [Heid, 1997] Heid, O. (1997). Robust EPI Phase Correction. In *Proceedings of the 5th Annual Meeting of ISMRM, Vancouver, British Columbia, Canada*, page 2014.
- [Heidemann et al., 2001] Heidemann, R. M., Griswold, M. A., Haase, A., and Jakob, P. M. (2001). VD-AUTO-SMASH imaging. *Magnetic Resonance in Medicine*, 45(6):1066–1074.
- [Henkelman, 1985] Henkelman, R. M. (1985). Measurement of signal intensities in the presence of noise in MR images. *Medical physics*, 12(2):232–233.
- [Hennig et al., 1986] Hennig, J., Nauerth, A., and Friedburg, H. (1986). RARE imaging: A fast imaging method for clinical MR. *Magnetic Resonance in Medicine*, 3(6):823–833.
- [Hennig et al., 2008] Hennig, J., Welz, A. M., Schultz, G., Korvink, J., Liu, Z., Speck, O., and Zaitsev, M. (2008). Parallel imaging in non-bijective, curvilinear magnetic field gradients: a concept study. *Magnetic Resonance Materials in Physics, Biology and Medicine*, 21(1-2):5–14.
- [Hennig et al., 2007] Hennig, J., Zhong, K., and Speck, O. (2007). MR-Encephalography: Fast multi-channel monitoring of brain physiology with magnetic resonance. *Neuroimage*, 34(1):212–219.
- [Hestenes and Stiefel, 1952] Hestenes, M. R. and Stiefel, E. (1952). Methods of conjugate gradients for solving linear systems.
- [Hu et al., 2010] Hu, L., Baxter, L., Pinnaduwege, D., Paine, T., Karis, J., Feuerstein, B., Schmainda, K., Dueck, A., Debbins, J., Smith, K., et al. (2010). Optimized preload leakage-correction methods to improve the diagnostic accuracy of dynamic susceptibility-weighted contrast-enhanced perfusion MR imaging in posttreatment gliomas. *American Journal of Neuroradiology*, 31(1):40–48.
- [Hu, 1994] Hu, X. (1994). On the "keyhole" technique. *Journal of Magnetic Resonance Imaging*, 4(2):231–231.
- [Huang et al., 2005] Huang, F., Akao, J., Vijayakumar, S., Duensing, G. R., and Limkeman, M. (2005). k-t GRAPPA: A k-space implementation for dynamic MRI with high reduction factor. *Magnetic Resonance in Medicine*, 54(5):1172–1184.
- [Hutchinson and Raff, 1988] Hutchinson, M. and Raff, U. (1988). Fast MRI data acquisition using multiple detectors. *Magnetic Resonance in Medicine*, 6(1):87–91.
- [Hyde et al., 1986] Hyde, J. S., Jesmanowicz, A., Francisz, W., Kneeland, J. B., Grist, T. M., and Campagna, N. F. (1986). Parallel image acquisition from noninteracting local coils. *Journal of Magnetic Resonance (1969)*, 70(3):512–517.
- [Jähne, 2013] Jähne, B. (2013). *Digitale Bildverarbeitung*. Springer-Verlag.

- [Jakob et al., 1998] Jakob, P., Grisowld, M., Edelman, R., and Sodickson, D. (1998). AUTO-SMASH: A self-calibrating technique for SMASH imaging. *Magnetic Resonance Materials in Physics, Biology and Medicine*, 7(1):42–54.
- [Johnson and Hutchison, 1985] Johnson, G. and Hutchison, J. (1985). The limitations of NMR recalled-echo imaging techniques. *Journal of Magnetic Resonance (1969)*, 63(1):14–30.
- [Johnson, 1928] Johnson, J. B. (1928). Thermal Agitation of Electricity in Conductors. *Physical Review*, 32:97–109.
- [Jones et al., 1993] Jones, R. A., Haraldseth, O., Müller, T. B., Rinck, P. A., and Øksendal, A. N. (1993). k-Space substitution: A novel dynamic imaging technique. *Magnetic Resonance in Medicine*, 29(6):830–834.
- [Jung and Kozerke, 2009] Jung, B. and Kozerke, S. (2009). Comparison of kt-SENSE and kt-GRAPPA applied to cardiac cine and phase contrast imaging. In *Proceedings of the 17th Annual Meeting of ISMRM*, 17.
- [Jung et al., 2011] Jung, B., Stalder, A. F., Bauer, S., and Markl, M. (2011). On the undersampling strategies to accelerate time-resolved 3D imaging using k-t-GRAPPA. *Magnetic Resonance in Medicine*, 66(4):966–975.
- [Jung et al., 2008] Jung, B., Ullmann, P., Honal, M., Bauer, S., Hennig, J., and Markl, M. (2008). Parallel MRI with extended and averaged GRAPPA kernels (PEAK-GRAPPA): Optimized spatiotemporal dynamic imaging. *Journal of Magnetic Resonance Imaging*, 28(5):1226–1232.
- [Kellman et al., 2001a] Kellman, P., Epstein, F. H., and McVeigh, E. R. (2001a). Adaptive sensitivity encoding incorporating temporal filtering (TSENSE). *Magnetic Resonance in Medicine*, 45(5):846–852.
- [Kellman et al., 2001b] Kellman, P., Epstein, H., and McVeigh, E. (2001b). Adaptive sensitivity encoding incorporating temporal filtering (TSENSE). In *Proceedings of the 9th Annual Meeting of ISMRM, Glasgow, Scotland*, page 445.
- [Kellman and McVeigh, 2005] Kellman, P. and McVeigh, E. R. (2005). Image reconstruction in SNR units: A general method for SNR measurement. *Magnetic Resonance in Medicine*, 54:1439–1447.
- [Kellner et al., 2013] Kellner, E., Mader, I., Mix, M., Splitthoff, D. N., Reiser, M., Foerster, K., Nguyen-Thanh, T., Gall, P., and Kiselev, V. G. (2013). Arterial input function measurements for bolus tracking perfusion imaging in the brain. *Magnetic Resonance in Medicine*, 69(3):771–780.
- [Kelton et al., 1989] Kelton, J. R., Magin, R. L., and Wright, S. M. (1989). An algorithm for rapid image acquisition using multiple receiver coils. In *Proceedings of the 8th Annual Meeting of SMRM*, page 1172.
- [Kholmovski and Parker, 2006] Kholmovski, E. and Parker, D. (2006). Spatially variant GRAPPA. In *Proceedings of the 14th Annual Meeting of ISMRM*, page 285.
- [Kwiat and Einav, 1995] Kwiat, D. and Einav, S. (1995). Preliminary experimental evaluation of an inverse source imaging procedure using a decoupled coil detector array in magnetic resonance imaging. *Medical Engineering & Physics*, 17(4):257–263.
- [Kwiat et al., 1991] Kwiat, D., Einav, S., and Navon, G. (1991). A decoupled coil detector array

- for fast image acquisition in magnetic resonance imaging. *Medical Physics*, 18(2):251–265.
- [Larkman et al., 2001a] Larkman, D. J., deSouza, N. M., Bydder, M., and Hajnal, J. V. (2001a). An investigation into the use of sensitivity-encoded techniques to increase temporal resolution in dynamic contrast-enhanced breast imaging. *Journal of Magnetic Resonance Imaging*, 14(3):329–335.
- [Larkman et al., 2001b] Larkman, D. J., Hajnal, J. V., Herlihy, A. H., Coutts, G. A., Young, I. R., and Ehnholm, G. (2001b). Use of multicoil arrays for separation of signal from multiple slices simultaneously excited. *Journal of Magnetic Resonance Imaging*, 13(2):313–317.
- [Levitt, 2001] Levitt, M. H. (2001). *Spin dynamics: basics of nuclear magnetic resonance*. John Wiley & Sons.
- [Liang, 2007] Liang, Z.-P. (2007). Spatiotemporal imaging with partially separable functions. In *IEEE International Symposium on Biomedical Imaging*, pages 988–991.
- [Liang et al., 1992] Liang, Z.-P., Boada, F., Constable, R., Haacke, E., Lauterbur, P., and Smith, M. (1992). Constrained reconstruction methods in MR imaging. *Rev Magn Reson Med*, 4(2):67–186.
- [Liang and Lauterbur, 2000] Liang, Z.-P. and Lauterbur, P. C. (2000). *Principles of Magnetic Resonance Imaging: A Signal Processing Perspective*. The Institute of Electrical and Electronics Engineers Press.
- [Lin et al., 2006] Lin, F.-H., Wald, L. L., Ahlfors, S. P., Hämmäläinen, M. S., Kwong, K. K., and Belliveau, J. W. (2006). Dynamic magnetic resonance inverse imaging of human brain function. *Magnetic Resonance in Medicine*, 56(4):787–802.
- [Liu et al., 2007] Liu, T., Kressler, B., Wang, K., and Wang, Y. (2007). Block circulant quasi-band matrix property for the SENSE unfolding in k-space and justification for GRAPPA. In *Proceedings of the Annual International Conference of the IEEE Engineering in Medicine and Biology Society*, volume 2008, pages 1659–1662.
- [Ljunggren, 1983] Ljunggren, S. (1983). A simple graphical representation of fourier-based imaging methods. *Journal of Magnetic Resonance (1969)*, 54(2):338–343.
- [Lustig and Pauly, 2010] Lustig, M. and Pauly, J. M. (2010). SPIRiT: Iterative self-consistent parallel imaging reconstruction from arbitrary k-space. *Magnetic Resonance in Medicine*, 64(2):457–471.
- [Lütcke et al., 2006] Lütcke, H., Merboldt, K.-D., and Frahm, J. (2006). The cost of parallel imaging in functional MRI of the human brain. *Magnetic Resonance Imaging*, 24(1):1–5.
- [Lutti et al., 2013] Lutti, A., Thomas, D. L., Hutton, C., and Weiskopf, N. (2013). High-resolution functional MRI at 3 T: 3D/2D echo-planar imaging with optimized physiological noise correction. *Magnetic Resonance in Medicine*, 69(6):1657–1664.
- [Maclaren et al., 2013] Maclaren, J., Herbst, M., Speck, O., and Zaitsev, M. (2013). Prospective motion correction in brain imaging: A review. *Magnetic Resonance in Medicine*, 69(3):621–636.
- [Madore, 2001] Madore, B. (2001). Using UNFOLD to remove artifacts in dynamic imaging. In *Proceedings of the 9th Annual Meeting of ISMRM, Glasgow, Scotland*, page 444.
- [Madore, 2002] Madore, B. (2002). Using UNFOLD to remove artifacts in parallel imaging and

- in partial-Fourier imaging. *Magnetic Resonance in Medicine*, 48(3):493–501.
- [Madore, 2004] Madore, B. (2004). UNFOLD-SENSE: A parallel MRI method with self-calibration and artifact suppression. *Magnetic Resonance in Medicine*, 52(2):310–320.
- [Madore et al., 1999] Madore, B., Glover, G. H., Pelc, N. J., et al. (1999). Unaliasing by Fourier-encoding the overlaps using the temporal dimension (UNFOLD), applied to cardiac imaging and fMRI. *Magnetic Resonance in Medicine*, 42(5):813–828.
- [Mansfield, 1977] Mansfield, P. (1977). Multi-planar image formation using NMR spin echoes. *Journal of Physics C: Solid State Physics*, 10(3):55.
- [Martino et al., 2011] Martino, F. D., Esposito, F., van de Moortele, P.-F., Harel, N., Formisano, E., Goebel, R., Ugurbil, K., and Yacoub, E. (2011). Whole brain high-resolution functional imaging at ultra high magnetic fields: An application to the analysis of resting state networks. *Neuroimage*, 57(3):1031–1044. Special Issue: Educational Neuroscience.
- [McGibney and Smith, 1993] McGibney, G. and Smith, M. (1993). An unbiased signal-to-noise ratio measure for magnetic resonance images. *Medical physics*, 20(4):1077–1078.
- [McGibney et al., 1993] McGibney, G., Smith, M. R., Nichols, S. T., and Crawley, A. (1993). Quantitative evaluation of several partial fourier reconstruction algorithms used in mri. *Magnetic Resonance in Medicine*, 30(1):51–59.
- [Miller and Joseph, 1993] Miller, A. J. and Joseph, P. M. (1993). The use of power images to perform quantitative analysis on low SNR MR images. *Magnetic Resonance Imaging*, 11(7):1051–1056.
- [Mintzopoulos et al., 2008] Mintzopoulos, D., Astrakas, L., Wiggins, G., Wald, L., Rosen, B., and Tzika, A. (2008). Improved BOLD detection at 3T using high-resolution GRAPPA EPI fMRI. In *In Proceedings of the 16th Annual Meeting of ISMRM*, volume 16, page 2375.
- [Moeller et al., 2010] Moeller, S., Yacoub, E., Olman, C. A., Auerbach, E., Strupp, J., Harel, N., and Ugurbil, K. (2010). Multiband multislice GE-EPI at 7 tesla, with 16-fold acceleration using partial parallel imaging with application to high spatial and temporal whole-brain fMRI. *Magnetic Resonance in Medicine*, 63(5):1144–1153.
- [Moore, 1920] Moore, E. (1920). On the reciprocal of the general algebraic matrix. *Bulletin of the American Mathematical Society*, 26(394-395):38.
- [Murphy et al., 2012] Murphy, M., Alley, M., Demmel, J., Keutzer, K., Vasanawala, S., and Lustig, M. (2012). Fast-SPIRiT compressed sensing parallel imaging MRI: scalable parallel implementation and clinically feasible runtime. *IEEE Transactions on Medical Imaging*, 31(6):1250–1262.
- [Narsude et al., 2015] Narsude, M., Gallichan, D., van der Zwaag, W., Gruetter, R., and Marques, J. P. (2015). Three-dimensional echo planar imaging with controlled aliasing: A sequence for high temporal resolution functional MRI. *Magnetic Resonance in Medicine*, page DOI: 10.1002/mrm.25835.
- [Newbould et al., 2006] Newbould, R., Skare, S., Clayton, D., Alley, M., Albers, G., Lansberg, M., and Bammer, R. (2006). PERMEATE: High temporal resolution multi-echo/multi-slice dynamic susceptibility contrast perfusion imaging using GRAPPA EPI. In *In Proceedings of the 14th Annual Meeting of ISMRM, Glasgow, Scotland*, volume 14, page 673.

- [Nyquist, 1928] Nyquist, H. (1928). Thermal Agitation of Electric Charge in Conductors. *Physical Review*, 32:110–113.
- [Ordidge et al., 1982] Ordidge, R., Mansfield, P., Doyle, M., and Coupland, R. (1982). Real time movie images by NMR. *The British journal of radiology*, 55(658):729–733.
- [Østergaard, 2005] Østergaard, L. (2005). Principles of cerebral perfusion imaging by bolus tracking. *Journal of Magnetic Resonance Imaging*, 22(6):710–717.
- [Østergaard et al., 1996a] Østergaard, L., Sorensen, A. G., Kwong, K. K., Weisskoff, R. M., Gyldensted, C., and Rosen, B. R. (1996a). High resolution measurement of cerebral blood flow using intravascular tracer bolus passages. Part II: Experimental comparison and preliminary results. *Magnetic Resonance in Medicine*, 36(5):726–736.
- [Østergaard et al., 1996b] Østergaard, L., Weisskoff, R. M., Chesler, D. A., Gyldensted, C., and Rosen, B. R. (1996b). High resolution measurement of cerebral blood flow using intravascular tracer bolus passages. Part I: Mathematical approach and statistical analysis. *Magnetic Resonance in Medicine*, 36(5):715–725.
- [Parrish and Hu, 1995] Parrish, T. and Hu, X. (1995). Continuous Update with Random Encoding (CURE): A New Strategy for Dynamic Imaging. *Magnetic Resonance in Medicine*, 33(3):326–336.
- [Paulson and Schmainda, 2008] Paulson, E. S. and Schmainda, K. M. (2008). Comparison of Dynamic Susceptibility-weighted Contrast-enhanced MR Methods: Recommendations for Measuring Relative Cerebral Blood Volume in Brain Tumors 1. *Radiology*, 249(2):601–613.
- [Pedersen et al., 2009] Pedersen, H., Kozerke, S., Ringgaard, S., Nehrke, K., and Kim, W. Y. (2009). k-t PCA: Temporally constrained k-t BLAST reconstruction using principal component analysis. *Magnetic Resonance in Medicine*, 62(3):706–716.
- [Penrose, 1955] Penrose, R. (1955). A generalized inverse for matrices. *Mathematical Proceedings of the Cambridge Philosophical Society*, 51:406–413.
- [Preibisch et al., 2003] Preibisch, C., Pilatus, U., Bunke, J., Hoogenraad, F., Zanella, F., and Lanfermann, H. (2003). Functional MRI using sensitivity-encoded echo planar imaging (SENSE-EPI). *Neuroimage*, 19(2):412–421.
- [Preibisch et al., 2008] Preibisch, C., Wallenhorst, T., Heidemann, R., Zanella, F. E., and Lanfermann, H. (2008). Comparison of parallel acquisition techniques generalized autocalibrating partially parallel acquisitions (GRAPPA) and modified sensitivity encoding (mSENSE) in functional MRI (fMRI) at 3T. *Journal of Magnetic Resonance Imaging*, 27(3):590–598.
- [Pruessmann, 2006] Pruessmann, K. P. (2006). Encoding and reconstruction in parallel MRI. *NMR in Biomedicine*, 19(3):288–299.
- [Pruessmann et al., 2001] Pruessmann, K. P., Weiger, M., Börnert, P., and Boesiger, P. (2001). Advances in sensitivity encoding with arbitrary k-space trajectories. *Magnetic Resonance in Medicine*, 46(4):638–651.
- [Pruessmann et al., 1999] Pruessmann, K. P., Weiger, M., Scheidegger, M. B., Boesiger, P., et al. (1999). SENSE: sensitivity encoding for fast MRI. *Magnetic Resonance in Medicine*, 42(5):952–962.
- [Purcell et al., 1946] Purcell, E. M., Torrey, H. C., and Pound, R. V. (1946). Resonance Absorp-

- tion by Nuclear Magnetic Moments in a Solid. *Physical Review*, 69:37–38.
- [Ra and Rim, 1993] Ra, J. B. and Rim, C. Y. (1993). Fast imaging using subencoding data sets from multiple detectors. *Magnetic Resonance in Medicine*, 30(1):142–145.
- [Rabi et al., 1938] Rabi, I., Zacharias, J., Millman, S., and Kusch, P. (1938). A New Method of Measuring Nuclear Magnetic Moment. *Physical Review*, 53:318–318.
- [Ramb, 2011] Ramb, R. (2011). Graphical Models in Time Series: From Basic Concepts to Latent Variables. Diplomarbeit (Diploma thesis), Philipps-Universität Marburg.
- [Ramb et al., 2013a] Ramb, R., Binter, C., Breuer, F., Kozerke, S., and Jung, B. (2013a). A g-factor metric for k-t-GRAPPA reconstructions. In *ISMRM workshop on Data Sampling and Image Reconstruction*.
- [Ramb et al., 2013b] Ramb, R., Binter, C., Breuer, F., Schultz, G., Zaitsev, M., Kozerke, S., and Jung, B. (2013b). A g-factor metric for k-t-GRAPPA reconstructions. In *Proceedings of the 21st Annual Meeting of ISMRM, Salt Lake City, USA*, page 4370.
- [Ramb et al., 2014a] Ramb, R., Binter, C., Schultz, G., Assländer, J., Breuer, F., Zaitsev, M., Kozerke, S., and Jung, B. (2014a). An analytical g-factor framework for k-t-GRAPPA/PEAK-GRAPPA. In *SFB workshop on Imaging with Modulated/Incomplete Data*.
- [Ramb et al., 2015a] Ramb, R., Binter, C., Schultz, G., Assländer, J., Breuer, F., Zaitsev, M., Kozerke, S., and Jung, B. (2015a). A g-factor metric for k-t-GRAPPA and PEAK-GRAPPA based parallel imaging. *Magnetic Resonance in Medicine*, 74(1):125–135.
- [Ramb et al., 2016a] Ramb, R., Christodoulou, A. G., Mader, I., Zaitsev, M., Liang, Z.-P., and Hennig, J. (2016a). High resolution CBV assessment with PEAK-EPI and PS-SPIRiT-EPI. In *Proceedings of the 24th Annual Meeting of ISMRM, Singapore*.
- [Ramb et al., 2013c] Ramb, R., Eichler, M., Ing, A., Thiel, M., Weiller, C., Grebogi, C., Schwarzbauer, C., Timmer, J., and Schelter, B. (2013c). The impact of latent confounders in directed network analysis in neuroscience. *Philosophical Transactions of the Royal Society of London A: Mathematical, Physical and Engineering Sciences*, 371(1997):20110612.
- [Ramb et al., 2014b] Ramb, R., Kellner, E., Dragonu, I., Testud, F., Mader, I., Hennig, J., Zaitsev, M., and Jung, B. (2014b). k-t-EPI: k-t-undersampled EPI acquisition and reconstruction in cerebral perfusion. In *Proceedings of the 22nd Annual Meeting of ISMRM, Milano, Italy*, page 4370.
- [Ramb et al., 2015b] Ramb, R., Levan, P., and Hennig, J. (2015b). PEAK-EPI: Feasibility and benefits of k-t-undersampled EPI acquisition and PEAK-GRAPPA reconstruction in fMRI. In *Proceedings of the 23rd Annual Meeting of ISMRM, Toronto, Canada*, page 3920.
- [Ramb et al., 2015c] Ramb, R., Levan, P., Zaitsev, M., and Hennig, J. (2015c). Feasibility of Resting-state fMRI in the orbitofrontal cortex with less distortion using PEAK-EPI. In *Proceedings of the 22nd Annual Meeting of OHBM, Honolulu, Hawaii, USA*.
- [Ramb et al., 2016b] Ramb, R., Mader, I., Jung, B., Hennig, J., and Zaitsev, M. (2016b). High resolution CBV assessment with PEAK-EPI: k-t-undersampling and reconstruction in echo planar imaging. *Magnetic Resonance in Medicine*, in press.
- [Ramb and Schultz, 2013] Ramb, R. and Schultz, G. (2013). Extended GRAPPA and Truncated SENSE: Separating Effects in Parallel Imaging. In *Proceedings of the 30th Annual Scientific*

Meeting of ESMRMB, Toulouse, France.

- [Riederer et al., 1988] Riederer, S. J., Tasciyan, T., Farzaneh, F., Lee, J. N., Wright, R. C., and Herfkens, R. J. (1988). MR fluoroscopy: Technical feasibility. *Magnetic Resonance in Medicine*, 8(1):1–15.
- [Robson et al., 2008] Robson, P. M., Grant, A. K., Madhuranthakam, A. J., Lattanzi, R., Sodickson, D. K., and McKenzie, C. A. (2008). Comprehensive quantification of signal-to-noise ratio and g-factor for image-based and k-space-based parallel imaging reconstructions. *Magnetic Resonance in Medicine*, 60:895–907.
- [Roemer et al., 1990] Roemer, P. B., Edelstein, W. A., Hayes, C. E., Souza, S. P., and Mueller, O. M. (1990). The NMR phased array. *Magnetic Resonance in Medicine*, 16(2):192–225.
- [Rosen et al., 1991a] Rosen, B. R., Belliveau, J. W., Aronen, H. J., Kennedy, D., Buchbinder, B. R., Fischman, A., Gruber, M., Glas, J., Weisskoff, R. M., Cohen, M. S., Hochberg, F. H., and Brady, T. J. (1991a). Susceptibility contrast imaging of cerebral blood volume: Human experience. *Magnetic Resonance in Medicine*, 22(2):293–299.
- [Rosen et al., 1991b] Rosen, B. R., Belliveau, J. W., Buchbinder, B. R., McKinstry, R. C., Porkka, L. M., Kennedy, D. N., Neuder, M. S., Fisel, C. R., Aronen, H. J., Kwong, K. K., Weisskoff, R. M., Cohen, M. S., and Brady, T. J. (1991b). Contrast agents and cerebral hemodynamics. *Magnetic Resonance in Medicine*, 19(2):285–292.
- [Rosen et al., 1990] Rosen, B. R., Belliveau, J. W., Vevea, J. M., and Brady, T. J. (1990). Perfusion imaging with NMR contrast agents. *Magnetic Resonance in Medicine*, 14(2):249–265.
- [Samsonov, 2008] Samsonov, A. A. (2008). On optimality of parallel MRI reconstruction in k-space. *Magnetic Resonance in Medicine*, 59(1):156–164.
- [Samsonov et al., 2006] Samsonov, A. A., Block, W. F., Arunachalam, A., and Field, A. S. (2006). Advances in locally constrained k-space-based parallel MRI. *Magnetic Resonance in Medicine*, 55(2):431–438.
- [Schmidt et al., 2005] Schmidt, C. F., Degonda, N., Luechinger, R., Henke, K., and Boesiger, P. (2005). Sensitivity-encoded (SENSE) echo planar fMRI at 3T in the medial temporal lobe. *Neuroimage*, 25(2):625–641.
- [Schmiedeskamp et al., 2012] Schmiedeskamp, H., Straka, M., Newbould, R. D., Zaharchuk, G., Andre, J. B., Olivot, J.-M., Moseley, M. E., Albers, G. W., and Bammer, R. (2012). Combined spin- and gradient-echo perfusion-weighted imaging. *Magnetic Resonance in Medicine*, 68(1):30–40.
- [Schmitt et al., 1998] Schmitt, F., Stehling, M. K., and Turner, R. (1998). *Echo-Planar Imaging: Theory, Technique, and Application*. Springer. ISBN-10: 3540631941.
- [Schnell et al., 2014] Schnell, S., Markl, M., Entezari, P., Mahadewia, R. J., Semaan, E., Stankovic, Z., Collins, J., Carr, J., and Jung, B. (2014). k-t GRAPPA accelerated four-dimensional flow MRI in the aorta: Effect on scan time, image quality, and quantification of flow and wall shear stress. *Magnetic Resonance in Medicine*, 72:522–533.
- [Schoenberg et al., 2007] Schoenberg, S. O., Baert, A., Dietrich, O., and Reiser, M. F. (2007). *Parallel imaging in clinical MR applications*. Springer Science & Business Media.
- [Schultz, 2013] Schultz, G. (2013). *Magnetic resonance imaging with nonlinear gradient fields: signal*

encoding and image reconstruction. Springer Spektrum. Available at <https://www.freidok.uni-freiburg.de/data/8706>.

- [Simonsen et al., 1999] Simonsen, C. Z., Østergaard, L., Vestergaard-Poulsen, P., Røhl, L., Bjørnerud, A., and Gyldensted, C. (1999). CBF and CBV measurements by USPIO bolus tracking: Reproducibility and comparison with Gd-based values. *Journal of Magnetic Resonance Imaging*, 9(2):342–347.
- [Skare et al., 2007] Skare, S., Newbould, R. D., Clayton, D. B., Albers, G. W., Nagle, S., and Bammer, R. (2007). Clinical multishot DW-EPI through parallel imaging with considerations of susceptibility, motion, and noise. *Magnetic Resonance in Medicine*, 57(5):881–890.
- [Sodickson and Manning, 1997] Sodickson, D. K. and Manning, W. J. (1997). Simultaneous acquisition of spatial harmonics (SMASH): Fast imaging with radiofrequency coil arrays. *Magnetic Resonance in Medicine*, 38(4):591–603.
- [Sodickson and McKenzie, 2001] Sodickson, D. K. and McKenzie, C. A. (2001). A generalized approach to parallel magnetic resonance imaging. *Medical Physics*, 28(8):1629–1643.
- [Stein and Shakarchi, 2011] Stein, E. M. and Shakarchi, R. (2011). *Fourier analysis: an introduction*, volume 1. Princeton University Press.
- [Sánchez-González et al., 2006] Sánchez-González, J., Tsao, J., Dydak, U., Desco, M., Boesiger, P., and Paul Pruessmann, K. (2006). Minimum-norm reconstruction for sensitivity-encoded magnetic resonance spectroscopic imaging. *Magnetic Resonance in Medicine*, 55(2):287–295.
- [Takhtajan, 2008] Takhtajan, L. A. (2008). *Quantum Mechanics for Mathematicians*. American Mathematical Society.
- [Torrey, 1956] Torrey, H. C. (1956). Bloch equations with diffusion terms. *Physical Review*, 104(3):563.
- [Tsao, 2002] Tsao, J. (2002). On the UNFOLD method. *Magnetic Resonance in Medicine*, 47(1):202–207.
- [Tsao et al., 2003a] Tsao, J., Boesiger, P., and Pruessmann, K. P. (2003a). k-t BLAST and k-t SENSE: Dynamic MRI with high frame rate exploiting spatiotemporal correlations. *Magnetic Resonance in Medicine*, 50(5):1031–1042.
- [Tsao et al., 2003b] Tsao, J., Kozerke, S., Boesiger, P., and Pruessmann, K. (2003b). Eight-fold acceleration in real-time cardiac imaging using kt BLAST and kt SENSE with SSFP and segmented EPI. In *In Proceedings of the 11th Annual Meeting of ISMRM*, volume 11, page 209.
- [Twieg, 1983] Twieg, D. B. (1983). The k-trajectory formulation of the NMR imaging process with applications in analysis and synthesis of imaging methods. *Medical Physics*, 10(5):610–621.
- [Uhlenbeck and Goudsmit, 1926] Uhlenbeck, G. E. and Goudsmit, S. (1926). Spinning electrons and the structure of spectra. *Nature*, 117:264–265.
- [van Osch et al., 2003] van Osch, M. J., Vonken, E.-j. P., Viergever, M. A., van der Grond, J., and Bakker, C. J. (2003). Measuring the arterial input function with gradient echo sequences. *Magnetic Resonance in Medicine*, 49(6):1067–1076.
- [Van Vaals et al., 1993] Van Vaals, J. J., Brummer, M. E., Thomas Dixon, W., Tuithof, H. H.,

- Engels, H., Nelson, R. C., Gerety, B. M., Chezmar, J. L., and Den Boer, J. A. (1993). "Keyhole" method for accelerating imaging of contrast agent uptake. *Journal of Magnetic Resonance Imaging*, 3(4):671–675.
- [Vidorreta et al., 2013] Vidorreta, M., Wang, Z., Rodríguez, I., Pastor, M. A., Detre, J. A., and Fernández-Seara, M. A. (2013). Comparison of 2D and 3D single-shot ASL perfusion fMRI sequences. *Neuroimage*, 66(0):662–671.
- [Walsh et al., 2000] Walsh, D. O., Gmitro, A. F., and Marcellin, M. W. (2000). Adaptive reconstruction of phased array MR imagery. *Magnetic Resonance in Medicine*, 43(5):682–690.
- [Wang et al., 2001] Wang, J., Kluge, T., Nittka, M., Jellus, V., Kuehn, B., and Kiefer, B. (2001). Parallel acquisition techniques with modified SENSE reconstruction mSENSE. In *Proceedings of the First Würzburg Workshop on Parallel Imaging Basics and Clinical Applications*, page 89.
- [Wang et al., 2005a] Wang, J., Zhang, B., Zhong, K., and Zhuo, Y. (2005a). Image Domain Based Fast GRAPPA Reconstruction and relative SNR degradation Factor. In *Proceedings of the 13th Annual Meeting of ISMRM, Miami, U.S.A.*, page 2428.
- [Wang et al., 2005b] Wang, Z., Wang, J., Connick, T. J., Wetmore, G. S., and Detre, J. A. (2005b). Continuous ASL (CASL) perfusion MRI with an array coil and parallel imaging at 3T. *Magnetic Resonance in Medicine*, 54(3):732–737.
- [Wansapura et al., 1999] Wansapura, J. P., Holland, S. K., Dunn, R. S., and Ball, W. S. (1999). NMR relaxation times in the human brain at 3.0 tesla. *Journal of magnetic resonance imaging*, 9(4):531–538.
- [Weisskoff et al., 1994] Weisskoff, R., Zuo, C. S., Boxerman, J. L., and Rosen, B. R. (1994). Microscopic susceptibility variation and transverse relaxation: Theory and experiment. *Magnetic Resonance in Medicine*, 31(6):601–610.
- [Wood and Henkelman, 1986] Wood, M. L. and Henkelman, R. M. (1986). Suppression of respiratory motion artifacts in magnetic resonance imaging. *Medical Physics*, 13:794–805.
- [Xiang and Henkelman, 1993] Xiang, Q.-S. and Henkelman, R. M. (1993). k-Space description for MR imaging of dynamic objects. *Magnetic Resonance in Medicine*, 29(3):422–428.
- [Yeh et al., 2005] Yeh, E., McKenzie, C., Ohlinger, M., and Sodickson, D. (2005). Parallel magnetic resonance imaging with adaptive radius in k-space (PARS): Constrained image reconstruction using k-space locality in radiofrequency coil encoded data. *Magnetic Resonance in Medicine*, 53:1383–1392.
- [Youla and Webb, 1982] Youla, D. C. and Webb, H. (1982). Image Restoration by the Method of Convex Projections: Part 1 - Theory. *IEEE Transactions on Medical Imaging*, 1(2):81–94.
- [Zaitsev et al., 2005] Zaitsev, M., D'Arcy, J., Collins, D. J., Leach, M. O., Zilles, K., and Shah, N. J. (2005). Dual-contrast echo planar imaging with keyhole: application to dynamic contrast-enhanced perfusion studies. *Physics in Medicine and Biology*, 50(19):4491.
- [Zaitsev et al., 2006] Zaitsev, M., Dold, C., Sakas, G., Hennig, J., and Speck, O. (2006). Magnetic resonance imaging of freely moving objects: prospective real-time motion correction using an external optical motion tracking system. *Neuroimage*, 31(3):1038–1050.
- [Zaitsev et al., 2001] Zaitsev, M., Zilles, K., and Shah, N. (2001). Shared k-space echo planar imaging with keyhole. *Magnetic Resonance in Medicine*, 45(1):109–117.

[Zhang et al., 2011] Zhang, J., Liu, C., and Moseley, M. E. (2011). Parallel reconstruction using null operations. *Magnetic Resonance in Medicine*, 66(5):1241–1253.

Acronyms

- ACS** autocalibration signal [66](#)
- ADC** analog-digital converter [27](#)
- bSSFP** balanced steady state free precession [46](#), [106](#)
- CBV** cerebral blood volume [88](#), [126](#), [135](#)
- DSC** dynamic susceptibility contrast [79](#), [87](#), [125](#), [126](#), [143](#), [152](#)
- EPI** echo planar imaging [25](#), [44](#), [76](#), [87](#)
- ETS** echo time shifting [127](#)
- extGRAPPA** extended GRAPPA [96–98](#)
- FLAIR** fluid attenuated inversion recovery [45](#), [143–145](#)
- FoV** field of view [35](#), [42](#)
- FWHM** full width at half maximum [37](#), [39](#), [51](#), [88](#), [115](#), [136](#)
- Gd** gadolinium [87](#)
- GE** gradient echo [45](#), [54](#), [87](#)
- GE-EPI** echo planar imaging with gradient echoes [45](#)
- GRAPPA** generalized autocalibrating partially parallel acquisitions [59](#), [61](#), [66](#)
- MR** magnetic resonance [11](#)
- MRI** magnetic resonance imaging [11](#), [13](#), [30](#), [35](#), [54](#), [59](#)
- NMR** nuclear magnetic resonance [9](#)
- PEAK-GRAPPA** parallel MRI with extended and averaged GRAPPA kernels [84](#)
- POCS** projection onto convex sets [55](#), [131](#)
- PS** partial separability [84](#), [157](#)
- PSF** point spread function [37–39](#), [50](#)
- RF** radiofrequency [15](#), [16](#)
- ROI** region of interest [43](#)
- SENSE** sensitivity encoding [59](#), [61](#)

SMASH simultaneous acquisition of spatial harmonics [59](#), [61](#), [65](#)
SNR signal-to-noise ratio [25](#), [39](#), [40](#), [42](#), [51](#)
SPiRiT iterative self-consistent parallel imaging reconstruction from arbitrary k-space [157](#)
SW Sliding Window [86](#), [105](#)
tPSF temporal point spread function [106](#), [115](#)
tRMSE temporal root mean square error [106](#), [122](#)
trSENSE truncated SENSE [96](#), [97](#)
tSNR temporal signal-to-noise-ratio [134](#)
UNFOLD unaliasing by Fourier-encoding the overlaps using the temporal dimension [82](#), [86](#)
WHO world health organization [143–145](#)

List of symbols

\check{A}, \check{a} operators are labeled by check marks [1](#)

\mathbf{A}, \mathbf{a} vectors are denoted with bold symbols [1](#)

A^* complex conjugate of A [1](#)

A^H Hermitian transpose of A [1](#)

α_{fa} flip angle [17, 47](#)

$\mathbf{B}_0 = (0, 0, B_0)^T$ static magnetic field (flux) [12](#)

B_0 field strength [12, 13, 16, 29, 51](#)

$\mathbf{B}_1(t) = (B_{1,x}(t), B_{1,y}(t), 0)^T$ time-dependent magnetic field / radiofrequency (RF) pulse [15, 16, 29](#)

$B_1^e(t)$ pulse envelope function [16, 26](#)

BW_f frequency bandwidth [22, 47](#)

BW, BW_{fe} bandwidth per pixel [47, 51](#)

BW_{pe} bandwidth per pixel in phase encoding direction [49, 51](#)

k_B Boltzmann constant [13, 22](#)

$\chi_{\mathbf{FoV}}, \chi_{\mathcal{K}_{finite}}, \chi_{\mathcal{K}_{finite,N}}, \chi_{\mathcal{K}_T}$ characteristic function [34, 37, 38, 50](#)

c coil sensitivities [19, 59](#)

\hat{c} in vivo coil sensitivities [66, 67](#)

$C_\alpha, C_\alpha^{\text{all}}$ diagonal matrix with coil sensitivities of coil α , applicable to a vector of pixels or - if superscript 'all' is used - to a vector of pixels and coils [94](#)

$\check{C}^{\text{fold}}, \check{C}_p^{\text{fold}}$ folding matrix, indexed to reference a specific pixel [64, 65](#)

$C^{\text{unfold}}, C_p^{\text{unfold}}$ unfolding matrix, indexed to reference a specific pixel [65, 94](#)

$\tilde{c}_{\alpha,\beta}$ vector that represents the coil sensitivity unfolding process from source coil β to target coil α [94](#)

$\tilde{C}_{\alpha,\beta}$ two-dimensional representation of $\tilde{c}_{\alpha,\beta}$ [95](#)

\tilde{C}_{x_p} matrix representation of the coil sensitivity based reconstruction weights of all target and source coils, fixing a single pixel [97](#)

$d, d_n, d_{n,\alpha}, d_{n,t,\alpha}$ the set of data samples of the MRI signal, also indexed to reference an individual sample n , a coil α or a time frames t [30, 31, 35, 36, 59, 80](#)

\hat{d} (noise affected) reconstructed set of data samples of the MRI signal 41

$\hat{\mathbf{w}}_{m,\alpha}, \hat{\mathbf{w}}_{m,\alpha}^\dagger$ vectorial representation of the reconstruction weights 67, 68

\mathbf{d}^{zf} vectorized zero-filled data samples of the MRI signal 55

$d^{\text{zf},2\text{D}}, d_\alpha^{\text{zf},2\text{D}}$ two-dimensional representation of the set of zero-filled data samples of the MRI signal, also indexed to reference individual coils 55, 69, 95

$d^{\text{zf},3\text{D}}, d_\alpha^{\text{zf},3\text{D}}$ three-dimensional (two spatial, one temporal dimension) representation of the set of zero-filled data samples of the MRI signal, also indexed to reference individual coils 85, 101

$\hat{d}^{\text{sub},2\text{D}}, \hat{d}_\alpha^{\text{sub},2\text{D}}$ noise affected two-dimensional representation of the reconstructed set of sub-Nyquist sampled data, as a result from parallel imaging reconstruction, also indexed to reference individual coils 69, 95

$\hat{d}^{\text{sub},3\text{D}}, \hat{d}_\alpha^{\text{sub},3\text{D}}$ noise affected three-dimensional (two spatial, one temporal dimension) representation of the reconstructed set of sub-Nyquist sampled data, as a result from the parallel imaging reconstruction, also indexed to reference individual coils 85, 101, 134

\check{D}^{ACS} in vivo encoding matrix 67

$\Delta R_2^*(t), \Delta \hat{R}_2^*(\mathbf{x}_p, t)$ dynamic changes of $1/T_2^*$, estimates of the rates for individual pixels 88, 135

$\Delta \mathbf{r}_s$ local distortion due to local field inhomogeneities 53

\mathcal{DFT} discrete Fourier transform 55, 64, 101

\mathcal{DFT}^{-1} discrete inverse Fourier transform 39, 70, 101

E Fourier encoding kernel 29

E_c coil sensitivity and Fourier encoding kernel 62

E_{ACS} in vivo sensitivity and Fourier encoding kernel 66

\check{E} encoding operator (depends on the encoding kernel) 62

$\varepsilon_d(k_n), \varepsilon_d(\mathbf{k}_k, \alpha), \varepsilon_I(x_m), \varepsilon_I(\mathbf{x}_p), \varepsilon_I^{\text{sub}}(\mathbf{x}_p, \alpha), \varepsilon_I^{\text{full}}(\mathbf{x}_p, \alpha), \varepsilon_I^{\text{sub}}(\mathbf{x}_p, \alpha), \tilde{\varepsilon}_I^{\text{full}}(\mathbf{x}_p, f, \alpha), \tilde{\varepsilon}_I^{\text{sub}}(\mathbf{x}_p, f, \alpha)$ random variables to describe data noise or image noise at certain k-space, pixel coordinates or temporal frequencies, and for individual coils, superscripts are used to indicate the data sampling and reconstruction involved 40, 41, 70, 71, 74, 75, 104

$\varepsilon_{I_\alpha}^{\text{sub}}, \varepsilon_{I_\beta}^{\text{fold}}$ two-dimensional representation of random variables to describe image noise of a set of samples or pixels for individual coils, superscripts are used to indicate the data sampling and reconstruction involved 74

$\tilde{\varepsilon}_{I_\alpha}^{\text{sub},3\text{D}}, \tilde{\varepsilon}_{I_\beta}^{\text{fold},3\text{D}}$ three-dimensional (two spatial, one temporal dimension) representation in x-f-space of random variables to describe image noise of a set of samples or pixels for individual coils, superscripts are used to indicate the data sampling and reconstruction involved 103

$\mathbf{FoV} := [-\frac{FoV}{2}, \frac{FoV}{2}]$ field of view along one dimension 34, 35

FoV, FoV_x, FoV_y length of the field of view along one dimension 35, 39

\mathcal{FT} Fourier transform 29

\mathcal{FT}^{-1} inverse Fourier transform 30, 37, 38, 50

$\mathbf{G}(t) = (G_x(t), G_y(t), G_z(t))^T$ gradients 26

γ gyromagnetic ratio 12, 13, 51

$g_{\mathbf{x}_p, \alpha}, g_{\mathbf{x}_p}$ uncombined and combined g-factor 73, 74, 76

$g_{\mathbf{x}_p f, \alpha}, g_{\mathbf{x}_p f}$ uncombined and combined g-factor in x-f-space of k-t-GRAPPA 104

$\hat{g}_{\mathbf{x}_p}^{\text{avg}}$ total g-factor of k-t-GRAPPA 105

$\hat{g}_{\mathbf{x}_p f}$ statistically derived g-factor in x-f-space of k-t-GRAPPA 109

$\hat{g}_{\mathbf{x}_p}^{\text{avg}}$ statistically derived temporally averaged g-factor of k-t-GRAPPA 109

$\mathbf{B}_{G_{\text{fe}}}(\mathbf{r}, t) = (0, 0, G_{\text{fe}}(t)x)^T$ frequency encoding gradient 27

$\mathbf{B}_{G_{\text{pe}}}(\mathbf{r}, t) = (0, 0, G_{\text{pe}}(t)y)^T$ phase encoding gradient 28

$\mathbf{B}_{G_{\text{slc}}}(\mathbf{r}, t) = (0, 0, G_{\text{slc}}(t)z)^T$ slice selection gradient 26

\mathcal{H} Hilbert space 9

\mathcal{H}^* dual Hilbert space 10

\mathcal{H}_s spin Hilbert space 11

$\mathbb{1}_{N_{\text{smp}}}, \mathbb{1}_{N_{\text{smp}} N_{\text{coils}}}$ identity matrix 71, 72

I, I^\dagger, \hat{I} general image representation, the additional dagger marks optimality in the case of a set of feasible image representations, the additional hat marks reconstructed images that are affected by image noise 31, 36, 41

$\hat{\mathbf{I}}$ vectorial image representation 63

$I^{\text{sub}}, \hat{I}^{\text{sub}}, \hat{I}_\alpha^{\text{sub}}$ (noise affected) two-dimensional image representation as a result from the parallel image reconstruction process from sub-Nyquist sampled data, also indexed to reference individual coils 70, 74, 76, 95

$\hat{\mathbf{I}}^{\text{fold}}, \hat{\mathbf{I}}_\alpha^{\text{fold}}$ vectorial image representation that contain fold-over artifacts, resulting from Fourier image reconstruction of sub-Nyquist sampled data, also indexed to reference individual coils 94

$I^{\text{fold}}, \hat{I}^{\text{fold}}, \hat{I}_\alpha^{\text{fold}}$ (noise affected) two-dimensional image representation that contain fold-over artifacts, resulting from Fourier image reconstruction of sub-Nyquist sampled data, also indexed to reference individual coils 70, 74, 76, 95

$\hat{I}^{\text{sub}, 3\text{D}}, \hat{I}_\alpha^{\text{sub}, 3\text{D}}, \hat{I}_t^{\text{sub}, 3\text{D}}$ noise affected three-dimensional (two spatial, one temporal dimension) image representation as a result from the parallel image reconstruction process from sub-Nyquist sampled data, also indexed to reference individual coils or time frames 85, 101, 102, 106

$\tilde{I}^{\text{fold}, 3\text{D}}, \tilde{I}_\alpha^{\text{fold}, 3\text{D}}$ noise affected three-dimensional (two spatial, one temporal dimension) image representation in x-f-space containing fold-over artifacts over temporal frequencies, as a

result from Fourier image reconstruction of sub-Nyquist sampled data, also indexed to reference individual coils [101–103](#)

$I_t^{\text{full,3D}}, I_t^{\text{full,3D}}$ three-dimensional image representation of a Fourier image reconstruction based on Nyquist-sampled data, also indexed to reference individual time frames [106](#)

$\tilde{I}_\alpha^{\text{sub,3D}}, \tilde{I}_\alpha^{\text{sub,3D}}$ noise affected three-dimensional (two spatial, one temporal dimension) image representation in x-f-space containing fold-over artifacts over temporal frequencies, as a result from image reconstruction of sub-Nyquist sampled data, also indexed to reference individual coils [103](#)

$\mathbf{k} := (k_x, k_y)^T$ k-space coordinates of frequency and phase [28](#)

\mathcal{K}_{smp} sampled k-space coordinates / k-space trajectory [30](#)

$\delta_{a,b}$ Kronecker delta [64, 105](#)

ε_{jkl} Levi-Civita symbol [11](#)

$m_\perp(\mathbf{r}, t)$ spatial magnetization density with spatial and temporal dependency [19](#)

$m_\perp^{\Delta\omega}(\Delta\omega, t)$ spectral magnetization density with resonance frequency and temporal dependency [19, 20](#)

$m_\perp(\mathbf{r}, 0)$ spatial magnetization density immediately after RF pulse excitation [19, 20, 27](#)

$\mathbf{M} := (M_x, M_y, M_z)^T$ macroscopic magnetization [13](#)

$\mathbf{M}^0 = (0, 0, M_z^0)^T$ macroscopic magnetization of the thermal equilibrium [13](#)

\mathbf{M}_{rot} (Larmor- or RF-)rotating frame of reference [15, 17](#)

$M_\parallel := M_z$ longitudinal magnetization [13, 18](#)

$M_\perp := M_x + iM_y$ transverse magnetization [13, 18](#)

N_{coils} number of coils [22, 59, 80](#)

N_{noise} number of noise samples [22](#)

$N_{\text{pix}} = N_x N_y$ number of pixels used in the image reconstruction, where N_x and N_y denote samples along the two image dimensions [39, 40, 60](#)

$N_{\text{smp}} = N_{\text{fe}} N_{\text{pe}}$ number of signal samples, where N_{fe} and N_{pe} denote samples along the frequency and phase encoding direction, respectively [30, 36, 39, 54, 59, 80](#)

$N_{\text{fe}}^{\text{ACS}}, N_{\text{pe}}^{\text{ACS}}$ number of ACS samples along frequency or phase encoding direction [67](#)

$B_{\text{fe}}, B_{\text{pe}}$ number of source samples along frequency or phase encoding direction addressed by the GRAPPA reconstruction kernel [67, 96, 98](#)

N_s number of spins in an ensemble [13](#)

N_{time} number of time frames [79, 80](#)

$\Delta\omega_{\text{cs}}$ chemical shift of Larmor frequencies between two types of tissue [52](#)

ω_{rf} excitation frequency [16, 20, 25](#)

Ω domain over which the two-dimensional image representation is defined [31, 35](#)

ω_0 Larmor frequency 12, 25, 51

Ω_ε sample space of a Gaussian distributed random variable 21

$p_\alpha(\mathbf{x}_m), p_\alpha, p_\alpha^{2D}, p_\alpha^{3D}, \mathbf{p}, \mathbf{p}_{\mathbf{x}_p}, \tilde{\mathbf{p}}_{\mathbf{x}_p f}$ coil weightings for the combination of images from different coils 60, 76, 85, 102, 104

$\mathbf{x}_p = (x_p, y_p)^T$ pixel coordinates in two-dimensional imaging 40, 71

\hbar Planck's constant 11–13

Ψ_{coils} receive coil covariance matrix 22, 60, 71

Ψ sample noise covariance matrix 71

$\hat{\Psi}, \hat{\Psi}^{\text{full}}$ image noise covariance matrix, superscripts are used to indicate the data sampling and reconstruction involved 71, 73

$\mathbf{r} := (x, y, z)^T$ spatial coordinates in \mathbb{R}^3 9, 25, 26

R reduction factor 54, 56, 65, 81

R_{net} net reduction factor 57, 133

s the complex MR signal 20, 21, 79

\hat{s}_0 estimate of the mean baseline magnitude signal 88

\check{S} sampling operator that selects samples according to the k-space coordinates / k-space trajectory 31, 36

\mathcal{C} set of coils 62

\mathcal{K} k-space described as set of k-space vectors or k-space coordinates 28

\mathcal{T} set of time frames 80

$\mathcal{F}_{\Delta t}$ set of resolved temporal frequencies 103

$\sigma^2(\cdot), \sigma(\cdot)$ variance and standard deviation 22, 40

σ_{cs} relative chemical shift factor of Larmor frequencies between two types of tissue 52

σ_{fe}, σ_{pe} standard deviation of the Gaussian kernel along frequency and phase encoding direction 97

$\check{\boldsymbol{\mu}} = (\check{\mu}_x, \check{\mu}_y, \check{\mu}_z)^T$ magnetic moment operator 12

$\check{\mathbf{S}} = (\check{S}_x, \check{S}_y, \check{S}_z)^T$ spin operator 11, 12

\tilde{s} the free induction decay MR signal with respect to k-space coordinates 29, 80

$[t_{\text{ADC},0}, t_{\text{ADC},1}]$ time interval for the analog-digital converter 27

$[t_{fe,0}, t_{fe,1}]$ time interval for the frequency encoding gradient 27, 28

$[t_{pe,0}, t_{pe,1}]$ time interval for the phase encoding gradient 28

$[t_p,0], t_p,1]$ time interval for the RF-pulse 15, 16, 27

$[t_{\text{slc},0}, t_{\text{slc},1}]$ time interval for the slice selection gradient 26, 28

- T_1 relaxation of the recovery of the longitudinal magnetization 14, 18
- T_2 relaxation of the transverse component 14, 18
- T_2^* relaxation of the transverse component when taking spectral deviations and the dephasing due to static field inhomogeneities into account 20, 46
- TE, TE_{eff} echo time or effective echo time 47, 49
- T_s absolute temperature 13, 22
- T_{es} time interval of echo spacing in EPI 48, 51
- T_{ACQS} time of image acquisition to sample one complete MR image 47
- $\text{tPSF}_{x_p, \alpha}(f), \text{tPSF}_{x_p}(f)$ the temporal point spread function over temporal frequencies for a reconstructed pixel (with respect to a coil) 106
- TR time of repetition 47
- $\text{tRMSE}(x_p)$ the temporal root mean square error in a reconstructed pixel 106
- $\text{tSNR}(x_p)$ the temporal signal-to-noise in a reconstructed pixel 134
- U raw MR signal / voltage induced in a coil according to Faraday's law of induction 19
- U_ε 'noise' voltage / voltage induced in a coil according to Faraday's law of induction without preceding RF pulse excitation 21, 22
- V imaged volume 25
- $w_{\alpha, \beta}^{2D}$ two-dimensional representation of the reconstruction weights as a convolution kernel, indexed to reference the target and source coils 69
- W_{x_p} matrix representation of the reconstruction weights in image space of all target and source coils, fixing a single pixel 74, 97
- $W_{\alpha, \beta}^{2D}$ two-dimensional representation of the reconstruction weights in image space, indexed to reference the target and source coils 70, 74, 76
- $w_{\alpha, \beta}^{3D}$ three-dimensional (two spatial, one temporal dimension) representation of the reconstruction weights as a convolution kernel, indexed to reference the target and source coils 85, 101
- $W_{x_p, f}$ matrix representation of the reconstruction weights in image space of all target and source coils, fixing a single pixel 103
- $\tilde{W}_{\alpha, \beta}^{3D}$ three-dimensional (two spatial, one temporal dimension) representation of the reconstruction weights in x-f-space, indexed to reference the target and source coils 101, 103

Acknowledgements

Jürgen Hennig	for guidance and mentoring, for trust and confidence, for providing the fertile ground for individual developments
Maxim Zaitsev	for sharing his knowledge on EPI and helpful discussions
Bernd Jung	for initializing the project and showing me the ropes (also literally in the alps)
Christian Binter and Sebastian Kozerke	for the open and constructive co-operation
Irina Mader	for the comprehensive clinical input
Hansjörg Mast	for the patient measurements
Ralf Deichmann	for sharing his EPI sequence which served as a basis for the sequence development
Elias Kellner	for sharing his perfusion analysis tool
Zhi-Pei Liang and his group	for inspiring conversations and sharing their knowledge with me
the Medical Physics group in Freiburg	for the wonderful group atmosphere, the funniest summer and winter events, discussions and proofreadings, for friendships
meiner großen Familie	für ihre Vielfältigkeit, für ihr Verständnis, für ihr Vertrauen in mich, für ihre fortwährende Unterstützung
Jakob	für so viel und dafür, dass er da ist